



HAL
open science

Ultrafast Laser Processing using Optimized Spatial Beam Control

Cyril Mauclair

► **To cite this version:**

Cyril Mauclair. Ultrafast Laser Processing using Optimized Spatial Beam Control. Optics / Photonics. Université Jean Monnet Saint Etienne, 2019. tel-04506968

HAL Id: tel-04506968

<https://hal.science/tel-04506968>

Submitted on 15 Mar 2024

HAL is a multi-disciplinary open access archive for the deposit and dissemination of scientific research documents, whether they are published or not. The documents may come from teaching and research institutions in France or abroad, or from public or private research centers.

L'archive ouverte pluridisciplinaire **HAL**, est destinée au dépôt et à la diffusion de documents scientifiques de niveau recherche, publiés ou non, émanant des établissements d'enseignement et de recherche français ou étrangers, des laboratoires publics ou privés.

Copyright

Ultrafast Laser Processing using Optimized Spatial Beam Control

Dr. Cyril Mauclair
Laboratoire Hubert Curien - IUT St-Etienne - 42000 St-Etienne
cyril.mauclair@univ-st-etienne.fr

July 2, 2019

Writing the so-called 'HDR' manuscript (standing for the french 'Habilitation à Diriger la Recherche') is a somewhat frightening exercise. It is naturally difficult to look back and try to summarize years of research and collaborations. More delicate is to present the advances in the frame of the most recent scientific and technological results while trying to correctly describe the state of the art. Anticipating the next developments of a fast-evolving field of research such as ultrafast laser machining is not an easier task either. However, this step appears to be indispensable in a researcher's career when the time comes to choose the next research efforts to be conducted. I would like here to use once and only once the famous sentence that this manuscript is written "to the best of my knowledge", hoping this will excuse any shortcomings and mistakes in describing the state of the art of ultrafast laser micro machining and how my work stands in this international context. Let me clarify straight away the unclear expression "my work". Behind this, one has to realize that this involve far more than what my brain alone could have ever produce, even under the most efficient drugs. Indeed, a very large group of people including patient and passionate PhD supervisors and co-supervisors, friendly and hard-working colleagues, long-suffering PhD students and postdocs altogether with an enthusiastic and caring community has to be recognized here. I also want to add on the list the many people from other scientific and research communities. It is puzzling how multi disciplinary approaches can bring together the right people at the right moment, creating the appropriate frame for breakthroughs and innovative work. I will try to give some examples of this fact that I had the chance to notice during my career. Ultrafast laser pulses have also this unique property to trigger a deep curiosity in anyone who comes to deal with them. Sometimes appearing as a 'magical solution' but still being in competition with much more experienced and mastered processes, this short wavepackets of light have not ceased to surprise the world and find more and more applications, not to mention here the 2018's Nobel Prize recognizing as a major breakthrough the possibility to amplify these pulses. I hope that this manuscript, with the efforts made to render the reading accessible and the concepts easily understandable, can trigger such interest to the largest possible audience.

Contents

I	Resume	7
1	Short Resume	9
2	Research work and Publications	13
2.1	Articles in peer-reviewed journals	13
2.2	Contributions to conferences	16
2.2.1	International conferences with proceedings	16
2.2.2	Invited talks (international conferences)	20
2.2.3	Invited talks (national conferences)	20
2.2.4	Conference organization participation	20
2.3	Books and contribution to collective textbooks	20
2.3.1	PhD Thesis	21
2.3.2	Projects reports	21
2.4	Supervision and patents	21
2.4.1	PhD thesis	21
2.4.2	Postdoctoral	22
2.4.3	Masters	22
2.4.4	Patents	22
2.5	International and national projects with financial support	22
2.5.1	Project correspondant for the laboratoire H. Curien	22
2.5.2	Also involved in :	23
2.6	Communications overview	24
2.7	Overview of PhD and Postdoc supervision	24
II	Ultrafast Laser Processing using Optimized Spatial Beam Control	25
3	Introduction	27
3.1	Local environment	27
3.2	Scientific and technological challenges	27
3.3	Outline	28
4	Spatial Shaping of ultrashort laser irradiations - Amplitude modulation	31
4.1	Basics	31
4.2	Spatial control through beam deflection - scanning	33
4.3	Beam truncation and imaging	36
4.4	Truncation effect on the focal volume	38
4.5	Advanced amplitude modulation - GPC	39
4.6	Conclusion	40

5	Spatial Shaping of ultrashort laser irradiations - Wavefront modulation	41
5.1	Basics	41
5.2	Parallel processing in 2D-3D with multiple laser spots	42
5.3	Shaping of the laser spot itself, or 'continuous' beam shaping	50
5.4	Shaping along the optical axis, the case of non-diffractive beams.	53
5.5	Conclusion	53
6	In-situ characterization of ultrashort laser irradiations	57
6.1	Motivation	57
6.2	In situ probing of bulk nanostructuring in fused silica	57
6.2.1	Ultrafast laser generation of bulk nanostructures	57
6.2.2	In-situ UV diffraction probing of the bulk nanostructures	59
6.2.3	Tuning the ultrafast irradiation from the in-situ UV probe	59
6.3	Structured Illumination Microscopy - SIM - for in-situ imaging	60
6.3.1	Introduction	60
6.3.2	Experimental set-up and performance of the SIM microscope	61
6.3.3	In-Situ LIPSS monitoring with SIM	63
6.4	Conclusion	68
7	Conclusion and perspectives	69
7.1	Spatial Beam Shaping	69
7.1.1	Short term developments	69
7.1.2	Long term : Combining Deflection and spatial beam shaping for new structuring	72
7.2	In-Situ Monitoring	72
7.2.1	Short term directions of research	73
7.2.2	Long term : increasing the resolving power	79
7.3	Connecting in-situ monitoring to optimization self-learning loops for applications	80
7.3.1	Laser beam control and in-situ monitoring for surface wettability control	84
7.3.2	Laser beam control and in-situ monitoring for presbyopia counteracting	85
III	Selected Articles	103
7.4	Dynamic ultrafast laser beam tailoring for multispot photo-inscription of photonic devices in bulk transparent materials	105
7.5	Ultrafast laser micro-cutting of stainless steel and PZT using a modulated line of multiple foci formed by spatial beam shaping	118
7.6	Ultrafast laser spatial beam shaping based on Zernike polynomials for surface processing	125
7.7	Delivery of molecules into human corneal endothelial cells by carbon nanoparticles activated by femtosecond laser	137
7.8	In-situ high-resolution visualization of laser-induced periodic nanostructures driven by optical feedback	151

Part I

Resume

Chapter 1

Short Resume

Dr. Ing. Mauclair Cyril

phone: +33 (0)6 88 29 00 30

cyril.mauclair@univ-st-etienne.fr

39 ans, married, 6 children

Professional

- Since 2018 Expert for the French ANR (Agence Nationale de la Recherche) and German DFG (Deutsche Forschungsgemeinschaft).
- Since 2016 Scientific consultant Start-up Keranova – Ophthalmic surgery machine (co-founder)
- Since 2011 **Assistant Professor** Lab. H. Curien St-Etienne – IUT GEII Saint Etienne
Spatial and temporal control of ultrashort laser pulses for micro/nano structuring.
-Co-supervision of **6 thesis, 5 post docs** et 2 Master.
Scientific animator GIE Manutech-USD (Projet Invest. Avenir ANR Equipex – 8M€)
- Since 2009 **Referee** Optics Express, Optics Letters, Journal of Optical Society of America Optics B, Optical Engineering, Optics and Lasers in Engineering, Journal of Laser Micro Nanomachining, Plos One.

Education

- 2006-2010 **PhD.** Photonics in cotutelle **French-Germany**, Freie Universität Berlin and Université J. Monnet St-Etienne (Max-Born Institut, Berlin and Lab. H. Curien, St-Etienne)
Spatio-temporal Ultrafast Laser Tailoring for Bulk Functionalization of Transparent Materials. Magna Cum Laude
- 2003-2006 **Master-Engineer** Telecom ST-Etienne (Optics Electronics) **Graduated First**

Volunteer

- 2013-2014 LDS Helping hands – Emmaüs (42)
- 2003/04/05 Banque alimentaire, 42.
- 2001-2003 Full-Time Missionary for the LDS Church - Greece Athens Mission

Languages et Computing

English: fluent (TOEFL 673/677), Greek: fluent, German: middle level, Spanish: basics
Computing: LabView, Matlab, C++, Origin, PSpice, Proteus Orcad, Texmaker, Office

Scientific publications

More than **70** articles and proceedings, 3 patents (1 currently submitted), see the Publication list hereafter¹

Scientific responsibilities

Coordinateur for **9** scientific projects, participation to **8** additional projects (international and national partners, see hereafter).

¹ See also this link: https://scholar.google.fr/citations?hl=fr&user=qJteuIAAAAJ&view_op=list_works&sortby=pubdate

Teachings (>2000h):

- 2011-Today: **Assistant Professor** (Maître de Conférences) IUT GEII St Etienne :
Lectures and labs in electronics, image treatment, physics, electromagnetism:
(~200h per year)
Lectures on Lasers and applications (Telecom St Etienne ~ 20h per year)
Lectures « Semaine de Photonique » (Telecom St Etienne, ~ 15h per year)
- 2006-2010 **Teaching assistant** in Photonics (~ 64h per year, Telecom St-Etienne)
- 2005 **Teacher** Acadomia St-Etienne (4 mois): Graduate level
- 2004-2005 **Teacher** English at Telecom St-Etienne: TOEFL preparation
- 2001 **Teaching assistant** in Physics Physique at l'UFR Sciences d'Angers

Organisation of the « **Semaine de la photonique** » 2012-2019 (15h per year - ~ 30 participants). One teaching week with invited lectures and labs in the Laboratoire Hubert Curien for Telecom St Etienne and Telecom Physique Strasbourg engineer students and for the doctoral school of University Jean Monnet St Etienne.

- Lectures on the fundamental aspects and the applications related to femtosecond laser pulses : ultrashort pulse generation, spatial and temporal shaping, applications examples with laboratory demonstrations in the Laboratoire Hubert Curien of pulse manipulation techniques, pulse characterization, surface and bulk structuring and nonlinear propagation effects.
- Invitation of various experts for lectures S. Valette MCF LTDS – femtosecond laser surface treatment for surface wettability and adhesion functions, S. Residori DR CNRS INPHYNI – nonlinear optics in liquid crystals, R. Stoian DR CNRS Lab H. Curien – ultrashort pulse generation and manipulation techniques and interaction with matter, JP Colombier Prof. Lab H Curien – Numerical simulation of ultrashort pulse propagation. Prof. P. Gain BIIGC (directeur service Ophtalmologie CHU St Etienne), applications of ultrashort pulses in ophtalmology.

Administrative (IUT – Technical University Institute):

2012-Today: Organization of the **Teaching evaluation** by the students IUT (online survey), supervision of the **tutoring, internship** supervision (5 per year), participation to student workshops (3-5 per year).

Chapter 2

Research work and Publications

2.1 Articles in peer-reviewed journals

1. Nicolas Huot, Razvan Stoian, Alexandre Mermillod-Blondin, Cyril Mauclair, and Eric Audouard (2007). “Analysis of the effects of spherical aberration on ultrafast laser-induced refractive index variation in glass”. In: *Optics Express* 15.19, pp. 12395–12408
2. Cyril Mauclair, Alexandre Mermillod-Blondin, Nicolas Huot, Eric Audouard, and Razvan Stoian (2008). “Ultrafast laser writing of homogeneous longitudinal waveguides in glasses using dynamic wavefront correction”. In: *Optics express* 16.8, pp. 5481–5492
3. Alexandre Mermillod-Blondin, Cyril Mauclair, Arkadi Rosenfeld, Jörn Bonse, Ingolf V Hertel, Eric Audouard, and Razvan Stoian (2008b). “Size correction in ultrafast laser processing of fused silica by temporal pulse shaping”. In: *Applied Physics Letters* 93.2, p. 021921
4. Razvan Stoian, Cyril Mauclair, Alexandre Mermillod-Blondin, Nicolas Huot, Eric Audouard, Jörn Bonse, Arkadi Rosenfeld, and Ingolf V Hertel (2009c). “Size corrections during ultrafast laser induced refractive index changes in bulk transparent materials”. In: *Jour. Las. Micro. Nano.* 2, n1
5. Cyril Mauclair, Guanghua Cheng, Nicolas Huot, Eric Audouard, Arkadi Rosenfeld, Ingolf V Hertel, and Razvan Stoian (2009c). “Dynamic ultrafast laser spatial tailoring for parallel micromachining of photonic devices in transparent materials”. In: *Optics express* 17.5, pp. 3531–3542
6. Guanghua Cheng, Konstantin Mishchik, Cyril Mauclair, Eric Audouard, and Razvan Stoian (2009). “Ultrafast laser photoinscription of polarization sensitive devices in bulk silica glass”. In: *Optics express* 17.12, pp. 9515–9525
7. Y Zhang, G Cheng, G Huo, Y Wang, W Zhao, Cyril Mauclair, Razvan Stoian, and R Hui (2009a). “The fabrication of circular cross-section waveguide in two dimensions with a dynamical slit”. In: *Laser physics* 19.12, p. 2236
8. Konstantin Mishchik, Guanghua Cheng, G Huo, Igor M Burakov, Cyril Mauclair, Alexandre Mermillod-Blondin, Arkadi Rosenfeld, Youcef Ouerdane, Aziz Boukenter, Olivier Parriaux, et al. (2010a). “Nanosize structural modifications with polarization functions in ultrafast laser irradiated bulk fused silica”. In: *Optics express* 18.24, pp. 24809–24824
9. Cyril Mauclair, Konstantin Mishchik, Alexandre Mermillod-Blondin, Arkadi Rosenfeld, Ingolf-Volker Hertel, Eric Audouard, and Razvan Stoian (2011b). “Optimization of the energy deposition in glasses with temporally-shaped femtosecond laser pulses”. In: *Physics Procedia* 12, pp. 76–81
10. Cyril Mauclair, Alexandre Mermillod-Blondin, S Landon, N Huot, Arkadi Rosenfeld, Ingolf-Volker Hertel, E Audouard, I Myiamoto, and Razvan Stoian (2011c). “Single-pulse

- ultrafast laser imprinting of axial dot arrays in bulk glasses”. In: *Optics letters* 36.3, pp. 325–327
11. Alexandre Mermillod-Blondin, Cyril Mauchair, Jörn Bonse, Razvan Stoian, Eric Audouard, Arkadi Rosenfeld, and Ingolf V Hertel (2011b). “Time-resolved imaging of laser-induced refractive index changes in transparent media”. In: *Review of Scientific Instruments* 82.3, p. 033703
 12. Cyril Mauchair, Alexandre Mermillod-Blondin, Arkadi Rosenfeld, Ingolf V Hertel, Eric Audouard, Isamu Miyamoto, and Razvan Stoian (2011a). “Multipoint Focusing of Single Ultrafast Laser Pulses.” In: *Journal of Laser Micro/Nanoengineering* 6.3
 13. Cyril Mauchair, Marian Zamfirescu, Jean-Philippe Colombier, Guanghua Cheng, Konstantin Mishchik, Eric Audouard, and Razvan Stoian (2012a). “Control of ultrafast laser-induced bulk nanogratings in fused silica via pulse time envelopes”. In: *Optics express* 20.12, pp. 12997–13005
 14. C. Mauchair, S. Landon, D. Pietroy, E. Baubeau, R. Stoian, and E. Audouard (2013). “Ultrafast Laser Machining of Micro Grooves on Stainless Steel with Spatially Optimized Intensity Distribution”. In: *JOURNAL OF LASER MICRO NANOENGINEERING* 8.1, 11–14. ISSN: 1880-0688. DOI: {10.2961/jlmm.2013.01.0003}
 15. Konstantin Mishchik, Andres Ferrer, A Ruiz de la Cruz, Alexandre Mermillod-Blondin, Cyril Mauchair, Youcef Ouerdane, Aziz Boukenter, Javier Solis, and Razvan Stoian (2013a). “Photoinscription domains for ultrafast laser writing of refractive index changes in BK7 borosilicate crown optical glass”. In: *Optical Materials Express* 3.1, pp. 67–85
 16. Razvan Stoian, Konstantin Mishchik, Guanghua Cheng, Cyril Mauchair, Ciro D’Amico, Jean-Philippe Colombier, and Marian Zamfirescu (2013b). “Investigation and control of ultrafast laser-induced isotropic and anisotropic nanoscale-modulated index patterns in bulk fused silica”. In: *Optical Materials Express* 3.10, pp. 1755–1768
 17. Konstantin Mishchik, Ciro D’Amico, Praveen Kumar Velpula, Cyril Mauchair, Aziz Boukenter, Youcef Ouerdane, and Razvan Stoian (2013b). “Ultrafast laser induced electronic and structural modifications in bulk fused silica”. In: *Journal of Applied Physics* 114.13, p. 133502
 18. Razvan Stoian, Jean-Philippe Colombier, Cyril Mauchair, Guanghua Cheng, MK Bhuyan, PK Velpula, and P Srisungsitthisunti (2014b). “Spatial and temporal laser pulse design for material processing on ultrafast scales”. In: *Applied Physics A* 114.1, pp. 119–127
 19. Ciro D’Amico, Guanghua Cheng, Cyril Mauchair, Johann Troles, Laurent Calvez, Virginie Nazabal, Celine Caillaud, Guillermo Martin, Brahim Arezki, Etienne Lecoarer, et al. (2014). “Large-mode-area infrared guiding in ultrafast laser written waveguides in Sulfur-based chalcogenide glasses”. In: *Optics express* 22.11, pp. 13091–13101
 20. Praveen Kumar Velpula, Manoj Kumar Bhuyan, Cyril Mauchair, Jean-Philippe Colombier, and Razvan Stoian (2014c). “Role of free carriers excited by ultrafast Bessel beams for submicron structuring applications”. In: *Optical Engineering* 53.7, p. 076108
 21. Sabrina Hammouti, B Beaugiraud, M Salvia, Cyril Mauchair, A Pascale-Hamri, Stéphane Benayoun, and Stéphane Valette (2015a). “Elaboration of submicron structures on PEEK polymer by femtosecond laser”. In: *Applied Surface Science* 327, pp. 277–287
 22. David Pietroy, Emmanuel Baubeau, Nicolas Faure, and Cyril Mauchair (2015). “Intensity profile distortion at the processing image plane of a focused femtosecond laser below the critical power: analysis and counteraction”. In: *Optics and Lasers in Engineering* 66, pp. 138–143
 23. Cyril Mauchair, David Pietroy, Yoan Di Maïo, Emmanuel Baubeau, Jean-Philippe Colombier, Razvan Stoian, and Florent Pigeon (2015b). “Ultrafast laser micro-cutting of stainless steel and {PZT} using a modulated line of multiple foci formed by spatial

- beam shaping”. In: *Optics and Lasers in Engineering* 67.0, pp. 212–217. ISSN: 0143-8166. DOI: <http://dx.doi.org/10.1016/j.optlaseng.2014.11.018>. URL: <http://www.sciencedirect.com/science/article/pii/S0143816614002905>
24. Clotilde Jumelle, Cyril Mauclair, Julien Houzet, Aurélien Bernard, Zhiguo He, Fabien Forest, Michel Peoc’h, Sophie Acquart, Philippe Gain, and Gilles Thuret (2015c). “Delivery of molecules into human corneal endothelial cells by carbon nanoparticles activated by femtosecond laser”. In: *PloS one* 10.7, e0132023
 25. Virginie Dumas, Alain Guignandon, Laurence Vico, Cyril Mauclair, Ximena Zapata, Marie Thérèse Linossier, Wafa Bouleftour, Julien Granier, Sylvie Peyroche, Jean-Claude Dumas, et al. (2015). “Femtosecond laser nano/micro patterning of titanium influences mesenchymal stem cell adhesion and commitment”. In: *Biomedical Materials* 10.5, p. 055002
 26. Sabrina Hammouti, A Pascale-Hamri, Nicolas Faure, B Beaugiraud, Matthieu Guibert, Cyril Mauclair, Stephane Benayoun, and S Valette (2015b). “Wear rate control of peek surfaces modified by femtosecond laser”. In: *Applied Surface Science* 357, pp. 1541–1551
 27. Ophélie Raimbault, Stephane Benayoun, Karine Anselme, Cyril Mauclair, Tatiana Bourgade, Anne-Marie Kietzig, Pierre-Luc Girard-Lauriault, Stephane Valette, and Christophe Donnet (2016). “The effects of femtosecond laser-textured Ti-6Al-4V on wettability and cell response”. In: *Materials Science and Engineering: C* 69, pp. 311–320
 28. Dorian Saint-Pierre, Julien Granier, Gregory Egaud, Emmanuel Baubeau, and Cyril Mauclair (2016). “Fast uniform micro structuring of DLC surfaces using multiple ultrashort laser spots through spatial beam shaping”. In: *Physics Procedia* 83, pp. 1178–1183
 29. Julien Houzet, Nicolas Faure, Mathieu Larochette, A-C Brulez, Stephane Benayoun, and Cyril Mauclair (2016). “Ultrafast laser spatial beam shaping based on Zernike polynomials for surface processing”. In: *Optics express* 24.6, pp. 6542–6552
 30. Clotilde Jumelle, Cyril Mauclair, Julien Houzet, Aurélien Bernard, Zhiguo He, Fabien Forest, Chantal Perrache, Philippe Gain, and Gilles Thuret (2016). “Delivery of macromolecules into the endothelium of whole ex vivo human cornea by femtosecond laser-activated carbon nanoparticles”. In: *British Journal of Ophthalmology*, bjophthalmol-2015
 31. Ophélie Raimbault, Stephane Benayoun, Karine Anselme, Cyril Mauclair, Tatiana Bourgade, Anne-Marie Kietzig, Pierre-Luc Girard-Lauriault, Stephane Valette, and Christophe Donnet (2016). “The effects of femtosecond laser-textured Ti-6Al-4V on wettability and cell response”. In: *Materials Science and Engineering: C* 69, pp. 311–320
 32. Clotilde Jumelle, Alina Hamri, Gregory Egaud, Cyril Mauclair, Stephanie Reynaud, Virginie Dumas, Sandrine Pereira, Thibaud Garcin, Philippe Gain, and Gilles Thuret (2017a). “Comparison of four methods of surface roughness assessment of corneal stromal bed after lamellar cutting”. In: *Biomedical optics express* 8.11, pp. 4974–4986
 33. Alberto Aguilar, Cyril Mauclair, Nicolas Faure, Jean-Philippe Colombier, and Razvan Stoian (2017a). “In-situ high-resolution visualization of laser-induced periodic nanostructures driven by optical feedback”. In: *Scientific reports* 7.1, p. 16509
 34. Julie Vera, Anne-Catherine Brulez, Elise Contraires, Mathieu Larochette, Nathalie Trannoy-Orban, Maxime Pignon, Cyril Mauclair, Stéphane Valette, and Stéphane Benayoun (2017). “Factors influencing microinjection molding replication quality”. In: *Journal of Micromechanics and Microengineering* 28.1, p. 015004
 35. Xxx Sedao, Matthieu Lenci, Anton Rudenko, Alina Pascale-Hamri, Jean-Philippe Colombier, and Cyril Mauclair (2018). “Additive and Subtractive Surface Structuring by Femtosecond Laser Induced Material Ejection and Redistribution”. en. In: *Materials* 11.12, p. 2456. DOI: 10.3390/ma11122456. URL: <https://www.mdpi.com/1996->

- 1944/11/12/2456 (visited on 02/04/2019)
36. Vanessa Belaud, Tatiana Petithory, Arnaud Ponche, Cyril Mauclair, Christophe Donnet, Laurent Pieuchot, Stephane Benayoun, and Karine Anselme (2018). “Influence of multiscale and curved structures on the migration of stem cells”. In: *Biointerphases* 13.6, p. 06D408. ISSN: 1934-8630. DOI: 10.1116/1.5042747. URL: <https://avs.scitation.org/doi/abs/10.1116/1.5042747> (visited on 05/21/2019)
 37. Anton Rudenko, Cyril Mauclair, Florence Garrelie, Razvan Stoian, and Jean-Philippe Colombier (2019c). “Self-organization of surfaces on the nanoscale by topography-mediated selection of quasi-cylindrical and plasmonic waves”. In: *Nanophotonics* 8.3, pp. 459–465. ISSN: 2192-8614. DOI: 10.1515/nanoph-2018-0206. URL: <https://www.degruyter.com/view/j/nanoph.ahead-of-print/nanoph-2018-0206/nanoph-2018-0206.xml> (visited on 05/21/2019)
 38. A. Rudenko, C. Mauclair, F. Garrelie, R. Stoian, and J. P. Colombier (2019a). “Light absorption by surface nanoholes and nanobumps”. In: *Applied Surface Science* 470, pp. 228–233. ISSN: 0169-4332. DOI: 10.1016/j.apsusc.2018.11.111. URL: <http://www.sciencedirect.com/science/article/pii/S0169433218331908> (visited on 05/21/2019)
 39. X. Sedao, M. Lenci, A. Rudenko, N. Faure, A. Pascale-Hamri, J. P. Colombier, and C. Mauclair (2019). “Influence of pulse repetition rate on morphology and material removal rate of ultrafast laser ablated metallic surfaces”. In: *Optics and Lasers in Engineering* 116, pp. 68–74. ISSN: 0143-8166. DOI: 10.1016/j.optlaseng.2018.12.009. URL: <http://www.sciencedirect.com/science/article/pii/S0143816618312855> (visited on 04/03/2019)

2.2 Contributions to conferences

2.2.1 International conferences with proceedings

1. Razvan Stoian, Alexandre Mermillod-Blondin, Cyril Mauclair, Nicolas Huot, Eric Audouard, Igor M Burakov, Nadezhda M Bulgakova, YP Meschcheryakov, Arkadi Rosenfeld, Anton Husakou, et al. (2008). “Designing laser-induced refractive index changes in thermal glasses”. In: *High-Power Laser Ablation VII*. vol. 7005. International Society for Optics and Photonics, p. 700518
2. Razvan Stoian, Alexandre Mermillod-Blondin, Cyril Mauclair, Nicolas Huot, Eric Audouard, Igor M Burakov, Nadezhda M Bulgakova, Yuri P Meschcheryakov, Arkadi Rosenfeld, and Ingolf V Hertel (2009b). “Optimizing laser-induced refractive index changes in thermal glasses”. In: *Ultrafast Phenomena XVI*. Springer, Berlin, Heidelberg, pp. 970–972
3. C. Mauclair, G. Cheng, N. Huot, E. Audouard, A. Rosenfeld, I. Hertel, and R. Stoian (2009a). “Dynamic ultrafast laser beam tailoring for multispot photo-inscription of photonic devices in bulk transparent materials”. In: *Proc. SPIE* 7205, pp. 720512–720512–10. DOI: 10.1117/12.808798. URL: <http://dx.doi.org/10.1117/12.808798>¹
4. Cyril Mauclair, Razvan Stoian, Jörn Bonse, Alexandre Mermillod-Blondin, Arkadi Rosenfeld, and Ingolf V Hertel (2009b). “Direct time resolved observation of energy deposition by ultrashort laser pulses in fused silica”. In: *Proc. LAMP the 5th International Congress on Laser Advanced Materials Processing*. (2009)

¹Selected by Research Highlights of Nature Photonics 3 5/242-243 (May 2009)

5. Razvan Stoian, Alexandre Mermillod-Blondin, Cyril Maucclair, Guanghua Cheng, Konstantin Mishchik, Arkadi Rosenfeld, Nadezhda M Bulgakova, Yuri Meshcheryakov, and Ingolf V Hertel (2009a). “Adaptive spatio-temporal techniques for smart ultrafast laser processing of optical glasses”. In: *The International Congress on Applications of Lasers & Electro-Optics, ICALEO 2009 ICALEO Proceedings*
6. Cyril Maucclair, Konstantin Mishchik, Alexandre Mermillod-Blondin, Jörn Bonse, Arkadi Rosenfeld, Ingolf V Hertel, Eric Audouard, and Razvan Stoian (2010). “Time-resolved observation of energy deposition in fused silica by ultrashort laser pulses in single and cumulative regime”. In: *Lasers and Electro-Optics (CLEO) and Quantum Electronics and Laser Science Conference (QELS), 2010 Conference on*. IEEE, pp. 1–2
7. Konstantin Mishchik, Guanghua Cheng, Cyril extbfMaucclair, Eric Audouard, Aziz Boukenter, Youcef Ouerdane, and Razvan Stoian (2010b). “Ultrafast Laser Photoinscription of Polarization Sensitive Devices in Bulk Silica Glass”. In: *Bragg Gratings, Photosensitivity, and Poling in Glass Waveguides*. Optical Society of America, BThD1
8. Alexandre Mermillod-Blondin, Cyril Maucclair, A Rosenfeld, Jörn Bonse, Razvan Stoian, and Eric Audouard (2011a). “Time-resolved imaging of bulk a-SiO₂ upon various ultrashort excitation sequences”. In: *Frontiers in Ultrafast Optics: Biomedical, Scientific, and Industrial Applications XI*. vol. 7925. International Society for Optics and Photonics, 79250R
9. Razvan Stoian, G Cheng, C Maucclair, A Mermillod-Blondin, K Mishchik, E Audouard, A Rosenfeld, and IV Hertel (2011). “3D adaptive spatio-temporal control of laser-induced refractive index changes in optical glasses”. In: *Laser-based Micro-and Nanopackaging and Assembly V*. vol. 7921. International Society for Optics and Photonics, 79210H
10. Konstantin Mishchik, Cyril Maucclair, Guanghua Cheng, Youcef Ouerdane, Aziz Boukenter, and Razvan Stoian (2011). “Structural modifications in bulk fused silica after interaction with ultrashort laser pulses”. In: *Advanced Laser Technologies*
11. Cyril Maucclair, Sébastien Landon, David Pietroy, Emmanuel Baubeau, Razvan Stoian, and Eric Audouard (2012b). “Ultrafast Laser Machining of Micro Grooves in Metals with Spatially Optimized Intensity Distribution”. In: *The 13th international conference on laser precision microfabrication*, p85
12. Razvan Stoian, Konstantin Mishchik, Cyril Maucclair, Jean-Philippe Colombier, Marian Zamfirescu, and Guanghua Cheng (2012). “Investigation and control of ultrafast laser-induced nanoscale patterns in bulk dielectric materials”. In: *Advanced Laser Technologies ALT*
13. Konstantin Mishchik, Andres Ferrer, A Ruiz de la Cruz, Alexandre Mermillod-Blondin, Cyril Maucclair, Youcef Ouerdane, Aziz Boukenter, Javier Solis, and Razvan Stoian (2013a). “Photoinscription domains for ultrafast laser writing of refractive index changes in BK7 borosilicate crown optical glass”. In: *Optical Materials Express* 3.1, pp. 67–85
14. Cyril Maucclair, David Pietroy, Emmanuel Baubeau, Razvan Stoian, and Eric Audouard (2013b). “Spatial shaping of femtosecond laser beam for high speed multi-scale surface structuring of materials”. In: *The 6th International Congress on Laser Advanced Materials Processing LAMP2013 July 23-26, 2013 Toki Messe, Niigata, Japan*
15. Clothile Jumelle, Nelly Campolmi, Aurélien Bernard, Simone Piselli, Emmanuel Baubeau, Cyril Maucclair, J Granier, Gregory Egaud, P Gain, and G Thuret (2013). “Improvement of delivery of molecules into corneal endothelium using nanoparticles activated by femtosecond laser pulses”. In: *Acta Ophthalmologica* 91.s252, pp. 0–0
16. Aurélien Bernard, Cyril Maucclair, Emmanuel Baubeau, J Granier, Gregory Egaud, Z He, N Campolmi, S Piselli, F Forest, M Peoc’h, et al. (2013). “Endothelial graft precutting from the epithelial and endothelial side with the femtosecond laser, on cornea stored in

- a new corneal bioreactor”. In: *Acta Ophthalmologica* 91.s252, pp. 0–0
17. Razvan Stoian, Konstantin Mishchik, Cyril Mauclair, Jean-Philippe Colombier, Marian Zamfirescu, and Guanghua Cheng (2013a). “Control of ultrafast laser-induced nanopatterns in bulk silica glass”. In: *EUROMAT 2013*
 18. Razvan Stoian, Konstantin Mishchik, Guanghua Cheng, M Zamfirescu, C Mauclair, and C d’Amico (2013c). “Investigation and Control of Ultrafast Laser-Induced Nanoscale Patterns in Bulk Fused Silica”. In: *MATEC Web of Conferences*. Vol. 8. EDP Sciences, p. 03007
 19. Praveen Kumar Velpula, Manoj Bhuyan, Cyril Mauclair, Jean-Philippe Colombier, and Razvan Stoian (2013). “Time-resolved dynamics of ultrafast Bessel and Gaussian beam propagation and energy deposition in transparent materials”. In: *EUROMAT 2013*
 20. Praveen Kumar Velpula, Manoj Bhuyan, Cyril Mauclair, Jean-Philippe Colombier, and Razvan Stoian (2014d). “Ultrafast imaging of free carriers: a controlled dynamics with chirped nondiffractive Bessel beams”. In: *SPIE Proceedings Series*. Vol. 8967. SPIE, p. 896711
 21. PK Velpula, MK Bhuyan, C Mauclair, JP Colombier, and R Stoian (2014a). “Ultrafast imaging of free carriers: controlled excitation with chirped ultrafast laser Bessel beams”. In: *Laser Applications in Microelectronic and Optoelectronic Manufacturing (LAMOM) XIX*. vol. 8967. International Society for Optics and Photonics, p. 896711
 22. Julien Zeligowski, Frédéric Mermet, Frédéric Antoni, Cyril Mauclair, Eric Fogarassy, and Eric Mottay (2014). “Novel industrial laser etching technics for sensors miniaturization applied to biomedical: a comparison of simulation and experimental approach”. In: *Laser Applications in Microelectronic and Optoelectronic Manufacturing (LAMOM) XIX*. vol. 8967. International Society for Optics and Photonics, 89670U
 23. Alberto Aguilar, Abundio Davila, Jorge Garcia-Marquez, and Cyril extbfMauclair (2014). “Phase extraction through multistep vortex filtering.” In: *9ème édition des Journées" IM-AGERIE OPTIQUE NON CONVENTIONNELLE" 19 et 20 mars 2014, ESPCI, 10 rue Vauquelin, Paris Amphithéâtre Langevin*
 24. Praveen Kumar Velpula, MK Bhuyan, Cyril Mauclair, Jean-Philippe Colombier, and Razvan Stoian (2014b). “High aspect ratio submicron fabrication in bulk dielectrics with non-diffractive ultrafast Bessel beams; dynamics and interaction regimes”. In: *Laser Precision Microfabrication*
 25. Sabrina Hammouti, Cyril Mauclair, Alina Hamri, and Stéphane Valette (2014). “Elaboration of submicron periodic structures on polymer surfaces by femtosecond laser”. In: *LPM 2014*
 26. Clothile Jumelle, Aurélien Bernard, Cyril Mauclair, N Campolmi, J Granier, Gregory Egaud, Odile Sabido, Philippe Gain, and Gilles Thuret (2014). “Femtosecond laser activated carbon nanoparticles for corneal gene therapy”. In: *LPM 2014*
 27. Cyril Mauclair, David Pietroy, Emmanuel Baubeau, and Razvan Stoian (2014). “Distortion of the intensity profile at the processing image plane of a focused femtosecond laser beam”. In: *LPM 2014*
 28. Cyril Mauclair (2014). “Ultrafast laser beam tailoring for efficient surface and bulk processing”. In: *Laser and Focused Ion Beam (LFIB) technologies for photonics collocated with the Euro-Asian conference on Integrated and Micro optics, namely, the European Conference on Integrated Optics (ECIO 17th) and the Asian MicroOptics Conference (MOC 19th)*²
 29. Razvan Stoian, Konstantin Mishchik, Cyril Mauclair, Praveen K Velpula, Manoj Bhuyan,

²Invited conference

- Jean-Philippe Colombier, Ciro D'Amico, Marian Zamfirescu, and Guanghua Cheng (2014a). "Control of Ultrafast Laser Nanostructuring of Glasses using Temporal and Spatial Pulse Design". In: *Bragg Gratings, Photosensitivity, and Poling in Glass Waveguides*. Optical Society of America, BW2D-6
30. Clothile Jumelle, Cyril Mauclair, Julien Houzet, Aurelien Bernard, Zhiguo He, Simone Piselli, Ch Perrache, Gregory Egaud, Emmanuel Baubeau, Philippe Gain, et al. (2015a). "Pore size assessment during corneal endothelial cells permeabilization by femtosecond laser activated carbon nanoparticles". In: *European Conference on Biomedical Optics*. Optical Society of America, 95420W
 31. Cyril Mauclair, Alberto Aguilar, J-P Colombier, Razvan Stoian, and Abundio Davila (2015a). "In-Situ Observation of Ultrafast Laser Induced Periodic Surface Structures on Metals by Optical Microscopy". In: *The European Conference on Lasers and Electro-Optics*. Optical Society of America, CM_2_4
 32. Clothile Jumelle, Cyril Mauclair, Julien Houzet, A Barnard, Zhiguo He, Simone Piselli, Ch Perrache, Philippe Gain, and Gilles Thuret (2015b). "Transfer of molecules into the endothelial cells of whole human corneas using carbon nanoparticles activated by femtosecond laser". In: *Acta Ophthalmologica* 93
 33. Cyril Mauclair and Julien Houzet (2016). "Ultrafast laser spatial beam shaping using an optically addressed liquid crystal optical valve". In: *Nice Optics*, p2³
 34. Cyril Mauclair, Alexandre Mermillod-Blondin, K Mishchik, Jörn Bonse, Arkadi Rosenfeld, Jean-Philippe Colombier, and Razvan Stoian (2016). "Excitation and relaxation dynamics in ultrafast laser irradiated optical glasses". In: *High Power Laser Science and Engineering* 4
 35. Cyril Mauclair, Nicolas Faure, and Julien Houzet (2016). "Towards top-hat spatial shaping of ultrafast laser beam based on Zernike polynomials". In: *Laser Sources and Applications III*. vol. 9893. International Society for Optics and Photonics, p. 989312
 36. V Belaud, S Benayoun, K Anselme, C Mauclair, and C Donnet (2016). "Influence of multiscale and curved structures on the behavior stem cells and macrophages". In: *European Material Research Society, E-MRS 2016, Fall Meeting*
 37. Alberto Aguilar, Jean-Philippe Colombier, Razvan Stoian, and Cyril Mauclair (2017b). "In situ observation of ultrafast laser induced micro nano structures using structured light illumination". In: *Laser-based Micro-and Nanoprocessing XI*. vol. 10092. International Society for Optics and Photonics, p. 1009220
 38. P Gain, C Jumelle, A Hamri, G Egaud, C Mauclair, S Reynaud, S Dumas, S Pereira, and G Thuret (2017). "Comparison of four technics of surface roughness assessment of corneal lamellar cuts". In: *Acta Ophthalmologica* 95.S259
 39. Rudenko Anton, Anthony Abou Saleh, X Sedao, Cyril Mauclair, Razvan Stoian, Tatiana Itina, Florent Pigeon, Florence Garrelie, and Jean-Philippe Colombier (2018). "Electromagnetic roughness-driven mechanisms of ultrashort laser-induced ripple formation on metal and dielectric surfaces". In: *8th international workshop on Laser Induced Periodic Surface Structures*. Bochum, Germany. URL: <https://hal.archives-ouvertes.fr/hal-02025834> (visited on 05/21/2019)
 40. Jean-Philippe Colombier, Anton Rudenko, Hao Zhang, Cyril Mauclair, Tatiana Itina, Florence Garrelie, and Razvan Stoian (2018). "Ultrafast Laser-Induced Surface and Bulk Nanostructuring: Similarities Revealed by Electromagnetic Modeling". en. In: URL: <https://hal-ujm.archives-ouvertes.fr/ujm-02018947> (visited on 05/21/2019)
 41. Anton Rudenko, Cyril Mauclair, Florence Garrelie, Razvan Stoian, and Jean-Philippe

³Invited conference

Colombier (2019b). "Multipulse dynamics of ultrashort laser interaction with metal targets by coupled electromagnetic and hydrodynamic simulations (Conference Presentation)". In: *Laser-based Micro- and Nanoprocessing XIII*. vol. 10906. International Society for Optics and Photonics, 109060B. DOI: 10.1117/12.2507222. URL: <https://www.spiedigitallibrary.org/conference-proceedings-of-spie/10906/109060B/Multipulse-dynamics-of-ultrashort-laser-interaction-with-metal-targets-by/10.1117/12.2507222.short> (visited on 05/21/2019)

2.2.2 Invited talks (international conferences)

1. "Spatial Beam Shaping" *UltraShort an Intense Laser Technology and Metrology (USIL) intensive program (ERASMUS)* Bordeaux, France, 2009
2. "Ultrafast laser tailoring for bulk photoinscription of photonic devices", *LASINOF workshop (Laser Interaction and new optical functionality)* Bordeaux, France, 2009
3. "Spatial Beam Shaping" and "Spatial Beam Metrology" *UltraShort and Intense Laser Technology and Metrology (USIL) intensive program (ERASMUS)* Bordeaux, France, 2010
4. "Spatial Beam Shaping" and "Spatial Beam Metrology" *UltraShort and Intense Laser Technology and Metrology (USIL) intensive program (ERASMUS)* Bordeaux, France, 2011
5. "Increasing speed and flexibility of ultrafast laser micromachining with spatial beam shaping", *FemtoMat*, Austria, 2013
6. "Maîtrise de la lubrification et du frottement par microstructuration laser des surfaces", *ASRH*, Neuchatel, Swiss, 2015
7. "Ultrafast laser surface structuring : the role of spatial beam control and in-situ characterization for process optimization", *Femtomat 2019*, Mauterndorf, Austria.

2.2.3 Invited talks (national conferences)

1. "Ultrafast laser beam tailoring for efficient surface and bulk tailoring", *LIFBT Nice*, Nice, France, 2014
2. "Contrôle de faisceau laser ultrabref pour la fonctionnalisation de surface à cadences industrielles", *Intersurfaces*, St-Etienne, France, 2015
3. "Contrôle de laser ultrabref pour le micro usinage de surface à hautes cadences", *JTT*, Clermont-Ferrand, France, 2016
4. "Mise en forme laser spatiale et temporelle", *Journée thématique Réseau Femto*, Paris, France, 2016
5. "Ultrafast laser spatial beam shaping using an optically addressed liquid crystal optical valve", *Nice Optics*, Nice, France, 2016

2.2.4 Conference organization participation

1. FemtoMat Mauterndorf Austria 2013
2. Journée Thématique du pôle Optique Rhône Alpes sur le thème Fonctionnalisation de Surfaces et Caractérisation, Saint-Etienne, France, 2014

2.3 Books and contribution to collective textbooks

1. Results from my research activity have also been reported in the following book chapter: R. Stoian, M. Wollenhaupt, T. Baumert, I. V. Hertel Pulse shaping in laser material process-

- ing 2008 in *Laser Precision Microfabrication, Springer Series in Optical Sciences*, Sugioka K., Meunier M., Pique A. Eds. (Springer Verlag, Heidelberg, in press)
2. Razvan STOIAN and Cyril MAUCLAIR (2018). *Photoinscription par laser à impulsions ultrabréves pour des systèmes optiques 3D*. fr. Text. URL: <https://www.techniques-ingenieur.fr/base-documentaire/electronique-photonique-th13/materiaux-pour-l-optique-42450210/photoinscription-par-laser-a-impulsions-ultrabreves-pour-des-systemes-optiques-3d-e6312/> (visited on 05/21/2019)

2.3.1 PhD Thesis

1. Cyril Mauclair (2010). “Spatio-temporal ultrafast laser tailoring for bulk functionalization of transparent materials”. PhD thesis. Saint Etienne

2.3.2 Projects reports

1. 1 rapport final ANR Nanomorphing ANR-07-BLANC-0301 (coord. LaHC, E. Audouard) 2011.
2. 5 rapports d'étapes clefs, Programme Innovation Stratégique Industrielle ISI-OSEO, projet ARTEMIS, 2010-2014.
3. 1 rapport à mi-parcours et 1 rapport final projet ANR Matetpro Topo INJECTION 2013-2016.
4. 1 rapport final projet Labex Manutech-Sise 2S-BIOLASE 2013-2016.
5. 1 rapport final projet Labex Manutech-Sise SERMONIS 2016-2017.
6. 1 rapport final projet Labex Manutech-Sise ICRAM 2015-2017.

2.4 Supervision and patents

2.4.1 PhD thesis

1. Interaction laser femtoseconde et tissu cornéen : application à la découpe des greffons cornéens humains. (A. Bernard - 2013 – collaboration BIIGC Pr. Gain et Pr. Thuret. Supervision 33%
2. Étude et optimisation des effets dynamiques des procédés d'ablation laser en régime ultracourt pour l'industrialisation, application à la découpe de PZT (Y. Di Maio - 2013 – convention CIFRE SAGEM) Supervision 45%
3. Novel industrial laser etching technics for sensors miniaturization applied to biomedical (J. Zelgowski - 2014 – convention CIFRE IREPA Laser et collaboration Telecom Physique Strasbourg Pr. Fogarassy). Supervision 30%
4. Delivery of molecule into human endothelial cells by nanoparticles activated by fs laser (C. Jumelle - 2015 – collaboration BIIGC Pr. Gain et Pr. Thuret Encadrement 33%
5. Elaboration of submicron periodic structures on polymer by femtosecond laser (S. Hammouti - 2015 – collaboration LTDS Lyon, MCF HDR S. Valette) Supervision 40%
6. Detection and in situ characterization of ripples with super resolution microscopy. (A. Aguilar Lab-H. Curien + CIO Mexique, 2016). Supervision 50%

2.4.2 Postdoctoral

1. Spatial beam shaping applied to laser surface structuring of steel for reduced friction in lubricated contact (D. Pietroy June-Dec 2012) – project OSEO Artemis (collaboration IREIS). Supervision 100%
2. Development of an efficient femtosecond laser micro and nano-machining system for rapid texturing of injection mold (J. Houzet 2014-2015) – project ANR Matetpro Topoinjection (collaboration LTDS) Supervision 100%
3. In-situ characterization of LIPSS with Structured Illumination Microscopy. (A. Aguilar 2016-2017) - Project SERMONIS. Supervision 100%
4. Optimization of ultrafast laser matter interaction for additive manufacturing (Dat Nguyen 2017-2019) – project FUI 3D Hybride. Supervision 50%
5. Ultrafast laser structuring of polymers for liquid repellent applications (Hyeon Jin Jung 2018-2019) - Project FUI Deperflex. Supervision 50%

2.4.3 Masters

1. Internship Master 1: Spatial beam shaping with Zernike Polynomials (Kassem Saab, 01/04/2013-01/08/2013). Supervision 100%
2. Internship Master 2: LIPSS detection with far field diffraction . (M. Royon, 01/04/2013-01/09/2013). Supervision 70%
3. Engineer: Optimization of scanning dynamics of ultrashort pulse structuring for industrial transfer (N. Compère 01/01/2013-01/07/2013). Supervision 100%

2.4.4 Patents

1. Aurelien Bernard, Philippe Gain, Cyril Maclair, and Gilles Thuret (2017). *Device and method for cutting a cornea or crystalline lens*. US Patent App. 15/517,480
2. FR-3049853-A1 and FR-3049847-A1, F. Romano, A. Bernard, C. Maclair (2017)
3. EP-3439593-A1, F. Romano, A. Bernard, C. Maclair, E. Baubeau (2019)
4. Dispositif permettant un traitement photonique de la cornée ex vivo par les 2 faces (Biface), submitted (SATT). Philippe Gain, Gilles Thuret, Cyril Maclair, Clotilde Jumelle, Gregory Egaud.

2.5 International and national projects with financial support

2.5.1 Project correspondent for the laboratoire H. Curien

1. Programme Innovation Stratégique Industrielle ISI-OSEO, projet ARTiculation Elaborée grâce à la Maîtrise de l'Ingénierie des Surface (ARTEMIS), academic partners : ENISE, ENSMSE, USTL et CETIM, industrial partners : LIFCO, PHYMAT, IMPULSION. Porteur : société IREIS (HEF). Laser surface texturing for reduction of friction coefficients. 2010-2014. Grant: 4 M€
2. Project MicroOSTEO Laboratory Equipment St-Etienne Métropole, collaboration ENISE Multiscale laser surface texturing for biomaterials. 2011-2012. Grant : 25k€

3. Project ANR Matetpro Topo INJECTION with LTDS, IREIS, ITECH, BD, CEMEF, Heyr-Moules, Multiscale texturation of polymers by laser surface processing of molds 2013-2016. Grant : 1M€
4. Project Labex Manutech-Sise 2S-BIOLASE with LTDS, Biomaterials surface structuring with femtosecond laser pulses. 2013-2016. Grant 67k€
5. Project Labex Manutech-Sise SERMONIS with LTDS Super resolution microscopy for characterization of surface micro-nanostructures induced by lasers. 2016-2017. Grant 66k€
6. Project Labex Manutech-Sise ICRAM Investigation of accumulation effects in ultrafast laser surface ablation 2015-2017. Grant 17k€
7. Project PEPS-DGA RugoMicro3D Roughness characterization during SLM-based manufacturing 2017-2019. Grant 19k€
8. Project FUI DEPERFLEX with LTDS, ICBMS, Manutech-USD, Sofileta, Sci & Surf, PROTEX, ALPEX, DEveloppement de traitements dePERlants sans FLuor pour le domaine tEXtile, 2018-2022. grant 120k€.
9. Project EUR Sleight Eagle Eye Anterior Segment Engineering with BIIGC, Manutech-USD and Kejako, 2019-2020. grant 92k€.

2.5.2 Also involved in :

1. ANR Nanomorphing ANR-07-BLANC-0301 (coord. LaHC, E. Audouard) with CNRS CEA Ecole Polytechnique 2007-2011.
2. ANR Equipex Manutech-USD. (<http://www.manutech-usd.fr>).
3. ANR Nanoflam SIMI 4 (coord. LaHC, R. Stoian) with FemtoST, CPTH Ecole Polytechnique 2011-2014.
4. ANR SMARTLASIR (coord. LaHC, R. Stoian) with EVC-Rennes, IPAG Grenoble, FemtoST. 2011-2014
5. ANR France-Roumanie DYLPSS (coord. J.P. Colombier), with NILPRP Bucarest 2012-2015
6. ANR Innovation Biomédicale SUPCO (BIIGC, GIE Manutech-USD), Femtosecond laser cutting and surfacing of carriers for corneal bioengineering. 2014-2018
7. ADEME Project IMOTEP (coord. LaHC, F. Garrelie) Innovation Moteur Propre with LTDS, IREIS, TOTAL, PSA, 2017-2022.
8. FUI Project 3D-Hybride (coord. LaHC, R. Stoian) Building of a Hybrid machine combining additive manufacturing (selective laser melting -SLM) and ultrafast laser subtractive machining 2017-2021.

2.6 Communications overview

Year	Conferences	Publications	PhD Cosupervision	PhD defenses	Postdoc.
2010	2	1			
2011	2	4	2		
2012	2	1	3		1
2013	2	4	5	3	
2014	6	3	4	1	1
2015	6	6	3	2	1
2016	6	5	1	1	1
2017	4	3			2
2018	2	2			2
2019	1	3			2(+2)
Total ⁴	41	39	6	7	5(+2)

2.7 Overview of PhD and Postdoc supervision

2011	2012	2013	2014	2015	2016	2017	2018	2019
	Thèse A. Bernard - BIIGC (33%)							
	Thèse Y. Di Maio - CIFRE Sagem (45%)							
	Thèse J. Zelgowski - CIFRE IREPA (30%)							
		Thèse C. Jumelle - BIIGC (33%)						
		Thèse S. Hammouti - LTDS (40%)						
		Thèse A. Aguilar - CIO (Mexique) (50%)						
	Postdoc. D. Pietroy (ARTEMIS)							
			Postdoc. J. Houzet (Topoinjection)					
					Postdoc. A. Aguilar (Sermonis)			
							Postdoc D. Nguyen (3D Hybride)	
							Postdoc H. Jin Jung (Deperflex)	
							Postdoc XXX (IMOTEP)	
							Postdoc XXX (Eagle)	

Part II

Ultrafast Laser Processing using Optimized Spatial Beam Control

Chapter 3

Introduction

3.1 Local environment

I have joined the Hubert Curien laboratory as an assistant professor (Maître de conférences) in 2011. This joint research unit (UMR 5516) of the Jean Monnet University, Saint-Etienne, the National Research Centre "CNRS" and the Institut d'Optique Graduate School is composed of about 240 members working on optics, photonics and microwave, computer science, telecom and image. My mission in the laboratory has been from the start associated to the ANR EQUIPEX project Manutech-USD (funded by the French National Research Agency ANR), which is a private/public entity next to the laboratory with the latest equipments in terms of ultrafast laser sources and characterization means. Its scope is to transfer the fundamental developments of surface structuring means, particularly related to the control of ultrafast laser pulses, to practical applications with the attained ambition of self-reliance (now employing 7 people). The Hubert Curien Laboratory is a member of the LABEX MANUTECH-SISE which is a ANR "Laboratoire d'Excellence" project whose ambition is to reach the highest international level in the field of surface and interface science and engineering. The objectives of the LABEX MANUTECH-SISE are to develop the understanding and control of surface phenomena, such as wear, friction, fatigue resistance, chemical reactivity, wettability, visual and tactile aspects. The aims of the LABEX are also focused on the creation and control of surface functionalities, such as in tribology, optics and chemistry, as well as on the optimization of advanced processes of surface and interface manufacturing at different scales, including ultrashort laser micromachining. The LABEX MANUTECH-SISE gathers an academic / company partnership, within the Lyon – St-Etienne area and comprehends five laboratories belonging to universities, engineering high schools and CNRS, and three industrial companies deeply involved in research and developments. This takes place in a larger ANR project that was more recently granted to the University Lyon-Saint-Etienne in 2017: the IDEXLYON that aims at building a world-class center of excellence and university. We also mention here the recent EUR (Ecole Universitaire de Recherche) Manutech-Sleight grant on the subject of the light-matter interaction that gathers 13 private and public partners, among which the Hubert Curien laboratory, Manutech-USD and the company Keranova (ophthalmic surgery machine) that I co-founded.

3.2 Scientific and technological challenges

It would be hard to imagine a more favorable scientific environment for a researcher whose centers of interest are the spatial shaping of ultrashort laser pulses and in-situ control of the

irradiation region. To clarify this, I would like to underline three of the main scientific and technological bottlenecks that are key elements to the success of the above mentioned exciting projects:

1. the laser surface/bulk treatment pace
2. the topological and physical characterization of the irradiated zone
3. automated tuning the laser parameters for the desired surface function

Each of these challenges can be addressed using the techniques of spatial shaping of ultrashort laser pulses and in-situ control. Indeed, spatial beam shaping is particularly suited to answer the problem of pace. By optical demultiplication and shaping of the laser spot, we have shown that it can drastically accelerate the laser treatment process (up to a hundred times when the laser energy is sufficient), inasmuch that unimaginable progresses in ophthalmic surgery were rendered possible, as it is shown in the following. Moreover, from the laboratory realizations before 2010 to the pre-industrial surface structuring machines of Manutech-USD, we could increase the surface processing speed from 6 cm²/min to 1 m²/min and 10 m²/min very soon. This was rendered possible thanks to spatial beam shaping employed with synchronized beam scanning at high laser repetition rate.

In-situ probing of the interaction zone can also bring key advantages to better understand and control the ultrafast laser irradiation outcome. By employing super resolution techniques, our work has demonstrated that inline characterization of the irradiated region with a ≈ 100 nm sub-diffraction resolution is possible, a ten-fold enhancement of the observation precision compared to the classic microscopy techniques that were employed before 2010 (such as brightfield and phase contrast microscopy). This has unveiled fundamental phase-locking mechanisms in the formation of LIPSS (laser induced periodic surface structure). It also appears as a powerful tool for in-situ characterization and optimization of the laser parameters. The third challenge (automated tuning of the laser parameters) is now at reach, by combining spatial control of the laser, in-situ probing of the interaction zone and efficient automated self-learning routines. If the concept is not new (it is very close to the well-known 'coherent control'), the maturity of the laser control tools (in space and in time), and the advances in optical in-situ quantitative observation make the technique ready for pre-industrial applications.

3.3 Outline

It is clear that the use of ultrafast laser sources for surface and bulk processing knows a growing interest. This trend is not limited to the fundamental aspects of the interaction which already constitutes a vast domain of exciting investigations. It also covers real life applications in various domains e.g surface treatment, material fine processing, biomedical tissue disruption and so on. Several scales of interaction are involved from the millimeter down to fractions of micrometers, depending on the focusing power utilized, the irradiation conditions on the sample and the physical properties of the irradiated zone. With the recent progress in the femtosecond laser technology, noticeably on the available power and repetition rate, exciting perspectives in processing on various materials with competitive throughputs are demonstrated. Moreover, due to the specificities of the interaction, ultrashort laser pulses can also achieve processing inside transparent materials. There, not only the laser focal point trajectory in three dimensions enables an increased flexibility, but also the focal volume can be spatially engineered allowing for totally new manufacturing processes down to the submicrometric scale.

The present report puts in light recent advances and remaining challenges in the use of ultrafast

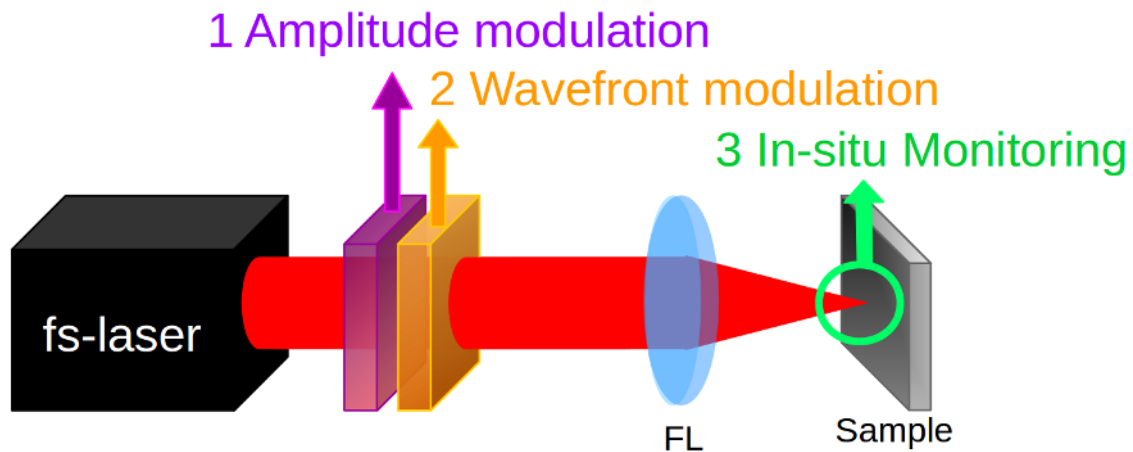


Figure 3.1 – Graphical scheme of the outline of the manuscript following the successive steps of spatially optimized ultrafast laser irradiation. FL: focusing lens or element.

lasers for material processing. It focuses on the optimization of the spatial control of the ultrafast laser beam and on the key advantages offered by in-situ monitoring of the processed zone. There are challenges to fully exploit each pulse produced by last generation ultrafast lasers at high energy and repetition rate. Spatial beam shaping of the laser intensity focal region is also mentioned in detail. Focal laser spots demultiplication is discussed with more advances in sculpting the intensity distribution in two and three dimensions with unique processing capabilities. In situ characterization down to the micrometric and nanometric scale has also opened new gates for advanced understanding and control of the irradiation outcome. The outline of this manuscript follows the path of an ultrashort laser pulse (a coherent light pulse of femtosecond to picosecond duration) from its birth -taken here as its release from the laser system- to its death, -when the carried light energy is coupled to the surface or into the bulk of the irradiated target through various mechanisms (see Fig.3.1). We first discuss the various tools for spatial control of ultrashort laser pulses that are described from the point of view of laser processing. These techniques involve the possibility to spatially deflect the pulse train using scanning mirrors, and the strategies of beam shaping using amplitude and/or wavefront modulation. Then, in-situ characterization of the irradiation region occupies the last part of the manuscript. The outline is as follows:

1. The first chapter mentions the control knob offered by spatial pulse overlap through beam deflection and the amplitude modulation technique with related advances involving static and reconfigurable modulation.
2. The second chapter concerns the wavefront modulation strategy that has gained a strong interest in the last ten years, because of the possibility offered to drastically speed up femtosecond processing through laser spot duplication. Our pioneering contribution and more advanced results are presented, underlining the current bottlenecks in terms of energy efficiency and beam shaping quality.
3. The third chapter focuses on the interest of in-situ monitoring of the irradiation zone especially for submicrometric bulk and surface structuring. A UV diffraction beam is successfully employed for inline characterization of the laser-generated bulk periodic nanostructures. This enables to better tune the temporal laser energy deposition that enhances the nanostructuring production. Also a full-field superresolution microscopic imaging on surfaces is used as in-situ monitoring tool for laser-induced periodic surface structures (LIPSS). The key advantages of the techniques permits inline evaluation of the LIPSS pattern evolution. This enables to observe key features of the LIPSS formation,

namely the pulse to pulse pattern spatial stability and 'absolute' phase that are simply not observable without the in-situ super resolution scheme.

4. Finally, the last chapter lists the perspectives on the subject of spatial beam control and in-situ monitoring. We anticipate that the next 'big' step of femtosecond processing is the connection between these two subjects through the use of self-learning strategies where the in-situ monitoring provides the necessary feedback for tuning the ultrafast irradiation.

Along this manuscript, a special effort is made to underline our contributions in the frame of the state of the art¹.

¹Our publication references are indicated in **bold**

Chapter 4

Spatial Shaping of ultrashort laser irradiations - Amplitude modulation

4.1 Basics

A very illustrative example of spatial beam control can be found in the report of the siege of Syracuse 212 BC. Following Archimedes instructions, numerous parabolic reflective surfaces (probably polished shields of Cu or bronze) were positioned to redirect and focus the light rays from the sun onto the Roman fleet boats (see Fig.4.1). Interestingly, the experience was repeated by a group of students of the MIT in October 2005. Fire ignition was obtained on wood ¹. Eventually, the city was invaded by the Romans showing that spatial beam control requires careful developments and optimisations. Let us focus on the spatial control of lasers beams.

When handling a light beam emitted from a stable laser cavity, the spatial intensity repartition of the fundamental mode detected in a given plane $I(x, y)$ is most of the time represented by a Gaussian distribution. In the frame of the paraxial approximation (i.e the transverse beam dimensions remain small enough compared to propagating distances), a quite famous solution to the scalar wave equation designed to represent laser emission is the Gaussian beam

¹see http://web.mit.edu/2.009/www/experiments/deathray/10_ArchimedesResult.html



Figure 4.1 – Left: Siege of Syracuse - Painting by Giulio Parigi, c. 1599 with an emphasis on the light rays. Right: MIT experiment's Archimedes Death Ray held in October, 2005 where fire ignition was demonstrated.

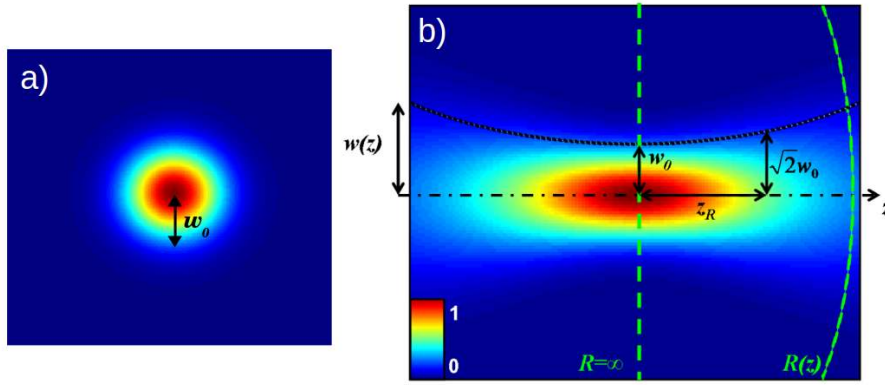


Figure 4.2 – Propagation of a Gaussian beam around the waist: The normalized intensity profile is plotted in the x-y plane a) and along the optical propagation axis z . The beam waist w_0 , Rayleigh range z_R and wavefront radius of curvature $R(z)$ are indicated.

[Siegman, 1990]. Thus, $\tilde{u}(x, y, z)$ takes then the form:

$$\tilde{u}(x, y, z) = \frac{u_0}{q(z)} \exp\left(-ik \frac{x^2 + y^2}{2q(z)}\right) \quad (4.1)$$

where

$$\frac{1}{q(z)} = \frac{1}{R(z)} - \frac{i\lambda}{\pi w^2(z)} = \frac{1}{q_0 + z} \quad (4.2)$$

$R(z)$ is the wavefront radius of curvature. It is worth noting the z dependency, meaning that any beam modulation in amplitude or in phase has a consequence in the transverse plane and along the propagation axis. $w(z)$ is the beam radius at $\frac{1}{e^2}$ of the intensity profile $I(x, y, z) = \tilde{u}(x, y, z) \times \tilde{u}(x, y, z)^*$ which follows a Gaussian distribution. $q(z)$ is the complex beam parameter. This quantity allows complete spatial definition of the Gaussian beam with the relation $q(z) = q_0 + z$. Taking the origin of the z -axis at $z = 0$ at the waist position $w(z) = w_0$ we have $R(z) = \infty$ meaning that at this point the wavefront is a plane orthogonal to the propagation axis (although not to be confused with a plane wave [Diels and Rudolph, 2006]). From these equations, it is evident that any modulation of amplitude and/or wavefront in a given x-y plane has an impact on the subsequent laser intensity distribution in further x-y planes and also along the z axis. For example, if a laser beam goes through a converging lens, the corresponding parabolic wavefront modulation can be taken into account by adding a phase term in the exponential of Eq. 4.1. This modulation enters in competition with the intrinsic divergence of the Gaussian beam ($\exp\left(-ik \frac{x^2 + y^2}{2q(z)}\right)$). Thus, the lens alters the beam size, ultimately leading to a focal spot. Similarly, if the laser beam encounters an attenuation mask (e.g beam truncation etc.), this amplitude modulation can be mathematically applied by a real amplitude distribution factor to Eq. 4.1 with consequences on the propagated laser beam profile.

The point is that modulating the laser beam in a certain plane permits to control the laser beam spatial characteristics in a further plane. Usually, this plane of interest is the focal plane of a lens or a focusing element, where both the maximum of intensity and ultimate resolution can be reached.

This report considers light pulses whose spectral bandwidth can be assumed thin enough so that any chromatic aberration can be disregarded in a first approximation. When dealing with ultrafast laser pulses from Ti:Sa lasers at 800 nm, the spectral bandwidth can be as large as 100 nm for a Fourier-limited 10 fs pulse, a pulse whose spectral components are not temporally

spread. [Diels and Rudolph, 2006]. In the other way around, 100 fs pulses carry a 10 nm spectral bandwidth. In this latter case and for thinner spectral bandwidth (e.g Ytterbium medium with ≈ 7 nm and 300 fs), it is quite reasonable to neglect the effect of chromatic aberration. Let us consider a simple converging lens. The chromatic aberrations implies that rays associated with the bluer part of the spectrum are focused further than the redder ones ². Given the focal length f of a lens of refractive index n , the axial spreading Δf around F along the propagation axis writes:

$$\frac{\Delta f}{f} = \frac{\Delta \lambda}{\lambda} \frac{\Delta n}{n-1} \quad (4.3)$$

with $\Delta \lambda \approx 10$ nm being the laser source relatively narrow spectral bandwidth centered on 800 nm and Δn the refractive index difference for the boundary wavelength of the laser spectrum obtained from the Sellmeier relations [Malitson, 1965]. For a fused silica lens, $\frac{\Delta f}{f} = 4.8 \times 10^{-6}$, corresponding to a few nanometers in the case of a focal length of $f = 1$ cm which is clearly negligible compared to the micrometric dimensions of the focal intensity distribution. This being said, research efforts have been carried to adapt spatial beam shaping techniques to the case of large spectral bandwidth ultrashort pulses. The strategy is based on consecutive diffractive optical elements for successive beam shaping followed by dispersion-related compensation [Torres-Peiró et al., 2013; Amako, Nagasaka, and Kazuhiro, 2002]. We must also point out that wavefront shaping with intensity feedback enables to overcome this types of non uniformities, thus requiring only one reconfigurable wavefront shaper [Hasegawa et al., 2016].

4.2 Spatial control through beam deflection - scanning

The most basic spatial control of the laser beam is the control of its direction with a mirror or a prism. This enables to redirect the beam and control the deposition of pulses on the sample surface or within the bulk of transparent materials. If this seems quite simple, the consequences are not straightforward because cumulative effects take place depending on the laser pulse overlap, energy, repetition rate and the physical properties of the material (that are also time-dependent). It is not possible within this discussion to list the immense variety of structures that can be obtained on surfaces or in the bulk from ultrashort laser pulse irradiation. For example, surface structures at multiple scale such as regular spikes, ripples, craters and grooves can be obtained by adjusting these laser parameters [Lehr and Kietzig, 2014; Dusser et al., 2010; Bizi-Bandoki et al., 2011]. A global trend is usually observed: the higher the deposited energy the larger the laser-induced structures. These surface structures are often accompanied by appealing modifications of the surface physical properties such as wettability [Bizi-Bandoki et al., 2011], light trapping [Vorobyev and Guo, 2011], color diffraction effect [Dusser et al., 2010], cellular differentiation [Dumas et al., 2015], improved tribological performance [Mourier et al., 2008] and wear resistance [Hammouti et al., 2015b]³. A few examples of such surface and bulk treatment relying on this spatial control of the laser energy deposition are illustrated in Fig.4.3.

The recent tremendous progress of the average power of the commercially available amplified ultrashort laser sources, now approaching the kW [Rußbüldt et al., 2010], has increased the requirement of high scanning speed devices. The average power augmentation is usually obtained by increasing the repetition rate towards MHz and even GHz. In these conditions,

²well-illustrated at <http://www.microscopyu.com/>

³The wear resistance of PEEK irradiated with ultrashort laser pulses was investigated during S. Hammouti's PhD (2012-2015) in collaboration with the LTDS

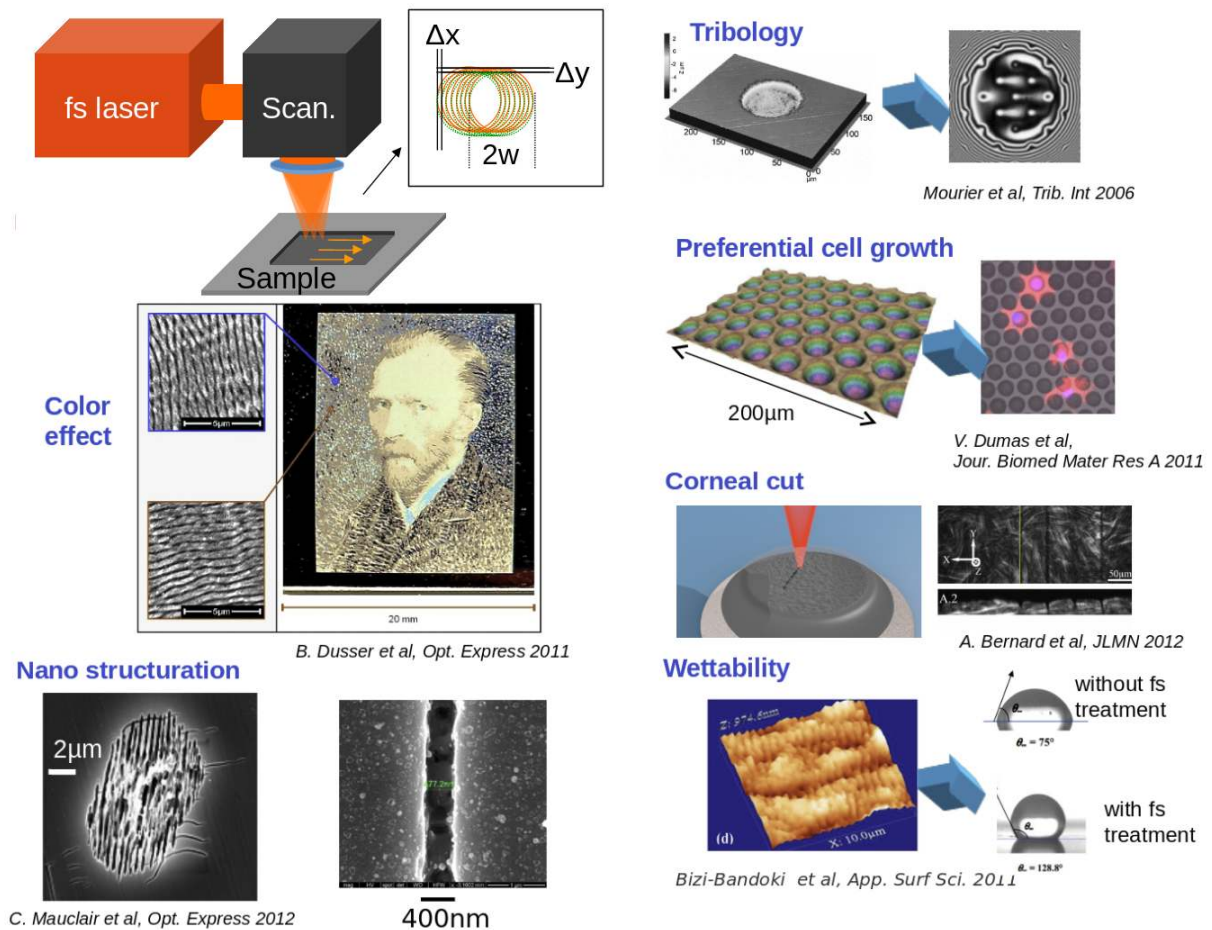


Figure 4.3 – Illustration of a scanning scheme allowing spatial control of the energy deposition by tuning the laser waist w and overlap Δx and Δy (Top left) with a few examples from our research group of surface and bulk treatment applications relying on this spatial control of energy deposition.

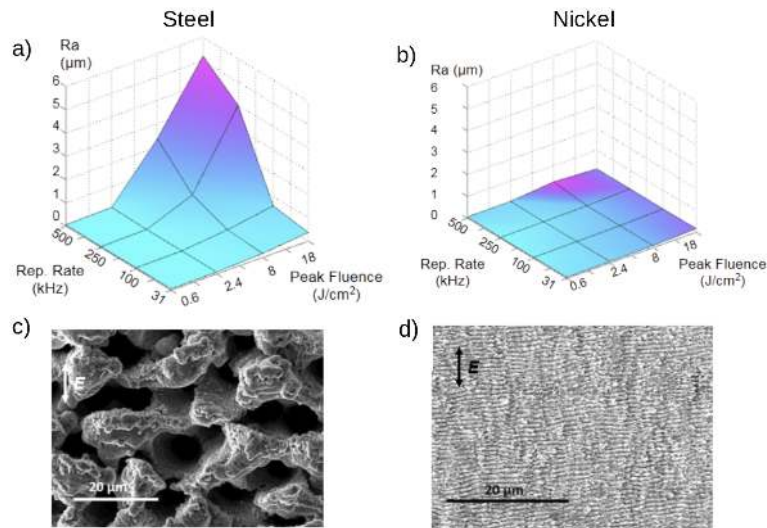


Figure 4.4 – a) and c) Roughness Ra is plotted against laser repetition rate and laser fluence for steel 316l and Ni respectively. b) SEM micrograph showing the rugged surface morphology obtained on steel at high fluence and repetition rate (8 J/cm^2 , 500 kHz). d) SEM micrograph showing the typical surface finishing of micro-machined Ni in similar conditions (8 J/cm^2 , 500 kHz). The white arrow points out the laser polarization.

the thermal relaxation between laser pulses is not complete even on metals, especially for high spatial overlap, thus a local increase of the temperature can lead the irradiated region to undesired thermal side effects such as melting⁴. [Bauer et al., 2015]. Very high speed scanning of the laser spot to reduce the overlap is now the bottleneck of femtosecond surface processing, leading to the use of high deflection speed polygonal scanners [Loor, 2013; Loeschner et al., 2015], or electro/acousto-optic scanners [Römer and Bechtold, 2014]. Let us mention here that at higher repetition rates (of a few GHz and above) intriguing phenomena occur where enhanced ablation is achieved with low onset of side thermal effects, referred to as the ablation-cooled regime [Kerse et al., 2016]. Within the kHz-MHz regime, we have recently shown that the surface roughness after laser surface scanning irradiation can be kept to low Ra levels when the laser energy and spatial scanning parameters are adequate, along with the sample surface physical properties [Sedao et al., 2019]⁵. More precisely, we have shown that on stainless steel 316L and Titanium alloy (TA6V), the processing window of the spatial laser energy deposition for low Ra ablation is much narrower than on Cu and Ni, even though the quantity of removed species remains constant (if properly measured by differential weighing). The reasons are related to the physical properties of the materials, especially the electron-phonon coupling constant γ and the thermal diffusion coefficient K . The electron-ion transfer occurs much faster for stainless steel and Ti than for Ni and Cu because of stronger γ . Considering K also indicates a stronger heat confinement for steel and Ti than for Cu and Ni. These observations can be linked to former results on Au, Cu and Ag, where the trend of γ seems to follow the probability of laser induced periodic surface structures (LIPSS) generation under ultrafast irradiation [Wang and Guo, 2005]. Spatial controlling of the laser beam through smart scanning can also lead to exotic structures as we observed and demonstrated in the paper [Sedao et al., 2018]. There, we took advantage of the re-deposited material associated with

⁴even though some melted structures can be of interest for specific surface functions, like hydrophobicity [Emelyanenko et al., 2015] and also to accelerate the process of percussion drilling [Ancona et al., 2008]

⁵This work was conducted within the Labex project ICRAM (2018).

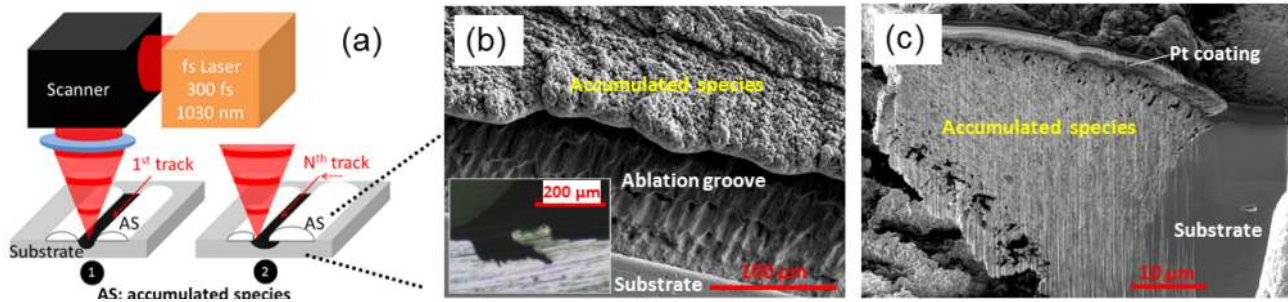


Figure 4.5 – Principle of ultrafast laser 'additive' manufacturing (LAM): (a) schematic of the laser process. The laser beam movement starts from the far side of the substrate and advances linearly towards the near side to form a scan track. The scan tracks start from the right side and end on the left. The number 1 represents the beginning and number 2 the end of the process; (b) SEM micrograph showing the site of ablation, and additively grown part. A mechanically prepared cross-section is given as inset to illustrate the longitudinal correlation between the ablation site and additively grown part. (c) A FIB milled cross-section of the additively fabricated part.

ultrashort laser ablation at high fluences - above the optimum laser fluence for efficient ablation (which is 2-4 times the ablation threshold [Neuenschwander et al., 2014]). In these conditions, the material ejecta can be accumulated along the scanning track of the laser spot, thus forming an 'additively' manufactured hill of a few hundred of micrometers as depicted in Fig.4.5. These grown structures were observed under SEM and also with a FIB-milled cross section in order to evaluate their link to the sample surface. These structures have shown particular wettability properties (notshown). By spatially controlling the laser spot trajectory, the geometry of the grown structures can be tuned. For example, trajectories following concentric circles could raise some circular spikes. In order to form more regular structures, an additional machining step has been proposed, using the ultrafast laser beam in the optimum fluence regime. There, precise ablation is achieved on the formerly grown structures enabling further sculpting by spatial control of the spot trajectory. Fig.4.6 shows pillars obtained with this process. These pillars are higher than the original surface with a much sharper contour. They also present some super hydrophobic properties. ⁶ As a conclusion for this section, scanning of the laser spot is a straightforward and very efficient control knob to drive the irradiation output. By tuning the laser spot size, overlap, trajectory and energy, sub-micrometric roughness surface ablation can be achieved on the one hand to grown pillars of 100 μm on the other. Nowadays very high repetition rates laser sources are now expecting faster scanning systems that are now the bottleneck of ultrafast processing in order to avoid thermal accumulation effects and further reduce the processing time. Similar conclusions can be drawn for surface and bulk structuring.

4.3 Beam truncation and imaging

Amplitude modulation of the incoming laser beam is a well-known solution that enables to control the laser intensity distribution in a plane situated further in the propagation. Using simple imaging of the amplitude mask on the irradiated workpiece, this technique is particularly efficient when simple shapes are desired. This is especially the case when these shapes are

⁶This work has also been achieved within the Labex project ICRAM (2018).

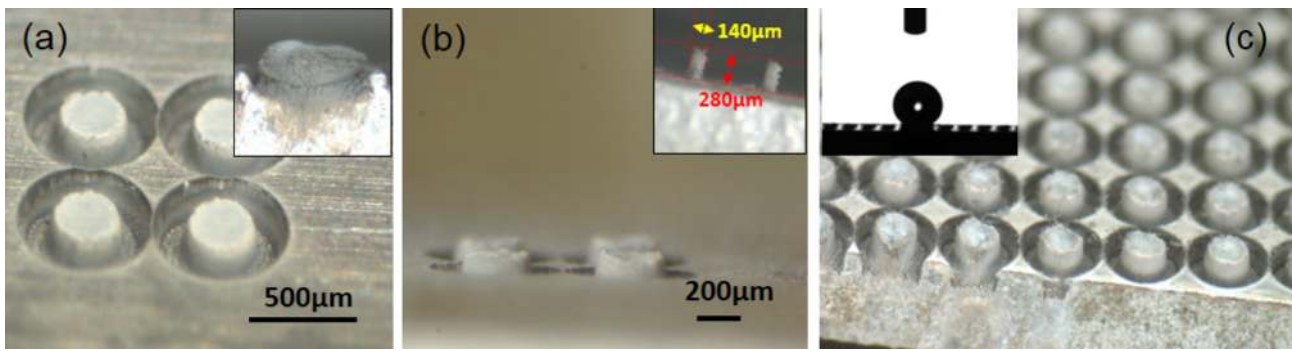


Figure 4.6 – (a) 4 sub-mm sized pillars made by the ultrafast LAM, followed by ultrafast laser ablation at the contour of the pillar blocks to sharpen the edges. The inset shows a single ultrafast LAM unit without its edge being sharpened; (b) Tilted view of the pillars. The pillars can be grown higher, at the cost of pillar diameter, as shown in the inset; (c) Pillars similar to those in (a) are fabricated on large scale for superhydrophobicity, as demonstrated in the inset (water drop volume 3 μL)

close to the native beam profile in shape and in size to reduce the laser energy waste (e.g, top-hat circular shapes, squared shapes and so on). The method is often employed when a high degree of regularity is required by the application, higher than the original laser beam profile. As an example, a surface network of very regular dimples on steel surfaces for friction reduction of the lubricated contact [Mourier et al., 2008] or for the study of cellular differentiation [Dumas et al., 2015]⁷ can be achieved using this technique. The desired laser spot shape can be obtained by simply putting an amplitude mask positioned among the focusing lens and optically conjugated with the processing plane as depicted by Fig.4.7 a). We recently investigated the challenge when imaging such an aperture with a single focusing lens [Pietroy et al., 2015]. One major drawback of this technique is that the image plane is usually formed after the focusing point of the lens. Thus, when using ultrashort laser pulses, the focal point in the air can be a region where nonlinear effects occur due to the laser high peak power as illustrated in Fig.4.7 b). These nonlinearities in the focal region can distort the laser propagation, affect the quality of imaging and quality of the ablation. With numerical calculation, we evaluated the amount of optical delay corresponding to the onset of nonlinear Kerr contribution. For this we simply assumed that the spatial distribution of the nonlinear refractive index followed the intensity distribution in the focal plane. We disregarded any absorption or diffusion effect in the focal plane as no plasma luminescence were observed experimentally in the air within the energy range that were studied. It can be seen Fig.4.7 b) that the image plane is distorted as the laser fluence increases comparing the profile of the laser to processed region on stainless steel. We proposed an efficient solution to this problem by adding a lens in order to avoid the formation of a focal point before reaching the image plane. In that case no deterioration of the image plane was observed. While this technique of beam shaping is quite simple, the major drawback is naturally the loss of laser energy. Also, clipping the beam with an aperture does not generate a flat intensity distribution because of the Gaussian distribution of the initial beam. These results were obtained with the OSEO project ARTEMIS during the postdoctoral stay of D. Pietroy (2012)

⁷This work on cellular differentiation was conducted with the collaboration of the LTDS within the St-Etienne Metropole project MicroOsteo

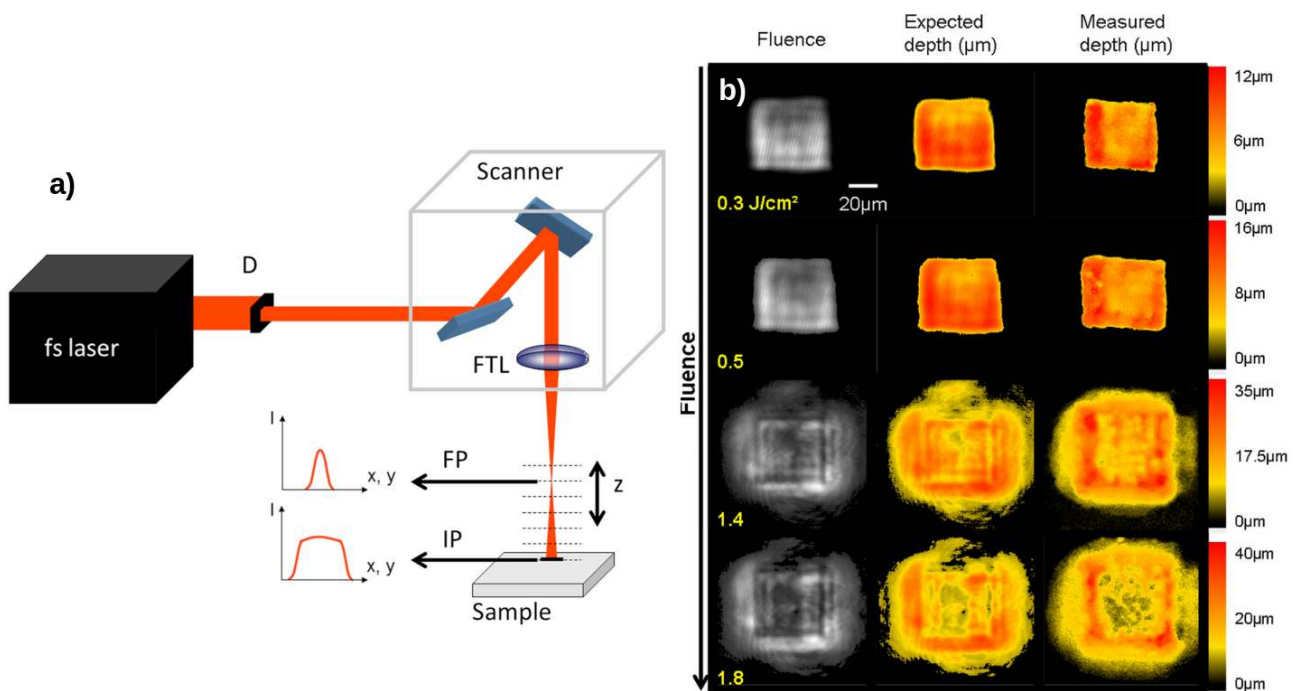


Figure 4.7 – a) Scheme of amplitude modulation using a diaphragm D conjugated by the f - θ lens (FTL) on the image processing plane (IP) after the focal point (FP). b) experimental evolution of the intensity distribution in the IP compared to the depth of related ablation crater on steel. Nonlinear effects at the FP distort the beam propagation, intensity profile and ablation profile.

4.4 Truncation effect on the focal volume

Partial beam clipping has an effect on the intensity distribution in the focal region of a lens. This effect is usually exploited in the x - y plane (transverse to the z propagation axis) but also along the propagation axis, i.e. in an x - z or an y - z plane. A well-known application is the use of a slit placed on the beam before the focusing lens. In that case, the focusing strength is stronger on x than on y if the slit edges are parallel to the y axis. Under certain conditions, this generates a circular intensity distribution in the y - z plane as depicted on Fig.4.8 a)-b). This technique, called slit shaping, is used for transverse waveguide writing in the bulk of transparent materials [Ams et al., 2005]. We have shown that it is possible to dynamically adjust the slit in order to photoinscribe curved waveguides [Zhang et al., 2009b] as illustrated on Fig.4.8 c)-d). We mention here that the astigmatism aberration can generate a similar beam distribution with reduced energy losses as shown by [Cruz et al., 2009].

Beam truncation can also be at the origin of the generation of multiple focal spots. We have studied this phenomenon in the bulk of fused silica and BK7 [Mauclair et al., 2011c]. More precisely, when a Gaussian beam is truncated by a circular aperture, it can be shown that the spatial light distribution around the focal plane shows several spots well aligned and regularly spaced along the optical axis z . The position of these spikes can be calculated numerically using a Fourier based propagation code in the paraxial approximation (see Fig.4.8 d-f)). Indeed this phenomenon has been described in the famous book of reference [Born and Wolf, 1999] where a focused truncated plane wave through a circular aperture is thoroughly studied. We took advantage of these intensity centers to generate arrays of dots in the bulk of BK7 and fused silica glass as shown in Fig.4.8 g). These results were obtained during my own PhD.

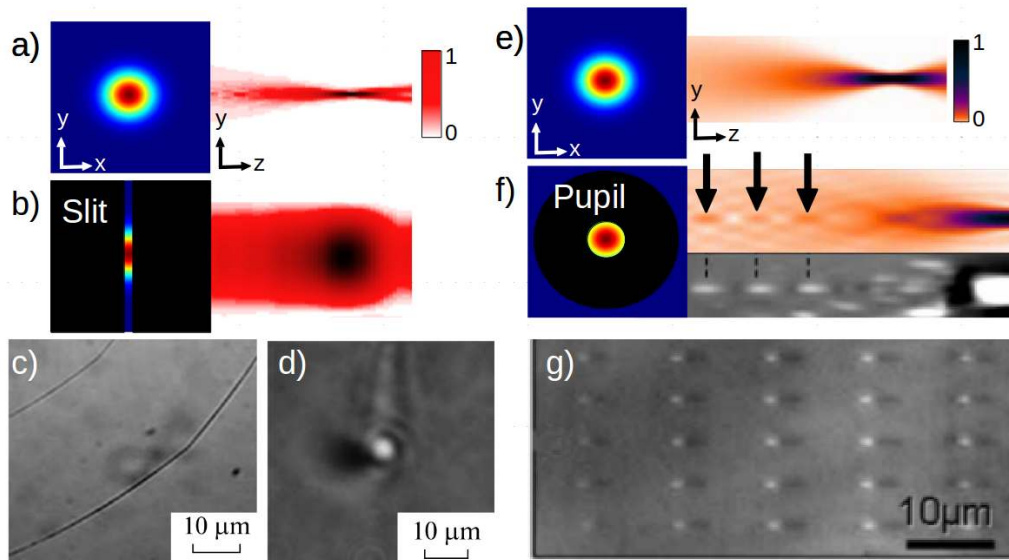


Figure 4.8 – Example of beam truncation that shapes the 3D beam shape, along the propagation axis. Slit truncation (b) numerically compared to non-truncated Gaussian beam (a) can generate a circular beam distribution in the y-z plane. By dynamically adjusting the slit, curved waveguides can be photoinscribed here in fused silica. (c) is a top view and d) a cross section observed with a phase contrast microscope). e) and f) compare the calculated beam modulation without and with pupil truncation. The pupil generates regular intensity spots before the focal region on the optical axis, shown by the arrows and observed in BK7 glass. f) shows an dot array photowritten in fused silica using the phenomenon. The intensity scalebars are normalized to 1.

4.5 Advanced amplitude modulation - GPC

Amplitude modulation can also be obtained using a spatial light modulator (SLM) in the so-called amplitude modulation as demonstrated by the group of W. Perrie [Kuang et al., 2015]. In that case the amplitude modulation can be achieved on different levels of intensity attenuation thanks to the possibility offered by the SLM to linearly control the attenuation strength in the amplitude modulation configuration as depicted on Fig.4.9 a) and b). This enables to counteract the Gaussian shape to flatten the desired intensity distribution, even though energy losses can be high. It has recently been shown that this technique can be combined with phase modulation technique to obtain duplicated arbitrary beam shapes for advanced parallel processing [Li et al., 2019].

We also have to mention here the technique of General Phase Contrast (GPC) at the frontier of amplitude and phase modulation [Palima and Glückstad, 2008]. This technique relies on the principle of phase contrast microscopy where the portion of the light beam that goes through phase objects is purposely put in interference with the non diffracted microscope beam. That way, the phase contrast is turned to an intensity contrast on the microscope camera. In the case of laser beam modulation, the plane of wavefront regulation corresponds to the plane of the phase object of the phase contrast microscope. In order to turn this phase modulation to an intensity modulation the general phase contrast method employs the use of a phase disk positioned in the focal plane of a lens, the phase contrast filter (PCF) as shown on Fig.4.9 a). The wavefront modulation plane is conjugated on the PCF through a lens and then the PCF is conjugated to the focal processing plane. They are theoretically low laser intensity losses and experimentally these were found very low [Bañas et al., 2014]. This technique gives

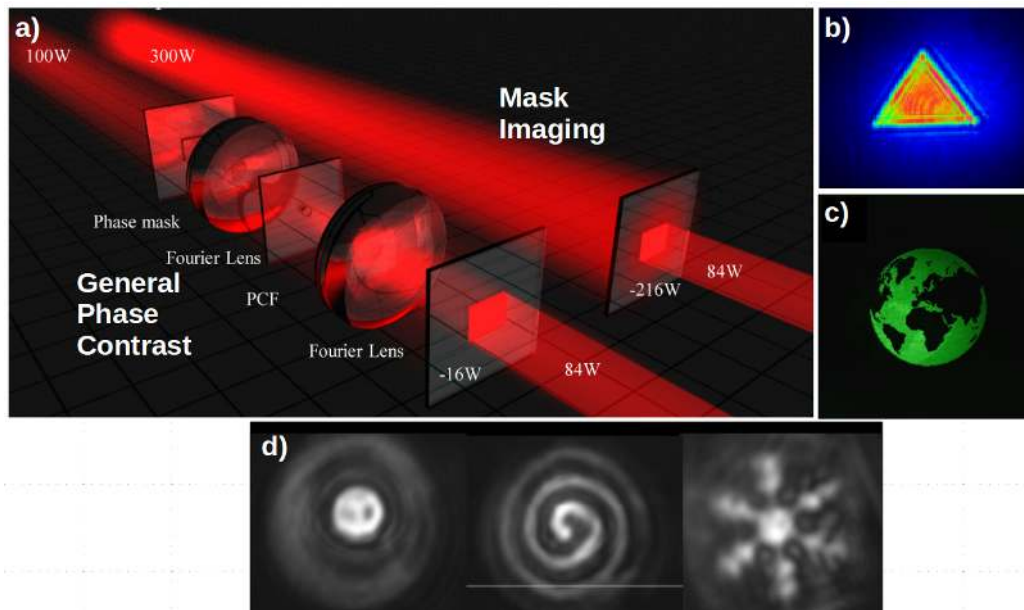


Figure 4.9 – Amplitude modulation techniques. a) compares mask imaging and GPC (adapted from [Bañas et al., 2014]). Shaped laser beams are shown in b) and c) for mask imaging (from [Kuang et al., 2015]) and GPC respectively. d) Experimental application of GPC to femtosecond pulses. Beam sizes are within the 50-100 μm range.

remarkable beam shaping qualities (see Fig.4.9 c)) and is successfully employed in the field of optical tweezers [Eriksen, Mogensen, and Glückstad, 2002].

Naturally the challenge with this technique is related to the small disk in the focal plane of the lens. In the case of femtosecond laser with high intensity this element can be damaged because of the laser focusing on the disk. We carried out some investigations using very long focal length to achieve GPC with femtosecond pulses as depicted on Fig.4.9 d) at low intensity level. It can be seen that the GPC technique provides good control of the laser intensity distribution. Sadly, when turning up laser energy, we observed a strong degradation of the laser distribution experimentally; even though we didn't observe any damage formation on the disk. A possible explanation can be found presumably in the onset of nonlinear propagation of the laser beam. These nonlinearities translate into uncontrolled spatial distribution of phase delay which in turn degrades the GPC interference relationship. These investigations were carried out during the postdoctoral stay of J. Houzet (2014-2015) within the ANR project 'Topoinjection' in collaboration with the LTDS.

4.6 Conclusion

As a short conclusion, if amplitude modulation is often disregarded because of the inherent energy losses, its simplicity of use in the case of imaging masks remains a strong advantage. Moreover, we have shown a way to overcome the problem of nonlinearities in air when using imaging on the sample surface. Beam truncation also permits to control the laser intensity distribution along the optical axis, e.g producing circular shapes (slit shaping) and multiple on-axis laser spots (pupil truncation). Advanced techniques involves variable intensity attenuations using SLMs and phase filtering following GPC. Both techniques can reduce the energy losses. However GPC is hardly applicable to high intensity laser pulses because of the phase filtering plane at the focal plane of lens.

Chapter 5

Spatial Shaping of ultrashort laser irradiations - Wavefront modulation

5.1 Basics

Modulation of the laser wavefront or spatial phase, is a very widespread technique both in laser processing and detection application fields. The main advantage is the absence of energetic losses in principle compared to amplitude modulation. Significant advances in terms of beam shaping performance, flexibility, adaptation to high power were recently demonstrated supported by progress of the technology and phase modulation calculation algorithms.

There are many devices that enable wavefront modulation of a laser beam. Let us cite SLMs (Spatial Light Modulator), DMs (Deformable Mirror), AOMs (Acousto-Optic Modulator), DOEs (Diffractive Optical Element). Each of these technologies have advantages and drawbacks that are continuously evolving. Key features are diffraction efficiency, spatial resolution, phase modulation range, power handling, reconfigurability, stability and response time. In the following, we will purposely focus on SLMs that have the historical advantages of resolution, stability¹, reconfigurability (relatively low response time of 20 ms). Recent progress of the technology in terms of fill factor, diffraction efficiency have solved the problem of the 0th order [Kuang et al., 2009]. Also, the power handling now remarkably approaches 200 W [Kaakkunen, Laakso, and Kujanpää, 2014; Zhu et al., 2018]. Spatial Light modulators usually rely on a birefringent liquid crystal (LC) layer, where the orientation of the LC can be electrically controlled. The LC molecules orientation linearly impacts their refractive index. When a laser traverses the LC layer with the proper polarization (parallel to the LC molecule orientation), it experiences a 2D-phase retardation map, depending on the LC orientation map i.e the electric field. Fig.5.1 illustrates the generation of a prism and a biprism phase mask and the modification of the laser intensity distribution that is beam deviation and spot duplication respectively.

Usually, the phase modulation plane corresponds to the object focal plane of the focusing lens. In this case, a Fourier transform permits to mathematically relate the complex laser amplitude of this plane to the focal plane under the paraxial approximation [Goodman, 2005]². Thus, the calculation of the proper phase modulation for a desired intensity distribution can be based on optimization algorithms relying on one or several Fourier Transforms. Without entering into details, let us mention the famous Gerchberg-Saxton algorithm, or Iterative Fourier Transform Algorithm (IFTA) [Gerchberg and Saxton, 1972]. This deterministic algorithm performs back

¹Phase flickering issues have been reported [Calderón-Hermosillo et al., 2013], depending on the electric addressing technology with a strong advantage for analogic addressing

²If the phase modulation is performed in another plane, a parabolic phase term may be added to the calculation

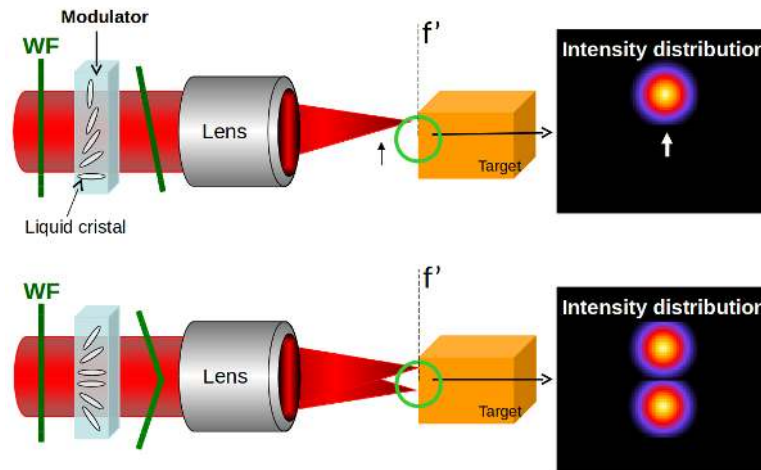


Figure 5.1 – Illustration of spatial beam shaping through wavefront (WF) modulation in the case of LC-SLM. Top: prism phase modulation that changes the spot position, bottom biprism modulation generating two distinct beams.

and forth propagations between the phase modulation plane and the focal intensity target plane, having as input the target intensity and the input beam amplitude. Iterations go on until a phase mask permits to obtain a intensity in the focal plane close enough to the target. Many improvements have been proposed for this algorithm, such as extension to N-planes (in 3 dimensions) [Sinclair et al., 2004], dynamic adaptation of the target intensity [Leonardo, Ianni, and Ruocco, 2007; Silvennoinen et al., 2014], introduction of a 'numb' region for high fidelity shaping [Gaunt and Hadzibabic, 2012; Bijnen et al., 2015] and so on.

When the intensity target is simply an array of distinct spots, the lens and gratings (LG) techniques must be mentioned here. The LG is based on the fact that each desired laser spot in the focal region corresponds to a given beam deflection and defocusing i.e a phase tilt and phase curvature (parabolic). A sum of each complex contribution permits to generate the desired phase mask, without the need of any optimization step [Liesener et al., 2000]. This strategy can also include position-dependent aberration correction and arbitrary intensity levels [Jesacher and Booth, 2010]. To some extent, the LG strategy is similar to the generation of spot arrays with Dammann cells [Dammann and Klotz, 1977] that has also been extended in the 3D [Yu et al., 2012]. The phase modulation can also be calculated based on a ensemble of Fresnel lenses, each lens corresponding to one laser spot [Hasegawa, Hayasaki, and Nishida, 2006].

5.2 Parallel processing in 2D-3D with multiple laser spots

One of the very first challenges of femtosecond laser processing concerns the cost and time. While ultrafast laser pulses permit to obtain high energy localization followed by precise structural modification (ablation, refractive index modification, local surface roughness etc.), these sources are still significantly more expensive than nanosecond pulses sources. Thus, femtosecond based processes are now still constricted to high value markets where the ultrashort character of the light pulses is determinant. One clear example of such an application is the well-known LASIK (laser in-situ keratomileusis) surgery and also the growing field of cataract surgery assisted by femtosecond laser pulses in the infra-red. There, the short pulse length allows precise in-volume cuts of of the cornea and crystalline lens, whereas longer pulses fail to deterministically localize the energy deposition. Femtosecond pulses can attain larger

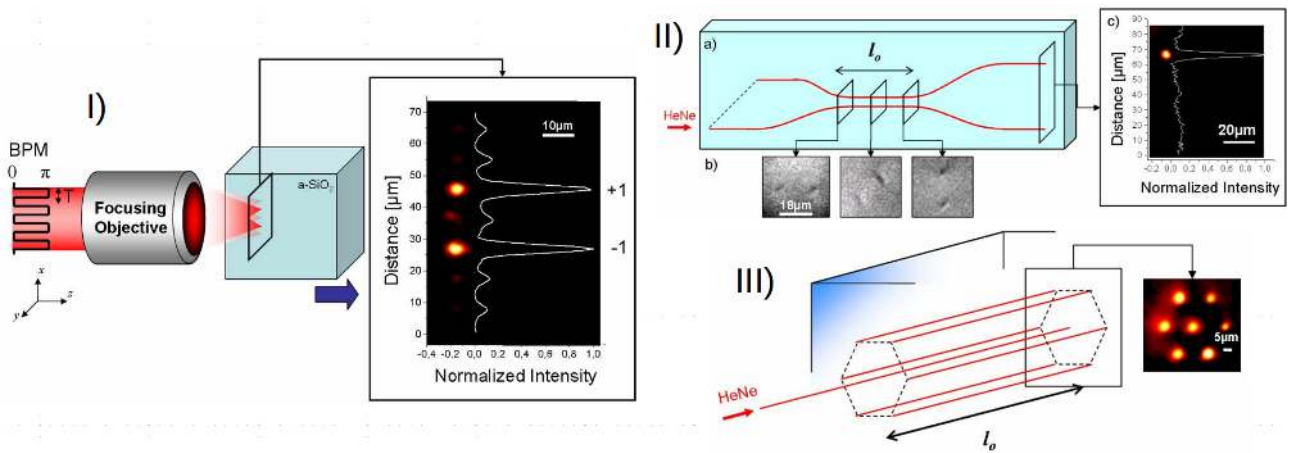


Figure 5.2 – I) Scheme of double spot operation. BPM: Binary phase mask. Insert: Double spot intensity profile inside the sample at the focus of the objective generated by a simple step grating phase at very low power captured by direct imaging on a CCD camera. The blue arrow shows the direction of motion of the sample for longitudinal photoinscription. II) (a) Schematic view of a bulk photowritten twisted X coupler achieved through dynamic multispot operation in a single scan. (b) Optical transmission microscopy pictures of the central region, showing 90° rotation. (c) Nearfield profile at the output of the top arm under 633 nm. III) Schematic view of a bulk photowritten 3D hexagonal light divider based on the coupling length l_0 . Insert: Nearfield profile under 633 nm injection in the central waveguide.

applications fields only with a drastic increase of the processing speed and the ratio source power/cost. As mentioned above, nowadays high repetition rate sources coupled with high speed scanning devices bring a relatively straightforward³ answer to these needs. However, spatial beam shaping can also significantly contribute to this effort, especially with wavefront modulation, i.e accompanied with very low energy losses. More precisely, wavefront shaping can duplicate the laser focal spots in several identical spots in the focal plane. Each of these spots can be seen as an added processing spot. The array of spots enables parallel processing of the bulk or surface. Using this technique, we could perform pioneering work on parallel waveguide writing in fused silica [Maclair et al., 2009a]. In this work, summarized on Fig.5.2, a binary phase mask (BPM) was applied to an SLM in order to generate 2 focal spots in the bulk of fused silica glass as shown on Fig.5.2 I). Upon translation of the sample synchronized with the reconfigurable phase mask, 3D photonic structures were produced such as light couplers (see Fig.5.2 II)), demultiplexers and dividers (see Fig.5.2 III)). The devices are based on evanescent coupling of light between adjacent waveguides in the weakly guiding mode. Interestingly, these results were highlighted especially regarding the reduction of the processing time :

"Cyril Maclair and co-workers from France and Germany have now demonstrated that the problem of speed can be solved by parallel photoinscription that uses multiple laser spots with reconfigurable patterns."⁴

We have naturally followed this work by increasing the number of processing spots as well as their control, especially for surface structuring and sample cutting as shown in Fig.5.3 and Fig.5.4. More precisely, we reported on an optimization of a line of laser spots to machine a network of micro-dimples with a high uniformity (<7% variations in diameter and depth) achieved on stainless steel (316l) and DLC (diamond like carbon) samples using a wavefront

³Even though the laser/scanner synchronization and beam positioning control needs fine technical tuning

⁴Nature Photonics | VOL 3 - MAY 2009 p260

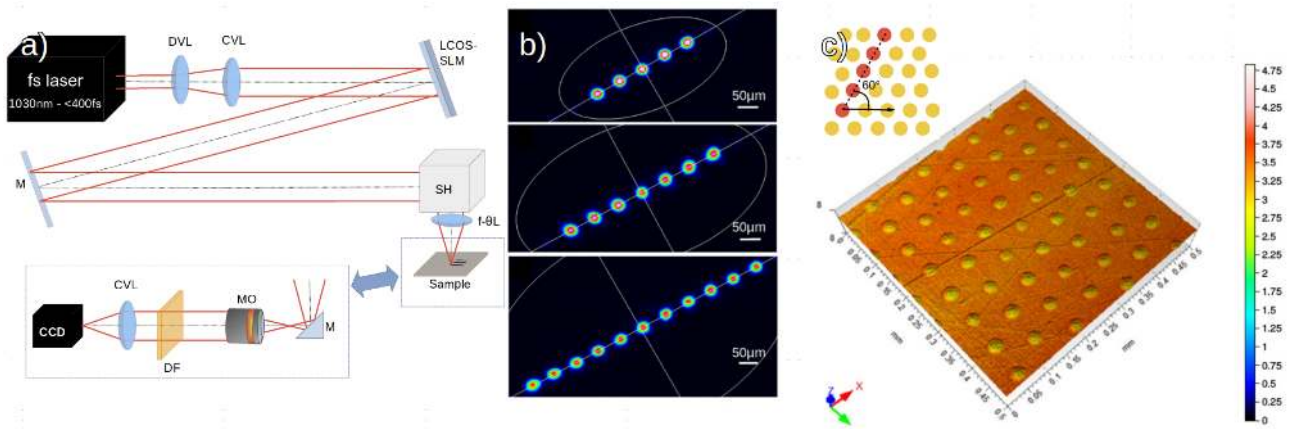


Figure 5.3 – a) Experimental set-up for sample irradiation and analysis of the beam shaping. DVL: Diverging Lens, CVL: Converging Lens, SLM: Spatial Light Modulator, M: Mirror, SH: Scanning Head, MO: Microscope Objective, DF: Optical Density Filter. b) Experimental intensity distribution observed with the CCD sensor in the case of 5, 7 and 11 parallel laser spots beam shaping. c) Surface topology of the DLC sample after micro-structuring using the 5 spot array translated at an angle of 60° . The eight scale is in micrometers

shaping with an SLM [Saint-Pierre et al., 2016] (see Fig.5.3 a))⁵. This network is a typical surface micro-structuring aiming at the reduction of friction coefficient in lubricated contacts [Mourier et al., 2008]. To achieve the surface network of ablated dimples in a parallelized process, the laser wavefront has been modulated in order to form arrays of 5-11 spots with an uniformity better than 5% (see Fig.5.3 b)). It is however possible to distinguish a slighter drop of uniformity in the cases of the 7 and 11 spots array, especially looking at the shape of the spots which is less circular than in the 5 spot case. In practice, these irregularities are transferred during the machining on the surface. Generally, this is not a problem for surface marking. However for the generation of a regular network of micro-dimples, this implies a lower control of the micro-dimple symmetry and this has to be avoided especially for applications where the laser-treated surface will undergo contacts and frictions. Concerning the phase mask calculation, a proper use of the IFTA algorithm is required. As a recall, the IFTA starts with a phase modulation in the SLM plane (or object plane) that can be chosen. We have experimentally found that a random phase mask at the start yields better results for an homogeneous spot array, even though a few 'tries' (up to 3-4) on the optimization loop (each one lasting a few seconds) may be necessary, especially for a higher number of desired spots. We also have implemented a slight amelioration of the IFTA, namely the weighted IFTA (wIFTA) [Leonardo, Ianni, and Ruocco, 2007]. From the experimental beam profile file, the IFTA target was adjusted to compensate for non uniformities among the laser spots. These adjustments can be automatized with a feedback loop on the intensity distribution or on the wavefront aberration [Hahn et al., 2006; Silvennoinen et al., 2014]. We have observed a high repeatability of the performance of the phase masks found by the IFTA throughout several weeks. The dimple network has been achieved by translating the five spot array with an angle of 60° , 10 pulses per dimple and a pulse energy of $28 \mu\text{J}$, at 167 kHz. A study of the dimple depths and diameters has been conducted to evaluate the homogeneity of the surface after laser processing. An example of the dimples depth and diameter measurements is shown in Fig.5.3 c). The mean dimple diameter is $30 \mu\text{m}$ and the mean depth is $0.51 \mu\text{m}$. It has been

⁵This work has been done in within the ANR EQUIPEX program Manutech-USD, during the building of the ultrafast texturing machines (2016)

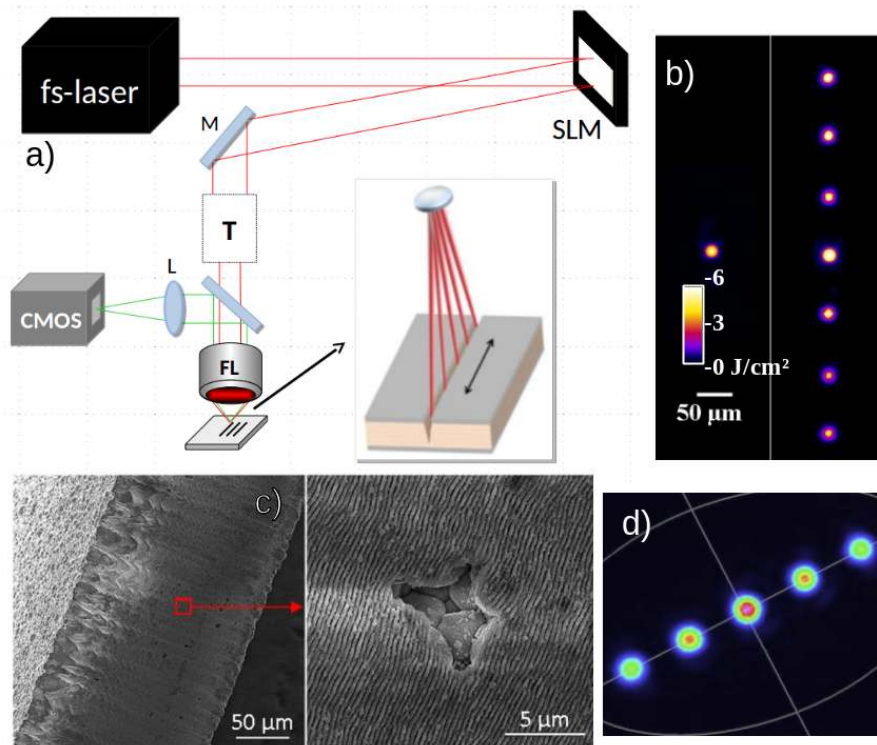


Figure 5.4 – a) Experimental setup M: mirror, T: telescope, L: lens, FL: focusing objective lens. The inset shows the sample translation direction with respect to the line of laser spots. b) Experimental beam profiles using a 25 mm converging lens with phase modulation. c) SEM micrographs of the PZT wafer cut walls with a zoom revealing LIPSS, usually witnessing a low onset of thermal effects. d) Example of gradient line-array of spots with controlled peak intensities.

observed a very good uniformity of the micro-dimples network with variations of depth and diameter below 7% across the sample surface. The capacity of wavefront shaping to achieve efficient parallel processing (here 5 times faster⁶) while maintaining a high level of energy control is key for the development of ultrafast laser applications. Moreover, wavefront shaping to obtain a line of spots is particularly adapted to increasing repetition rate and scanning speeds. As an illustration, this permits to lower the processing time of a roller tapet (5 cm diameter) to 4 seconds, generating this exact dimple network. this corresponds to a surfacing speed of $v = 5 \text{ cm}^2/\text{s}$. Within the IMOTEP project, the processing time will be reduced well below one second using higher repetition rate (1 MHz), higher pulse energy ($300 \mu\text{J}$) permitting to use at least 10 parallel spots and higher scanning speed (100 m/s). This should permit to gain a $50\times$ factor on the surfacing speed, i.e $v \approx 250 \text{ cm}^2/\text{s}$, that is $1.5 \text{ m}^2/\text{min}$. This has to be compared to our first results at the beginning of the the ANR Equipex Manutech project without beam shaping and at lower repetition rates. At that time, a single roller tapet surfacing would last 3 minutes. We have adapted this technique with a similar experimental set up (see Fig.5.4 a) for fast cutting of $180 \mu\text{m}$ thick PZT wafers [Mauclair et al., 2015c]. Line-arrays of $N = 3$ and 7 spots (Fig.5.4 b)) have been generated with good uniformity (better than 10%) and for two kinds of focusing lenses, 25 mm and 50 mm (not shown). For this application, the line-array has been translated parallel to its own direction, to perform N passes in one scan of the shaped beam. Wafer cutting could be achieved N times faster than with single spot cutting. Some

⁶Indeed, the processing time is a bit more reduced because of the reduction of the scanning path and also a lower number of time-consuming half-turns.

wafer cut walls are illustrated on Fig.5.4 c). Using the same wIFTA routine, modulated line arrays were generated (see Fig.5.4 d)) i.e with an intensity gradient between the peaks in order to identify optimal conditions for possibly faster cutting rates. These investigations were carried out during the PhD of Y. Di Maio (2012-2015). As mentioned above, a widespread application where ultrashort pulses have a undisputable advantage over longer laser pulses is the LASIK and femtocat eye surgery [Juhasz et al., 1999]. There also, wavefront shaping for parallel tissue ablation offers a key advantage in terms of speed, precision, safety and patient comfort. The treatment of eye myopia, hyperopia, and astigmatism by LASIK necessitates the creation of a corneal flap that can be achieved using a mechanical blade (microkeratome) or the ultrashort laser pulses as illustrated on Fig.5.5 I)A and B. After the corneal cut, the surgeon opens the flap (Fig.5.5 I) B). An UV laser (usually an excimer) is then directed on the corneal tissues to ablate following a topographical scheme that compensates for the eye's aberration (Fig.5.5 I)C). Central ablation zones correct for myopia and peripheral zones for hyperopia. The UV radiation (below 200 nm) is absorbed in the extreme surface of the tissues, allowing for a precise adjustment of the ablation depth i.e the final corneal thickness. Finally, the surgeon puts the corneal flap back in place (Fig.5.5 I)D). A key element of any surgery is the duration. In the case of the flap creation, it must be clear that the eye is firmly maintained ('docked') by a suction ring that augments the internal eye pressure and is very uncomfortable. Without entering in to the detail of the various docking technologies, the main idea is that the docking time must be as short as possible for comfort and also for safety issues since the procedure is quite evidently not physiological (eye pressure augmentation may also imply secondary effects). The docking is not necessary for the UV laser step, using an eye-tracker system that launches the UV pulses at the right moment and position. The interest of a phase modulation for the flap generation is clarified by Fig.5.5 II and III. With the phase mask positioned on the laser path before reaching the photodisruption plan, the ultrafast laser beam is modulated in order to form an array of N laser spots for disruption of eye tissues - the so-called Matrix technology from Keranova⁷. The laser cutting time is then reduced by a factor even superior to N , because of the scanning path is also reduced (less turning points that also saves a significant amount of time). Thus, a flap can now be achieved well below the second ($v < 1 \text{ cm}^2/\text{s}$ (Fig.5.5 IV), compared to the 6-10 s offered by the current systems. The preliminary results were first demonstrated during the PhD of A. Bernard (2010-2013) in collaboration with the BIIGC laboratory. It is now pursued within the start-up Keranova especially on the cristalline lens as explained below. The interest of parallelized disruption becomes even more evident when thinking about the cataract surgery. Upon aging (most of the time), the human cristalline lens gradually loses transparency and eventually becomes opaque (see Fig.5.6 a)), with an ultimate blinding effect for the patient that is the cataract (from the Latin *cataracta* i.e "water fall"). There are several grades of cataract before the lens becomes opaque which are characterized by faded colors, blurry vision and difficult seeing at night. The World Health Organization has estimated in 2015 that 51% of world blindness is due to cataract i.e 20 millions people. Surgery of the cataract is the most widespread surgery in the world, and has been recorded as early as 500 BCE in the manuscript of ancient India Sushruta Samhita. Accounts in Greece from Galen of Pergamon (ca. 2nd century CE) are also famous. The main idea of the surgery is to remove the opaque lens to recover eyesight. Intraocular implants (IOL), in the form of folded polymer lenses, are deposited after the lens removal to reconstitute the focusing power of

⁷See patents :

- WO-201605539-A1, A. Bernard, P. Gain, C. Mauclair, G. Thuret (2016)
- FR-3049853-A1 and FR-3049847-A1, F. Romano, A. Bernard, C. Mauclair (2017)
- EP-3439593-A1, F. Romano, A. Bernard, C. Mauclair, E. Baubeau (2019)

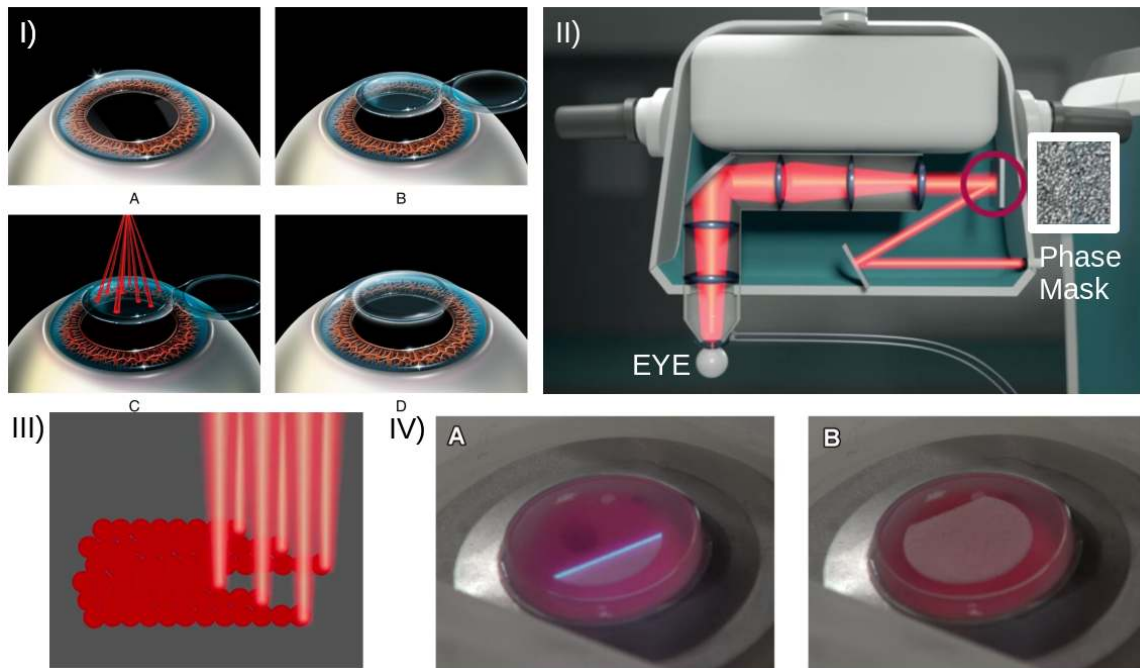


Figure 5.5 – I) LASIK steps detailed in the text (from <http://eyesurgerysingapore.blogspot.com/2012/02/>). II) Keranova's Matrix laser head involving phase modulation permitting to duplicate the number of laser spots. III) Illustration of parallel photodisruption with 6 spots, drastically reducing the surgery duration. IV) Example of less-than-a-second complete flap generation in human cornea.

the removed lens. In order to remove the lens, many techniques were developed. Today, the use of a phacoemulsifier is common. This handpiece allows for emulsification of the lens thanks to ultrasonic vibration of its metallic needle and aspiration of the debris through its tip. If the surgery is well-known, there is risk using the handheld phacoemulsifier that can perforate the posterior lens capsular bag during the surgery. Nowadays, femtosecond pulses are used to perform a pre-cut pattern on the crystalline lens to ease the phacoemulsifier step as shown on Fig.5.6 b). In order to achieve this pattern, the laser beam is scanned in the 3 dimensions to achieve the desired pattern. During this step that can be relatively long, the patient's eye is docked. Here, it can be argued that the benefit brought the femtosecond pulses is relatively low compared to the eye-docking necessity, especially having in mind that the phacoemulsifier is still necessary.

The use of several laser spots in parallel permits to perform an entire emulsification of the lens in a reduced time. Three dimensional spots arrays (not shown) are achieved using wavefront modulation as explained earlier in order to fill as fast as possible the ablated volume. The density of irradiated planes is such that the debris are small enough ($\approx 100 \mu\text{m}$) to be directly removed with a regular irrigation-aspiration system. There, no phacoemulsifier is required. The start-up Keranova, with which I have the great pleasure to work, has recently successfully performed the first in human clinical complete photoemulsification of a crystalline lens with no need of phacoemulsifier (see Fig.5.6c) and d)). The procedure lasts below 40 seconds during which more than 3×10^6 impacts are achieved in the volume of the crystalline lens for full photoemulsification. Related to corneal research, we have also studied the femtosecond laser assisted transfection of corneal cells. Without entering into details, the endothelial cells of the corneal do not naturally renew. Since their main function is to preserve to corneal transparency, there

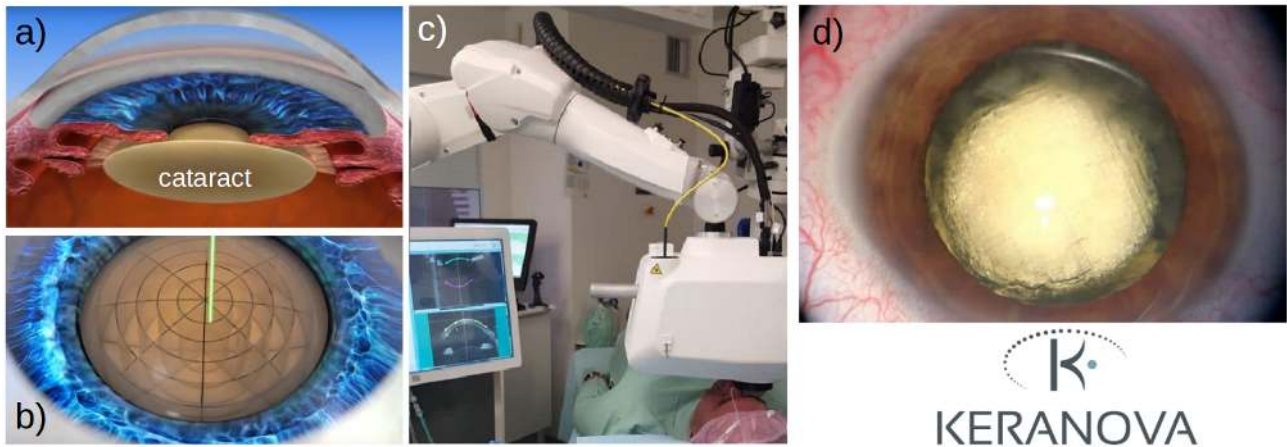


Figure 5.6 – a) Illustration of cataract, opaque crystalline lens that needs replacement by an intra ocular lens (IOL) from <http://www.smartvisionclinic.com>. b) Typical femtosecond-assisted cataract surgery where laser pulses generate a few pre-cut planes to ease the further step of ultrasound assisted emulsification before suction. c) First in human clinical achievement of Matrix complete laser emulsification in january 2019 <http://www.keranova.fr>. d) Detail of the entirely emulsified crystalline lens, ready for suction that did not require the hand-held ultrasound emulsification.

number is of utmost importance for successful corneal graft. The cell membrane poration permits the introduction of plasmids that can reprogram the cell in order to augment their number. We have successfully used the nano-particle assisted method (Carbon NP) for plasmid transfection on cellular layers with a carefully tuned femtosecond irradiation [Jumelle et al., 2015c]. The process involves the generation of an acoustic wave that briefly permeabilizes the cell membrane as illustrated in Fig.5.7 I). In an effort to avoid the use of NP, we have employed spatial beam shaping to obtain a large number of parallel foci along with a strong focalisation using a microscope objective. There, the poration process is a direct consequence of the laser focused intensity as depicted in Fig.5.7 II). A matrix of 225 parallel laser spots was achieved as shown on Fig.5.7 III) (beam in situ analysis) and IV) (Si wafer irradiation for verification). After thorough investigations, a process window has been found where calcein molecules could be successfully transferred into a human corneal cell layer (green region of Fig.5.7 V)) with low cell mortality (red region of Fig.5.7 V)) and without the need of NP. This study has been conducted during the PhD work of C. Jumelle (2012-2015) in collaboration with the BIIGC. Increasing the number of parallel laser spots increases the complexity of the phase mask, because of the highest spatial frequencies involved. In these cases, the limitations inherent to the SLM (phase stroke, fill factor and resolution) does not permit to physically reproduce the desired phase modulation [Hasegawa et al., 2016]. In that case, all the light that is not diffracted following the desired phase modulation reaches the optical axis, constituting the zeroth order. This is accompanied by a reduction of the uniformity among the spots. It can be compensated by automated feedback and adjustment of the IFTA target [Hasegawa et al., 2016] and the zeroth order can be hidden with an amplitude mask in a conjugated plane.

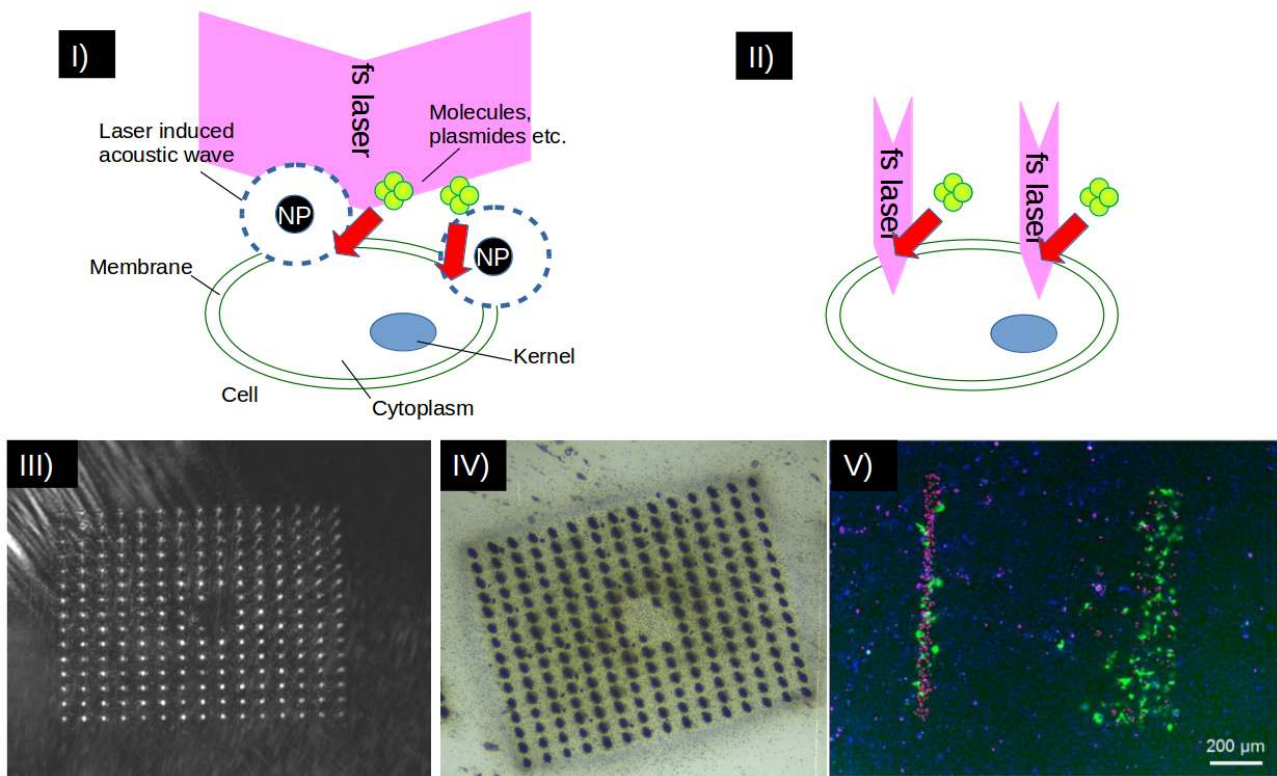


Figure 5.7 – I) Illustration NP assisted transfection where the fs laser pulses interaction with the NP induces an acoustic wave that permeabilizes the cell membranes allowing for the introduction of molecules in the cell cytoplasm. II) Scheme of NP-free transfection thanks to strong focusing of massive parallel laser spots, where each spot directly induces a transient poration. III) In situ beam analysis of the 225 spots array on the membrane layer. The matrix width is $165\ \mu\text{m}$. IV) Si-wafer irradiation for spot separation verification. V) Successful NP-free parallel transfection (large green region on the right corresponding to cells transfected with calcein) with low mortality (red coloration regions).

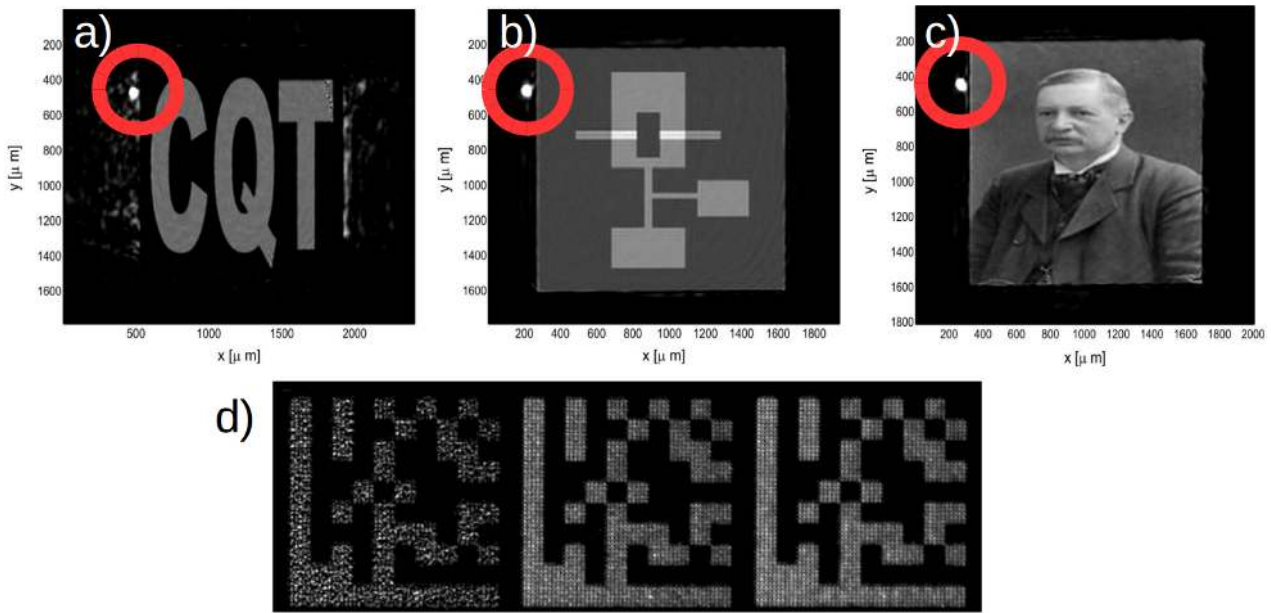


Figure 5.8 – Examples of beam shaping of continuous shapes. a)-c) Experimental shapes obtained from improved IFTA algorithm (MRAF see text) from [Bijnen, 2013]. The Speckle pattern is well observable on the non-optimized ('dumb') region on a), it is hidden on b) and c). The very intense 0^{th} order is pointed out by the red circle. b) Atomtronic OR-gate, c): Portrait of Johannes Rydberg Swedish physicist. d) Experimental intensity profiles of datamatrix of $\approx 400 \mu\text{m}$ width, the reduction of speckle is achieved using averaging of 16 images with phase-shifted phase masks from [Parry et al., 2011]

5.3 Shaping of the laser spot itself, or 'continuous' beam shaping

Wavefront-based spatial beam shaping also enables to directly shape the laser spot, i.e its intensity distribution, using programmable SLM [Sanner et al., 2005]. The interest is to adapt the laser beam distribution to the desired application. The shaping of the intensity distribution is usually designed in a $x - y$ plane perpendicular to the z propagation axis, but it can be of interest to also control the beam distribution along the z axis as explained hereafter. The progress in terms of spatial beam shaping of continuous distribution is quite remarkable. The field of atoms cooling has fueled the discipline, requiring complex beam shapes serving as traps with high uniformity requirements as shown on Fig.5.8 a)-c). Noteworthy, the spectacular beam shaping quality is based on a big compromise on the energy efficiency. In fact, a large amount of the energy is directed in the 0^{th} order as indicated in the red circles on Fig.5.8 a)-c). The energetic waste is so strong that the CCD sensor is saturated. Moreover, these beam shaping techniques are usually based on a modified IFTA algorithm that allows some 'dumb regions' where the constraints on the intensity distribution are released. In other words, the outer region of the target distribution can be as chaotic as needed to optimize the target region. This is clearly observable on Fig.5.8 a) where Speckle patterns surround the 'CQT' beam shape. This technique is referred to as the Mixed-Region-Amplitude-Freedom (MRAF) algorithm [Gaunt and Hadzibabic, 2012; Bijnen, 2013]. This dumb region also contributes to the energetic waste, insomuch as it is difficult to have the information in the publications. It is possible however from Fig.5.8 a) to estimate that more than half of the total energy is wasted

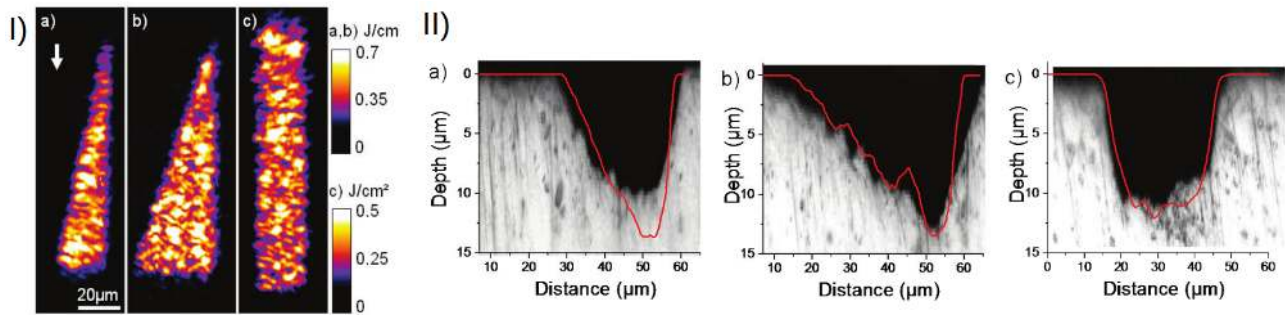


Figure 5.9 – I) Experimental intensity distributions of continuous spatial beam shaping in the processing focal plane. Examples for triangular (a and b) and rectangular (c) profiles. The white arrow shows the sample translation axis. Comparison of microscopic images of micro grooves on stainless steel (side view) with calculation of their cross sectional profile (red line) from the experimental fluence distribution. a), b) and c) correspond to the experimental continuous fluence distributions shown I) a), b) and c) respectively, see [Mauclair et al., 2013a]

in 0^{th} order and in the dumb region. In this situation, the benefit of wavefront modulation in terms of energetic preservation compared to amplitude modulation clearly becomes disputable. Thus, the above-mentioned research efforts concerning amplitude modulation are justified (see Sec.4). Fig.5.8 d) shows another example of beam shaping from [Parry et al., 2011]. Detrimental Speckle effects yielding strong non-uniformities are clearly visible on the beam shape. When compared to Fig.5.8 a)-c), one can wonder why such a non uniform shaping is still worth publication. The answer is simply because of the energy efficiency and application of this beam shape. Indeed, Fig.5.8 d) refers to a surface machining application. It is obvious that in that case, it is not possible to allow a 'dumb' region, neither a strong 0^{th} order to interact with the machined surface, even if these solutions can correct for the spot non-uniformities. Thus, the beam shapes keep these problematic non-uniformities. The originality of the work is the demonstration of the possibility to average the Speckle effect upon multiple irradiations. More precisely, the phase mask undergoes a slight modification (phase-shifting) between the laser pulses that changes the Speckle pattern. That way, an averaging effect permits to obtain a smoother deposited energy distribution (see Fig.5.8 d) right)). We have shown that the averaging effect can also be obtained by scanning the laser spot to generate micro-grooves of controlled profile [Mauclair et al., 2013a]. Fig.5.9 I) presents some arbitrary intensity distributions that can generate such controlled micro-grooves upon scanning (vertically on Fig.5.9 I)). The corresponding micro-groove sections were imaged using optical microscopy (after cutting) and a good correspondence with the expected profile (estimated from the experimental ablation rate) could be observed (see Fig.5.9 II)). This work has been conducted within the OSEO project ARTEMIS during the postdoctoral stay of D. Pietroy (2012).

In the quest to adapt the beam shape to the desired surface structuring, generating a line-shaped beam enables to reach the highest surfacing speed as we have shown in [Mauclair, Desrus, and Saint-Pierre, 2017]. The desired line shape was obtained from the IFTA algorithm, with a cylindrical lens as a starting condition. The length of the line shape is determined by the fluence required to generate LIPSS and the available laser power. Performing a scan perpendicular to the line permits to reach the maximum surface structuring speed at the maximum available repetition rate. The limitation of the speed is then due to either the maximum scanning speed or the maximum repetition rate (for a given pulse overlap). Fig.5.10 a) b) and c) present the experimental intensity distribution, static irradiation of stainless steel and a surface after treatment showing LIPSS, respectively. The surfacing speed was $v = 10 \text{ cm}^2/\text{s}$ using the full

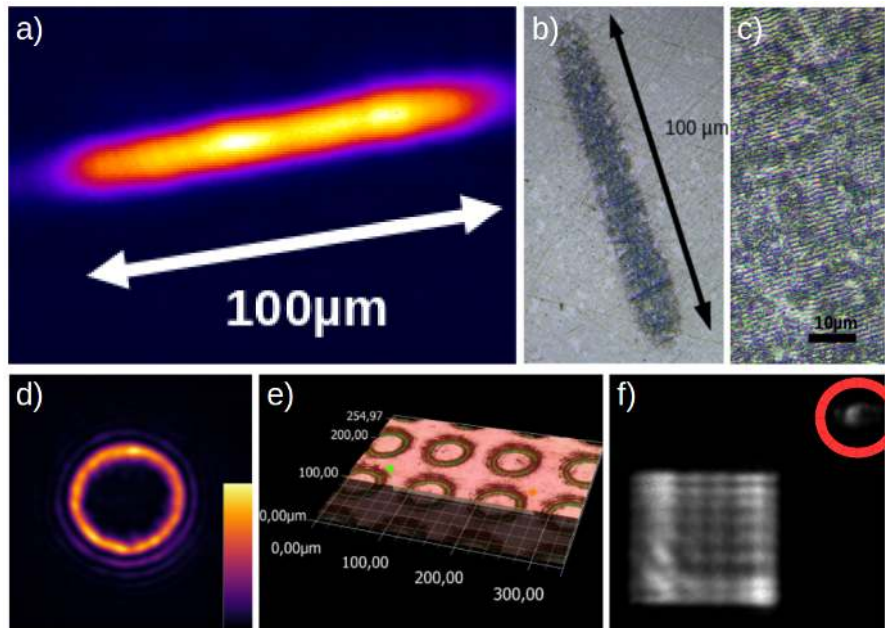


Figure 5.10 – a)-e) From [Mauclair, Desrus, and Saint-Pierre, 2017]. a) Line-shaped intensity distribution using IFTA algorithm starting with a cylindrical. b) microscopy picture of an impact on stainless steel showing the generation of LIPSS (Peak fluence is 0.7 J/cm^2 , 5 pulses at 250 kHz). c) Full surface LIPSS structuring at 250 kHz using the intensity distribution of a) with a lateral spacing of $21 \mu\text{m}$. The scanning is perpendicular to the line, the generation of LIPSS is observable on the microscopic picture. The method permits to use the full power of the laser source and thus to reach its maximum processing speed d) Annular shaped beam of $50 \mu\text{m}$ diameter obtained with a vortex-type phase mask (see text) and corresponding surface ablation site on steel e). f) Squared top-hat intensity distribution using wIFTA with low 0^{th} order (less than 5% of the total energy - red circle) and good homogeneity.

available power of 10 W at a repetition rate of 167 kHz. Within the IMOTEP project, the same surfacing will be obtained at a pace of $v = 1500 \text{ cm}^2/\text{s}$, i.e $v = 9 \text{ m}^2/\text{min}$.

Annular beams can also be of interest depending on the application. Those beams can be generated using spiral phase mask [Yao and Padgett, 2011]. Surface machining using this kind of beams is illustrated by Fig.5.10 d) and e) showing an annular beam distribution and the corresponding surface structuring. ⁸ Fig.5.10 f) presents our last effort in terms of continuous beam shaping without any averaging. A compromise must be found to reach a sufficient beam homogeneity without to much energy loss as underlined by the relatively low 0^{th} order. We obtained this beam shape with wIFTA based on the experimental intensity distribution. It is interesting to push the beam shaping technique towards user-defined machining results. By using the experimental ablation rate, it is possible to deduce a desired laser intensity distribution from a desired ablation profile, in a first approximation. However, as seen before the non perfect SLM's optical response may significantly alter the experimental laser distribution. We have proposed an alternative phase mask calculation method that can be adapted to the phase modulator optical performance [Houzet et al., 2016]. It is possible to characterize any wavefront modulator thanks to the orthogonal basis of Zernike aberration polynomials [Jewel, Akondi, and Vohnsen, 2013]. Using the adapted number of Zernike polynomials according

⁸This work has been done in within the ANR EQUIPEX program Manutech-USD, during the building of the ultrafast texturing machines (2017)

to this performance, an optimization algorithm numerically determines their coefficients to obtain the desired wavefront modulation. Fig.5.11 A) presents the phase mask calculation strategy. From the groove ablation target, the desired intensity distribution is calculated. Then, the Zernike coefficients are optimized using simulated annealing in order to find a phase modulation that can produce the desired beam shape. The approach is numerically verified in Fig.5.11 B) on a top-hat and a three-step intensity profile. Naturally, a higher number of Zernike coefficient permits to better follow the target shape, i.e lower RMS error compared to the target, thus more efficient beam shaping, (see Fig.5.11 B) c)). When applied experimentally to the SLM, the phase mask permits to obtain intensity distribution as shown on the inset of Fig.5.12 a). Upon beam scanning, the desired three-step ablation profile is obtained as shown in Fig.5.12 a) and c). Surprisingly enough, the trefoil aberration is the major contribution to correctly shape the beam (see the polynomials coefficients in Fig.5.11 A) III)). This demonstrates that the simulated annealing optimization has found a solution that could not be easily anticipated, and that could fit with the relatively low quality of the SLM's optical response. This advances were obtained during the postdoctoral stay of J. Houzet (2014-2015) within the ANR project 'Topoinjection' in collaboration with the LTDS.

5.4 Shaping along the optical axis, the case of non-diffractive beams.

A remarkable type of solution to the propagation equation is the non-diffractive beam that is usually referred to as the Bessel beam [Courvoisier et al., 2009]. Experimentally, this beam can be obtained using an axiconic phase modulation as depicted by Fig.5.13 a)-c). The intensity distribution follows a Bessel distribution resembling a concentric interference pattern with a more intense central lobe and regularly spaced annulus (for the zeroth order Bessel beam, higher orders presenting a dark core are also achievable). The non-diffracting properties are experimentally translated into very long axial region where the beam size and intensity remain constant, thus easing the task of surface positioning [Courvoisier et al., 2009]. However, the annulus can also interact with the surface yielding uncontrolled ablation or marking, a precise control of the laser intensity is thus mandatory. A strong advantage of this beam relates to processing of very high aspect ratio channels in the bulk of transparent materials [Bhuyan et al., 2010] with evident applications in high precision glass cutting. In the case of an interaction in the bulk of glass, we have shown that the Bessel beams present a strong interest for an efficient energy deposition on the optical axis, particularly for picosecond pulse duration [Velpula et al., 2014c]⁹. This longer pulse duration permits to reduce nonlinear propagation effect before reaching the optical axis, thus enhancing the localization of the energy deposition. This is illustrated in Fig.5.13 d) where the non linear Schroedinger equation has been used to calculate the deposited fluence for 60 fs and 1.8 ps pulse. The picosecond case enables to better concentrate the energy. This is also observable from the much stronger experimental plasma luminescence in the case of the picosecond irradiation as shown in Fig.5.13 d).

5.5 Conclusion

We have seen that spatial control of ultrafast beams can be done by deflection, beam truncation, amplitude and wavefront modulation. We have brought to the state of the art to each of these

⁹Work during the ANR project Smart-Lasir (2011-2014)

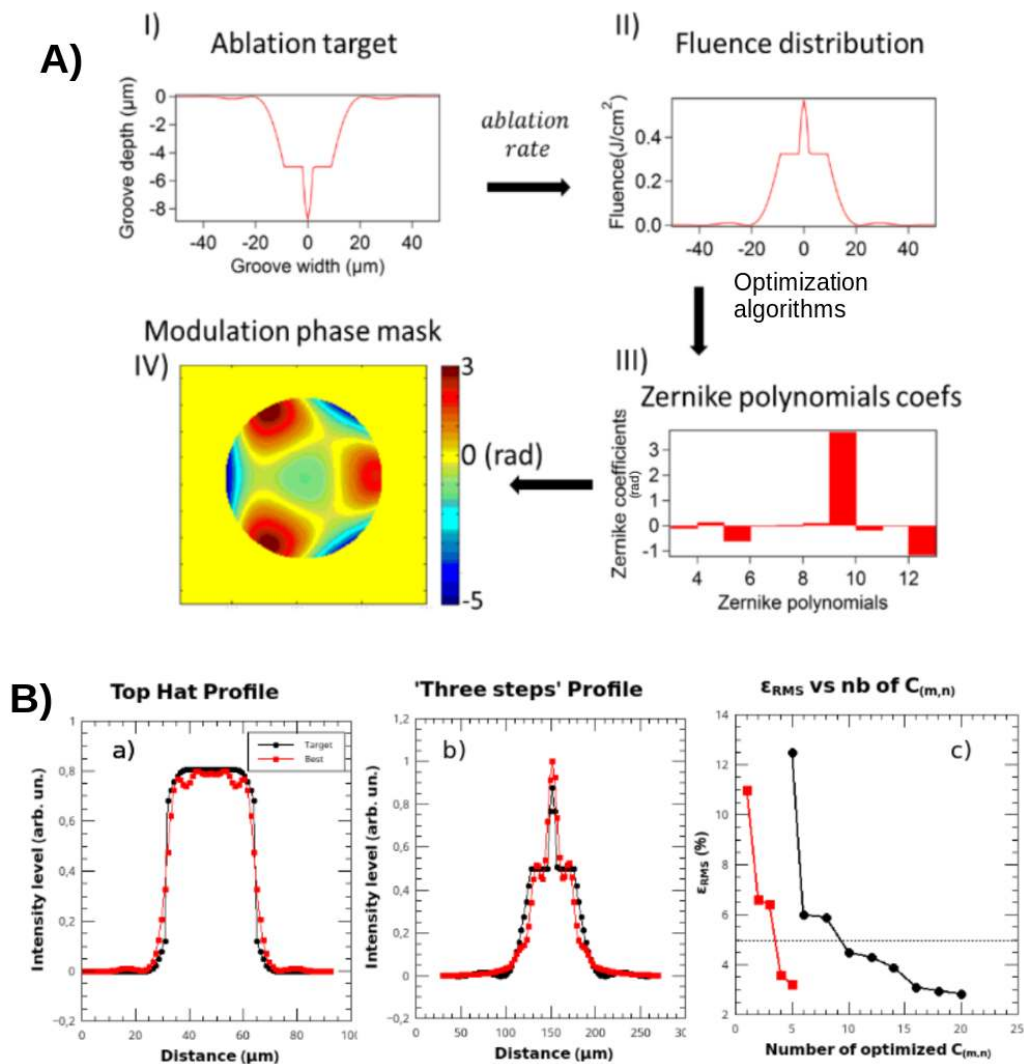


Figure 5.11 – From [Houzet et al., 2016]. A) Calculation strategy for the modulation phase mask I) desired groove profile II) numerical calculation of corresponding fluence distribution based on the empirical ablation rate [11] III) Zernike polynomials coefficients obtained by optimization from II) IV) corresponding phase mask obtained numerically that can be applied to the phase modulator. The number of optimized Zernike polynomials can be adjusted according to the performances of the phase modulator. B) Numerical results of phase mask calculation through optimization of the Zernike coefficients. Comparison of the calculated intensity cross section (red squares) and the target (black disks) for a top-hat distribution a) and 'three steps' intensity distribution b) at the focal plane of a lens. c) Evaluation of the best attainable RMS error with the number of coefficients involved in the optimization for the top-hat (red squares) and three-steps (black disks) target

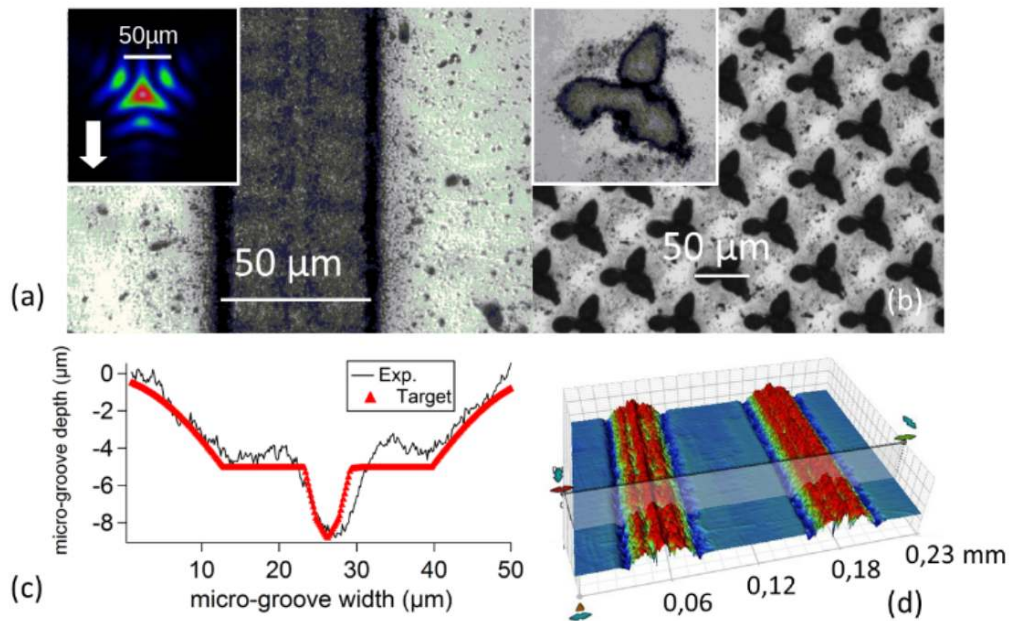


Figure 5.12 – From [Houzet et al., 2016]. a): "three-steps" shape micro-groove (optical microscopy) processed by translating the spatially shaped beam illustrated in the insert corresponding to the experimental beam in Fig. 5 (b), b): micro-dimples achieved with the same beam (zoom in the insert). c) horizontal profile of the micro-groove (black line) a) compared to the targeted ablation profile (red triangles) d) corresponding injected polycarbonate topology (interferometric microscopy).

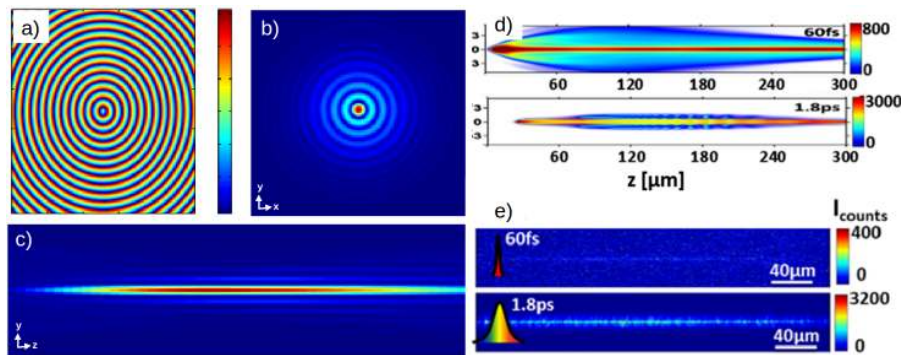


Figure 5.13 – a)-c) Numerical calculation of Bessel beam propagation generated from an axiconic phase a). Intensity distribution in a transverse plane b) and along the optical axis c). d) NLSE calculation of the deposited fluence (J/cm^3) for a 60 fs (top) and a 1.8 ps (bottom) pulse in the case of a Bessel beam. e) corresponding plasma luminescence showing a more efficient energy deposition in the case of the longer pulse duration, due to a lower onset of nonlinear propagation effects, see [Velpula et al., 2014c].

techniques, with pioneering work on the subject of laser spot duplication through wavefront modulation, enabling parallelized processing. Noteworthy, all of these techniques are accompanied with trade offs regarding energy efficiency and beam shaping quality. The possibility to find a good compromise has been shown by taking into account the beam modulator performance in the calculation of the modulation mask. There, the help of a self learning algorithm (here simulated annealing) has permitted to determine adapted coefficients of Zernike polynomials. These coefficients has enabled to experimentally obtain the desired ablation profile because the optimization was performed on the polynomials that the SLM was able to correctly reproduce. Control of the beam in three dimensions has also been discussed, for parallel processing and in the case of non diffractive beams, underlining the possibility to strongly confine the laser energy on the optical axis with reduced non linear propagation effects.

Chapter 6

In-situ characterization of ultrashort laser irradiations

6.1 Motivation

For optimal control of the process, the result of the ultrafast laser irradiation usually requires extended analysis and characterizations. For this discussion, an exhaustive list of all the characterization means is not necessary. However, it can be noted that imaging at sub micrometric scales is the common way of doing, usually using SEM, AFM or interferometric probes [Schade et al., 2010]. Usually these measurements are conducted with systems that enable high resolution imaging below the usual diffraction limit of visible light. A particularly illustrative example is the generation of LIPSS whose characteristic sizes are relatively close to the laser wavelength, depending on the types of LIPSS. Similar self-organized nano-gratings can also be formed in the bulk of glasses, with birefringent properties. More generally, any laser-induced roughness, inhomogeneities or material redeposition can range between a few nanometers to a few micrometers. Thus, characterization of these structures can sometimes be conducted by optical means when the resolution is sufficient, however it is most of the time more interesting to observe the irradiated zone with thinner resolution for a better understanding and optimization of the interaction. In that case, the irradiated sample must be taken to a dedicated equipment such as the AFM or the SEM, ex-situ. This additional step is time-consuming and, as we will see below, may complicate the understanding of the laser-matter interaction. If optical characterization means are particularly handy because the probing light can easily share the same optical path as the structuring beam, there is a need for a sufficient resolution in order to elucidate the formation of micro and nanostructures upon ultrafast laser irradiation. To achieve this, the light diffraction barrier must be overcome using super resolution techniques, or indirect probing such as diffraction of a coherent beam. In the following, we underline two situations where in situ probing has been determinant to better understand and control the laser matter interaction for bulk and surface nano structuring.

6.2 In situ probing of bulk nanostructuring in fused silica

6.2.1 Ultrafast laser generation of bulk nanostructures

Ultrafast laser generation of bulk nanostructures [Taylor, Hnatovsky, and Simova, 2008] is a intriguing phenomenon, appearing as a succession of variable density planes in bulk glassy materials. These planes are typically spaced by $\lambda/2n$, n being the refractive index and λ the

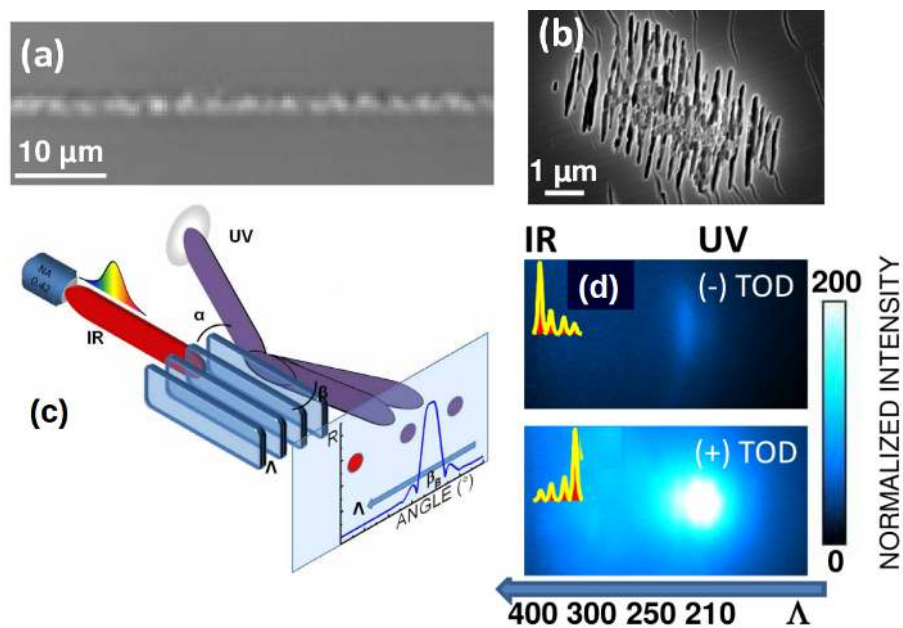


Figure 6.1 – From [Mauclair et al., 2012a]: Typical manifestation of type II traces in fused silica with the associated nanogratings. (a) PCM trace of type II modifications. (b) Cross-section of the traces showing the nanoscale arrangement (electron microscopy). (c) Schematic design of the experimental setup with the IR irradiation and the UV diffraction probing parts. α is the angle of incidence on the gratings with respect to the IR axis, β the diffraction angle (in the material). (d) UV diffraction patterns originating from scanned ($5 \mu\text{m/s}$) traces for negative (top) and positive (bottom) third order dispersed pulses, with the corresponding periodicity scaling.

irradiating laser wavelength. In fused silica ($\alpha\text{-SiO}_2$), the transformation is known as type II and requires more energetic irradiation conditions than usually for obtaining smooth and isotropic refractive index changes. The ability to generate periodic nanoscale organization in the bulk has led to the development of a new optical functionalities such as light polarization-dependent guiding, controlled phase retardation, or 5D information storage [Mishchik et al., 2010a, Shimotsuma et al., 2010; Zhang et al., 2013]. These remarkable functions are related specifically to the characteristics of these embedded nanoscale patterns. These structures can present a large range of periodicities ($\Lambda=150\text{-}500\text{ nm}$) with an alignment perpendicular to the laser polarization, and a negative index variation with birefringence. A typical example of nanostructured volume traces is given in Fig.6.1 a)-b), which depicts low index type II structures [Cheng et al., 2009]. A phase contrast microscopy (PCM) picture is shown in Fig.6.1 a) along with a cross-section under SEM (Fig.6.1 b)) revealing the change of optical properties and the periodic arrangement at the nanoscale, respectively. It is quite evident that, if the SEM pictures provide the most information on the irradiation outcome, this post mortem analysis is very much time-consuming. Thus an optimization of the laser parameters using this analysis cannot be exhaustive in a reasonable time. We have therefore proposed a method of in-situ real-time observation and control of the volume nanogratings induced by ultrashort pulses in $\alpha\text{-SiO}_2$ [Mauclair et al., 2012a].

6.2.2 In-situ UV diffraction probing of the bulk nanostructures

The photoinscription scheme is based on infrared ultrashort laser pulses with variable temporal envelopes via programmable design. The probing approach relies on the diffraction properties of the subwavelength pattern in UV (355 nm) accessing directly their periodicity (see Fig.6.1 c)), with the functional parameter being the writing pulse temporal envelope tailored on a picosecond scale. The optical diffraction method does not provide a direct imaging of the nanoscale structure, due to evident resolution limitation. On the other hand, the diffraction signal on the periodic structuring is naturally strongly affected by the grating periodicity and optical retardation contrast that alter the diffraction angle and intensity, respectively; just like a phase grating. This method is a sensitive and rapid for evaluating periodic patterns [Young et al., 1983], with the possibility to follow time-resolved evolution with pump-probe apparatus (not shown here).

6.2.3 Tuning the ultrafast irradiation from the in-situ UV probe

In short, we have tested asymmetric temporal pulse shapes containing fast series of pulses with monotonously varying intensities based on third order dispersion (TOD) as they were shown to possibly better localize electronic densities on surfaces [Englert et al., 2007]. Positive and negative TOD pulses with a statistical duration of approximately 1300 fs generate the photoinscription inside the fused silica sample. The UV probing beam is directed onto the modified region and the diffracted beam is collected on a CCD sensor, allowing for the evaluation of the diffraction angle and intensity. The shorter the nanostructure periodicity is, the larger the diffraction angle is (see Fig.6.1 d)). The trace induced by positive TOD sequences leads shows a stronger diffraction pattern and a slightly smaller period than the negative TOD counterpart, as denoted in Fig.6.1 d) where the diffraction angle β is smaller for the negative TOD sequence. It is expectable for positive TOD pulses that multiphotonic ionization acts efficiently since the beginning of the ultrashort irradiation. Thus, collisional ionization is more efficient during the main pulse and also during the subsequent lower intensity pulses of the positive TOD sequence. The situation is more favorable for hot carrier generation than for negative TOD pulses where

low intensity pulses lead the series. There, multiphotonic ionization is not particularly active before the end of the sequence. This is reflected in the size of the low index part in the static trace (not shown). In addition, these behaviors were confirmed at various writing speeds (5 and 50 $\mu\text{m/s}$) and input powers below or around the critical power for self-focusing (3 MW). These results clearly demonstrate the interest in-situ evaluation of the irradiated zone for the optimization of the irradiation outcome. This study was conducted within the ANR project DYLPSS in collaboration with the NILPRP Bucarest (2012-2015). Not only the experimental time can be significantly saved, but also a thinner understanding of the interaction is then at reach. Also, if this study was conducted in open-loop, with systematic tests and analysis for different temporal envelopes, a closed-loop optimization scheme naturally comes in mind. As our group has often demonstrated, close-loop optimizations based on self-learning strategies can tune the temporal and spatial aspect of the ultrafast excitation towards desired modifications. This strategies, based on evolutionary optimization scheme, have been employed for experimental and numerical optimization of the laser-matter interaction. For example, this has permitted to force the borosilicate glass (BK7) response to femtosecond pulses towards local increase of the refractive index [Mermillod-Blondin et al., 2008a]. Also, the structuring zone in the bulk of fused silica could be significantly localized [Mermillod-Blondin et al., 2008b] as well as in deep photowriting of BK7 glass [Mauclair et al., 2008]. The question of closed-loop optimizations based on self-learning algorithms will be discussed from a more general point of view in the last chapter.

6.3 Structured Illumination Microscopy - SIM - for in-situ imaging

6.3.1 Introduction

To overcome the diffraction limit in optical microscopy, a variety of optical techniques have been developed to keep the advantages of non-contact and non-destructive characterization offered by light [Tkaczyk, 2010]. For instance, Stimulated Emission Depletion (STED) microscopy is a super resolution technique based on functional groups of molecules that show fluorescence; it can achieve a lateral resolution of 20 nm [Hell and Wichmann, 1994]. Also, stochastic super resolution techniques such as STORM and PALM can be used to overcome the optical diffraction limit for fluorescent samples [Rust, Bates, and Zhuang, 2006; Betzig et al., 2006; Hess, Girirajan, and Mason, 2006]. These optical super resolution techniques are particularly suited for samples with fluorophores.

Structured illumination microscopy (SIM) is a full-field super resolution optical technique using a sinusoidal amplitude modulation of the light projected on the sample. This type of microscopy was first demonstrated on fluorescent polystyrene micro-spheres [Gustafsson, 2000] and is used for analysis of biological samples [Sonnen et al., 2012; Kner et al., 2009] previously stained by fluorophores [Gustafsson, 2005], reaching up to a lateral resolution of 50 nm in biological samples [Rego et al., 2012]. Modifications on SIM have been proposed e.g. using adaptive optics [Débarre et al., 2008], Speckled illumination [Lim et al., 2011; Mudry et al., 2012] or the nonlinear response of the fluorophores [Gustafsson, 2005], the latter permitting to further improve the resolution. We have employed the SIM technique for in-situ investigation of irradiated surfaces.

SIM is usually employed for samples previously stained with fluorophores [Gustafsson, 2000; Saxena, Eluru, and Gorthi, 2015; Rego and Shao, 2015; Montgomery and Leong-Hoi, 2015], especially on biologic samples [Hirano, Matsuda, and Hiraoka, 2015], but it can be

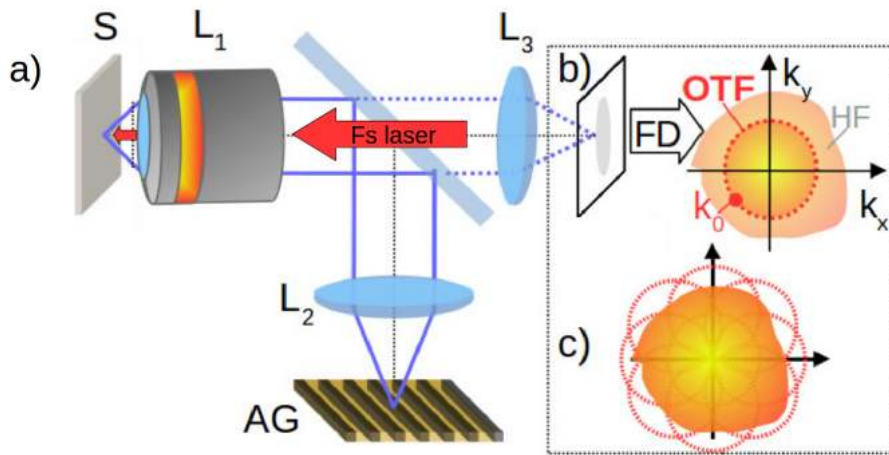


Figure 6.2 – SIM adapted for in-situ monitoring of ultrafast laser irradiation (red arrow). a) An incoherent beam (blue lines) images an amplitude grating (AG) over the sample (S) by the 4f system (objective L_1 + lens L_2) so that the sample is shined with a periodic illumination, whose period is close to the objective’s diffraction limit (corresponding to k_0). The back reflected light is imaged on a CCD sensor through L_1 and L_3 . b) Scheme of the SIM principle. In the Fourier domain (FD) the standard microscope OTF can be seen as a low pass filter (red circle) blocking the sample high frequencies (HF) above k_0 . The sinusoidal illumination shifts the sample information in the Fourier Domain by k_0 , thus enabling to reveal some of the HF information of the sample. By successive rotations the AG, HF domains can be stitched together to increase the imaged frequency space up to a radius of $2 \times k_0$, thus doubling the resolution (c).

employed without any fluorophores, like metallic nanoparticles [Wang, Lee, and Lee, 2009]. By projecting an amplitude grid (AG) over the sample using incoherent light as depicted in Fig. 6.2a), the standard resolution restriction of the microscope optical transfer function (OTF) can be overcome as illustrated in Fig. 6.2 b) and c). The SIM microscopy relies on the fact that a microscope optical transfer function (OTF) can be seen as a low pass filter for the observed objects spatial frequencies. Shortly, the OTF frequency limit (cutoff frequency k_0) in the Fourier Domain (FD) is related to the diffraction limit of the microscope corresponding to its point spread function (PSF). The sinusoidal illumination on the object turns to a frequency shift corresponding to the sinusoidal modulation in the FD, thus revealing some high frequencies within the microscope’s OTF. Once the high frequency lobe is isolated for a given direction, the carrier caused by the fringes is removed using the Fourier method [Takeda, Ina, and Kobayashi, 1982]. Combining the high frequency lobe of all the frequency domain directions, allows us to build an extended version of the optical transfer function of the microscope. If the sinusoidal modulation has a period close to diffraction limit, the shift in the FD permits to unveil an extended OTF region whose cutoff frequency is twice the cutoff of the standard optical microscope, achieving super resolution of twice as standard microscopy, see Fig 6.2 c).

6.3.2 Experimental set-up and performance of the SIM microscope

The experimental set-up to observe specular samples can be seen in Fig. 6.2. A LED source was used for the setup with a central wavelength of $\lambda = 405$ nm and a bandwidth of 13 nm, the light was filtered by a diffuser and collimated, achieving an uniform incoherent epi-illumination. The objective NA is 0.9, yielding a Rayleigh criterion of $c_R = 275$ nm in bright-field mode.

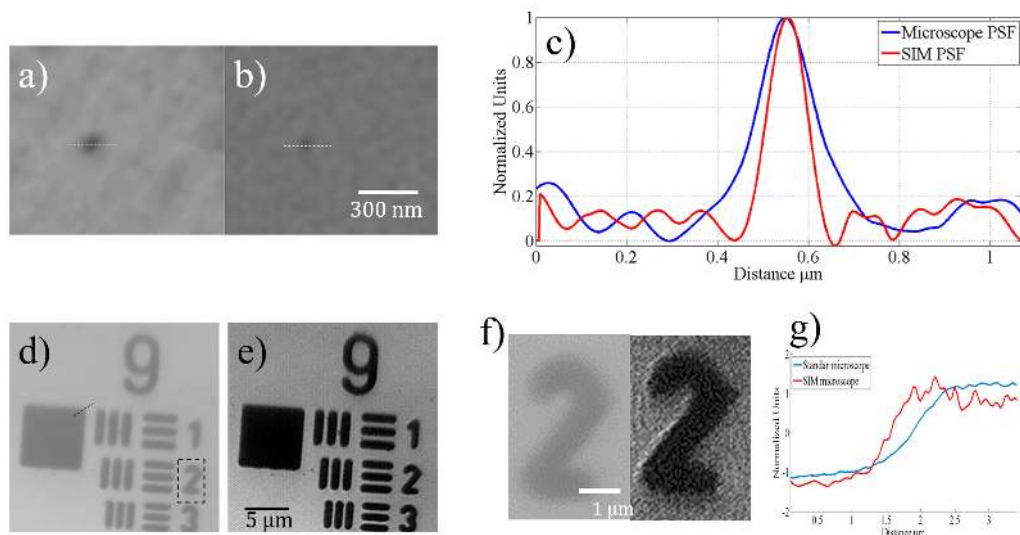


Figure 6.3 – Evaluation of the SIM microscope performance. Image of a ≈ 50 nm surface artefact on a Si wafer using conventional microscope a) and the SIM microscope b) with cross sections in c) showing the resolution enhancement in the case of the SIM microscope (resolution limit of ≈ 155 nm). USAF refractive test grid imaged by the standard microscope d) and by SIM microscope e) with a detail (f) of the indicated region in d) ('2' on the USAF target) with the corresponding cross section g). Again the SIM apparatus clearly enables a sharper detection below the diffraction limit of the standard brightfield microscope.

The analyzed samples were specular samples. The structured illumination light projection was performed using an amplitude grating. The grating used in our experiment is a Ronchi ruling with a period of 60 lines per mm. The grating is mounted over rotation and translation stages, such as its position and rotation can be quickly and precisely adjusted for data gathering for the spectral domain OTF extension process. The grating is placed in the focal plane of lens L_2 ($f = 100\text{mm}$), so it can be projected just in the back focal plane of the microscope objective by means of a beam splitter. The grating magnification is given by the ratio of the focal distance of the microscope objective L_1 ($f = 1.8$ mm) and lens L_2 , thus the period of the fringes on the samples is 300 nm, which is purposely very close to c_R . The performance of the microscope was analyzed to verify that super resolution is achieved through the algorithm and the experimental setup. The PSF of the microscope provides a good idea concerning the performance of the whole system in terms of resolution. For its measurement, a surface artifact of ≈ 50 nm on silicon wafer was imaged under normal and SIM microscopy as seen in Fig 6.3 a) and b), respectively. The comparison of the analyzed spot can be seen in Fig. 6.3a)-c). By comparing the PSFs, it can be seen clearly a reduction of the main lobe, so the cut off frequency of the microscope is higher with the super resolution technique. The radius at first zero of the PSFs can be measured to make an objective comparison and analyze the minimum object that can be analyzed with this constructed microscope. A reduction of 44% of the PSF radius is achieved. Theoretically, the reduction should be 50%. Meaning that in optimal circumstances the microscope should achieve double of resolution as a typical microscope. The 6% error is due to the slight difference between c_R and the period of the fringes on the sample as explained above. Using this experimental apparatus, the microscope resolution is 155 nm. instead of the 140 nm expected by theory. For analyzing the performance on specular surface and have a better idea of the performance of the technique, a reflective USAF test was used to inspect the

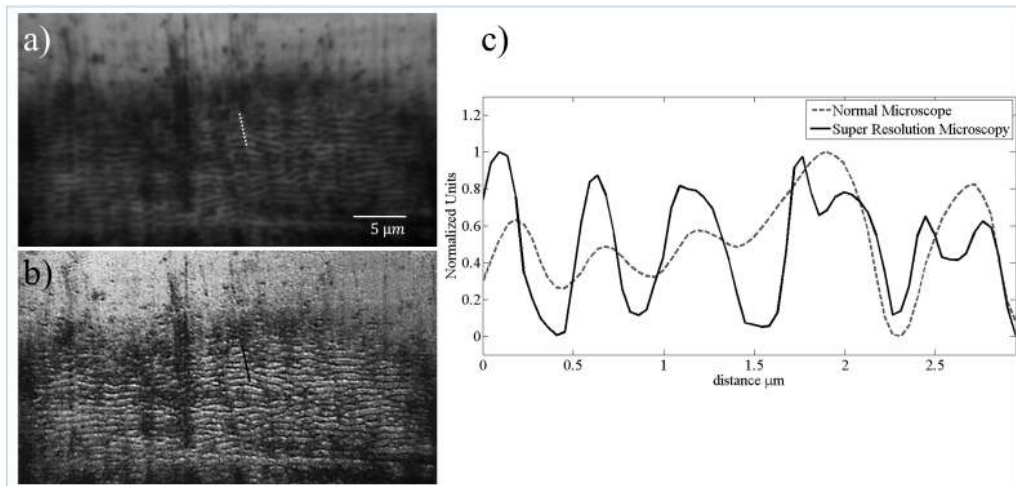


Figure 6.4 – In-situ imaging of LIPSS generated by the ultrafast laser irradiation over stainless steel 316L. a) Impact imaged by standard brightfield microscope, the same region imaged using SIM. c) cross section of the pictures, where it can be seen that the SIM (solid line) permits to better distinguish ripples peaks.

resolution of the microscope. The sample is a metallic thin film deposited over glass, where the edge of the film was analyzed on the microscope. Fig. 6.3d)-g) shows the comparison of the obtained images. Fig. 6.3d) corresponds to the analyzed object without modifications to a normal microscope; meanwhile Fig. 6.3 e) corresponds to the super resolution set-up. A cross section of the pointed areas can be appreciated on Fig. 6.3f)-g), where the edge is clearly sharper in the SIM super resolution image. Fig. 6.4 shows the nano-structures generated by ultrashort infrared (800 nm) light pulses from an amplified Ti: sapphire ultrafast laser system. It can be observed in Fig. 6.4 a) that some structures cannot be distinguished due the diffraction limit. However using the super resolution SIM setup a super resolution image of the nano-structures is obtained as it can be seen in Fig. 6.4b). As the resolution is enhanced by a factor ≈ 2 compared to the regular brightfield microscope, the imaging of the edges of the LIPSS is improved as well. A transversal cross section of the image is plotted in Fig. 6.4 c) with again a sharper imaging of the LIPSS pattern in the case of the SIM. This is particularly visible on the right side of the cross section. There, the SIM permits to distinguish 4 LIPSS peaks where the standard brightfield microscopy reveals only 2 peaks. This work has been performed during the PhD of Dr. A Aguilar (2012-2015) in collaboration with the CIO Leon, Mexico.

6.3.3 In-Situ LIPSS monitoring with SIM

The SIM microscopy technique was employed for in-situ monitoring of the pulse-to-pulse formation of LIPSS under ultrafast laser irradiation. This characterization mean has permitted to follow the gradual formation of the LSFL (Low Spatial Frequency Frequency) LIPSS from virgin sample surface to the development and stabilization of the ripple pattern after a few tens of pulses. The material choice was motivated the quality of ripples formation. The LIPSS alignment, which suffers often from periodicity errors and bifurcations believed to originate from self-organizational dynamics [Varlamov et al., 2009], shows a remarkable regularity in laser irradiated metallic glasses [Zhang et al., 2014]. We have applied the structured illumination microscopy (SIM) to observe and reconstruct the LIPSS pattern evolution behavior during multipulse sequence. This allows to clearly define the topography role in establishing and growing rippled patterns [Aguilar et al., 2017a]. The optical resolution allows for a

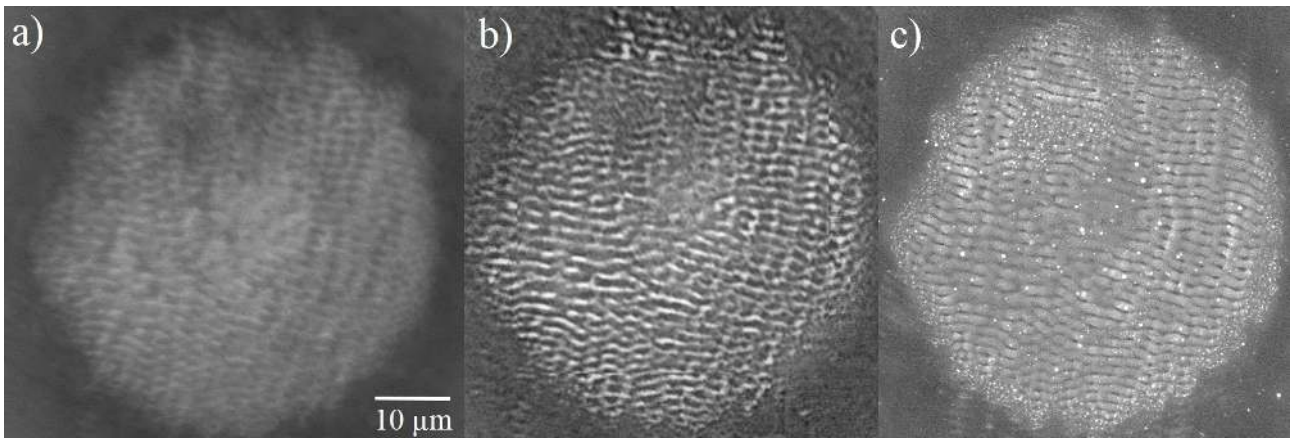


Figure 6.5 – From [Aguilar et al., 2017a]. Imaging of LIPSS generated by ultrafast laser irradiation over bulk metallic glass, BMG using a) regular brightfield microscopy, b) SIM and c) SEM. The SIM reaches a sufficient resolution of a clear observation of the LIPSS pattern in-situ.

very high quality in the optical imaging with resolving features not observable in standard optical microscopy. The in-situ implementation of the technique permits to observe the gradual development of regular structures from rough surfaces under multipulse exposure on the same site. This allows to put forward the mechanisms occurring during the pulse to pulse irradiation that relates to the spatial pattern. By analyzing the evolving relief on a single site, an accurate analysis on the role of light coupling on complex topographies is conducted. We demonstrate intrinsic phase-locking stabilizing patterns and periodicities during ripples growth that is related to surface corrugation and light scattering. The technique allows equally to define a second feedback that can phase-lock and stabilize the pattern from independent random sites. The mechanism is intrinsically related to the self-interference between the driving and scattered light.

High-resolution microscopy observation

A $Zr_{41.2}Ti_{13.8}Cu_{12.5}Ni_{10}Be_{25.5}$ (atom%) metallic superalloy undercooled to a glassy structure (bulk metallic glass, BMG) Schroers et al., 2007; Wang, Dong, and Shek, 2004 is used for laser nanostructuring, in the conditions where its thermoplasticity above the glass transition temperature can render high quality LIPSS Zhang et al., 2014; Li et al., 2016. Single-side polished Zr-BMG samples ($Ra < 20$ nm) with a diameter of 8 mm and a thickness of 3 mm were used in the experiment. Polishing was done using diamond paste and alumina powder with grit size down to $0.1 \mu m$. The sample, positioned on high precision XYZ stages, was then subject to ultrafast laser irradiation derived from an amplified Ti:Sapphire laser system delivering 120 fs laser pulses at a nominal repetition rate of 1 kHz and 800 nm incident wavelength. Single pulse where selected using electro-optical and mechanical shutters and are impinging on the surface along the normal direction. The irradiation geometry follows a common path with the observation tool, with a rather tight focusing. For each pulse, the in-situ SIM-picture acquisition was performed in order to follow the pulse-to pulse LIPSS growth. The results of laser irradiation on the Zr-based metallic glass sample are depicted in Fig. 6.5(a–c) using different microscopy techniques including standard optical reflection microscopy (Fig.6.5(a)), SIM (Fig.6.5(b)), and scanning electron microscopy (Fig.6.5(c), SEM). The figure shows clearly the potential of structured illumination microscopy to resolve topography details with high resolution. Even if the SIM resolution is evidently below the SEM, the SIM is well-adapted

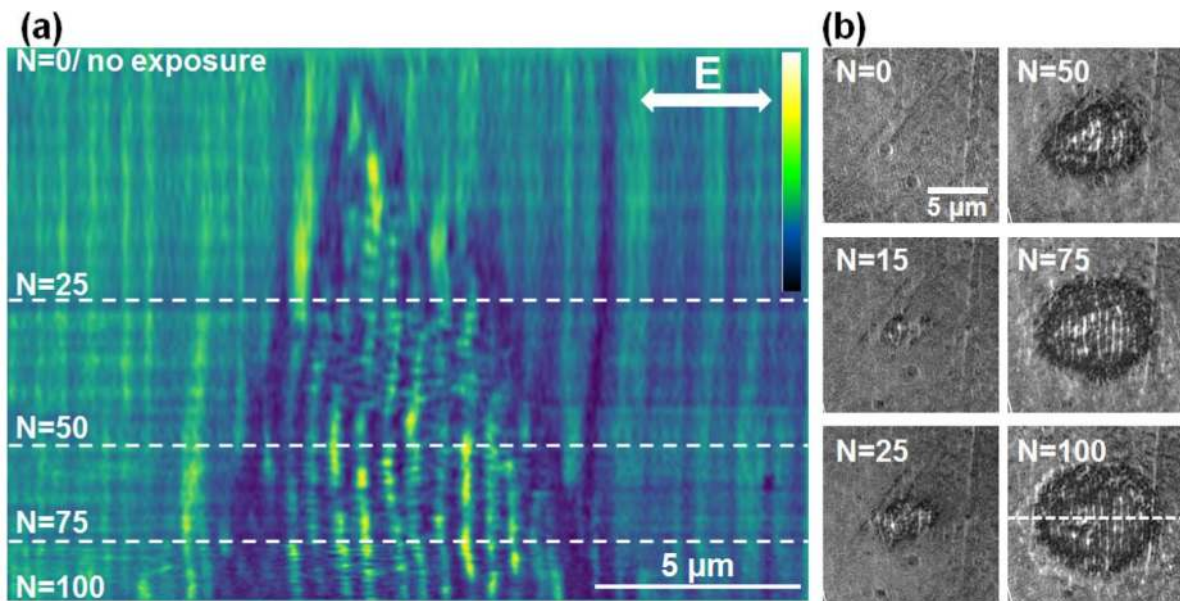


Figure 6.6 – From [Aguilar et al., 2017a]. Evolution on LSFL formation on Zr-BMG in the low fluence regime (peak fluence of 0.09 J/cm^2). (a) Evolution of a section profile with the number of pulses N (false colors). Sectional cuts made on LIPSS images are concatenated together for each N . The LIPSS pattern is visible after a relatively high number of pulses. Light colors represent zones of higher elevation. (b) Samples of the original SIM images. The direction of the electric field and the position of the sectioning line are given on the figures.

to LSFL LIPSS related observations. Moreover, the SIM has been implemented in-situ, within the irradiation set-up. Thus, the the SIM technique is applied for in-situ observation of ripple development on specific sites with successive pulses incident on the same site. Various fluence regimes are used, unveiling clearly remarkable phenomena accompanying LIPSS formation.

Fluence-dependent ripple evolution

We observe now the gradual development of ripples on a single irradiated site for different incident laser fluences, starting from the threshold vicinity to ablative regimes. The results are shown in Figs. 6.6 and 6.7. The irradiation sequence starts on the pristine polished surface and stops at the full development of the ripples pattern. First a low fluence (peak fluence of 0.09 J/cm^2) is used to generates LIPSS on the BMG surface with a period in the range of 700 nm , slightly evolving with the number of incident pulses and fluence. The pattern begins to be observable at a relatively high number of pulses ($N > 10$). This indicates that the modifications after each pulse are minimal, the structures growth is slow, resembling an erosion phenomena, and rely on incubation effects. The results of irradiation with increasing number of pulses (N) on the same site are given in Fig. 6.6. The patterns are analyzed in the following way. For successive number of pulses incident on the same site, full-field SIM images were taken and processed. A section is then made across the impact zone and, for each image corresponding to a given N , the resulting profiles (ripples relief) are concatenated and displayed in Fig. 6.6 a) for the whole N sequence. Thus the evolution at a specific location can be reconstructed. These profiles are horizontal cuts across a vertical arrangement of ripples and display the regular modulation. This representation gives an indication of the topography development with N , where the lateral dimension corresponds to structure periodic topography and the vertical dimension shows the irradiation development with the number of pulses (N). Fig. 6.6 b) shows

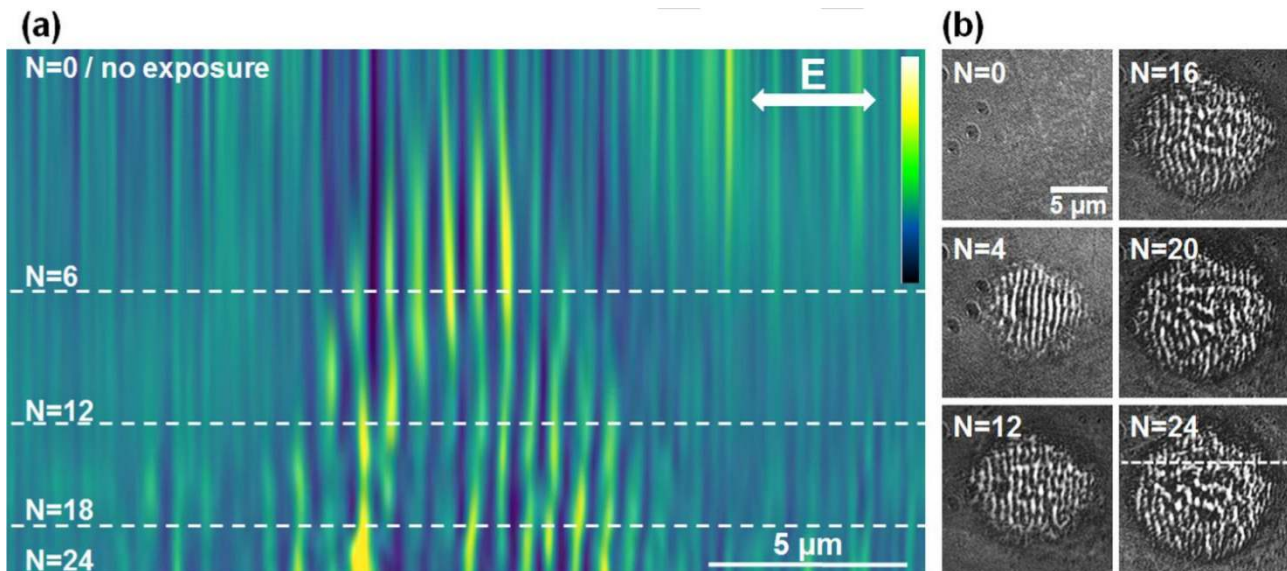


Figure 6.7 – From [Aguilar et al., 2017a]. Evolution on LIPSS formation on Zr-BMG in a high fluence regime (peak fluence of 0.31 J/cm^2). (a) Evolution of a section profile with the number of pulses N (false colors). Sectional cuts made on LIPSS images are concatenated together for each N . At this regime, the rippled pattern appears early in the pulse sequence, and is then followed by the formation of an ablation crater. Light colors represent zones of higher elevation. (b) Samples of the original SIM images. The direction of the electric field and the position of the sectioning line are given on the figures.

examples of different N sequences at the same spot, from where the section was sampled (the position of the sectioning line is given in the figure for the case $N = 100$). If topography features appear after several pulses, the ripple pattern starts to be visible from $N = 30$. The pattern acquires good visibility after $N = 50$ and shows a remarkable spatial stability with well-defined topographical features preserving their positions for the present experimental conditions. It is though expectable that the period will further decrease for a high number of pulses, a situation not analyzed here. We underline here that this observation of this pattern stability is greatly facilitated the in-situ SIM imaging. Indeed it would be experimentally very difficult and time-consuming to move the sample from the irradiation set-up to an external analysis apparatus after each pulse (AFM or SEM); not to mention the possible additional surface scratches and/or slight modification under AFM or SEM. Re-positioning at the exact same position would also be a challenge.

Another fluence regime is investigated, corresponding to a relatively high fluence (peak fluence of 0.31 J/cm^2) where the rippled pattern disappear in the central region after a certain number of pulses with the apparition of an ablation crater at the center. The results are displayed in Figs. 6.7 a), b). We see that the topography features appear already from the first pulse and the structures are well defined for a low number of pulses. With the number of pulses, hydrodynamic movement from the melt is observed culminating with large disordered melting and ablation feature appearing in the crater.

In all cases, we observe a continuity of the pattern from pulse to pulse (also in a intermediate fluence regime not shown here). The features of the profiles are spatially constant. This is a remarkable outcome, observable only with an in-situ observation technique with a sufficiently high resolution, such as the SIM microscopy employed here. The ripple pattern stays stable during the ripples growth with the increasing number of pulses for all fluence ranges. The surface relief stabilizes and becomes reinforced with each pulse, indicating that the topography

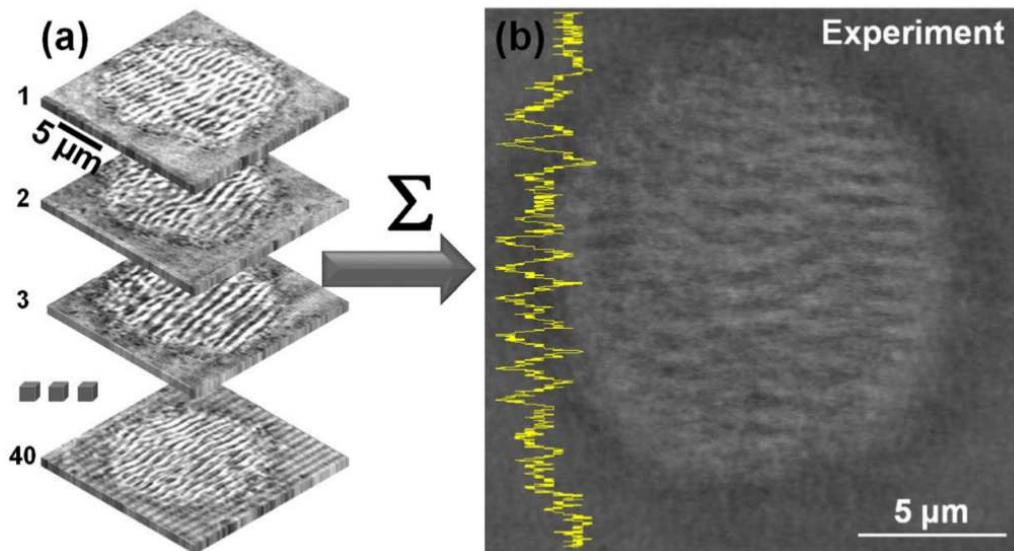


Figure 6.8 – From [Aguilar et al., 2017a] a) Individual images (40) of LIPSS sites on various different zones of the sample. b) The mean result of the images in a) showing a visible periodic pattern in the sum of the various irradiated zones, suggesting a quasi-stable pattern despite of different initial roughness conditions due to the various irradiation position. A line section is also shown to underline the regular spatial modulation. As the average of random corrugation patterns would give an uniform gray level distribution, this result clearly indicates a common absolute pattern of the LIPSS.

can lock the pattern distribution. The relief acts as an effective phase and mode-locking mechanism. This type of stabilizing mechanism is important in developing strategies for patterning larger areas, stitching together nanostructured domains and achieving high-quality surface structuring upon laser scanning. Numerical calculations (not shown) based 3D Maxwell's equations within the Finite-Difference Time-Domain (FDTD) method could confirm that the location of maximal energy absorption does not evolve from pulse to pulse [Aguilar et al., 2017a]. This corroborates the scenario based on a scattering and interference effect creating the periodicity and strong light trapping, reinforcing the pattern contrast. If the corrugation effect related to pulse-to-pulse evolution can involve a more complex physical picture relying on local ablation, growth, or lateral diffusion of the resulting pattern via liquid displacement, depending on the thermomechanical conditions, the main features of the stabilizing feedback are essentially related to interference and potential light trapping.

Stable LIPSS pattern on random roughness distribution

We have observed above a first type of pulse to pulse optical feedback based on the interference of scattered wavelets with the incident field and light trapping. This was facilitated by SIM enabling to follow in-situ the gradual development of LIPSS on a single irradiated region. A unique site possesses a single initial distribution of scattering centers, which presumably constrains the LIPSS pattern. Throughout the experiments, we have unexpectedly noticed that the LIPSS pattern would remain identical despite of the initial irradiation site on the sample. This is because the in-situ method allows to compare the irradiation results on different zones on the surface. We have thus performed the experiment for $N = 4$ laser pulses per site on 40 different initial zones on the sample surface. That way, the initial surface scattering centers

distribution of each of the irradiation site is distinct. After acquiring all images, where the relative alignment is ensured by the observation method, we added the images and observed the result. The procedure is schematically described in Fig. 6.8 a) and the result is shown in Fig. 6.8 b). The result preserves clearly a periodic character indicating a common absolute pattern of the LIPSS despite the random character on the initial irradiation sites, i.e the initial surface inhomogeneities. The average of random corrugation patterns before irradiation has given an uniform gray level distribution because of their random spatial distribution. We have equally performed calculations using the electromagnetic model starting from several random initial distributions and summed the results with similar results. The phase of the final pattern was found to be defined by the the laser electric field but not by the initial roughness properties. This is what we observed both numerically and experimentally where the initial surface roughness is randomly distributed. These results were obtained during the postdoctoral stay of A. Aguilar within the Labex roject 'Sermonis' (2016-2017).

6.4 Conclusion

The importance of in-situ monitoring of the irradiated region has been underlined. By using a UV laser probe, the periodicity of ultrafast laser-induced nanogratings in the bulk of fused silica can be optically evaluated within the irradiation set-up. This has permitted to tune the temporal shape of the femtosecond irradiation to control the nanogratings characteristics. We also have demonstrated that a super resolution microscopy technique can be employed to precisely monitor the formation of LIPSS on metallic surfaces. This in-situ imaging set-up has unveiled two physical mechanisms involved in the generation of LIPSS. These results show that in-situ monitoring is particularly adapted to understand and control the laser irradiation outcome, especially when the imaging resolution is sufficient.

Chapter 7

Conclusion and perspectives

7.1 Spatial Beam Shaping

We have seen that spatial control of ultrafast beams can be done by deflection, beam truncation, amplitude and wavefront modulation. We have brought to the state of the art to each of these techniques, with pioneering work on the subject of laser spot duplication through wavefront modulation, enabling parallelized processing. Noteworthy, all of these techniques are accompanied with trade offs regarding energy efficiency and beam shaping quality. The possibility to find a good compromise has been shown by taking into account the beam modulator performance in the calculation of the modulation mask. There, the help of a self-learning algorithm (here simulated annealing) has permitted to determine adapted coefficients of Zernike polynomials. These coefficients has enabled to experimentally obtain the desired ablation profile because the optimization was performed on the polynomials that the SLM was able to correctly reproduce. Control of the beam in three dimensions has also been discussed, for parallel processing and in the case of non diffractive beams, underlining the possibility to strongly confine the laser energy on the optical axis with reduced non linear propagation effects. Let us try to have a broader point of view and envisage the main directions of research that should now be taken.

7.1.1 Short term developments

Beam shaping in the three dimensions - non diffractive beams

We have discussed above the possibility to shape the laser intensity in the three dimensions from amplitude or wavefront modulation, and particularly along the optical axis thanks to non-diffracting beams. Several research groups are pursuing investigations in order to generate curved beams [Mathis et al., 2013; Rodrigo et al., 2013], controlled intensity variations along the beam propagation [Cizmar and Dholakia, 2009] and tubular non diffracting beam shapes [Xie et al., 2015]. The potential of non-diffractive beams applied to ultrashort laser processing is vast. Interesting perspectives are related to their self healing properties that we could recently evaluate in the case of metal ablation in the presence of metallic particles as shown in Fig.7.1 a). These preliminary results were obtained during the postdoctoral stay of Dat. NGuyen within the FUI project 3DHybrid (2018-2019) in collaboration with Manutech-USD and the WeAre-Aerospace company. When compared to the regular Gaussian beam, the beam self-reconstruction is remarkable. This property is well-known in the field of microscopy [Planchon et al., 2011]. Another very interesting feature of Bessel beams is related to the possibility to 'image' the axiconic phase through a regular 4f system. By carefully choosing the focal lengths ratio, it is possible to generate a very tight beam at the focal plane of a rather long working

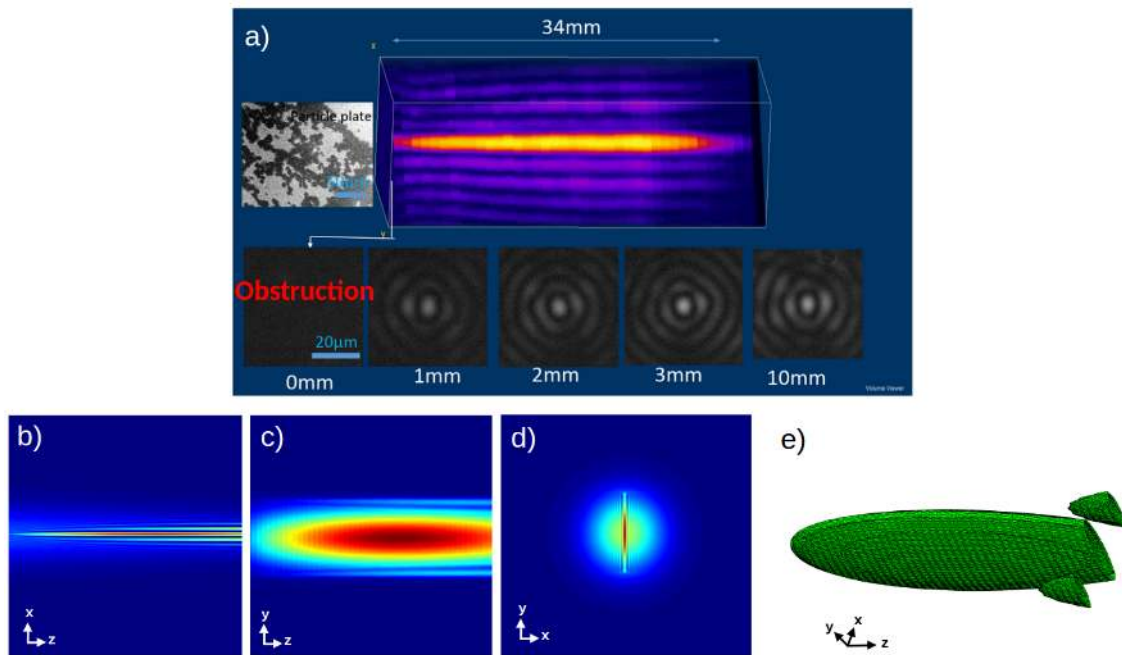


Figure 7.1 – a) Self reconstructing of a Bessel beam after a plane of obstruction by $\approx 20 \mu\text{m}$ metallic particles (3D reconstruction from experimental beam analysis). b)-e) 'Bessel Blade' beam obtained numerically and represented from different points of view, z being the optical axis.

distance lens. We have experimentally shown that a 3-5 fold decrease of the beam diameter is at reach, compared to the Gaussian beam, using a 10 cm converging lens. This is a strong advantage in any situation where the sample geometry does not allow for tight focusing, for example on some complex workpiece. More important, this feature should allow to reach the human crystalline lens without strong focusing (i.e possibly without patient interface) despite the physiological limitation of the eye acceptance angle. Naturally a special care should be taken to limit the laser intensity on the retina that could be problematic if the beam non-diffraction zone is too long.

Controlling the transverse intensity distribution of these types of non-diffractive beams is also of interest as illustrated by very first numerical results on Fig.7.1 b)-d). There, a 'Bessel Blade' is numerically achieved by mixing an axiconic phase modulation with a biprism phase yielding a blade-like intensity distribution. Applications of such beam shapes can be easily imagined such as planar waveguide photoinscription, microcutting of planes in tissues, transparent materials and so on. Collaborations on that matter are naturally envisaged with Manutech-USD when dealing with the cutting of transparent materials and also with the BIIGC laboratory and Keranova for enhanced controlled of the laser induced photodisruption of tissues. In that frame, we have recently obtained a grant from the IDEXLYON for the "Eagle" project (Eye Anterior segment Laser Engineering) in partnership with Manutech-USD and the Kejako company. The project's main objective is to counteract the solidification of the human crystalline lens by proper irradiation schemes, i.e the generation of cutting planes in the volume [Lubatschowski et al., 2010], and the microperforation of cellular membranes within the lens cortex as illustrated by Fig.7.2 a) and b) respectively.

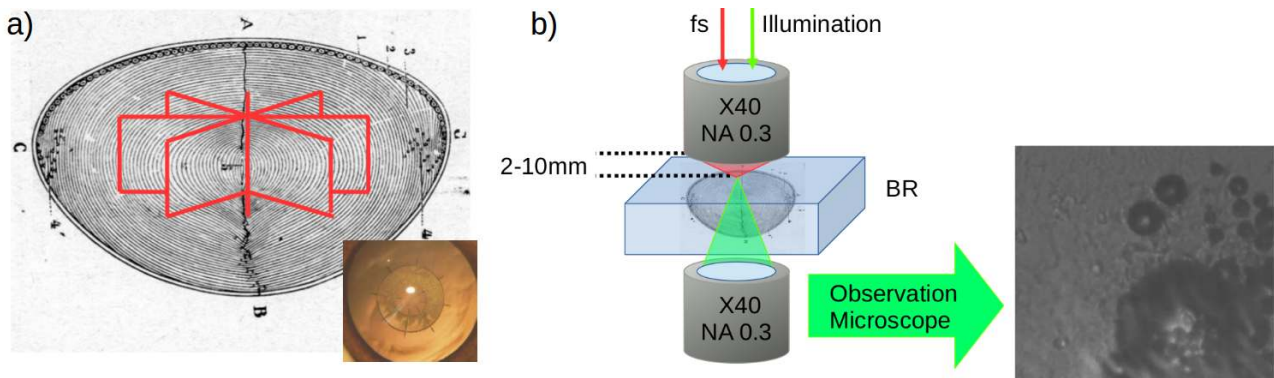


Figure 7.2 – a) Example of gliding planes geometry in crystalline lens to restore the accommodation, the photography in the inset is from the work of [Lubatschowski et al., 2010]. b) Illustration of the set-up for cell membrane perforation in the lens cortex, following the results depicted in Fig.5.7. The use of parallel tightly focused multiple spots and non diffracting beams are planned within the Eagle project.

Beam shaping fidelity and flexibility

As mentioned above, each of the beam shaping techniques suffers from a compromise between the beam shape quality and energetic efficiency. For example, high quality beam shaping (Speckle-free) requires the sacrifice of 'dumb' regions where the laser intensity is not controlled along with a very intense zeroth order. Interestingly, we have shown that it is possible to take into account the beam modulator performance in the calculation of the phase modulation γ using the Zernike polynomials. If this work has illustrated the concept of considering the real-life system limitations for the phase mask calculations, further efforts are to be conducted. In particular, the full modeling of the SLM's optical response should be the subject of dedicated research projects. More precisely, investigations should be oriented on the liquid crystal layer optical properties (linear and non linear), the resolution of the addressing electric field and how it translates on the liquid crystal layer, the power handling limitation as well as thermal stabilization effects upon cooling [Zhu et al., 2018]. This model is indispensable to conduct proper phase mask calculation that could take into account all the limitations and possibly overcome these shortcomings. To achieve this, a finer understanding of the behavior and optical properties of the liquid crystal layer and the whole SLM is required. In order to do so, a collaboration with the group of Walter Perrie in Liverpool could be of interest along with the group of Stefania Residori (Institut de Physique de Nice) specialized in the liquid crystal optical properties and control with whom we have conducted preliminary work on optically addressed SLMs.

Also, the use optically addressed SLM should be considered more closely, especially because of the high power handling capacity and larger achievable active surface. There, the SLM's phase response requires a careful modeling, especially concerning the attainable resolution that is limited by the optical addressing [Sanner et al., 2005].

In parallel, self learning strategies should be employed in-situ on the experimentally measured laser intensity to further increase the experimental beam shaping quality while maintaining a good efficiency.

Combining Deflection and spatial beam shaping for higher speeds

The most evident step to take in the near future relates to the quest of speed and reduction of the processing costs. This naturally directs to combine the quickest deflection means, such as

polygonal scanner, resonant mirrors, with laser spot duplication along with the highest repetition rate (now reaching GHz). Indeed, these research efforts are currently being conducted by many groups and ours (especially within the current ADEME project IMOTEP). Even if this is not presumably very original, it is surely an indispensable step to take in order to see ultrafast laser processing conquer more and more application fields. The gain of scanning speed is required in order to minimize pulse overlap so that thermal accumulation and other cumulative effects can be avoided.

7.1.2 Long term : Combining Deflection and spatial beam shaping for new structuring

In my opinion, there is an opportunity here to explore new surface and bulk structuring regimes. The key idea is to take advantage of the transient phenomena that do not have sufficient time to end between the successive pulses, for example, residual temperature increase, plasma, ejected species. This follows the concept of exploiting the redeposited materials as explained in the beginning of this manuscript. In the same direction, let us mention the so-called cooled ablation regime that has recently been demonstrated for GHz bursts of ultrashort pulses [Kerse et al., 2016]. In that regime, ablation rates 3-10 times higher than low repetition rate conditions were experimentally shown with low onset of post irradiation thermal effects. While the exact mechanisms of this interaction is still under debate, one can intuitively understand that this ablation takes advantage of the out of equilibrium state (a fraction of microsecond separate the successive pulses within the burst). This regime is clearly counterintuitive to the community as it was until recently widely accepted that femtosecond processes should remain below the MHz regime to avoid thermal effects or plasma screening [Ancona et al., 2008; König, Nolte, and Tünnermann, 2005; Bauer et al., 2015]. Combining advanced scanning and spatial beam shaping could lead to controlled temperature gradient, redeposition and ablation on surface and in the bulk, thus generating new structures. Following the same direction, the field of welding of transparent materials (glass, polymers and also opaque substrate) through high repetition rate irradiations [Miyamoto et al., 2007] could also benefit from advanced beam shaping. There the heat source shape and displacement could be controlled by the 3D beam shape and trajectory, respectively. Again, the temperature distribution as well as the heat flow could be precisely tuned for dedicated demanding applications.

7.2 In-Situ Monitoring

We have seen that direct imaging of the irradiated area or indirect probing through diffracted beam permits to better understand and master the ultrafast irradiation outcome. In particular, the formation of bulk nanograting in fused silica can be probed by UV diffraction. From the diffraction signal (position and intensity), the amount, regularity and period of these nanostructures can be inferred. The in-situ detection has permitted to experimentally tune the laser pulse temporal shape in order to favorize shorter periods (see Sec.6.2). Concerning direct imaging, we have used structured illumination microscopy (SIM) for in-situ imaging of LIPSS on Zr-BMG. The SIM has enabled to reach a sufficient resolution (below the light diffraction limit) for inline characterization of the LIPSS pattern. This observation of the pulse to pulse pattern birth and evolution during the ultrafast pulse sequence has revealed two essential physical mechanisms in the formation of LIPSS pattern, namely a feedback mechanism that stabilize the nano-pattern during the pulse sequence, and an absolute phase of the LIPSS pattern that is independent of the initial surface roughness distribution. In both cases, it is

clear that in-situ characterization is an essential step to take in order to completely master the irradiation outcome. We discuss in the following a few promising directions of research and developments concerning in-situ characterization that could literally trigger drastic changes on the task of defining process parameters.

7.2.1 Short term directions of research

Increasing the resolving power

The most evident direction of developments is "turning the knobs further" on the resolution. Besides the lack of originality, the quest of enhanced imaging spatial resolution permits to put several imaging techniques in competition. This triggers systematic comparisons between the surface characterization means in terms of performances and limitations. For example, we have recently compared the ability of chromatic confocal microscopy (CCM) with scanning electron microscopy, atomic force microscopy (AFM) and focus-variation microscopy (FVM) to characterize corneal surfaces of variable roughness after ultrafast laser cutting [Jumelle et al., 2017b]¹. We found that, as depicted on Fig.7.3, the small area allowed by AFM hinders conclusive roughness analysis, especially with irregular cuts while CCM allows analysis of large surfaces while keeping a good evaluation of the surface. More generally, this competition among characterization means is highly beneficial for the field. Fig.7.4 presents some interesting examples of in-situ monitoring of surface laser structuring found in the literature. An experimental tool combining SEM, FIB (focused ion beam) and ultrafast laser pulses is shown in Fig.7.4 a)-b). In that case, the femtosecond pulses are used to accelerate the milling step usually conducted by the FIB [Echlin et al., 2015], however, it is interesting to note that such an apparatus is achievable with a high degree of accuracy. Following this idea, Fig.7.4 c) presents a SEM micrograph of regular nanodot formation on the surface of Si under multiple ns pulse irradiation. The SEM picturing has also been achieved in-situ to follow the pulse to pulse evolution of the nanodot pattern as depicted on Fig.7.4 d) [Watanabe et al., 2010]. As another example of advanced in-situ monitoring of the LIPSS growth, the group of [Watanabe et al., 2010] has employed a synchrotron X ray source to achieve small-angle X-ray scattering under grazing incidence, as shown on Fig.7.4 e). Similarly, the work on ultrafast X-ray diffraction of Sokolwski-Tinten of has to be recognized here, with remarkable observation of extreme physical phenomena [Siders et al., 1999].

Using high resolution characterization means for in-situ monitoring is therefore a natural direction to take. SEM appears as a particularly adapted candidate due to the capacity to investigate relatively large areas of a few tens of micrometers with nanometric resolution. The issues in integrating a femtosecond beam within a SEM could relate to the onset of ejected species from the ultrafast irradiation. Also, the SEM observation beam can modify the surface properties between each irradiation however the work of [Echlin et al., 2015] and [Watanabe et al., 2010] clearly demonstrate that this is at reach. Integrating the ultrafast beam into an AFM is in my opinion even simpler than in a SEM, however, the AFM point to point scanning strategy is very time-consuming.

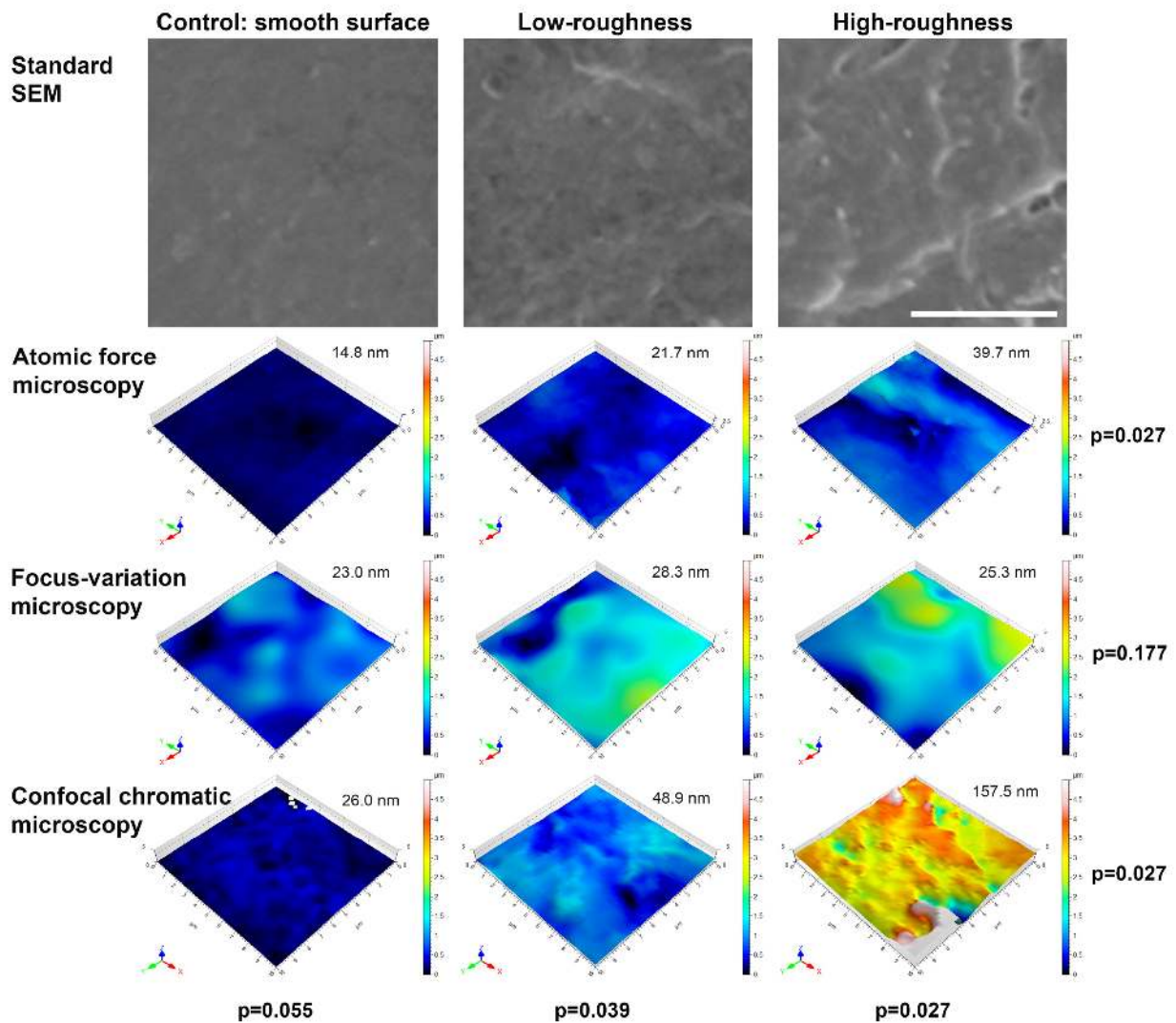


Figure 7.3 – From [Jumelle et al., 2017b]. Direct comparison of scanning electron microscopy, atomic force microscopy, focus-variation microscopy and chromatic confocal microscopy for the characterization of the surface of corneal lamellae. Lamellae with low and high roughness are measured with the naturally smooth surface of the Bowman membrane from $10 \times 10 \mu\text{m}^2$ areas selected at random site. Each height-map is presented with its measured roughness value (nm).

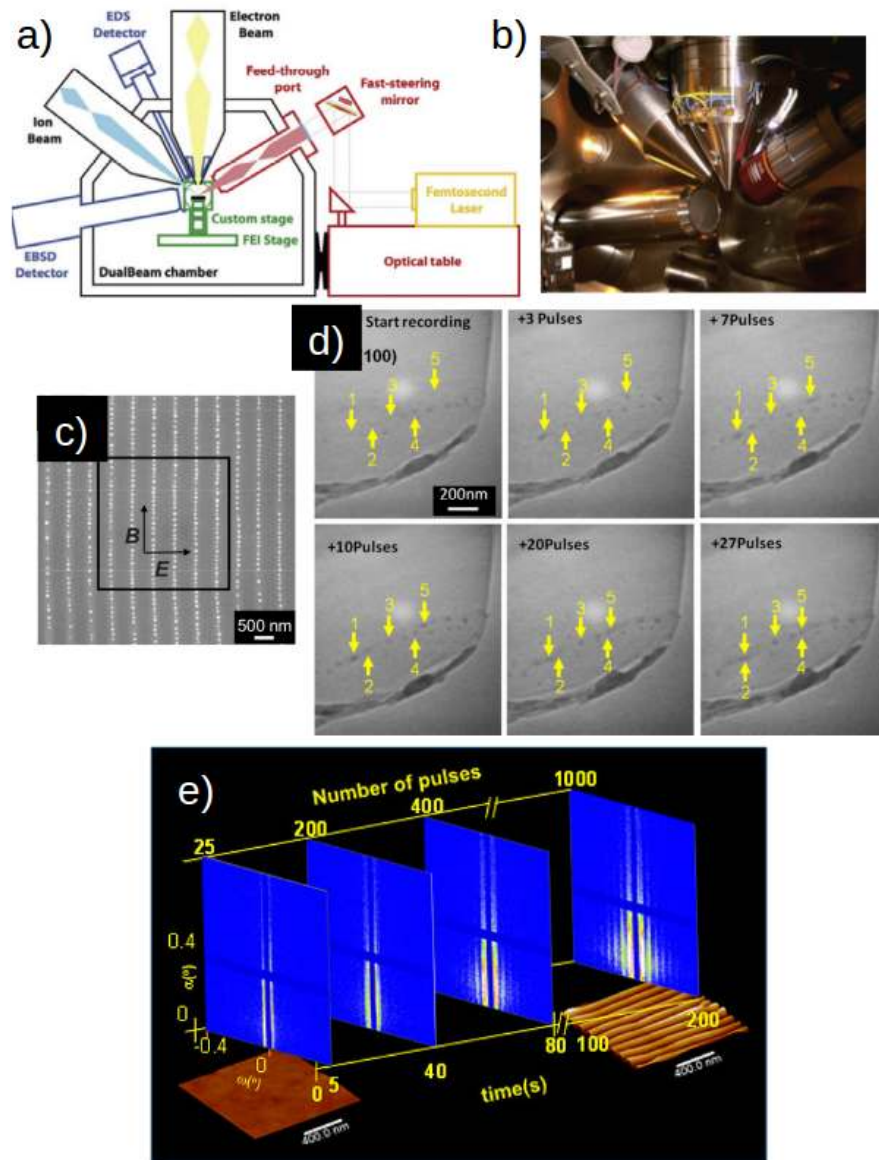


Figure 7.4 – a) Adapted from [Echlin et al., 2015], experimental apparatus "TriBeam" combining SEM, FIB and ultrafast laser irradiation, b) photography of the various probes. Here the laser serves as a milling tool. c) Adapted from [Watanabe et al., 2010], SEM picture of regular nanodot formation on Si under ns laser pulse irradiation. d) Pulse to pulse formation observed in-situ under SEM. e) Adapted from [Rebollar et al., 2015], sequence of LIPSS patterns acquired in-situ as a function of both time and number of pulses for a spin-coated PTT film laser irradiated with a ns laser under grazing incidence small-angle X-ray scattering.

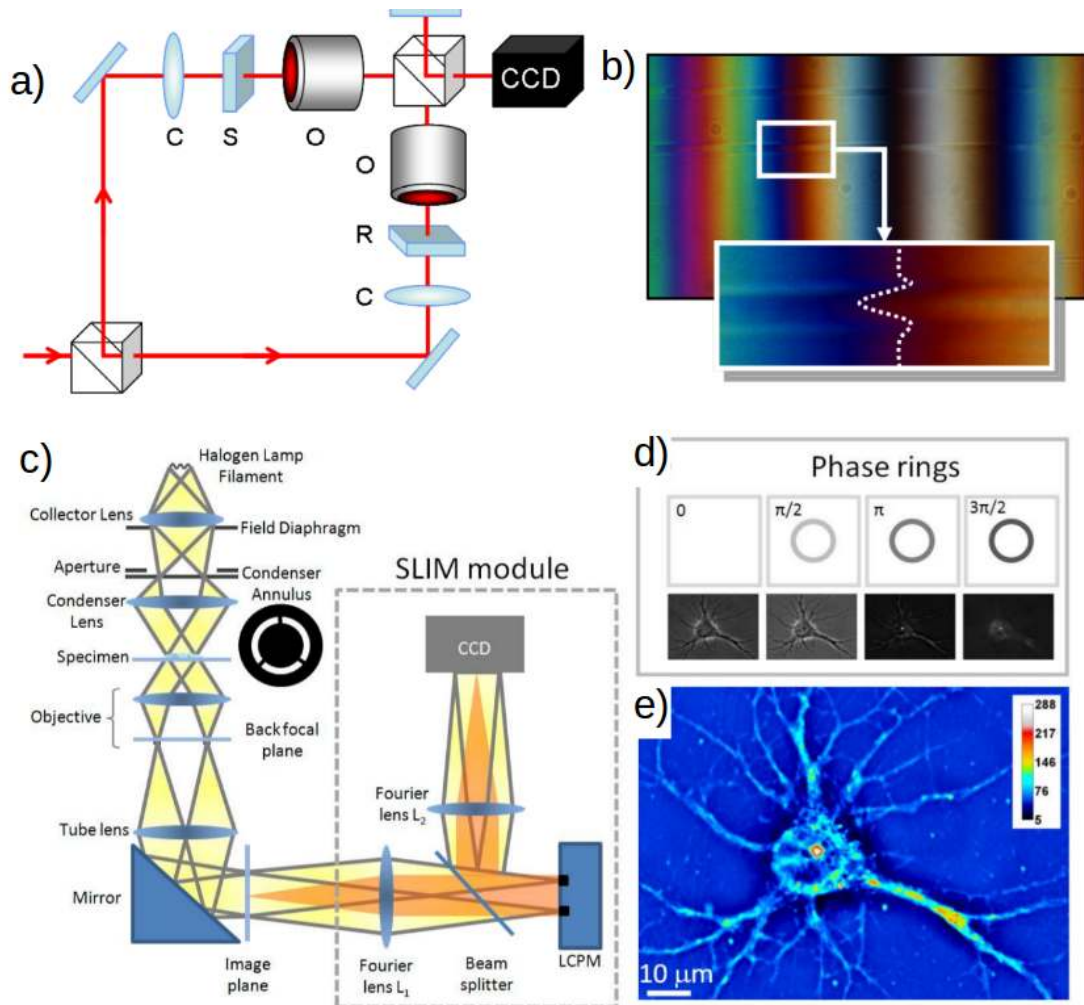


Figure 7.5 – a) Illustration of the light pathway in the Mach Zender Microscopy (MZM) C: condenser, O: microscope objective, S: sample with phase object, R: reference sample. set up. The Mach Zender configuration splits the source light into two arms (object and reference arm) whose only difference relies in the phase object to be analyzed. The fringes distortions in the image formed by the recombined beam are directly related to the refractive index modulation to be measured. b) MZM image of two bulk laser photowritten waveguides in BK7 glass. c)-e) From [Wang et al., 2011] c) Schematic setup for SLIM. The LCPM (liquid crystal phase modulator) permits to vary the phase ring retardation that is usually constant in a conventional phase contrast microscope d) The phase rings and their corresponding images recorded by the CCD. e) SLIM quantitative phase image of a hippocampal neuron.

Quantitative imaging for in-situ monitoring

Most of the well-known optical microscopy techniques do not give a quantitative measurement of the optical thickness (i.e the optical retardation or phase distribution) of the observed sample. Brightfield microscopy is not directly sensitive to phase retardations, and phase contrast microscopy as well as differential interference contrast microscopy provide a qualitative picture of the inspected phase object. When inducing bulk modification from ultrafast laser irradiation, the knowledge of the quantitative change in the refractive index is of paramount importance, especially for application involving light guiding micro-circuits, but also when evaluating the thickness of cells, tissues or liquids. More complex microscope systems, such as the Mach Zender Microscope permit to have a 2D mapping of the sample phase distribution from the interference fringes pattern as illustrated by Fig.7.5 a) and b). This microscope is however quite tricky to use (identical samples are required in both arms) and its alignment is an issue. The group of G. Popescu has developed several quantitative microscopy techniques that are more straightforward such as the spatial light interference microscopy (SLIM) [Wang et al., 2011] and the diffraction phase microscopy (DPM) [Popescu et al., 2006]. The SLIM is shown on Fig.7.5 c) and d). The SLIM technique can be seen as a phase contrast microscope with a reconfigurable phase retardation ring. A spatial light modulator permits to generate the various phase retardations, thus enabling to reconstruct the phase distribution of the object quantitatively. If there are no gain in the spatial resolution, contrary to the SIM microscope, the advantage of quantitative phase measurement enables to measure laser induced phase objects, but also liquid thickness, cell thickness and so on. The DFM technique (not shown) also enables such measurements, with the advantage of single picture imaging. We have very recently acquire such a system at the Hubert Curien Laboratory for in-situ examination of the laser-induced modification in the bulk of glass. The technique will potentially be used on the Eagle project for cell membrane poration imaging.

Ptychography for in-situ high resolution imaging with long working distances

Most of the time, surface structuring is conducted by scanners equipped with relatively long distance f - θ lenses. Those cannot be used for precise imaging mostly because of their small numerical aperture and long focal lengths that produce low resolution images. The working distance of the scanner is related to the focal length, and consequently to the scanning field on the sample surface. Better imaging can be obtained with shorter focal length. However, this is at the expense of a reduced scanning field. As the surface structuring speed is a key challenge, the scanning field and focal length must remain as large as possible. A solution to this problem has been demonstrated by the group of [Zheng, Horstmeyer, and Yang, 2013] using Fourier Ptychographic microscopy (FPM). There, high resolution images can be obtained even by imaging through a low numerical aperture and long focal length lens. The FPM technique require sequential image acquisition for different illumination angles. By combining the pictures, high resolution pictures can be reconstructed. The picture resolution is directly linked to the maximum illumination angle. This illustrated for transparent sample imaging on Fig.7.6 a). The performance of the technique has permitted to significantly enhance the resolving power by a factor of 6, achieving an equivalent imaging NA of 0.5 using a 0.08 NA lens. The FPM can naturally be adapted to reflective surfaces within surface scanning irradiation scheme as shown in Fig.7.6 d). The potential of the technique is related to its use in surface structuring and also for additive manufacturing. There, the layer by layer 3D

¹This investigations were done in the frame of the ANR project SupCo in collaboration with the BIIGC laboratory (2014-2018).

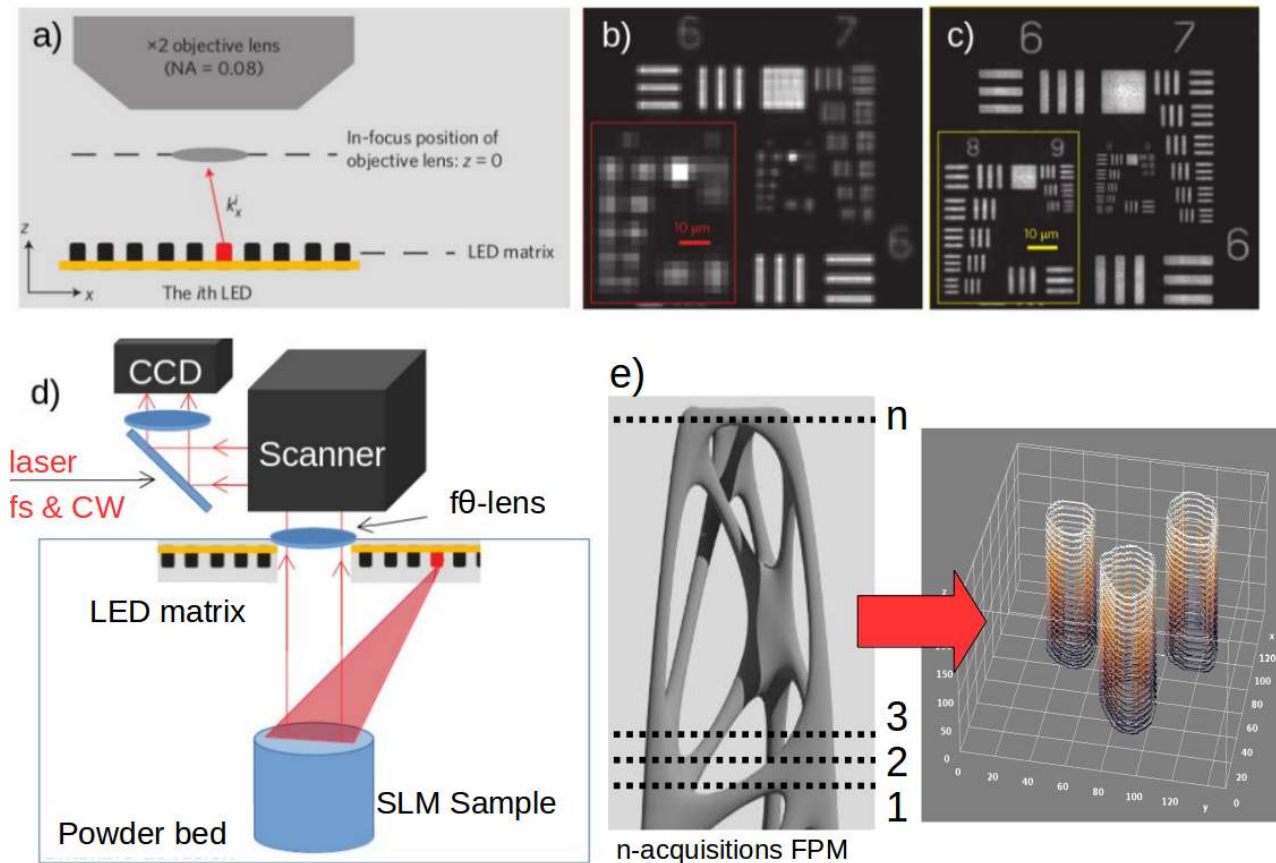


Figure 7.6 – a)-c) From [Zheng, Horstmeyer, and Yang, 2013] a) Principle of the Fourier Ptychographic Microscopy (FPM). A LED Matrix enables sequential illumination with various angles. The pictures formed through the low NA lens (0.08) are then numerically associated to reconstruct a higher resolution image (equivalent to NA=0.5) b) Imaging of an USAF target without reconstruction; c) with FPM reconstruction. d) adaptation of the FPM technique for laser structuring of laser beam melting imaging through low NA scanners. d) principle of 3D reconstruction of a selective laser melting (SLM) workpiece imaged by FPM.

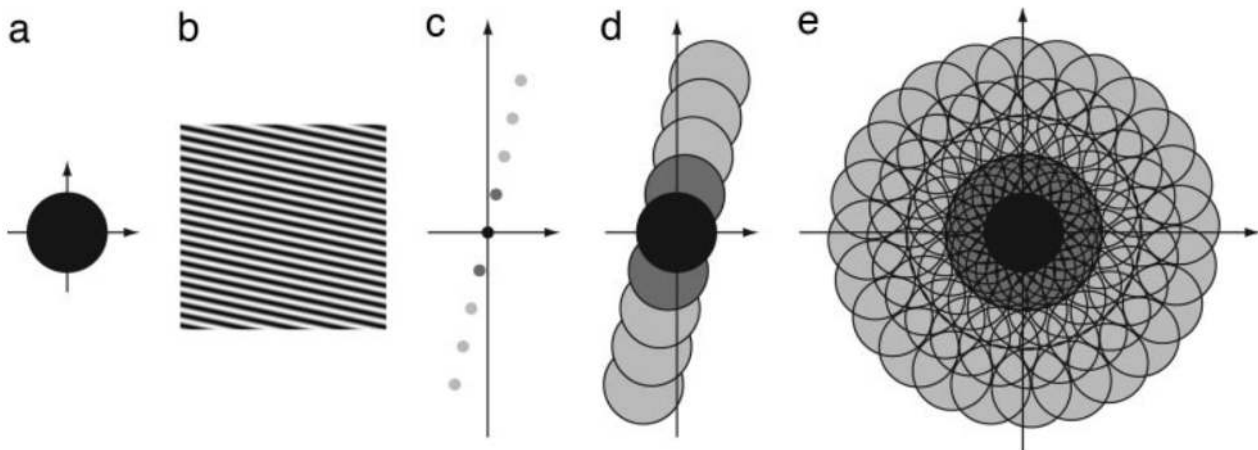


Figure 7.7 – a) From [Gustafsson, 2005], nonlinear SIM. (a) The region of frequency space that is observable by conventional microscopy with (b) An example of a sinusoidal illumination pattern. (c) nonlinear emission pattern in the frequency space from the fluorescence that presents high order harmonics (light gray spots) (d) Observable regions for conventional microscopy (black), linear SIM (dark gray), and nonlinear SIM microscopy (light gray) based on those three lowest harmonics. (e) Corresponding extension of the OTF regions if the procedure is repeated with other pattern orientations. below 50 nm resolution has been demonstrated.

imaging of the laser printed workpiece is highly desirable especially with high resolution that could qualify surface roughness of embedded inner parts. This is schematically illustrated by Fig.7.6 e). This project is supported by the PEPS DGA program and is currently conducted at the Hubert Curien Laboratory in close relationship with the FUI 3D-Hybrid project involving Manutech-USD, WeAre-Aerospace, ENISE and ENMSE.

7.2.2 Long term : increasing the resolving power

Optical detection means must also be considered in the quest for the ideal in-situ monitoring tool. Following our efforts in integrating a SIM for in-situ monitoring (see Sec.6.2), we have to consider techniques that can further enhance the resolving power. Regular SIM permits to divide by 2 the resolution limit of a standard brightfield microscope. A few years after the first demonstration of SIM, an extended version of SIM has been proposed, namely the Non linear SIM [Gustafsson, 2005]. There, the resolution limit can be theoretically infinitely small, by exploiting the non linear response of the fluorophores as illustrated in Ffig.7.7. The nonlinear response of fluorescence presents high harmonics that can be exploited to shift the object spatial frequencies in the microscope's OTF, similarly to the SIM with a larger frequency shift. Remarkable resolution enhancement has been demonstrated, below 50 nm. In principle, the nonlinear SIM relies on a nonlinear response affecting the light emitted from the object. It is thus expectable that the nonlinear SIM can be employed on any surfaces or transparent volumes where nonlinear response can occur. Developments in that directions are currently conducted, however it has to be underlined here that the nonlinear SIM requires many more image acquisitions and treatment than the standard SIM. This is illustrated in Fig.7.7 e) where each circle of the FD corresponds to an image acquisition. In our current standard SIM set-up, one super resolution image acquisition (i.e 15 images) lasts 40 s. This time is mostly due to the Ronchi grating rotations and translations. This time is comparable to the commercial solution of Zeiss. It is evident the nonlinear SIM requires longer acquisition time and a larger

computational effort. It is interesting to note that in a sense, the nonlinear SIM tends to have similar drawbacks as STORM, PALM and STED in term of acquisition time but also in terms of exposure amount. Also, enlight a sample to trigger nonlinear response is evidently a tricky experimental step as the probed region is pushed towards its 'limit'. In other words, the light dose difference (in intensity, or in exposure time) between nonlinear response and permanent sample damage may be sometimes small, and possibly smaller than the light source instabilities, thus rendering such imaging problematic. More generally, it appears that super resolution optical means are often based on the accumulation of data points (scanning points as in STED microscopy) or several full field images (STORM, SIM, nonlinear SIM). This is a very restrictive feature, especially for time-resolved investigations. Pump-probe monitoring of the interaction zone can have the time resolution of ultrafast laser pulses i.e down to a few tens of femtoseconds, only if a single light flash is enough, like in standard microscopy, or for beam diffraction. Thus, the quest of high resolution in space is at the expense of resolution in time. A possible answer to that paradigm for SIM would be to acquire each of the required image in a parallel manner, i.e with a dedicated beam path. However, since a minimum of 9 pictures is needed for SIM, the corresponding apparatus would be far too complex.

Thus, another level of equipment is required if both temporal and spatial resolution are desired at the femtosecond and nanometric level, respectively. An example of this kind of work is illustrated in Fig.7.8 from [Karl et al., 2018]. On this so-called table-top system, an extreme UV ultrashort beam (30 nm wavelength, 10 fs) generated from high harmonic generation serves as stroboscopic light source. The diffracted signal is then collected and treated following the coherent diffraction imaging method that reconstructs the amplitude and phase of the object from the diffraction pattern, with a spatial transverse resolution of 38 nm. This table-top demonstration did not require large facilities such as synchrotron or FEL, even if the experimental effort is remarkable. The resolution (30 nm transversally, combined with ≈ 10 fs temporally) represents a significant advance in full-field dynamic imaging capabilities. This complex apparatus could evidently be used for in-situ probing of the ultrafast laser interaction on surfaces, unveiling physical phenomena at ultrashort timescales and at quasi-nanometric spatial resolution. However, we have to keep in mind that brightfield optical microscopy pushed to the UV range and using high NA immersion microscope objective can also reach below 100 nm spatial resolution with direct fullfield imaging and with a temporal resolution close to that of ultrafast laser source. This simpler and more robust and stable experimental scheme appear more adapted for in-situ probing, especially if an automated optimization of the laser parameters is conducted (see below). Going in the opposite direction, by using large facilities such as the synchrotron radiation [Watanabe et al., 2010], or X-ray diffraction [Siders et al., 1999], or FEL sources can also be of interest when specific physical questions have to be elucidated because of the relatively limited available time of use.

7.3 Connecting in-situ monitoring to optimization self-learning loops for applications

The advances and technological developments surrounding ultrafast laser processing are remarkable, especially on the side of fundamental investigations. The concept of in-situ monitoring has constantly accompanied most of the ultrafast laser-matter interaction investigations. If the primary scope of in-situ monitoring is a better observation and understanding of the interaction, the following step is a better control of the interaction. Noteworthy, the 'control' step can bypass the observation/understanding steps. A famous example of this concept is the field of coherent control. A famous article [Judson and Rabitz, 1992], smartly entitled

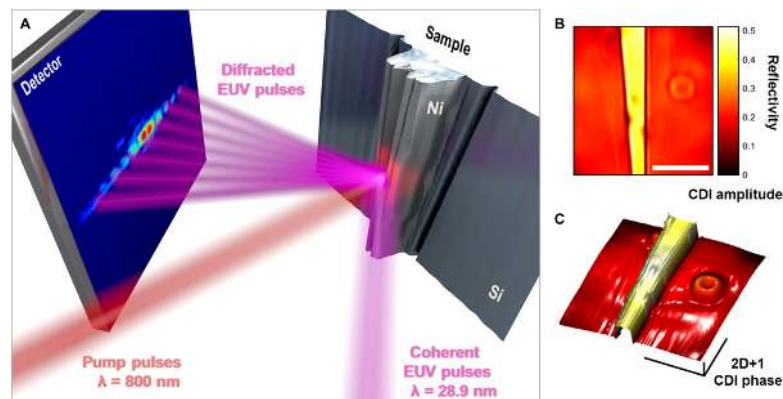


Figure 7.8 – From [Karl et al., 2018], A) EUV pump-probe apparatus allowing for both high spatial and temporal resolution. A nickel nanoantenna is irradiated by an IR pump beam and the dynamics are measured by an EUV probe beam. The scattered EUV light is collected on an EUV-sensitive CCD. B) Quantitative amplitude image. Scale bar, $5 \mu\text{m}$. C) Height map of the sample, obtained from the reconstructed phase image. Scale bar $5 \mu\text{m}$, the colorscale is in nm.

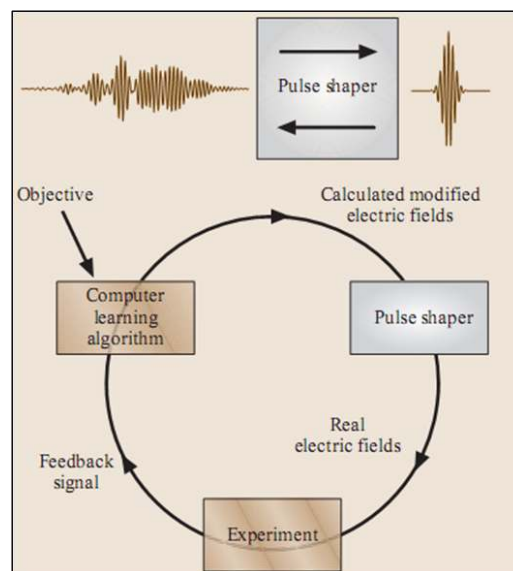


Figure 7.9 – Illustration of an optimization algorithm. Several pulse shapes (but it can be extended to any laser parameters) are tested and receive a score according to their adaptation to the problem (e.g the most intense spectral emission at a given wavelength). The optimization algorithms are able to iteratively propose more and more adapted laser pulse parameters, without any knowledge of the physical relationship between the pulse parameters and the irradiation outcome.

'Teaching lasers to control molecules', has shown the concept of tuning the ultrafast irradiation (the temporal pulse shape) in order to trigger targeted molecular transitions. The tuning is performed thanks to optimization algorithm, such as evolutionary algorithms, that test several pulses parameters (individuals) and attributes them a score (fitness) depending on the success (for example the intensity of a given spectral line corresponding to the targeted transition). The optimization continues by testing several 'generations' of pulses shapes obtained from the best fitting individuals, mimicking the evolutionary concept of adaptation to the environment as illustrated in Fig.7.9. We have applied this concept to control the result of ultrafast irradiation in the bulk of borosilicate and fused silica glass [Mermillod-Blondin et al., 2008a; Mermillod-Blondin et al., 2008b]. Also, we have used this kind of strategy for spatial beam shaping to generate an arbitrary groove profile (see Sec.5.3). Interestingly, the optimal beam shape that was found does not resemble at first sight the desired ablation profile (see Fig.5.12). However, upon scanning, the desired profile was obtained. It is interesting to note that these algorithms can find unexpected solutions. Thus, the performance of these stochastic optimization routines are impressive even after only a few hundreds of iterations, having in mind the very large search space (here all the laser shaping possibilities). An interesting direction of research is to extent this concept of self learning, or machine learning algorithms to the definition of laser process parameters. This concept has been proposed to optimize the laser intensity distribution in the frame of spatial beam shaping [Campbell et al., 2007] and direct interference patterning [Mikhaylov et al., 2019]. However, more exciting is the use of the irradiation outcome as the feedback for the optimization algorithm. Indeed, the search space for defining adapted processing parameters depending on the application is growing, due to the increase of flexibility offered by nowadays commercial ultrafast sources. Currently, just to name a few of these parameters we can easily list pulse energy E_{pulse} , numbers N , duration τ_{pulse} , repetition rate, spatial overlap Δx and Δy , repetition rate inside burst, spatial and temporal intensity distribution $I(x, y, z, t)$ and so on. Of course the search space explodes if any gradient during the irradiation is necessary, for example, gradient within the burst, or spatially evolving gradients. Usually, systematic tests are semi automatically conducted by varying e.g the pulses energy, repetition rate and so on. Considering the impressive search space, self learning algorithms may bring an answer to the nowadays challenge to find the correct laser process parameters for a desired surface or bulk function. If the scope of ultrafast laser irradiation is simply a layer removal or a 2.5 D machining, it is clear the 'manual' determination of the better process parameters seems more adapted. However, when thinking about more complex surface or bulk functions, such as wettability control, antibacterial or self cleaning effect, biocellular differentiation and so on, it is almost impossible to anticipate which types of structuring and at which level (micro or nanometric) will be the most adapted. The concept is illustrated in Fig.7.10 where the connection between the two main subjects of this work, beam modulation and in-situ monitoring, is 'optimally' achieved with self-learning strategies. The challenge is now to find experimental solutions adapted to the desired application to put in place such optimization schemes. Thus, we must develop and anticipate e.g automated wettability measurement, analysis of nanostructures from super resolution imaging and so on. Then, from the optimal solution found by the search algorithm, we must expect further opportunities of finer understanding and control of the interaction. In the following, we illustrate this with two prospective examples of surface and bulk functionalization with self learning optimization scheme. We first discuss the possibility to build an automated self-learning apparatus for wettability functionalization via optimized laser beam control and in situ evaluation of the droplet thickness and dynamics. Then, a likewise strategy is proposed for controlling the mechanical properties of the human crystalline lens, with the scope of presbyopia counteracting.

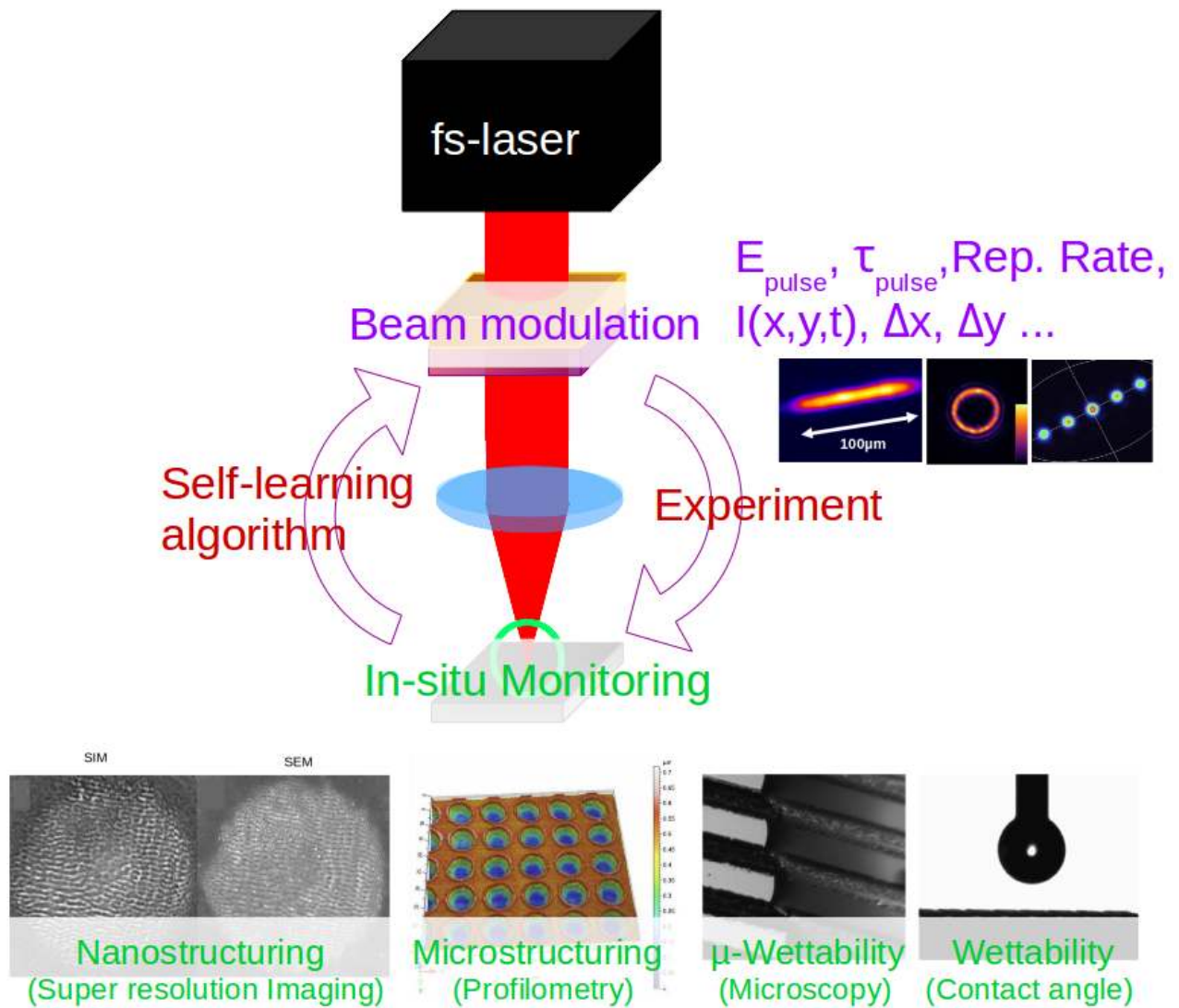


Figure 7.10 – Self-learning strategies for optimization of ultrafast laser beam parameters based on in-situ monitoring of the application scope e.g nanostructuring with LIPSS that can be evaluated using super resolution imaging, micrometric structuring, roughness control that can be measured using interferometric probes, wettability that can be characterized from the triplet line dynamics or from the liquid drop contact angle and so on.

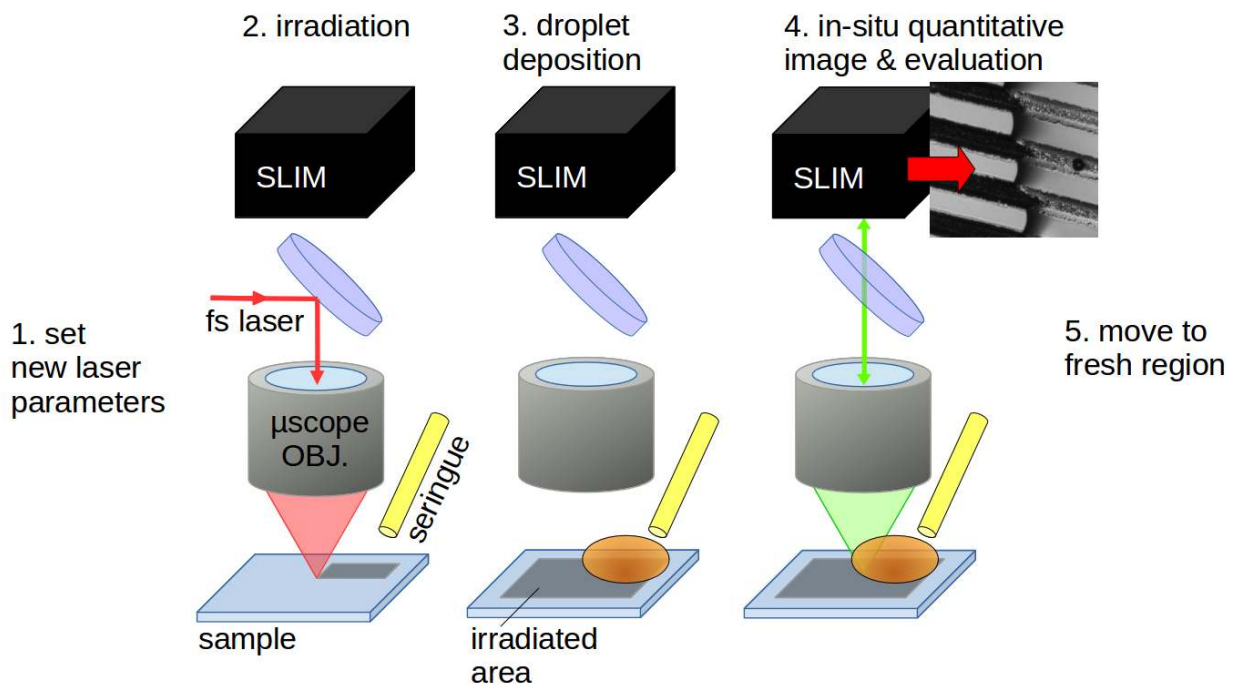


Figure 7.11 – Self learning routine for automated optimization of laser parameters for surface wettability control. Detail of the iteration steps enabling the testing of a given set of laser parameters. The detail of the 5 steps is given in the text.

7.3.1 Laser beam control and in-situ monitoring for surface wettability control

A relevant example of application where the use of in-situ monitoring, beam control and self-learning routines is the laser surface treatment for wettability control of surfaces. The relationship between the laser parameters, the irradiation conditions (depending on fluence, pulse duration, overlap, repetition rate, spatial and temporal pulse profile and so on) and the final surface wettability properties is quite evidently very complicated. The prediction of the irradiation outcome with a given set of laser irradiation conditions, in terms of surface topology and material distribution, from numerical simulations is already a very complex question that must be treated with multiphysical approaches (see [Rudenko et al., 2019c]). The prediction of wettability properties obviously adds to these difficulties, especially having in mind that these properties depend on both topological and chemical properties of the surface. Thus, finding a set of optimal laser irradiations conditions from theoretical considerations is still quite far. However, this challenging question is a typical problematic that can be addressed by self-learning routines. As illustrated by Fig.7.11, we propose here an automated apparatus that can evaluate the wettability properties of the irradiation outcome in-situ. The wettability evaluation relies on the measurement of the extent and thickness of constant-volume water (or other liquid) droplet based on quantitative phase evaluation using spatial light interference microscopy (SLIM) [Wang et al., 2011] or diffraction phase microscopy (DPM) [Popescu et al., 2006]. Thus, thousands of laser parameter combinations could be automatically investigated and optimized. Each set of laser parameters can thus be automatically tested and graded for the optimization. It could be argued that the stochastic algorithms need a significant amount of iterations to converge towards global optimum solutions (i.e a set of proper laser parameters), thus making them unrealistic for experimental realization. However, from our experience using evolutionary algorithms on temporal shaping (see [Mermillod-Blondin et al., 2008a]

and[Mermillod-Blondin et al., 2008b]), a range of 3000-10000 iterations were necessary, each iteration lasting between 1-2 seconds. One iteration involved :

1. Laser temporal shape modulation
2. Irradiation of the bulk
3. Picturing of the irradiated zone (in-situ phase contrast microscopy)
4. evaluation of the irradiation success
5. sample translation to a fresh region

Thus, an optimization would last up to 3-4 hours. The number of iterations is directly related to the search space, which was enormous in these latter work². In the case of laser parameters optimization, the search space can be much smaller, for example involving 10 fluence values, 10 overlap values, 10 repetition rates, 10 pulse durations and so on, thus reducing the required number of iteration for sufficient convergence of the algorithm. In that case, it is reasonable to consider slightly longer iteration steps (e.g up to 5 seconds) than from our previous work. The wettability properties evaluation step would involve (see Fig.7.11):

1. Laser parameters adjustments (repetition rate, energy, overlap)
2. Irradiation of the surface
3. Automated liquid droplet deposition
4. In-situ quantitative measurement of the liquid extent and thickness by SLIM or DFM
5. Sample translation to a fresh region

The self-learning routine can go on finding the optimal set of laser parameters even on several days, given the robustness and stability of nowadays ultrafast sources. Among the difficulties that can be anticipated, the problem of stabilization of the wettability properties of the surface, especially when the laser irradiation is conducted in the air. This issue can be addressed to a certain extent by controlling the ambient gas.

7.3.2 Laser beam control and in-situ monitoring for presbyopia counteracting

An exciting potential application of this self-learning strategy concerns the counteracting of presbyopia. Upon aging, the human crystalline lens thickness and mechanical properties are altered. This leads to a reduction of the accommodation strength that is the presbyopia. This usually occurs around 45-50 years old with a reduction of the ability of the patient to focus on close objects. In order to give an idea, the lens accommodation ability ranges from more than 20 dioptres for a child (closest object \approx 5 cm) down to 1 dioptre at age 60 (closest object \approx 1 m). The origin of the lens aging and losses of flexibility is well-related to the augmentation of the amount of intermolecular disulfide bonds -S-S- as observed by [Yu et al., 1985]. The reduction of these bonds (by chemical means) has been shown to restore and even augment the lens flexibility on old mice (see [Garner and Garner, 2016]). Without entering into details, it is expected that the augmentation of the intermolecular disulfide bonds reduces the nutrients circulation and increases the lens stiffness. Similarly, it is interesting to note that the disulfide are the crosslinking groups that result from the vulcanization of rubber. These linkages in rubber are crosslinkers that strongly affect the rheology of the material. Consequently, breaking of these particular intermolecular bonds is a promising option towards presbyopia counteracting. Experimental evidences on the possibility to achieve this by chemical

²The pulse temporal shape was encoded on a phase mask of 128 pixels, each pixel having 256 possible values, yielding 256^{128} possibilities

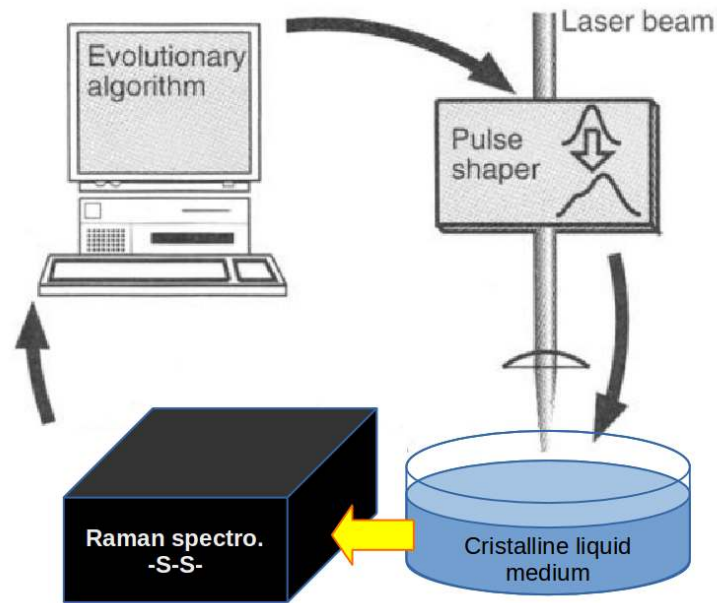


Figure 7.12 – Adapted from [Judson and Rabitz, 1992]. The self-learning loop optimizes the temporal pulse shape based on its efficiency in reducing the concentration of disulfide bonds, which is measured in-situ by the Raman spectrometer.

means have recently been provided, with the expected effect of restoring the lens flexibility on mouses [Garner and Garner, 2016]. The question is now, can this be obtained with a modulated ultrafast laser irradiation? In the work of [Fung et al., 2005], the disulfide bond cleavage is obtained using a UV irradiation at 157 nm. It is evident that this UV beam can not be used for presbyopia treatment as it would not reach the bulk of the crystalline lens, being absorbed by the cornea. However, this result presumably indicates that an energetic transition of 7.9 eV can lead to the -S-S- cleavage. Using ultrafast pulses, the multiphotonic absorption mechanism can reach this transition through the coherent interaction of several IR-photons within the bulk of the transparent media. It is expected however that the associated high intensity level triggers also several unwanted transitions and bulk modifications. The possibility of selectively trigger molecular transition thanks to temporally shaped pulses has been demonstrated in the famous paper [Judson and Rabitz, 1992]. Noteworthy, optimal pulse shapes were obtained using self learning routines, without a priori knowledge of the optimal pulse temporal form. This strategy can be applied for the specific cleavage of the disulfide bond. Happily, the relative concentration of disulfide bond can be measured using Raman spectroscopy [Yu et al., 1985]. This measurement can provide the necessary feedback for the self learning routine as illustrated by Fig.7.12.

Bibliography

- Aguilar, Alberto, Abundio Davila, Jorge Garcia-Marquez, and Cyril extbfMauclair (2014). "Phase extraction through multistep vortex filtering." In: *9ème édition des Journées" IMAGERIE OPTIQUE NON CONVENTIONNELLE" 19 et 20 mars 2014, ESPCI, 10 rue Vauquelin, Paris Amphithéâtre Langevin*.
- Aguilar, Alberto, Cyril Mauclair, Nicolas Faure, Jean-Philippe Colombier, and Razvan Stoian (2017a). "In-situ high-resolution visualization of laser-induced periodic nanostructures driven by optical feedback". In: *Scientific reports* 7.1, p. 16509.
- Aguilar, Alberto, Jean-Philippe Colombier, Razvan Stoian, and Cyril Mauclair (2017b). "In situ observation of ultrafast laser induced micro nano structures using structured light illumination". In: *Laser-based Micro-and Nanoprocessing XI*. Vol. 10092. International Society for Optics and Photonics, p. 1009220.
- Amako, Jun, Kimio Nagasaka, and Nishida Kazuhiro (2002). "Chromatic-distortion compensation in splitting and focusing of femtosecond pulses by use of a pair of diffractive optical elements". EN. In: *Optics Letters* 27.11, pp. 969–971. ISSN: 1539-4794. DOI: 10.1364/OL.27.000969. URL: <https://www.osapublishing.org/ol/abstract.cfm?uri=ol-27-11-969> (visited on 04/01/2019).
- Ams, M., G. Marshall, D. Spence, and M. Withford (2005). "Slit beam shaping method for femtosecond laser direct-write fabrication of symmetric waveguides in bulk glasses". In: *Opt. Express* 13.15, pp. 5676–5681. DOI: 10.1364/OPEX.13.005676. URL: <http://www.opticsexpress.org/abstract.cfm?URI=oe-13-15-5676> (visited on 01/20/2010).
- Ancona, A., F. Röser, K. Rademaker, J. Limpert, S. Nolte, and A. Tünnermann (2008). "High speed laser drilling of metals using a high repetition rate, high average power ultrafast fiber CPA system". EN. In: *Optics Express* 16.12, pp. 8958–8968. ISSN: 1094-4087. DOI: 10.1364/OE.16.008958. URL: <http://www.osapublishing.org/abstract.cfm?uri=oe-16-12-8958> (visited on 09/11/2015).
- Anton, Rudenko, Anthony Abou Saleh, X Sedao, Cyril Mauclair, Razvan Stoian, Tatiana Itina, Florent Pigeon, Florence Garrelie, and Jean-Philippe Colombier (2018). "Electromagnetic roughness-driven mechanisms of ultrashort laser-induced ripple formation on metal and dielectric surfaces". In: *8th international workshop on Laser Induced Periodic Surface Structures*. Bochum, Germany. URL: <https://hal.archives-ouvertes.fr/hal-02025834> (visited on 05/21/2019).
- Bauer, Franziska, Andreas Michalowski, Thomas Kiedrowski, and Stefan Nolte (2015). "Heat accumulation in ultra-short pulsed scanning laser ablation of metals". EN. In: *Optics Express* 23.2, pp. 1035–1043. ISSN: 1094-4087. DOI: 10.1364/OE.23.001035. URL: <http://www.osapublishing.org/abstract.cfm?uri=oe-23-2-1035> (visited on 01/27/2017).
- Bañas, Andrew, Oleksii Kopylov, Mark Villangca, Darwin Palima, and Jesper Glückstad (2014). "GPC light shaper: static and dynamic experimental demonstrations". en. In: *Optics Express* 22.20, p. 23759. ISSN: 1094-4087. DOI: 10.1364/OE.22.023759. URL: <http://www.opticsinfobase.org/abstract.cfm?URI=oe-22-20-23759> (visited on 03/16/2015).

- Belaud, V, S Benayoun, K Anselme, C Mauclair, and C Donnet (2016). “Influence of multiscale and curved structures on the behavior stem cells and macrophages”. In: *European Material Research Society, E-MRS 2016, Fall Meeting*.
- Belaud, Vanessa, Tatiana Petithory, Arnaud Ponche, Cyril Mauclair, Christophe Donnet, Laurent Pieuchot, Stephane Benayoun, and Karine Anselme (2018). “Influence of multiscale and curved structures on the migration of stem cells”. In: *Biointerphases* 13.6, p. 06D408. ISSN: 1934-8630. DOI: 10.1116/1.5042747. URL: <https://avs.scitation.org/doi/abs/10.1116/1.5042747> (visited on 05/21/2019).
- Bernard, Aurélien, Cyril Mauclair, Emmanuel Baubeau, J Granier, Gregory Egaud, Z He, N Campolmi, S Piselli, F Forest, M Peoc’h, et al. (2013). “Endothelial graft precutting from the epithelial and endothelial side with the femtosecond laser, on cornea stored in a new corneal bioreactor”. In: *Acta Ophthalmologica* 91.s252, pp. 0–0.
- Bernard, Aurelien, Philippe Gain, Cyril extbfMauclair, and Gilles Thuret (2017). *Device and method for cutting a cornea or crystalline lens*. US Patent App. 15/517,480.
- Betzig, E., G.H. Patterson, R. Sougrat, O.W. Lindwasser, S. Olenych, J.S Bonifacino, M.W. Davidson, J. Lippincott-Schwartz, and H.F. Hess (2006). “Imaging intracellular fluorescent proteins at nanometer resolution”. In: *Science* 313.5793, pp. 1642–1645.
- Bhuyan, M. K., F. Courvoisier, P. A. Lacourt, M. Jacquot, R. Salut, L. Furfaro, and J. M. Dudley (2010). “High aspect ratio nanochannel machining using single shot femtosecond Bessel beams”. In: *Appl. Phys. Lett.* 97.8, p. 081102. ISSN: 00036951. DOI: 10.1063/1.3479419. URL: <http://link.aip.org/link/APPLAB/v97/i8/p081102/s1&Agg=doi> (visited on 11/09/2010).
- Bijnen, R. M. W. van, C. Ravensbergen, D. J. Bakker, G. J. Dijk, S. J. J. M. F. Kokkelmans, and E. J. D. Vredenburg (2015). “Patterned Rydberg excitation and ionization with a spatial light modulator”. en. In: *New Journal of Physics* 17.2, p. 023045. ISSN: 1367-2630. DOI: 10.1088/1367-2630/17/2/023045. URL: <https://doi.org/10.1088%2F1367-2630%2F17%2F2%2F023045> (visited on 04/06/2019).
- Bijnen, Rick van (2013). “Quantum Engineering with Ultracold Atoms”. PhD thesis. Eindhoven University of Technology.
- Bizi-Bandoki, P., S. Benayoun, S. Valette, B. Beaugiraud, and E. Audouard (2011). “Modifications of roughness and wettability properties of metals induced by femtosecond laser treatment”. In: *Applied Surface Science*. E-MRS 2010 Spring Meeting Symposium R. "Laser Processing and Diagnostics for Micro and Nano Applications" 257.12, pp. 5213–5218. ISSN: 0169-4332. DOI: 10.1016/j.apsusc.2010.12.089. URL: <http://www.sciencedirect.com/science/article/pii/S0169433210018180> (visited on 07/09/2015).
- Born, M. and E. Wolf (1999). *Principles of Optics: Electromagnetic Theory of Propagation, Interference and Diffraction of Light*. 7th. Cambridge University Press. ISBN: 0-521-64222-1.
- Calderón-Hermosillo, Yuliana, Jorge García-Márquez, Rafael Espinosa-Luna, Noé Alcalá Ochoa, Víctor López, Alberto Aguilar, Enrique Noé-Arias, and Yasser Alayli (2013). “Flicker in a twisted nematic spatial light modulator”. In: *Optics and Lasers in Engineering* 51.6, pp. 741–748. ISSN: 0143-8166. DOI: 10.1016/j.optlaseng.2013.01.013. URL: <http://www.sciencedirect.com/science/article/pii/S0143816613000328> (visited on 12/06/2017).
- Campbell, S., S. M. F. Triphan, R. El-Agmy, A. H. Greenaway, and D. T. Reid (2007). “Direct optimization of femtosecond laser ablation using adaptive wavefront shaping”. In: *J. Opt. A* 9.11, pp. 1100–1104. ISSN: 1464-4258. URL: <http://www.iop.org/EJ/abstract/1464-4258/9/11/022> (visited on 01/20/2010).

- Cheng, Guanghua, Konstantin Mishchik, Cyril Mauchair, Eric Audouard, and Razvan Stoian (2009). “Ultrafast laser photoinscription of polarization sensitive devices in bulk silica glass”. In: *Optics express* 17.12, pp. 9515–9525.
- Cizmar, T. and Kishan Dholakia (2009). “Tunable Bessel light modes: engineering the axial propagation”. In: *Optics Express* 17.18, pp. 15558–15570. DOI: 10.1364/OE.17.015558. URL: <http://www.opticsexpress.org/abstract.cfm?URI=oe-17-18-15558> (visited on 06/02/2010).
- Colombier, Jean-Philippe, Anton Rudenko, Hao Zhang, Cyril Mauchair, Tatiana Itina, Florence Garrelie, and Razvan Stoian (2018). “Ultrafast Laser-Induced Surface and Bulk Nanostructuring: Similarities Revealed by Electromagnetic Modeling”. en. In: URL: <https://hal-ujm.archives-ouvertes.fr/ujm-02018947> (visited on 05/21/2019).
- Courvoisier, F., P.-A. Lacourt, M. Jacquot, M. K. Bhuyan, L. Furfaro, and J. M. Dudley (2009). “Surface nanoprocessing with nondiffracting femtosecond Bessel beams”. In: *Opt. Lett.* 34.20, pp. 3163–3165. DOI: 10.1364/OL.34.003163. URL: <http://ol.osa.org/abstract.cfm?URI=ol-34-20-3163> (visited on 04/13/2010).
- Cruz, A. Ruiz de la, A. Ferrer, W. Gawelda, D. Puerto, M. Galván Sosa, J. Siegel, and J. Solis (2009). “Independent control of beam astigmatism and ellipticity using a SLM for fs-laser waveguide writing”. EN. In: *Optics Express* 17.23, pp. 20853–20859. ISSN: 1094-4087. DOI: 10.1364/OE.17.020853. URL: <https://www.osapublishing.org/oe/abstract.cfm?uri=oe-17-23-20853> (visited on 01/24/2019).
- Dammann, H. and E. Klotz (1977). “Coherent Optical Generation and Inspection of Two-dimensional Periodic Structures”. In: *Optica Acta: International Journal of Optics* 24.4, pp. 505–515. ISSN: 0030-3909. DOI: 10.1080/713819570. URL: <https://doi.org/10.1080/713819570> (visited on 04/06/2019).
- Débarre, Delphine, Edward J Botcherby, Martin J Booth, and Tony Wilson (2008). “Adaptive optics for structured illumination microscopy”. In: *Optics express* 16.13, pp. 9290–9305.
- Diels, J.-C. and W. Rudolph (2006). *Ultrashort Laser Pulse Phenomenon: Fundamentals, Techniques, and Applications on a Femtosecond Time Scale*. 2nd. Academic Press Inc. ISBN: 0122154932.
- Dumas, Virginie, Alain Guignandon, Laurence Vico, Cyril Mauchair, Ximena Zapata, Marie Thérèse Linossier, Wafa Bouleftour, Julien Granier, Sylvie Peyroche, Jean-Claude Dumas, et al. (2015). “Femtosecond laser nano/micro patterning of titanium influences mesenchymal stem cell adhesion and commitment”. In: *Biomedical Materials* 10.5, p. 055002.
- Dusser, B., Z. Sagan, H. Soder, N. Faure, J.P. Colombier, M. Jourlin, and E. Audouard (2010). “Controlled nanostructures formation by ultra fast laser pulses for color marking”. In: *Opt. Express* 18.3, pp. 2913–2924. DOI: 10.1364/OE.18.002913. URL: <http://www.opticsexpress.org/abstract.cfm?URI=oe-18-3-2913> (visited on 10/21/2010).
- D’Amico, Ciro, Guanghua Cheng, Cyril Mauchair, Johann Troles, Laurent Calvez, Virginie Nazabal, Celine Caillaud, Guillermo Martin, Brahim Arezki, Etienne Lecoarer, et al. (2014). “Large-mode-area infrared guiding in ultrafast laser written waveguides in Sulfur-based chalcogenide glasses”. In: *Optics express* 22.11, pp. 13091–13101.
- Echlin, McLean P., Marcus Straw, Steven Randolph, Jorge Filevich, and Tresa M. Pollock (2015). “The TriBeam system: Femtosecond laser ablation in situ SEM”. In: *Materials Characterization* 100, pp. 1–12. ISSN: 1044-5803. DOI: 10.1016/j.matchar.2014.10.023. URL: <http://www.sciencedirect.com/science/article/pii/S104458031400326X> (visited on 04/29/2019).
- Emelyanenko, Alexandre M., Farida M. Shagieva, Alexandr G. Domantovsky, and Ludmila B. Boinovich (2015). “Nanosecond laser micro- and nanotexturing for the design of a superhydrophobic coating robust against long-term contact with water, cavitation, and

- abrasion". In: *Applied Surface Science*. ISSN: 0169-4332. DOI: 10.1016/j.apsusc.2015.01.202. URL: <http://www.sciencedirect.com/science/article/pii/S0169433215002445> (visited on 02/06/2015).
- Englert, L., B. Rethfeld, L. Haag, M. Wollenhaupt, Cristian Sarpe-Tudoran, and T. Baumert (2007). "Control of ionization processes in high band gap materials via tailored femtosecond pulses". In: *Opt. Express* 15.26, pp. 17855–17862. DOI: 10.1364/OE.15.017855. URL: <http://www.opticsexpress.org/abstract.cfm?URI=oe-15-26-17855>.
- Eriksen, René L., Paul C. Mogensen, and Jesper Glückstad (2002). "Multiple-beam optical tweezers generated by the generalized phase-contrast method". In: *Optics Letters* 27.4, pp. 267–269. DOI: 10.1364/OL.27.000267. URL: <http://ol.osa.org/abstract.cfm?URI=ol-27-4-267> (visited on 03/16/2015).
- Fung, Y. M. Eva, Frank Kjeldsen, Oleg A. Silivra, T. W. Dominic Chan, and Roman A. Zubarev (2005). "Facile Disulfide Bond Cleavage in Gaseous Peptide and Protein Cations by Ultraviolet Photodissociation at 157 nm". In: *Angewandte Chemie International Edition* 44.39, pp. 6399–6403. ISSN: 1521-3773. DOI: 10.1002/anie.200501533. URL: <https://www.onlinelibrary.wiley.com/doi/abs/10.1002/anie.200501533> (visited on 05/29/2019).
- Gain, P, C Jumelle, A Hamri, G Egaud, C Mauclair, S Reynaud, S Dumas, S Pereira, and G Thuret (2017). "Comparison of four technics of surface roughness assessment of corneal lamellar cuts". In: *Acta Ophthalmologica* 95.S259.
- Garner, William H. and Margaret H. Garner (2016). "Protein Disulfide Levels and Lens Elasticity Modulation: Applications for Presbyopia". en. In: *Investigative Ophthalmology & Visual Science* 57.6, pp. 2851–2863. ISSN: 1552-5783. DOI: 10.1167/iovs.15-18413. URL: <https://iovs.arvojournals.org/article.aspx?articleid=2526363> (visited on 05/29/2019).
- Gaunt, Alexander L. and Zoran Hadzibabic (2012). "Robust Digital Holography For Ultracold Atom Trapping". en. In: *Scientific Reports* 2, p. 721. ISSN: 2045-2322. DOI: 10.1038/srep00721. URL: <https://www.nature.com/articles/srep00721> (visited on 04/06/2019).
- Gerchberg, R. W. and W. O. Saxton (1972). "A practical algorithm for the determination of the phase from image and diffraction plane pictures". In: *Optik*, pp. 237–246. URL: http://en.wikipedia.org/wiki/Gerchberg%E2%80%93Saxton_algorithm (visited on 01/20/2010).
- Goodman, Joseph W. (2005). *Introduction To Fourier Optics*. 3rd. Roberts & Company Publishers. ISBN: 0-9747077-2-4.
- Gustafsson, Mats GL (2000). "Surpassing the lateral resolution limit by a factor of two using structured illumination microscopy". In: *Journal of microscopy* 198.2, pp. 82–87.
- (2005). "Nonlinear structured-illumination microscopy: wide-field fluorescence imaging with theoretically unlimited resolution". In: *Proceedings of the National Academy of Sciences of the United States of America* 102.37, pp. 13081–13086.
- Hahn, J., H. Kim, K. Choi, and B. Lee (2006). "Real-time digital holographic beam-shaping system with a genetic feedback tuning loop". In: *Appl. Opt.* 45.5, pp. 915–924. DOI: 10.1364/AO.45.000915. URL: <http://ao.osa.org/abstract.cfm?URI=ao-45-5-915> (visited on 02/08/2010).
- Hammouti, Sabrina, Cyril Mauclair, Alina Hamri, and Stéphane Valette (2014). "Elaboration of submicron periodic structures on polymer surfaces by femtosecond laser". In: *LPM 2014*.
- Hammouti, Sabrina, B Beaugiraud, M Salvia, Cyril Mauclair, A Pascale-Hamri, Stéphane Benayoun, and Stéphane Valette (2015a). "Elaboration of submicron structures on PEEK polymer by femtosecond laser". In: *Applied Surface Science* 327, pp. 277–287.

- Hammouti, Sabrina, A Pascale-Hamri, Nicolas Faure, B Beaugiraud, Matthieu Guibert, Cyril Mauclair, Stephane Benayoun, and S Valette (2015b). “Wear rate control of peek surfaces modified by femtosecond laser”. In: *Applied Surface Science* 357, pp. 1541–1551.
- Hasegawa, S., Y. Hayasaki, and N. Nishida (2006). “Holographic femtosecond laser processing with multiplexed phase Fresnel lenses”. In: *Opt. Lett.* 31.11, pp. 1705–1707. DOI: 10.1364/OL.31.001705. URL: <http://ol.osa.org/abstract.cfm?URI=ol-31-11-1705> (visited on 01/20/2010).
- Hasegawa, Satoshi, Haruyasu Ito, Haruyoshi Toyoda, and Yoshio Hayasaki (2016). “Massively parallel femtosecond laser processing”. EN. In: *Optics Express* 24.16, pp. 18513–18524. ISSN: 1094-4087. DOI: 10.1364/OE.24.018513. URL: <https://www.osapublishing.org/oe/abstract.cfm?uri=oe-24-16-18513> (visited on 04/10/2019).
- Hell, S.W and J. Wichmann (1994). “Breaking the diffraction resolution limit by stimulated emission: stimulated-emission-depletion fluorescence microscopy”. In: *Optics Letters* 19.11, pp. 780–782.
- Hess, S.T, T.P.K. Girirajan, and M.D. Mason (2006). “Ultra-high resolution imaging by fluorescence photoactivation localization microscopy”. In: *Biophysical Journal* 91.11, pp. 4258–4272.
- Hirano, Yasuhiro, Atsushi Matsuda, and Yasushi Hiraoka (2015). “Recent advancements in structured-illumination microscopy toward live-cell imaging”. In: *Microscopy*, dfv034.
- Houzet, Julien, Nicolas Faure, Mathieu Larochette, A-C Brulez, Stephane Benayoun, and Cyril Mauclair (2016). “Ultrafast laser spatial beam shaping based on Zernike polynomials for surface processing”. In: *Optics express* 24.6, pp. 6542–6552.
- Huot, Nicolas, Razvan Stoian, Alexandre Mermillod-Blondin, Cyril Mauclair, and Eric Audouard (2007). “Analysis of the effects of spherical aberration on ultrafast laser-induced refractive index variation in glass”. In: *Optics Express* 15.19, pp. 12395–12408.
- Jesacher, Alexander and Martin J. Booth (2010). “Parallel direct laser writing in three dimensions with spatially dependent aberration correction”. In: *Optics Express* 18.20, pp. 21090–21099. DOI: 10.1364/OE.18.021090. URL: <http://www.opticsexpress.org/abstract.cfm?URI=oe-18-20-21090> (visited on 10/13/2010).
- Jewel, A., V. Akondi, and V. Vohnsen (2013). “A direct comparison between a mems deformable mirror and a liquid crystal spatial light modulator in signal-based wavefront sensing”. In: *J. Eur. Opt. Soc, Rapid Publ. A* 8.
- Judson, Richard S. and Herschel Rabitz (1992). “Teaching lasers to control molecules”. In: *Physical Review Letters* 68.10, pp. 1500–1503. DOI: 10.1103/PhysRevLett.68.1500. URL: <https://link.aps.org/doi/10.1103/PhysRevLett.68.1500> (visited on 01/15/2019).
- Juhasz, T., F. H. Loesel, R. M. Kurtz, C. Horvath, J. F. Bille, and G. Mourou (1999). “Corneal refractive surgery with femtosecond lasers”. In: *IEEE Journal of Selected Topics in Quantum Electronics* 5.4, pp. 902–910. ISSN: 1077-260X. DOI: 10.1109/2944.796309.
- Jumelle, Clothile, Nelly Campolmi, Aurélien Bernard, Simone Piselli, Emmanuel Baubeau, Cyril Mauclair, J Granier, Gregory Egaud, P Gain, and G Thuret (2013). “Improvement of delivery of molecules into corneal endothelium using nanoparticles activated by femtosecond laser pulses”. In: *Acta Ophthalmologica* 91.s252, pp. 0–0.
- Jumelle, Clothile, Aurélien Bernard, Cyril Mauclair, N Campolmi, J Granier, Gregory Egaud, Odile Sabido, Philippe Gain, and Gilles Thuret (2014). “Femtosecond laser activated carbon nanoparticles for corneal gene therapy”. In: *LPM 2014*.
- Jumelle, Clothile, Cyril Mauclair, Julien Houzet, Aurelien Bernard, Zhiguo He, Simone Piselli, Ch Perrache, Gregory Egaud, Emmanuel Baubeau, Philippe Gain, et al. (2015a). “Pore size assessment during corneal endothelial cells permeabilization by femtosecond laser activated

- carbon nanoparticles". In: *European Conference on Biomedical Optics*. Optical Society of America, 95420W.
- Jumelle, Clothile, Cyril Mauclair, Julien Houzet, A Barnard, Zhiguo He, Simone Piselli, Ch Perrache, Philippe Gain, and Gilles Thuret (2015b). "Transfer of molecules into the endothelial cells of whole human corneas using carbon nanoparticles activated by femtosecond laser". In: *Acta Ophthalmologica* 93.
- Jumelle, Clotilde, Cyril Mauclair, Julien Houzet, Aurélien Bernard, Zhiguo He, Fabien Forest, Michel Peoc'h, Sophie Acquart, Philippe Gain, and Gilles Thuret (2015c). "Delivery of molecules into human corneal endothelial cells by carbon nanoparticles activated by femtosecond laser". In: *PloS one* 10.7, e0132023.
- Jumelle, Clotilde, Cyril Mauclair, Julien Houzet, Aurélien Bernard, Zhiguo He, Fabien Forest, Chantal Perrache, Philippe Gain, and Gilles Thuret (2016). "Delivery of macromolecules into the endothelium of whole ex vivo human cornea by femtosecond laser-activated carbon nanoparticles". In: *British Journal of Ophthalmology*, bjophthalmol–2015.
- Jumelle, Clotilde, Alina Hamri, Gregory Egaud, Cyril Mauclair, Stephanie Reynaud, Virginie Dumas, Sandrine Pereira, Thibaud Garcin, Philippe Gain, and Gilles Thuret (2017a). "Comparison of four methods of surface roughness assessment of corneal stromal bed after lamellar cutting". In: *Biomedical optics express* 8.11, pp. 4974–4986.
- (2017b). "Comparison of four methods of surface roughness assessment of corneal stromal bed after lamellar cutting". EN. In: *Biomedical Optics Express* 8.11, pp. 4974–4986. ISSN: 2156-7085. DOI: 10.1364/BOE.8.004974. URL: <https://www.osapublishing.org/boe/abstract.cfm?uri=boe-8-11-4974> (visited on 04/30/2019).
- Kaakkunen, Jarno J. J., Petri Laakso, and Veli Kujanpää (2014). "Adaptive multibeam laser cutting of thin steel sheets with fiber laser using spatial light modulator". In: *Journal of Laser Applications* 26.3, p. 032008. ISSN: 1938-1387. DOI: 10.2351/1.4883935. URL: <http://scitation.aip.org/content/lia/journal/jla/26/3/10.2351/1.4883935> (visited on 06/27/2014).
- Karl, Robert M., Giulia F. Mancini, Joshua L. Knobloch, Travis D. Frazer, Jorge N. Hernandez-Charpak, Begoña Abad, Dennis F. Gardner, Elisabeth R. Shanblatt, Michael Tanksalvala, Christina L. Porter, Charles S. Bevis, Daniel E. Adams, Henry C. Kapteyn, and Margaret M. Murnane (2018). "Full-field imaging of thermal and acoustic dynamics in an individual nanostructure using tabletop high harmonic beams". en. In: *Science Advances* 4.10, eaau4295. ISSN: 2375-2548. DOI: 10.1126/sciadv.aau4295. URL: <https://advances.sciencemag.org/content/4/10/eaau4295> (visited on 05/01/2019).
- Kerse, Can, Hamit Kalaycıoğlu, Parviz Elahi, Barbaros Çetin, Denizhan K. Kesim, Önder Akçaalan, Seydi Yavaş, Mehmet D. Aşık, Bülent Öktem, Heinar Hoogland, Ronald Holzwarth, and Fatih Ömer Ilday (2016). "Ablation-cooled material removal with ultrafast bursts of pulses". en. In: *Nature* 537.7618, pp. 84–88. ISSN: 0028-0836. DOI: 10.1038/nature18619. URL: <http://www.nature.com/nature/journal/v537/n7618/abs/nature18619.html> (visited on 05/11/2017).
- Kner, Peter, Bryant B Chhun, Eric R Griffis, Lukman Winoto, and Mats GL Gustafsson (2009). "Super-resolution video microscopy of live cells by structured illumination". In: *Nature methods* 6.5, pp. 339–342.
- König, J., S. Nolte, and A. Tünnermann (2005). "Plasma evolution during metal ablation with ultrashort laser pulses". In: *Opt. Express* 13.26, pp. 10597–10607. DOI: 10.1364/OPEX.13.010597. URL: <http://www.opticsexpress.org/abstract.cfm?URI=oe-13-26-10597>.
- Kuang, Zheng, Dun Liu, Walter Perrie, Stuart Edwardson, Martin Sharp, Eamonn Fearon, Geoff Dearden, and Ken Watkins (2009). "Fast parallel diffractive multi-beam femtosecond laser surface micro-structuring". In: *Applied Surface Science* 255.13–14, pp. 6582–6588. ISSN:

- 0169-4332. DOI: 10.1016/j.apsusc.2009.02.043. URL: <http://www.sciencedirect.com/science/article/pii/S0169433209001974> (visited on 05/29/2014).
- Kuang, Zheng, Jiangning Li, Stuart Edwardson, Walter Perrie, Dun Liu, and Geoff Dearden (2015). “Ultrafast laser beam shaping for material processing at imaging plane by geometric masks using a spatial light modulator”. In: *Optics and Lasers in Engineering* 70, pp. 1–5. ISSN: 0143-8166. DOI: 10.1016/j.optlaseng.2015.02.004. URL: <http://www.sciencedirect.com/science/article/pii/S0143816615000172> (visited on 04/06/2019).
- Lehr, Jorge and Anne-Marie Kietzig (2014). “Production of homogenous micro-structures by femtosecond laser micro-machining”. In: *Optics and Lasers in Engineering* 57, pp. 121–129. ISSN: 0143-8166. DOI: 10.1016/j.optlaseng.2014.01.012. URL: <http://www.sciencedirect.com/science/article/pii/S014381661400013X> (visited on 06/02/2015).
- Leonardo, Roberto Di, Francesca Ianni, and Giancarlo Ruocco (2007). “Computer generation of optimal holograms for optical trap arrays”. EN. In: *Optics Express* 15.4, pp. 1913–1922. ISSN: 1094-4087. DOI: 10.1364/OE.15.001913. URL: <https://www.osapublishing.org/oe/abstract.cfm?uri=oe-15-4-1913> (visited on 04/06/2019).
- Li, Chen, Guanghua Cheng, Xxx Sedao, Wei Zhang, Hao Zhang, Nicolas Faure, Damien Jamon, Jean-Philippe Colombier, and Razvan Stoian (2016). “Scattering effects and high-spatial-frequency nanostructures on ultrafast laser irradiated surfaces of zirconium metallic alloys with nano-scaled topographies”. In: *Opt. Express, OE* 24.11, pp. 11558–11568.
- Li, Jiangning, Yue Tang, Zheng Kuang, Joerg Schille, Udo Loeschner, Walter Perrie, Dun Liu, Geoff Dearden, and Stuart Edwardson (2019). “Multi imaging-based beam shaping for ultrafast laser-material processing using spatial light modulators”. In: *Optics and Lasers in Engineering* 112, pp. 59–67. ISSN: 0143-8166. DOI: 10.1016/j.optlaseng.2018.09.002. URL: <http://www.sciencedirect.com/science/article/pii/S0143816618307115> (visited on 03/25/2019).
- Liesener, J., M. Reicherter, T. Haist, and H. J. Tiziani (2000). “Multi-functional optical tweezers using computer-generated holograms”. In: *Optics Communications* 185.1, pp. 77–82. ISSN: 0030-4018. DOI: 10.1016/S0030-4018(00)00990-1. URL: <http://www.sciencedirect.com/science/article/pii/S0030401800009901> (visited on 04/06/2019).
- Lim, Daryl, Tim N Ford, Kengyeh K Chu, and Jerome Mertz (2011). “Optically sectioned in vivo imaging with speckle illumination HiLo microscopy”. In: *Journal of biomedical optics* 16.1, pp. 016014–016014.
- Loeschner, Udo, Joerg Schille, Andre Streek, Tommy Knebel, Lars Hartwig, Robert Hillmann, and Christian Endisch (2015). “High-rate laser microprocessing using a polygon scanner system”. In: *Journal of Laser Applications* 27.S2, pp. –. DOI: <http://dx.doi.org/10.2351/1.4906473>. URL: <http://scitation.aip.org/content/lia/journal/jla/27/S2/10.2351/1.4906473>.
- Loor, R. De (2013). “Polygon Scanner System for Ultra Short Pulsed Laser Micro-Machining Applications”. In: *Physics Procedia* 41. Lasers in Manufacturing (LiM 2013), pp. 544–551.
- Lubatschowski, Holger, Silvia Schumacher, Michael Fromm, Alfred Wegener, Heike Hoffmann, Uwe Oberheide, and Georg Gerten (2010). “Femtosecond lentotomy: generating gliding planes inside the crystalline lens to regain accommodation ability”. en. In: *Journal of Biophotonics* 3.5-6, pp. 265–268. ISSN: 1864-0648. DOI: 10.1002/jbio.201000013. URL: <https://onlinelibrary.wiley.com/doi/abs/10.1002/jbio.201000013> (visited on 04/04/2019).
- Malitson, I. H. (1965). “Interspecimen Comparison of the Refractive Index of Fused Silica”. In: *J. Opt. Soc. Am.* 55.10, pp. 1205–1208. DOI: 10.1364/JOSA.55.001205. URL: <http://www.opticsinfobase.org/abstract.cfm?URI=josa-55-10-1205>.

- Mathis, Amaury, Luc Froehly, Luca Furfaro, Maxime Jacquot, John Michael Dudley, and François Courvoisier (2013). “Direct machining of curved trenches in silicon with femtosecond accelerating beams”. In: *Jour. of European Optical Society* 8, p. 13019.
- Mauclair, C., G. Cheng, N. Huot, E. Audouard, A. Rosenfeld, I. Hertel, and R. Stoian (2009a). “Dynamic ultrafast laser beam tailoring for multispot photo-inscription of photonic devices in bulk transparent materials”. In: *Proc. SPIE* 7205, pp. 720512–720512–10. DOI: 10.1117/12.808798. URL: <http://dx.doi.org/10.1117/12.808798>.
- Mauclair, C., S. Landon, D. Pietroy, E. Baubeau, R. Stoian, and E. Audouard (2013). “Ultrafast Laser Machining of Micro Grooves on Stainless Steel with Spatially Optimized Intensity Distribution”. In: *JOURNAL OF LASER MICRO NANOENGINEERING* 8.1, 11–14. ISSN: 1880-0688. DOI: {10.2961/jlmm.2013.01.0003}.
- Mauclair, C, S Landon, D Pietroy, E Baubeau, R Stoian, and E Audouard (2013a). “Ultrafast laser machining of micro grooves on stainless steel with spatially optimized intensity distribution”. In: *Journal of Laser Micro Nanoengineering* 8.1, p. 11.
- Mauclair, Cyril (2010). “Spatio-temporal ultrafast laser tailoring for bulk functionalization of transparent materials”. PhD thesis. Saint Etienne.
- (2014). “Ultrafast laser beam tailoring for efficient surface and bulk processing”. In: *Laser and Focused Ion Beam (LFIB) technologies for photonics collocated with the Euro-Asian conference on Integrated and Micro optics, namely, the European Conference on Integrated Optics (ECIO 17th) and the Asian MicroOptics Conference (MOC 19th)*.
- Mauclair, Cyril, Hélène Desrus, and Dorian Saint-Pierre (2017). “Advances in spatial beam shaping for ultrafast laser surface functionalization”. In: *Laser In Manufacturing 2017*.
- Mauclair, Cyril, Nicolas Faure, and Julien Houzet (2016). “Towards top-hat spatial shaping of ultrafast laser beam based on Zernike polynomials”. In: *Laser Sources and Applications III*. Vol. 9893. International Society for Optics and Photonics, p. 989312.
- Mauclair, Cyril and Julien Houzet (2016). “Ultrafast laser spatial beam shaping using an optically addressed liquid crystal optical valve”. In: *Nice Optics*, p2.
- Mauclair, Cyril, Alexandre Mermillod-Blondin, Nicolas Huot, Eric Audouard, and Razvan Stoian (2008). “Ultrafast laser writing of homogeneous longitudinal waveguides in glasses using dynamic wavefront correction”. In: *Optics express* 16.8, pp. 5481–5492.
- Mauclair, Cyril, Razvan Stoian, Jörn Bonse, Alexandre Mermillod-Blondin, Arkadi Rosenfeld, and Ingolf V Hertel (2009b). “Direct time resolved observation of energy deposition by ultrashort laser pulses in fused silica”. In: *Proc. LAMP the 5th International Congress on Laser Advanced Materials Processing.(2009)*.
- Mauclair, Cyril, Guanghua Cheng, Nicolas Huot, Eric Audouard, Arkadi Rosenfeld, Ingolf V Hertel, and Razvan Stoian (2009c). “Dynamic ultrafast laser spatial tailoring for parallel micromachining of photonic devices in transparent materials”. In: *Optics express* 17.5, pp. 3531–3542.
- Mauclair, Cyril, Konstantin Mishchik, Alexandre Mermillod-Blondin, Jörn Bonse, Arkadi Rosenfeld, Ingolf V Hertel, Eric Audouard, and Razvan Stoian (2010). “Time-resolved observation of energy deposition in fused silica by ultrashort laser pulses in single and cumulative regime”. In: *Lasers and Electro-Optics (CLEO) and Quantum Electronics and Laser Science Conference (QELS), 2010 Conference on*. IEEE, pp. 1–2.
- Mauclair, Cyril, Alexandre Mermillod-Blondin, Arkadi Rosenfeld, Ingolf V Hertel, Eric Audouard, Isamu Miyamoto, and Razvan Stoian (2011a). “Multipoint Focusing of Single Ultrafast Laser Pulses.” In: *Journal of Laser Micro/Nanoengineering* 6.3.
- Mauclair, Cyril, Konstantin Mishchik, Alexandre Mermillod-Blondin, Arkadi Rosenfeld, Ingolf-Volker Hertel, Eric Audouard, and Razvan Stoian (2011b). “Optimization of the energy

- deposition in glasses with temporally-shaped femtosecond laser pulses”. In: *Physics Procedia* 12, pp. 76–81.
- Mauclair, Cyril, Alexandre Mermillod-Blondin, S Landon, N Huot, Arkadi Rosenfeld, Ingolf Volker Hertel, E Audouard, I Myiamoto, and Razvan Stoian (2011c). “Single-pulse ultrafast laser imprinting of axial dot arrays in bulk glasses”. In: *Optics letters* 36.3, pp. 325–327.
- Mauclair, Cyril, Marian Zamfirescu, Jean-Philippe Colombier, Guanghua Cheng, Konstantin Mishchik, Eric Audouard, and Razvan Stoian (2012a). “Control of ultrafast laser-induced bulk nanogratings in fused silica via pulse time envelopes”. In: *Optics express* 20.12, pp. 12997–13005.
- Mauclair, Cyril, Sébastien Landon, David Pietroy, Emmanuel Baubeau, Razvan Stoian, and Eric Audouard (2012b). “Ultrafast Laser Machining of Micro Grooves in Metals with Spatially Optimized Intensity Distribution”. In: *The 13th international conference on laser precision microfabrication*, p85.
- Mauclair, Cyril, David Pietroy, Emmanuel Baubeau, Razvan Stoian, and Eric Audouard (2013b). “Spatial shaping of femtosecond laser beam for high speed multi-scale surface structuring of materials”. In: *The 6th International Congress on Laser Advanced Materials Processing LAMP2013 July 23-26, 2013 Toki Messe, Niigata, Japan*.
- Mauclair, Cyril, David Pietroy, Emmanuel Baubeau, and Razvan Stoian (2014). “Distortion of the intensity profile at the processing image plane of a focused femtosecond laser beam”. In: *LPM 2014*.
- Mauclair, Cyril, Alberto Aguilar, J-P Colombier, Razvan Stoian, and Abundio Davila (2015a). “In-Situ Observation of Ultrafast Laser Induced Periodic Surface Structures on Metals by Optical Microscopy”. In: *The European Conference on Lasers and Electro-Optics*. Optical Society of America, CM_2_4.
- Mauclair, Cyril, David Pietroy, Yoan Di Maïo, Emmanuel Baubeau, Jean-Philippe Colombier, Razvan Stoian, and Florent Pigeon (2015b). “Ultrafast laser micro-cutting of stainless steel and {PZT} using a modulated line of multiple foci formed by spatial beam shaping”. In: *Optics and Lasers in Engineering* 67.0, pp. 212 –217. ISSN: 0143-8166. DOI: <http://dx.doi.org/10.1016/j.optlaseng.2014.11.018>. URL: <http://www.sciencedirect.com/science/article/pii/S0143816614002905>.
- Mauclair, Cyril, David Pietroy, Yoan Di Maio, Emmanuel Baubeau, Jean-Philippe Colombier, Razvan Stoian, and Florent Pigeon (2015c). “Ultrafast laser micro-cutting of stainless steel and PZT using a modulated line of multiple foci formed by spatial beam shaping”. In: *Optics and Lasers in Engineering* 67, pp. 212–217.
- Mauclair, Cyril, Alexandre Mermillod-Blondin, K Mishchik, Jörn Bonse, Arkadi Rosenfeld, Jean-Philippe Colombier, and Razvan Stoian (2016). “Excitation and relaxation dynamics in ultrafast laser irradiated optical glasses”. In: *High Power Laser Science and Engineering* 4.
- Mermillod-Blondin, A., I. M. Burakov, Yu. P. Meshcheryakov, N. M. Bulgakova, E. Audouard, A. Rosenfeld, A. Husakou, I. V. Hertel, and R. Stoian (2008a). “Flipping the sign of refractive index changes in ultrafast and temporally shaped laser-irradiated borosilicate crown optical glass at high repetition rates”. In: *Phys. Rev. B* 77.10, p. 104205. DOI: 10.1103/PhysRevB.77.104205. URL: <http://link.aps.org/doi/10.1103/PhysRevB.77.104205> (visited on 02/08/2010).
- Mermillod-Blondin, Alexandre, Cyril Mauclair, Arkadi Rosenfeld, Jörn Bonse, Ingolf V Hertel, Eric Audouard, and Razvan Stoian (2008b). “Size correction in ultrafast laser processing of fused silica by temporal pulse shaping”. In: *Applied Physics Letters* 93.2, p. 021921.
- Mermillod-Blondin, Alexandre, Cyril Mauclair, A Rosenfeld, Jörn Bonse, Razvan Stoian, and Eric Audouard (2011a). “Time-resolved imaging of bulk a-SiO₂ upon various ultrashort

- excitation sequences”. In: *Frontiers in Ultrafast Optics: Biomedical, Scientific, and Industrial Applications XI*. Vol. 7925. International Society for Optics and Photonics, 79250R.
- Mermillod-Blondin, Alexandre, Cyril Mauclair, Jörn Bonse, Razvan Stoian, Eric Audouard, Arkadi Rosenfeld, and Ingolf V Hertel (2011b). “Time-resolved imaging of laser-induced refractive index changes in transparent media”. In: *Review of Scientific Instruments* 82.3, p. 033703.
- Mikhaylov, Dmitriy, Baifan Zhou, Thomas Kiedrowski, Ralf Mikut, and Andrés F. Lasagni (2019). “Machine learning aided phase retrieval algorithm for beam splitting with an LCoS-SLM”. In: *Laser Resonators, Microresonators, and Beam Control XXI*. Vol. 10904. International Society for Optics and Photonics, p. 109041M. DOI: 10.1117/12.2508673. URL: <https://www.spiedigitallibrary.org/conference-proceedings-of-spie/10904/109041M/Machine-learning-aided-phase-retrieval-algorithm-for-beam-splitting-with/10.1117/12.2508673.short> (visited on 05/01/2019).
- Mishchik, Konstantin, Guanghua Cheng, G Huo, Igor M Burakov, Cyril Mauclair, Alexandre Mermillod-Blondin, Arkadi Rosenfeld, Youcef Ouerdane, Aziz Boukenter, Olivier Parriaux, et al. (2010a). “Nanosize structural modifications with polarization functions in ultrafast laser irradiated bulk fused silica”. In: *Optics express* 18.24, pp. 24809–24824.
- Mishchik, Konstantin, Guanghua Cheng, Cyril Mauclair, Eric Audouard, Aziz Boukenter, Youcef Ouerdane, and Razvan Stoian (2010b). “Ultrafast Laser Photoinscription of Polarization Sensitive Devices in Bulk Silica Glass”. In: *Bragg Gratings, Photosensitivity, and Poling in Glass Waveguides*. Optical Society of America, BThD1.
- Mishchik, Konstantin, Cyril Mauclair, Guanghua Cheng, Youcef Ouerdane, Aziz Boukenter, and Razvan Stoian (2011). “Structural modifications in bulk fused silica after interaction with ultrashort laser pulses”. In: *Advanced Laser Technologies*.
- Mishchik, Konstantin, Andres Ferrer, A Ruiz de la Cruz, Alexandre Mermillod-Blondin, Cyril Mauclair, Youcef Ouerdane, Aziz Boukenter, Javier Solis, and Razvan Stoian (2013a). “Photoinscription domains for ultrafast laser writing of refractive index changes in BK7 borosilicate crown optical glass”. In: *Optical Materials Express* 3.1, pp. 67–85.
- Mishchik, Konstantin, Ciro D’Amico, Praveen Kumar Velpula, Cyril Mauclair, Aziz Boukenter, Youcef Ouerdane, and Razvan Stoian (2013b). “Ultrafast laser induced electronic and structural modifications in bulk fused silica”. In: *Journal of Applied Physics* 114.13, p. 133502.
- Miyamoto, I., A. Horn, J. Gottmann, D. Workmann, and F. Yoshino (2007). “Fusion welding of glass using femtosecond laser pulses with high-repetition rates”. In: *J. Laser Micro / Nanoeng.* 2.1, pp. 57–63.
- Montgomery, P C and A Leong-Hoi (2015). “Emerging optical nanoscopy techniques”. In: *Journal of Nanotechnology, Science and Applications* 8, pp. 31–44.
- Mourier, L., D. Mazuyer, A. A. Lubrecht, C. Donnet, and E. Audouard (2008). “Action of a femtosecond laser generated micro-cavity passing through a circular EHL contact”. In: *Wear*. 10th International Conference on Metrology and Properties of Engineering Surfaces 264.5–6, pp. 450–456. ISSN: 0043-1648. DOI: 10.1016/j.wear.2006.08.037. URL: <http://www.sciencedirect.com/science/article/pii/S0043164807001822> (visited on 07/09/2015).
- Mudry, Emeric, Kamal Belkebir, J Girard, Julien Savatier, E Le Moal, C Nicoletti, Marc Allain, and Anne Sentenac (2012). “Structured illumination microscopy using unknown speckle patterns”. In: *Nature Photonics* 6.5, pp. 312–315.
- Neuenschwander, B., B. Jaeggi, M. Schmid, and G. Hennig (2014). “Surface Structuring with Ultra-short Laser Pulses: Basics, Limitations and Needs for High Throughput”. In: *Physics Procedia* 56, pp. 1047–1058. DOI: 10.1016/j.phpro.2014.08.017. URL: <http://www.sciencedirect.com/science/article/pii/S187538921400162X>.

- Palima, Darwin and Jesper Glückstad (2008). “Gaussian to uniform intensity shaper based on generalized phase contrast”. en. In: *Optics Express* 16.3, p. 1507. ISSN: 1094-4087. DOI: 10.1364/OE.16.001507. URL: <http://www.opticsinfobase.org/abstract.cfm?URI=oe-16-3-1507> (visited on 03/16/2015).
- Parry, Jonathan P., Rainer J. Beck, Jonathan D. Shephard, and Duncan P. Hand (2011). “Application of a liquid crystal spatial light modulator to laser marking”. EN. In: *Applied Optics* 50.12, pp. 1779–1785. ISSN: 1539-4522. DOI: 10.1364/AO.50.001779. URL: <http://www.osapublishing.org/abstract.cfm?uri=ao-50-12-1779> (visited on 07/09/2015).
- Pietroy, David, Emmanuel Baubeau, Nicolas Faure, and Cyril Mauclair (2015). “Intensity profile distortion at the processing image plane of a focused femtosecond laser below the critical power: analysis and counteraction”. In: *Optics and Lasers in Engineering* 66, pp. 138–143.
- Planchon, Thomas A., Liang Gao, Daniel E. Milkie, Michael W. Davidson, James A. Galbraith, Catherine G. Galbraith, and Eric Betzig (2011). “Rapid three-dimensional isotropic imaging of living cells using Bessel beam plane illumination”. en. In: *Nature Methods* 8.5, pp. 417–423. ISSN: 1548-7105. DOI: 10.1038/nmeth.1586. URL: <https://www.nature.com/articles/nmeth.1586> (visited on 04/23/2019).
- Popescu, G., T. Ikeda, R. R. Dasari, and M. S. Feld (2006). “Diffraction phase microscopy for quantifying cell structure and dynamics”. In: *Opt. Lett.* 31.6, pp. 775–777. DOI: 10.1364/OL.31.000775. URL: <http://ol.osa.org/abstract.cfm?URI=ol-31-6-775> (visited on 03/31/2010).
- Raimbault, Ophélie, Stephane Benayoun, Karine Anselme, Cyril Mauclair, Tatiana Bourgade, Anne-Marie Kietzig, Pierre-Luc Girard-Lauriault, Stephane Valette, and Christophe Donnet (2016). “The effects of femtosecond laser-textured Ti-6Al-4V on wettability and cell response”. In: *Materials Science and Engineering: C* 69, pp. 311–320.
- Rebollar, Esther, Daniel R. Rueda, Ignacio Martín-Fabiani, Álvaro Rodríguez-Rodríguez, Mari-Cruz García-Gutiérrez, Giuseppe Portale, Marta Castillejo, and Tiberio A. Ezquerro (2015). “In Situ Monitoring of Laser-Induced Periodic Surface Structures Formation on Polymer Films by Grazing Incidence Small-Angle X-ray Scattering”. In: *Langmuir* 31.13, pp. 3973–3981. ISSN: 0743-7463. DOI: 10.1021/acs.langmuir.5b00285. URL: <https://doi.org/10.1021/acs.langmuir.5b00285> (visited on 04/29/2019).
- Rego, E Hesper and Lin Shao (2015). “Practical structured illumination microscopy”. In: *Advanced Fluorescence Microscopy: Methods and Protocols*, pp. 175–192.
- Rego, E Hesper, Lin Shao, John J Macklin, Lukman Winoto, Göran A Johansson, Nicholas Kamps-Hughes, Michael W Davidson, and Mats GL Gustafsson (2012). “Nonlinear structured-illumination microscopy with a photoswitchable protein reveals cellular structures at 50-nm resolution”. In: *Proceedings of the National Academy of Sciences* 109.3, E135–E143.
- Rodrigo, José A., Tatiana Alieva, Eugeny Abramochkin, and Izan Castro (2013). “Shaping of light beams along curves in three dimensions”. EN. In: *Optics Express* 21.18, pp. 20544–20555. ISSN: 1094-4087. DOI: 10.1364/OE.21.020544. URL: <https://www.osapublishing.org/oe/abstract.cfm?uri=oe-21-18-20544> (visited on 04/23/2019).
- Rudenko, A., C. Mauclair, F. Garrelie, R. Stoian, and J. P. Colombier (2019a). “Light absorption by surface nanoholes and nanobumps”. In: *Applied Surface Science* 470, pp. 228–233. ISSN: 0169-4332. DOI: 10.1016/j.apsusc.2018.11.111. URL: <http://www.sciencedirect.com/science/article/pii/S0169433218331908> (visited on 05/21/2019).
- Rudenko, Anton, Cyril Mauclair, Florence Garrelie, Razvan Stoian, and Jean-Philippe Colombier (2019b). “Multipulse dynamics of ultrashort laser interaction with metal targets by coupled electromagnetic and hydrodynamic simulations (Conference Presentation)”. In: *Laser-based Micro- and Nanoprocessing XIII*. Vol. 10906. International Society for Optics and Photonics, 109060B. DOI: 10.1117/12.2507222. URL: <https://www.spiedigitallibrary.org/>

org/conference-proceedings-of-spie/10906/109060B/Multipulse-dynamics-of-ultrashort-laser-interaction-with-metal-targets-by/10.1117/12.2507222.short (visited on 05/21/2019).

- Rudenko, Anton, Cyril Mauclair, Florence Garrelie, Razvan Stoian, and Jean-Philippe Colombier (2019c). “Self-organization of surfaces on the nanoscale by topography-mediated selection of quasi-cylindrical and plasmonic waves”. In: *Nanophotonics* 8.3, pp. 459–465. ISSN: 2192-8614. DOI: 10.1515/nanoph-2018-0206. URL: <https://www.degruyter.com/view/j/nanoph.ahead-of-print/nanoph-2018-0206/nanoph-2018-0206.xml> (visited on 05/21/2019).
- Rust, M.J, M. Bates, and X. Zhuang (2006). “Sub-diffraction-limit imaging by stochastic optical reconstruction microscopy (STORM)”. In: *Nature Methods* 3.10, pp. 793–796.
- Rußbüldt, Peter, Torsten Mans, Martin Hermans, Dieter Hoffmann, and Dirk Wortmann (2010). “Powerscaling of Ultrafast Lasers”. en. In: *Laser Technik Journal* 7.2, pp. 41–44. ISSN: 1863-9119. DOI: 10.1002/latj.201090024. URL: <http://onlinelibrary.wiley.com/doi/10.1002/latj.201090024/abstract> (visited on 09/29/2015).
- Römer, G.R.B.E. and P. Bechtold (2014). “Electro-optic and Acousto-optic Laser Beam Scanners”. In: *Physics Procedia* 56. 8th International Conference on Laser Assisted Net Shape Engineering {LANE} 2014, pp. 29–39. ISSN: 1875-3892. DOI: <http://dx.doi.org/10.1016/j.phpro.2014.08.092>. URL: <http://www.sciencedirect.com/science/article/pii/S1875389214002375>.
- Saint-Pierre, Dorian, Julien Granier, Gregory Egaud, Emmanuel Baubeau, and Cyril Mauclair (2016). “Fast uniform micro structuring of DLC surfaces using multiple ultrashort laser spots through spatial beam shaping”. In: *Physics Procedia* 83, pp. 1178–1183.
- Sanner, Nicolas, Nicolas Huot, Eric Audouard, Christian Larat, Jean-Pierre Huignard, and Brigitte Loiseaux (2005). “Programmable focal spot shaping of amplified femtosecond laser pulses”. In: *Opt. Lett.* 30.12, pp. 1479–1481. DOI: 10.1364/OL.30.001479. URL: <http://ol.osa.org/abstract.cfm?URI=ol-30-12-1479>.
- Saxena, Manish, Gangadhar Eluru, and Sai Siva Gorthi (2015). “Structured illumination microscopy”. In: *Advances in Optics and Photonics* 7.2, pp. 241–275.
- Schade, M., O. Varlamova, J. Reif, H. Blumtritt, W. Erfurth, and H. S. Leipner (2010). “High-resolution investigations of ripple structures formed by femtosecond laser irradiation of silicon”. en. In: *Analytical and Bioanalytical Chemistry* 396.5, pp. 1905–1911. ISSN: 1618-2650. DOI: 10.1007/s00216-009-3342-3. URL: <https://doi.org/10.1007/s00216-009-3342-3> (visited on 04/30/2019).
- Schroers, Jan, Tranquoc Nguyen, Sean O’Keefe, and Amish Desai (2007). “Thermoplastic forming of bulk metallic glass—Applications for MEMS and microstructure fabrication”. In: *Mater. Sci. Eng. A-Struct.* Proceedings of the 12th International Conference on Rapidly Quenched & Metastable Materials 449–451, pp. 898–902. ISSN: 0921-5093.
- Sedao, X., M. Lenci, A. Rudenko, N. Faure, A. Pascale-Hamri, J. P. Colombier, and C. Mauclair (2019). “Influence of pulse repetition rate on morphology and material removal rate of ultrafast laser ablated metallic surfaces”. In: *Optics and Lasers in Engineering* 116, pp. 68–74. ISSN: 0143-8166. DOI: 10.1016/j.optlaseng.2018.12.009. URL: <http://www.sciencedirect.com/science/article/pii/S0143816618312855> (visited on 04/03/2019).
- Sedao, Xxx, Matthieu Lenci, Anton Rudenko, Alina Pascale-Hamri, Jean-Philippe Colombier, and Cyril Mauclair (2018). “Additive and Subtractive Surface Structuring by Femtosecond Laser Induced Material Ejection and Redistribution”. en. In: *Materials* 11.12, p. 2456. DOI: 10.3390/ma11122456. URL: <https://www.mdpi.com/1996-1944/11/12/2456> (visited on 02/04/2019).

- Shimotsuma, Yasuhiko, Masaaki Sakakura, Peter G Kazansky, Martynas Beresna, Jiarong Qiu, Kiyotaka Miura, and Kazuyuki Hirao (2010). “Ultrafast Manipulation of Self-Assembled Form Birefringence in Glass”. In: *Advanced materials* 22.36, pp. 4039–4043.
- Siders, C. W., A. Cavalleri, K. Sokolowski-Tinten, Cs Tóth, T. Guo, M. Kammler, M. Horn von Hoegen, K. R. Wilson, D. von der Linde, and C. P. J. Barty (1999). “Detection of Nonthermal Melting by Ultrafast X-ray Diffraction”. en. In: *Science* 286.5443, pp. 1340–1342. ISSN: 0036-8075, 1095-9203. DOI: 10.1126/science.286.5443.1340. URL: <https://science.sciencemag.org/content/286/5443/1340> (visited on 05/01/2019).
- Siegman, A. E. (1990). *Lasers*. 2nd. University Science Books, U.S. ISBN: 0935702113.
- Silvennoinen, Martti, Jarno Kaakkunen, Kimmo Paivasaari, and Pasi Vahimaa (2014). “Parallel femtosecond laser ablation with individually controlled intensity”. In: *Optics Express* 22.3, pp. 2603–2608. DOI: 10.1364/OE.22.002603. URL: <http://www.opticsexpress.org/abstract.cfm?URI=oe-22-3-2603> (visited on 05/28/2014).
- Sinclair, Gavin, Jonathan Leach, Pamela Jordan, Graham Gibson, Eric Yao, Zsolt John Laczik, Miles J. Padgett, and Johannes Courtial (2004). “Interactive application in holographic optical tweezers of a multi-plane Gerchberg-Saxton algorithm for three-dimensional light shaping”. EN. In: *Optics Express* 12.8, pp. 1665–1670. ISSN: 1094-4087. DOI: 10.1364/OPEX.12.001665. URL: <https://www.osapublishing.org/oe/abstract.cfm?uri=oe-12-8-1665> (visited on 05/29/2018).
- Sonnen, Katharina F, Lothar Schermelleh, Heinrich Leonhardt, and Erich A Nigg (2012). “3D-structured illumination microscopy provides novel insight into architecture of human centrosomes”. In: *Biology open*, BIO20122337.
- STOIAN, Razvan and Cyril MAUCLAIR (2018). *Photoinscription par laser à impulsions ultrabrèves pour des systèmes optiques 3D*. fr. Text. URL: <https://www.techniques-ingenieur.fr/base-documentaire/electronique-photonique-th13/materiaux-pour-l-optique-42450210/photoinscription-par-laser-a-impulsions-ultrabreves-pour-des-systemes-optiques-3d-e6312/> (visited on 05/21/2019).
- Stoian, Razvan, Alexandre Mermillod-Blondin, Cyril Mauclair, Nicolas Huot, Eric Audouard, Igor M Burakov, Nadezhda M Bulgakova, YP Mescheryakov, Arkadi Rosenfeld, Anton Husakou, et al. (2008). “Designing laser-induced refractive index changes in “thermal” glasses”. In: *High-Power Laser Ablation VII*. Vol. 7005. International Society for Optics and Photonics, p. 700518.
- Stoian, Razvan, Alexandre Mermillod-Blondin, Cyril Mauclair, Guanghua Cheng, Konstantin Mishchik, Arkadi Rosenfeld, Nadezhda M Bulgakova, Yuri Meshcheryakov, and Ingolf V Hertel (2009a). “Adaptive spatio-temporal techniques for smart ultrafast laser processing of optical glasses”. In: *The International Congress on Applications of Lasers & Electro-Optics, ICALEO 2009 ICALEO Proceedings*.
- Stoian, Razvan, Alexandre Mermillod-Blondin, Cyril Mauclair, Nicolas Huot, Eric Audouard, Igor M Burakov, Nadezhda M Bulgakova, Yuryi P Mescheryakov, Arkadi Rosenfeld, and Ingolf V Hertel (2009b). “Optimizing laser-induced refractive index changes in “thermal” glasses”. In: *Ultrafast Phenomena XVI*. Springer, Berlin, Heidelberg, pp. 970–972.
- Stoian, Razvan, Cyril Mauclair, Alexandre Mermillod-Blondin, Nicolas Huot, Eric Audouard, Jörn Bonse, Arkadi Rosenfeld, and Ingolf V Hertel (2009c). “Size corrections during ultrafast laser induced refractive index changes in bulk transparent materials”. In: *Jour. Las. Micro. Nano*. 2, n1.
- Stoian, Razvan, G Cheng, C Mauclair, A Mermillod-Blondin, K Mishchik, E Audouard, A Rosenfeld, and IV Hertel (2011). “3D adaptive spatio-temporal control of laser-induced refractive index changes in optical glasses”. In: *Laser-based Micro-and Nanopackaging and Assembly V*. Vol. 7921. International Society for Optics and Photonics, 79210H.

- Stoian, Razvan, Konstantin Mishchik, Cyril Maclair, Jean-Philippe Colombier, Marian Zamfirescu, and Guanghua Cheng (2012). “Investigation and control of ultrafast laser-induced nanoscale patterns in bulk dielectric materials”. In: *Advanced Laser Technologies ALT*.
- (2013a). “Control of ultrafast laser-induced nanopatterns in bulk silica glass”. In: *EUROMAT 2013*.
- Stoian, Razvan, Konstantin Mishchik, Guanghua Cheng, Cyril Maclair, Ciro D’Amico, Jean-Philippe Colombier, and Marian Zamfirescu (2013b). “Investigation and control of ultrafast laser-induced isotropic and anisotropic nanoscale-modulated index patterns in bulk fused silica”. In: *Optical Materials Express* 3.10, pp. 1755–1768.
- Stoian, Razvan, Konstantin Mishchik, Guanghua Cheng, M Zamfirescu, C Maclair, and C d’Amico (2013c). “Investigation and Control of Ultrafast Laser-Induced Nanoscale Patterns in Bulk Fused Silica”. In: *MATEC Web of Conferences*. Vol. 8. EDP Sciences, p. 03007.
- Stoian, Razvan, Konstantin Mishchik, Cyril Maclair, Praveen K Velpula, Manoj Bhuyan, Jean-Philippe Colombier, Ciro D’Amico, Marian Zamfirescu, and Guanghua Cheng (2014a). “Control of Ultrafast Laser Nanostructuring of Glasses using Temporal and Spatial Pulse Design”. In: *Bragg Gratings, Photosensitivity, and Poling in Glass Waveguides*. Optical Society of America, BW2D–6.
- Stoian, Razvan, Jean-Philippe Colombier, Cyril Maclair, Guanghua Cheng, MK Bhuyan, PK Velpula, and P Srisungsthisunti (2014b). “Spatial and temporal laser pulse design for material processing on ultrafast scales”. In: *Applied Physics A* 114.1, pp. 119–127.
- Takeda, Mitsuo, Hideki Ina, and Seiji Kobayashi (1982). “Fourier-transform method of fringe-pattern analysis for computer-based topography and interferometry”. In: *JosA* 72.1, pp. 156–160.
- Taylor, R., C. Hnatovsky, and E. Simova (2008). “Applications of femtosecond laser induced self-organized planar nanocracks inside fused silica glass”. en. In: *Laser & Photonics Reviews* 2.1-2, pp. 26–46. ISSN: 1863-8899. DOI: 10.1002/lpor.200710031. URL: <http://onlinelibrary.wiley.com/doi/10.1002/lpor.200710031/abstract> (visited on 12/15/2014).
- Tkaczyk, Tomasz S (2010). *Field guide to microscopy*. SPIE Press, Beillingham.
- Torres-Peiró, S., J. González-Ausejo, O. Mendoza-Yero, G. Mínguez-Vega, P. Andrés, and J. Lancis (2013). “Parallel laser micromachining based on diffractive optical elements with dispersion compensated femtosecond pulses”. EN. In: *Optics Express* 21.26, pp. 31830–31836. ISSN: 1094-4087. DOI: 10.1364/OE.21.031830. URL: <https://www.osapublishing.org/oe/abstract.cfm?uri=oe-21-26-31830> (visited on 04/01/2019).
- Varlamov, S., M. Bestehorn, O. Varlamova, and J. Reif (2009). “The laser polarization as control parameter in the pattern formation”. In: Preprint at <https://arxiv.org/abs/0902.4374>.
- Velpula, PK, MK Bhuyan, C Maclair, JP Colombier, and R Stoian (2014a). “Ultrafast imaging of free carriers: controlled excitation with chirped ultrafast laser Bessel beams”. In: *Laser Applications in Microelectronic and Optoelectronic Manufacturing (LAMOM) XIX*. Vol. 8967. International Society for Optics and Photonics, p. 896711.
- Velpula, Praveen Kumar, Manoj Bhuyan, Cyril Maclair, Jean-Philippe Colombier, and Razvan Stoian (2013). “Time-resolved dynamics of ultrafast Bessel and Gaussian beam propagation and energy deposition in transparent materials”. In: *EUROMAT 2013*.
- Velpula, Praveen Kumar, MK Bhuyan, Cyril Maclair, Jean-Philippe Colombier, and Razvan Stoian (2014b). “High aspect ratio submicron fabrication in bulk dielectrics with non-diffractive ultrafast Bessel beams; dynamics and interaction regimes”. In: *Laser Precision Microfabrication*.
- Velpula, Praveen Kumar, Manoj Kumar Bhuyan, Cyril Maclair, Jean-Philippe Colombier, and Razvan Stoian (2014c). “Role of free carriers excited by ultrafast Bessel beams for submicron structuring applications”. In: *Optical Engineering* 53.7, p. 076108.

- Velpula, Praveen Kumar, Manoj Bhuyan, Cyril Mauclair, Jean-Philippe Colombier, and Razvan Stoian (2014d). “Ultrafast imaging of free carriers: a controlled dynamics with chirped nondiffractive Bessel beams”. In: *SPIE Proceedings Series*. Vol. 8967. SPIE, p. 896711.
- Vera, Julie, Anne-Catherine Brulez, Elise Contraires, Mathieu Larochette, Nathalie Trannoy-Orban, Maxime Pignon, Cyril Mauclair, Stéphane Valette, and Stéphane Benayoun (2017). “Factors influencing microinjection molding replication quality”. In: *Journal of Micromechanics and Microengineering* 28.1, p. 015004.
- Vorobyev, A. Y. and Chunlei Guo (2011). “Direct creation of black silicon using femtosecond laser pulses”. In: *Applied Surface Science* 257.16, pp. 7291–7294. ISSN: 0169-4332. DOI: 10.1016/j.apsusc.2011.03.106. URL: <http://www.sciencedirect.com/science/article/pii/S0169433211004703> (visited on 04/01/2019).
- Wang, Chun-Chieh, Kuang-Li Lee, and Chau-Hwang Lee (2009). “Wide-field optical nanoprofilometry using structured illumination”. EN. In: *Optics Letters* 34.22, pp. 3538–3540. ISSN: 1539-4794. DOI: 10.1364/OL.34.003538. URL: <https://www.osapublishing.org/ol/abstract.cfm?uri=ol-34-22-3538> (visited on 04/26/2019).
- Wang, Jincheng and Chunlei Guo (2005). “Ultrafast dynamics of femtosecond laser-induced periodic surface pattern formation on metals”. In: *Applied Physics Letters* 87.25, p. 251914. ISSN: 0003-6951. DOI: 10.1063/1.2146067. URL: <https://aip.scitation.org/doi/full/10.1063/1.2146067> (visited on 04/02/2019).
- Wang, W. H., C. Dong, and C. H. Shek (2004). “Bulk metallic glasses”. In: *Mater. Sci. Eng. R* 44.2–3, pp. 45–89.
- Wang, Zhuo, Larry Millet, Mustafa Mir, Huafeng Ding, Sakulsuk Unarunotai, John Rogers, Martha U. Gillette, and Gabriel Popescu (2011). “Spatial light interference microscopy (SLIM)”. EN. In: *Optics Express* 19.2, pp. 1016–1026. ISSN: 1094-4087. DOI: 10.1364/OE.19.001016. URL: <http://www.osapublishing.org/abstract.cfm?uri=oe-19-2-1016> (visited on 10/14/2015).
- Watanabe, S., Y. Yoshida, S. Kayashima, S. Yatsu, M. Kawai, and T. Kato (2010). “In situ observation of self-organizing nanodot formation under nanosecond-pulsed laser irradiation on Si surface”. In: *Journal of Applied Physics* 108.10, p. 103510. ISSN: 0021-8979. DOI: 10.1063/1.3512888. URL: <https://aip.scitation.org/doi/abs/10.1063/1.3512888> (visited on 04/29/2019).
- Xie, Chen, Vytautas Jukna, Carles Milián, Remo Giust, Ismail Ouadghiri-Idrissi, Tatiana Itina, John M. Dudley, Arnaud Couairon, and Francois Courvoisier (2015). “Tubular filamentation for laser material processing”. en. In: *Scientific Reports* 5, srep08914. ISSN: 2045-2322. DOI: 10.1038/srep08914. URL: <https://www.nature.com/articles/srep08914> (visited on 09/14/2017).
- Yao, Alison M. and Miles J. Padgett (2011). “Orbital angular momentum: origins, behavior and applications”. EN. In: *Advances in Optics and Photonics* 3.2, pp. 161–204. ISSN: 1943-8206. DOI: 10.1364/AOP.3.000161. URL: <https://www.osapublishing.org/aop/abstract.cfm?uri=aop-3-2-161> (visited on 04/17/2019).
- Young, Jeff F., J. S. Preston, H. M. van Driel, and J. E. Sipe (1983). “Laser-induced periodic surface structure. II. Experiments on Ge, Si, Al, and brass”. In: *Physical Review B* 27.2, pp. 1155–1172. DOI: 10.1103/PhysRevB.27.1155. URL: <https://link.aps.org/doi/10.1103/PhysRevB.27.1155> (visited on 04/29/2019).
- Yu, Junjie, Changhe Zhou, Wei Jia, Wugang Cao, Shaoqing Wang, Jianyong Ma, and Hongchao Cao (2012). “Three-dimensional Dammann array”. EN. In: *Applied Optics* 51.10, pp. 1619–1630. ISSN: 2155-3165. DOI: 10.1364/AO.51.001619. URL: <https://www.osapublishing.org/ao/abstract.cfm?uri=ao-51-10-1619> (visited on 04/06/2019).

- Yu, N. T., D. C. DeNagel, P. L. Pruett, and J. F. Kuck (1985). “Disulfide bond formation in the eye lens”. eng. In: *Proceedings of the National Academy of Sciences of the United States of America* 82.23, pp. 7965–7968. ISSN: 0027-8424. DOI: 10.1073/pnas.82.23.7965.
- Zelgowski, Julien, Frédéric Mermet, Frédéric Antoni, Cyril Mauclair, Eric Fogarassy, and Eric Mottay (2014). “Novel industrial laser etching technics for sensors miniaturization applied to biomedical: a comparison of simulation and experimental approach”. In: *Laser Applications in Microelectronic and Optoelectronic Manufacturing (LAMOM) XIX*. Vol. 8967. International Society for Optics and Photonics, 89670U.
- Zhang, Jingyu, Mindaugas Gecevičius, Martynas Beresna, and Peter G. Kazansky (2013). “5D Data Storage by Ultrafast Laser Nanostructuring in Glass”. EN. In: *CLEO: 2013 Postdeadline (2013), paper CTh5D.9*. Optical Society of America, CTh5D.9. DOI: 10.1364/CLEO_SI.2013.CTh5D.9. URL: https://www.osapublishing.org/abstract.cfm?uri=CLEO_SI-2013-CTh5D.9 (visited on 04/27/2019).
- Zhang, W., G. Cheng, X. D. Hui, and Q. Feng (2014). “Abnormal ripple patterns with enhanced regularity and continuity in a bulk metallic glass induced by femtosecond laser irradiation”. In: *Appl. Phys. A: Mat. Sci. Process.* 115.4, pp. 1451–1455.
- Zhang, Y, G Cheng, G Huo, Y Wang, W Zhao, Cyril Mauclair, Razvan Stoian, and R Hui (2009a). “The fabrication of circular cross-section waveguide in two dimensions with a dynamical slit”. In: *Laser physics* 19.12, p. 2236.
- Zhang, Y., G. Cheng, G. Huo, Y. Wang, W. Zhao, C. Mauclair, R. Stoian, and R. Hui (2009b). “The fabrication of circular cross-section waveguide in two dimensions with a dynamical slit”. en. In: *Laser Physics* 19.12, p. 2236. ISSN: 1555-6611. DOI: 10.1134/S1054660X0923008X. URL: <https://doi.org/10.1134/S1054660X0923008X> (visited on 04/06/2019).
- Zheng, Guoan, Roarke Horstmeyer, and Changhui Yang (2013). “Wide-field, high-resolution Fourier ptychographic microscopy”. en. In: *Nature Photonics* 7.9, pp. 739–745. ISSN: 1749-4885. DOI: 10.1038/nphoton.2013.187. URL: <http://www.nature.com/nphoton/journal/v7/n9/full/nphoton.2013.187.html> (visited on 04/11/2017).
- Zhu, G, D. Whitehead, W. Perrie, O. J. Allegre, V. Olle, Q. Li, Y. Tang, K. Dawson, Y. Jin, S. P. Edwardson, L. Li, and G. Dearden (2018). “Thermal and optical performance characteristics of a spatial light modulator with high average power picosecond laser exposure applied to materials processing applications”. In: *Procedia CIRP*. 10th CIRP Conference on Photonic Technologies [LANE 2018] 74, pp. 594–597. ISSN: 2212-8271. DOI: 10.1016/j.procir.2018.08.080. URL: <http://www.sciencedirect.com/science/article/pii/S2212827118308643> (visited on 03/25/2019).

Part III
Selected Articles

7.4 Dynamic ultrafast laser beam tailoring for multipot photo-inscription of photonic devices in bulk transparent materials

C. Maclair, G. Cheng, N. Huot, E. Audouard, A. Rosenfeld, I. Hertel, and R. Stoian (2009a). “Dynamic ultrafast laser beam tailoring for multipot photo-inscription of photonic devices in bulk transparent materials”. In: *Proc. SPIE 7205*, pp. 720512–720512–10. DOI: 10.1117/12.808798. URL: <http://dx.doi.org/10.1117/12.808798>

This article was written during my PhD. Noteworthy, the augmentation of the speed of femtosecond bulk laser processing was not an initial objective of my PhD work. However, the laser demultiplication enabled by spatial beam shaping was the starting point of the further developments that led spatial beam shaping to integrate pre-industrial laser machining environments through the Manutech-USD project.

Dynamic ultrafast laser spatial tailoring for parallel micromachining of photonic devices in transparent materials

C. Mauclair,^{1,2} G. Cheng,¹ N. Huot,¹ E. Audouard,¹ A. Rosenfeld,² I. V. Hertel,^{2,3} R. Stoian,¹

¹Laboratoire Hubert Curien, UMR 5516 CNRS, Université Jean Monnet,
42000 Saint Etienne, France

²Max-Born Institut für Nichtlineare Optik und Kurzzeitspektroskopie, Max-Born-Str. 2A,
D-12489 Berlin, Germany

³Freie Universität Berlin Fachbereich Physik, Arnimallee 14, 14195 Berlin, Germany
razvan.stoian@univ-st-etienne.fr

Abstract: Femtosecond laser processing of bulk transparent materials can generate localized positive changes of the refractive index. Thus, by translation of the laser spot, light-guiding structures are achievable in three dimensions. Increasing the number of laser processing spots can consequently reduce the machining effort. In this paper, we report on a procedure of dynamic ultrafast laser beam spatial tailoring for parallel photoinscription of photonic functions. Multispot operation is achieved by spatially modulating the wavefront of the beam with a time-evolutive periodical binary phase mask. The parallel longitudinal writing of multiple waveguides is demonstrated in fused silica. Using this technique, light dividers in three dimensions and wavelength-division demultiplexing (WDD) devices relying on evanescent wave coupling are demonstrated.

© 2009 Optical Society of America

OCIS codes: (010.1080) Active or adaptive optics; (140.3390) Laser materials processing; (230.7370) Waveguides

References and links

1. K. M. Davis, K. Miura, N. Sugimoto, and K. Hirao, "Writing waveguides in glass with a femtosecond laser," *Opt. Lett.* **21**, 1729–1731 (1996).
2. E. N. Glezer, M. Milosavljevic, L. Huang, R. J. Finlay, T.-H. Her, J. P. Callan, and E. Mazur, "Three-dimensional optical storage inside transparent materials," *Opt. Lett.* **21**, 2023–2025 (1996).
3. K. Itoh, W. Watanabe, S. Nolte, and C. Schaffer, "Ultrafast processes for bulk modification of transparent materials," *MRS Bull.* **31**, 620–625 (2006).
4. A. Mermillod-Blondin, I. M. Burakov, Yu. P. Meshcheryakov, N. M. Bulgakova, E. Audouard, A. Rosenfeld, A. Husakou, I. V. Hertel, and R. Stoian, "Flipping the sign of refractive index changes in ultrafast and temporally shaped laser-irradiated borosilicate crown optical glass at high repetition rates," *Phys. Rev. B* **77**, 104205/1–8 (2008).
5. D. Wortmann, M. Ramme, and J. Gottmann, "Refractive index modification using fs-laser double pulses," *Opt. Express* **15**, 10149–10153 (2007).
6. E. Bricchi, B. G. Klappauf, and P. G. Kazansky, "Form birefringence and negative index change created by femtosecond direct writing in transparent materials," *Opt. Lett.* **29**, 119–121 (2004).
7. Y. Sikorski, A.A. Said, P. Bado, R. Maynard, C. Florea, and K.A. Winick, "Optical waveguide amplifier in Nd-doped glass written with near-IR femtosecond laser pulses," *Electron. Lett.* **36**, 226–227 (2000).
8. S. Campbell, R. R. Thomson, D. P. Hand, A. K. Kar, D. T. Reid, C. Canalias, V. Pasiskevicius, and F. Laurell, "Frequency-doubling in femtosecond laser inscribed periodically-poled potassium titanyl phosphate waveguides," *Opt. Express* **15**, 17146–17150 (2007).

9. G. Della Valle, S. Taccheo, R. Osellame, A. Festa, G. Cerullo, and P. Laporta, "1.5 μm single longitudinal mode waveguide laser fabricated by femtosecond laser writing," *Opt. Express* **15**, 3190–3194 (2007).
10. S. M. Eaton, H. Zhang, M. L. Ng, J. Li, W. Chen, S. Ho, and P. R. Herman, "Transition from thermal diffusion to heat accumulation in high repetition rate femtosecond laser writing of buried optical waveguides," *Opt. Express* **16**, 9443–9458 (2008).
11. D. J. Little, M. Ams, P. Dekker, G. D. Marshall, J. M. Dawes, and M. J. Withford, "Femtosecond laser modification of fused silica: the effect of writing polarization on Si-O ring structure," *Opt. Express* **16**, 20029–20037 (2008).
12. H. Zhang, S. M. Eaton, and P. R. Herman, "Low-loss Type II waveguide writing in fused silica with single picosecond laser pulses," *Opt. Express* **14**, 4826–4834 (2006).
13. Y. Cheng, K. Sugioka, K. Midorikawa, M. Masuda, K. Toyoda, M. Kawachi, and K. Shihoyama, "Control of the cross-sectional shape of a hollow microchannel embedded in photostructurable glass by use of a femtosecond laser," *Opt. Lett.* **28**, 55–57 (2003).
14. R. Osellame, S. Taccheo, M. Marangoni, R. Ramponi, P. Laporta, D. Polli, S. De Silvestri, and G. Cerullo, "Femtosecond writing of active optical waveguides with astigmatically shaped beams," *J. Opt. Soc. Am. B* **20**, 1559–1567 (2003).
15. C. Mauchair, A. Mermillod-Blondin, N. Huot, E. Audouard, and R. Stoian, "Ultrafast laser writing of homogeneous longitudinal waveguides in glasses using dynamic wavefront correction," *Opt. Express* **16**, 5481–5492 (2008).
16. A. Mermillod-Blondin, C. Mauchair, A. Rosenfeld, J. Bonse, I. V. Hertel, E. Audouard, and R. Stoian, "Size correction in ultrafast laser processing of fused silica by temporal pulse shaping," *Appl. Phys. Lett.* **93**, 021921–021924 (2008).
17. S. Li, G. Yu, C. Zheng, and Q. Tan, "Quasi-Dammann grating with proportional intensity array spots," *Opt. Lett.* **33**, 2023–2025 (2008).
18. S. Hasegawa, Y. Hayasaki, and N. Nishida, "Holographic femtosecond laser processing with multiplexed phase Fresnel lenses," *Opt. Lett.* **31**, 1705–1707 (2006).
19. J. W. Goodman, *Introduction to Fourier Optics* (2nd ed. McGraw-Hill, Singapore, 1996).
20. C. Yu, J. Park, J. Kim, M. Jung, and S. Lee, "Design of Binary Diffraction Gratings of Liquid Crystals in a Linearly Graded Phase Model," *Appl. Opt.* **43**, 1783–1788 (2004).
21. R. Graf, A. Fernandez, M. Dubov, H.J. Brueckner, B.N. Chichkov, and A. Apolonski, "Pearl-chain waveguides written at megahertz repetition rate," *Appl. Phys. B* **87**, 21–27 (2007).
22. N. Sanner, N. Huot, E. Audouard, C. Larat, J.-P. Huignard, and B. Loiseaux, "Programmable focal spot shaping of amplified femtosecond laser pulses," *Opt. Lett.* **30**, 1479–1481 (2005).
23. C. Hnatovsky, R. S. Taylor, E. Simova, V. R. Bhardwaj, D. M. Rayner, and P. B. Corkum, "High-resolution study of photoinduced modification in fused silica produced by a tightly focused femtosecond laser beam in the presence of aberrations," *J. Appl. Phys.* **98**, 013517/1–5 (2005).
24. Z. Wang, K. Sugioka, Y. Hanada, and K. Midorikawa, "Optical waveguide fabrication and integration with a micro-mirror inside photosensitive glass by femtosecond laser direct writing," *Appl. Phys. A* **88**, 699–704 (2007).
25. D. Christodoulides, N. Demetrios, F. Lederer, and Y. Silberberg, "Discretizing light behaviour in linear and nonlinear waveguide lattices," *Nature (London)* **424**, 817–823, (2003).
26. T. Pertsch, P. Dannberg, W. Elflein, A. Bräuer, and F. Lederer, "Optical Bloch Oscillations in Temperature Tuned Waveguide Arrays," *Phys. Rev. Lett.* **83**, 4752–4755 (1999).
27. A. Szameit, F. Dreisow, H. Hartung, S. Nolte, A. Tuennermann, and F. Lederer "Quasi-incoherent propagation in waveguide arrays," *Appl. Phys. Lett.* **90**, 241113–241116 (2007).
28. A. Szameit, D. Bloemer, J. Burghoff, T. Schreiber, T. Pertsch, S. Nolte, A. Tuennermann, and F. Lederer, "Discrete Nonlinear Localization in Femtosecond Laser Written Waveguides in Fused Silica," *Opt. Express* **13**, 10552–10557 (2005).
29. A. Yariv, *Optical Electronics* (4th ed. Saunders College Publ., 1991).
30. A. Szameit, F. Dreisow, T. Pertsch, S. Nolte, and A. Tuennermann, "Control of directional evanescent coupling in fs laser written waveguides," *Opt. Express* **15**, 1579–1587 (2007).
31. A. W. Snyder, "Coupled mode theory for optical fibers," *J. Opt. Soc. Am.* **62**, 1267–1277 (1972).
32. P. D. McIntyre, and A. W. Snyder, "Power transfer between nonparallel and tapered optical fibers," *J. Opt. Soc. Am.* **64**, 286–288 (1974).
33. A. Szameit, D. Bloemer, J. Burghoff, T. Pertsch, S. Nolte, and A. Tuennermann, "Hexagonal waveguide arrays written with fs-laser pulses," *Appl. Phys. B* **82**, 507–512 (2006).

1. Introduction

Ultrafast laser processing of bulk transparent materials [1, 2] experiences an increasing interest as it continuously demonstrates its capability to achieve more and more complex embedded photonic structures in a few-steps process (see [3] and references therein). The nonlinear in-

teraction between the infrared femtosecond pulses and the dielectric materials allows localized modifications of the material structural properties. These changes depend on the material's response to the laser solicitation and on the laser irradiation spatio-temporal characteristics [4,5]. These structural modifications may modify several optical properties such as birefringence, absorption, and refractive index [6], serving as means of optical functionalization. In fused silica, defect centers, densification, and thermo-mechanical effects have been identified in the femtosecond laser irradiated zone accompanied by index changes with emphasis on an increase of the refractive index on a micrometer scale [3]. This outcome can be seen as the building block of more complex photonic devices. In other words, by translation of the single laser spot, light-guiding structures are achievable in the three dimensions [3]. Relying on this processing principle, several groups were able to photoinscribe rather complex embedded optical components, particularly in fused silica [1–3] but also in other media of optical interest, fabricating gain waveguides [7], frequency-doubling waveguides [8] and femtosecond-written lasers [9]. Great efforts were carried out to define proper irradiation conditions in order to improve the quality of the laser written structures. Techniques based on controlling the aspect of the focal region at different repetition rates and polarization regimes emerged [10,11]. Among the main characteristics of interest are found the amplitude of the refractive index increase [5,10], propagation losses [12], cylindrical symmetry [13,14] and compensation of the wavefront distortion during the photoinscription process of deep structures [15,16]. Whereas the three-dimensional photoinscription access constitutes a clear advantage over multilayer lithographic techniques, the single laser focal spot must undergo potentially complicated movements with respect to the sample in order to draw the whole photonic structure. This single spot operation (SSO) may involve long processing times when the writing of several complex structures is envisaged.

A binary phase mask, when placed at the object plane of a focusing lens, enables the generation of multiple laser spots [17]. Static multispot machining of glass relying on this technique was recently reported [18]. We present in the following a time-saving method giving access to dynamic multispot operation (DMSO) with variable and reconfigurable patterns and we successfully apply it to the parallel fabrication of light guiding structures in the bulk. Dynamic multispot operation based on laser wavefront modulation constitutes a step forward as it enables the simultaneous processing of several embedded structures, thus lowering the process time and reducing the complexity of the mechanical support. The paper is organized as follows. After a brief analytical outline pointing out the DMSO through spatial phase modulation, details of the experimental apparatus will be given. Then, the demonstration of parallel longitudinal writing of waveguides is presented followed by examples of photonic structures based on DMSO in the two and three dimensions (2D and 3D).

2. Description of dynamic multispot operation

In the object plane of a focusing objective, an optically addressed spatial light modulator (SLM) imprints a binary phase-only mask (BPM) $\phi(x)$ of period T and amplitude $\Delta\phi$ on the laser wavefront as shown on Fig. 1. For simplicity, it is considered infinite in the x direction and invariant in the y direction, z being the laser propagation axis. In the frame of the Fraunhofer approximation and supposing that the SLM reproduces perfectly the BPM, the diffraction efficiency η of the m -th order is given by [19] :

$$\eta_{m \neq 0} = \frac{1 - \cos(\Delta\phi)}{2} \text{sinc}^2\left(\frac{\pi m}{2}\right). \quad (1)$$

And for the 0-th order:

$$\eta_0 = \frac{1 + \cos(\Delta\phi)}{2}. \quad (2)$$

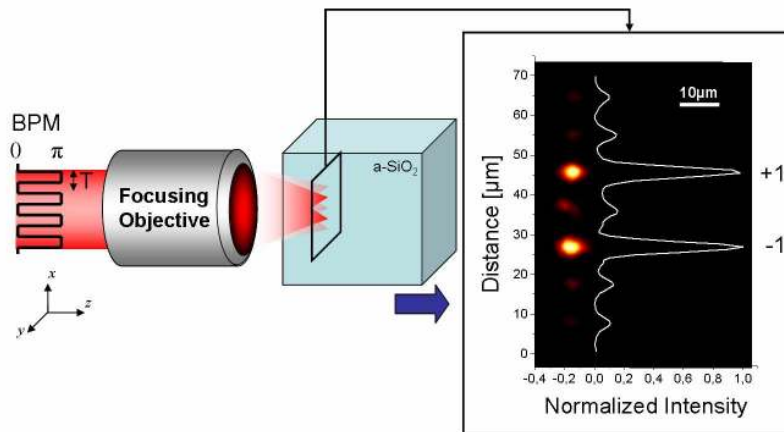


Fig. 1. (color online): Scheme of double spot operation. BPM: Binary phase mask. Insert: Double spot intensity profile inside the sample at the focus of the objective generated by a simple step grating phase at very low power captured by direct imaging on a CCD camera. The blue arrow shows the direction of motion of the sample for longitudinal photoinscription.

For the ideal binary grating, the even orders disappear regardless of the phase step value $\Delta\phi$. Moreover, when $\Delta\phi = \pi$, not only does no diffraction occur at the 0-th order but the first order efficiency becomes much higher than the other orders, thus constituting two available laser spots for laser processing. In that case, adding the positive and negative first order efficiency shows that these two peaks gather 82% of the incoming light. By varying the period T of the BPM, the separation of the two spots becomes an accessible parameter to be controlled during photoinscription through the SLM.

From the experimentally-obtained double spot beam profile depicted in Fig. 1(insert), it is worth noting that the spots corresponding to the +1 and -1 orders show an expected circular symmetry. As foreseen, these two peaks widely surpass other diffracted orders. Evaluating the relative portion of power contained in these two processing spots by summing the corresponding intensity levels permits to realize that approximately one third of the total power is left into the non-processing orders. This additional spreading out of usable power compared to the above-mentioned 18% is inherent to the incapacity of the continuous liquid crystal layer of the SLM to reproduce perfectly the sharp steps of the desired BPM [20]. These losses can be reduced through the design of more complex phase masks with iterative optimization algorithms [17]. However, in view of the nonlinear response of the interaction, only the high intensity peaks contribute to the structuring process and in the frame of the present work, the simple step grating phase mask is sufficient for the DMSO demonstration purpose. Moreover, this phase modulation offers a straightforward way to control the position of the two spots by varying its period; a feature more difficult to obtain in the case of more complex phase masks.

3. Experiment

The choice of fused silica glass is motivated by its numerous potential applications in the fields of integrated optics and microfluidics. Moreover, this well-known material has been thoroughly investigated in order to identify several femtosecond waveguide writing regimes [1, 12, 21]. Polished fused silica parallelepipedic samples are irradiated with 150 fs pulses from an 800 nm

100 kHz Ti:Sapphire ultrafast regenerative amplifier laser system. Used at 10 kHz, the system delivers an usable power of 30 mW. A computer driven electromechanical shutter, synchronized with the movements of the positioning system (Physik Instrumente M-126.DG) permits the writing of longitudinal structures in the bulk of the sample. A long working distance microscope objective (numerical aperture NA=0.3) is employed to focus the femtosecond beam in the silica glass. The diameter D_b of the beam at $1/e^2$ is 1.5 mm and is adjusted with respect to the objective aperture diameter $D_a = 3$ mm resulting in a truncation ratio of 0.5.

A spatial light modulator (SLM) imaged in the object plane of the focusing objective performs user-defined spatial phase modulation of the processing femtosecond beam. This programmable optical valve based on a continuous liquid crystal layer is optically addressed using a video projector [22]. This versatile tool [15, 22] is used to produce two processing laser spots of controllable separation as described in the previous section.

As a rapid observation mean, a Zernike-type positive optical phase-contrast microscopy (PCM) system is set to study the laser-irradiated areas. The observation axis is perpendicular to the laser propagation direction and presents a sub- μm depth of field. A precise optical alignment permits the real-time imaging of the laser-exposed zones and subsequent optical transformations. PCM is particularly adapted for the study of femtosecond-induced phase objects as it optically translates a two-dimension map of optical path variations into a gray-level picture captured in our case by a high-resolution Charge-Coupled Device (CCD) camera. In the frame of positive PCM and for relatively small phase shift values, a darker region relative to the background corresponds to an increase of the refractive index while white regions indicate its lowering or the onset of absorbing/diffusing regions. Consequently, this qualitative mapping of the refractive index allows for rapid estimations of the index variation subsequent to various irradiation conditions. The structures were imaged in PCM in a side view geometry, perpendicular to the pulse propagation axis.

4. Results and discussion

We mention here that all the photowritten structures presented below were achieved in the so-called longitudinal configuration, where the sample is translated parallel to the laser propagation (see Fig. 1). One of the main advantages of this technique is found in the cylindrical symmetry of the photoinscribed structure while transverse waveguide writing generally requires additional strategies to preserve this symmetry [13, 14]. However, the major challenge to be faced in the longitudinal configuration concerns the spherical aberrations due the air-glass interface through which the laser passes to reach its target [23]. The subsequent degradation of the intensity profile at the focus becomes more important when high NAs and deep focusing are considered. Using the formalism depicted in [23], it is possible to estimate the decrease of the focused spot peak intensity with the depth of the spot in the sample for a given NA. In our case, the relatively low effective $NA = 0.2$ resulting from the small beam truncation preserved 84% of the non-aberrated axial peak intensity at 8 mm deep spot in the bulk, allowing us to write longitudinal structures of similar size without prohibitive optical degradation. In addition, it is of interest to point out that, at constant sample velocity, the accumulated spatial rate of deposited energy remains constant during longitudinal writing regardless of the position of the spot in the sample. Those considerations plead in favor of a rather restricted spherical aberration influence in the photowriting conditions presented in this work. Even though the devices depicted hereafter were achieved in the longitudinal configuration, it is worth noting that the extent of the DMSO technique to the transversal case for bulk parallel waveguide writing is straightforward.

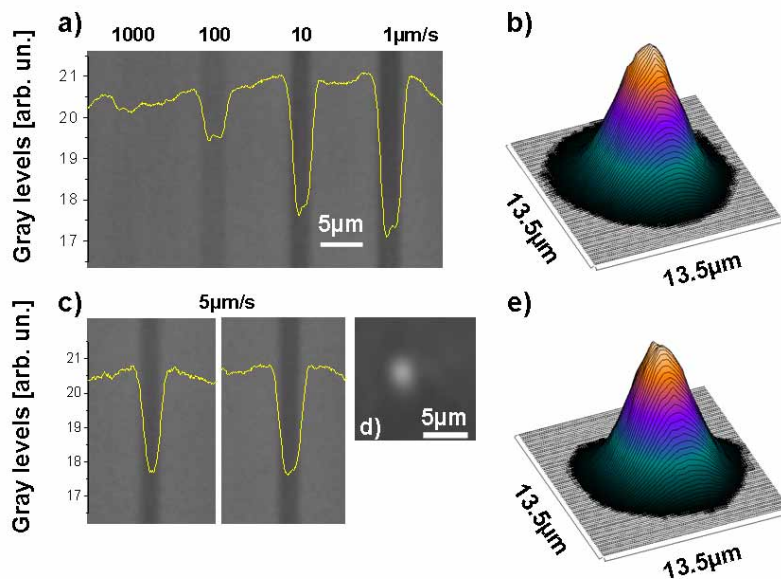


Fig. 2. (color online): Comparison between single and double spot longitudinal photoinscription of waveguides in fused silica. Up: Single spot operation, down double spot operation. (a) Side view PCM picture of SSO photowritten waveguides written at different translation speeds at 10 kHz, 8 mW, superposed with transversal cross section of the relative gray scale decrease indicating a positive change of the refractive index (see text body). (b) corresponding nearfield profile of 633 nm injected guide written at 5 $\mu\text{m/s}$, 10 kHz, 8 mW in single spot operation. (c) PCM picture of two simultaneously photowritten waveguides through double spot operation at 5 $\mu\text{m/s}$, 10 kHz, 24 mW. (d) Optical transmission microscope picture of the cross section of one of the waveguides in (c) in white light illumination. (e) nearfield profile of one of the waveguides pictured in (c) at 633 nm.

4.1. Processing window for parallel longitudinal waveguide writing

To demonstrate the capability of the DMSO to generate similar bulk photoinscribed devices as SSO, longitudinal waveguides were written using both techniques in a regime which usually delivers smooth and nonbirefringent traces. A first set of SSO investigations were carried out with various scan velocities for the glass sample at a power level of 8 mW (measured after the objective) with a repetition rate of 10 kHz (see Fig. 2(a)) i.e; slightly below the single pulse modification threshold. The PCM side image along with its gray scale cross section denotes a relative gray scale decrease after the passage of the femtosecond laser for translation speeds below 10 $\mu\text{m/s}$. These darker structures under positive PCM mainly indicate an increase of the refractive index. They are not readily detectable under normal transmission microscopy (not shown) and present light guiding properties when injected with HeNe radiation at 633 nm. We mention here that in those scanning conditions, moving away from this relatively soft interaction regime by using higher laser power results in strongly scattering structures with poor or no guiding property. Based on this processing window, several 8 mm-long buried waveguides were written at 5 $\mu\text{m/s}$ with 8 mW for characterization. Fig. 2(b) depicts a typical nearfield mode under HeNe laser injection at 633 nm imaged on a CCD camera with a 20x objective associated with a 200 mm positive lens. The light is guided along the center of the modified

area and the nearfield mode presents a size of $7\ \mu\text{m}$ at $1/e^2$, larger than the transverse dimension of the structure ($3.5\ \mu\text{m}$) evaluated at $1/e^2$ on the PCM image. The averaged amplitude of the refractive index change was estimated to be of approximately $\Delta n = 1.6 \times 10^{-4}$ through the waveguide NA measurement in the farfield. This rather low value [3] was confirmed using a mode solving software assuming a step index profile. The guides show an excellent cylindrical symmetry, visible on the nearfield mode and the structure itself. Using the method reported in [24], propagation losses of less than 0.7 dB/cm were evaluated, which approaches the best values reported so far for bulk photowritten waveguides in fused silica [3].

Using the DMSO, identical light guides were simultaneously photoinscribed by pairs in one pass. Taking advantage of the two spots available at the focus of the objective, dual structures with a separation of $s = 56\ \mu\text{m}$ were achieved in a single motor scan at $5\ \mu\text{m/s}$ under the full available power of 24 mW, after the focusing objective. For this purpose, a step grating phase mask of π amplitude at 800 nm with $\nu = 14$ periods across the clear aperture of the objective was displayed with the SLM during the sample displacement. Imaging the focusing plane on a CCD camera, the linear relationship between ν and s was experimentally determined. The PCM side image and nearfield mode of the waveguides are pictured in Fig. 2(c) and Fig. 2(e), respectively. The amplitude of the refractive index change as well as the propagation losses were found to be identical to the SSO written waveguides at 8 mW, same speed (Fig. 2(b)), verifying our estimation of the power spread in the other diffraction orders mentioned in Section 2. The clean cylindrical symmetry is also observable on the nearfield mode as well as on the cross section microscope image (Fig. 2(d)). These results clearly demonstrate the possibility to write buried photonic devices in parallel with a very simple phase function. Observing the processing conditions and comparing them to the available output of the laser, it appeared necessary to restrict the DMSO to two spots in our case in order to preserve enough energy to trigger the proper waveguide writing regime in fused silica. However, there is no a priori restriction to increase this number to higher values in the absence of this limiting factor. Having identified this processing window for parallel photoinscription, efforts were carried out in order to achieve more complex photonic devices based on this principle.

4.2. 2D photonic components

Embedded waveguide arrays have been recently investigated pointing out to novel behavioral aspects [25] when light propagates in discrete propagation spaces due to the evanescent light coupling between neighboring guides. In particular, linear effects such as Bloch oscillations [26], light localization, and quasi-incoherent propagation [27] were theoretically predicted and experimentally verified in femtosecond photowritten waveguides arrays. Nonlinear behaviours in the form of spatial solitons were underlined as well in such structures [28] indicating the possibility of obtaining new-types of nonlinear components written by femtosecond lasers. We aim to demonstrate here that complex 2D and 3D arrays and matrices of light guiding structures can be efficiently written using DMSO. In the following, examples of 2D photonic devices relying on evanescent coupling achieved with DMSO are presented, performing various optical functions. Evanescent coupling between parallel waveguides is supported by a precise formalism [29] and has been recently studied in the case of transversal waveguides written in fused silica by femtosecond optical irradiation [30]. Due to the relative asymmetry of such waveguides, investigations were carried out underlining the coupling efficiency variations between two waveguides when their relative position changes. Using an additional static beam shaping technique, transverse waveguides with rotational symmetry were achieved fully counteracting this asymmetry feature [30]. In the longitudinal configuration for waveguide writing, the resulting guides keep the circular symmetry of the irradiation beam permitting to set aside those considerations when the processing spot is aberration-free. It is therefore justified to adopt in a

first approach the formalism proposed by Yariv [29] for planar waveguides to design embedded light dividers based on evanescent coupling. Several main concepts are given below.

In this frame, when only one of a pair of parallel and homogeneous identical waveguides is injected with light, the coupling length l_c after which the light is entirely evanescently coupled in the adjacent waveguide writes (also known as the half beat length):

$$l_c = \frac{\pi}{2\kappa}, \quad (3)$$

κ being the coupling coefficient defined by:

$$\kappa = \frac{2h^2 p \times \exp(-ps)}{\beta(w + 2/p)(h^2 + p^2)}. \quad (4)$$

In the above expression, the parameters can be written as

$$\begin{aligned} h &= (n_1^2 k_0^2 - \beta^2)^{1/2} \\ p &= (\beta^2 - n_0^2 k_0^2)^{1/2} \\ \beta &= k_0 n_{eff}. \end{aligned} \quad (5)$$

n_0 and n_1 being respectively the refractive index of the surrounding medium and of the guides, n_{eff} the effective index of the guided mode which obeys $n_0 < n_{eff} < n_1$. w is the waveguide width, s the separation distance between the two parallel waveguides, k_0 the wave number of the injected light and β the propagation constant. The coupling coefficient κ was experimentally evaluated for several waveguide pairs using the method described in [30]. Having access to all the other terms of Eq. (4), the effective index n_{eff} could then be estimated.

In the case of a cylindrical guide surrounded by N other identical waveguides having equal distance to the main one at vertices of a polygon [31], the coupling coefficient κ_N for the light to be transmitted to the surrounding structures reads:

$$\kappa_N = \kappa \sqrt{N}. \quad (6)$$

The corresponding coupling l_{cN} length is then:

$$l_{cN} = \frac{l_c}{\sqrt{N}}. \quad (7)$$

In that case, the maximum power transfer F between the center and the surrounding waveguides writes:

$$\begin{aligned} F &= 1 && \text{if } 1 \leq N < 3 \\ &= \left[1 + \left(\frac{\kappa_{ss}}{\kappa_{cs} \sqrt{N}} \right)^2 \right]^{-1} && \text{otherwise.} \end{aligned} \quad (8)$$

where κ_{ss} is the coupling coefficient between the adjacent external waveguides and κ_{cs} from the central waveguide to one of the surrounding ones.

For example, in the case of two parallel waveguides with the above-mentioned characteristics ($\Delta n = 1.6 \times 10^{-4}$ and $w = 3.5 \mu\text{m}$), the coupling length l_c becomes 1.6 mm for a separation s of $9 \mu\text{m}$ and 633 nm light injection. Similarly, an excited waveguide placed in between two identical guides generates a coupling length l_{c2} of 1.1 mm; $s, w, \Delta n$ and k_0 being the same. In these two cases, we have $F = 1$, meaning that all the light is evanescently coupled after the

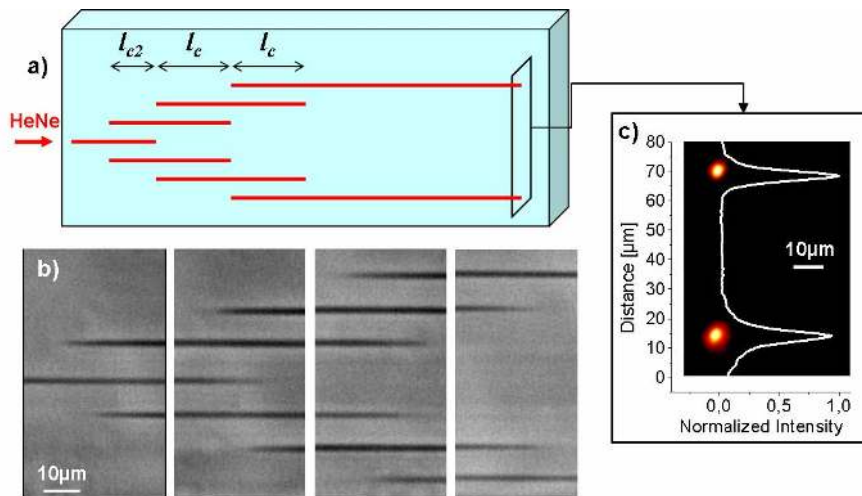


Fig. 3. (color online): Bulk photowritten light divider based on evanescent coupling of injected waves in partial arrays achieved through double spot operation at 24 mW total power and 5 $\mu\text{m/s}$ scan velocity: (a) schematic view of the structure: The conditions followed by l_c and l_{c2} enabling evanescent coupling from the central to the external guides are given in the text. (b) Assemblage of PCM side-pictures of the device, its total length is 8.2 mm and the lateral separation between tracks is 9 μm . (c) Nearfield profile under HeNe injection at 633 nm.

coupling length. Based on these results, it is then possible to design the concept of a light divider reposing on a successive combination of parallel waveguides with defined lengths and separation allowing evanescent coupling from a seed waveguide to two or more output waveguides. The DMSO technique appears as an ideal processing solution as it offers the flexibility to photoinscribe a pair of coupled waveguides simultaneously.

Figure 3 presents an example of a structure achieved by this technique. This device was photoinscribed in five subsequent steps under the irradiation conditions announced in the experimental section (24 mW, 5 $\mu\text{m/s}$). A single uniaxial motion control is sufficient to achieve the whole divider. A first 5 mm-scan of the sample under femtosecond laser exposure generated the two external waveguides. During this first move, the SLM was imprinting the above-mentioned $[0 - \pi]$ phase mask on the femtosecond laser beam with a high cycling frequency. Lowering the number of periods ν , two subsequent scans were performed to write the two other waveguide pairs of lower separation. Then the central waveguide was written at lower power 8 mW without any wavefront modulation. Consequently, the transverse distance between the guides is $s = 9 \mu\text{m}$. The successive translations of the sample were performed in order to have the above-calculated optimal coupling lengths l_c and l_{c2} as shown in Fig. 3(a). An assemblage of PCM side-images of the structure is depicted in Fig. 3(b) to illustrate the result; the slight asymmetries are presumably due to unwanted beam wavefront distortions caused by SLM imperfections. The divider nearfield profile is presented in Fig. 3(c) when 633 nm radiation is coupled into the central waveguide. With a splitting ratio of approximately 1:1, the light dividing operation is clearly verified. Moreover, further investigations put into light the absence of nearfield mode at the output of the intermediate waveguides, thus confirming light dividing through total evanescent coupling. Losses of the device, apart from the propagation losses, were evaluated to be approximately 30% expectedly mostly related to machining imperfections.

Considering a pair of identical waveguides injected in only one arm, a variation of the excit-

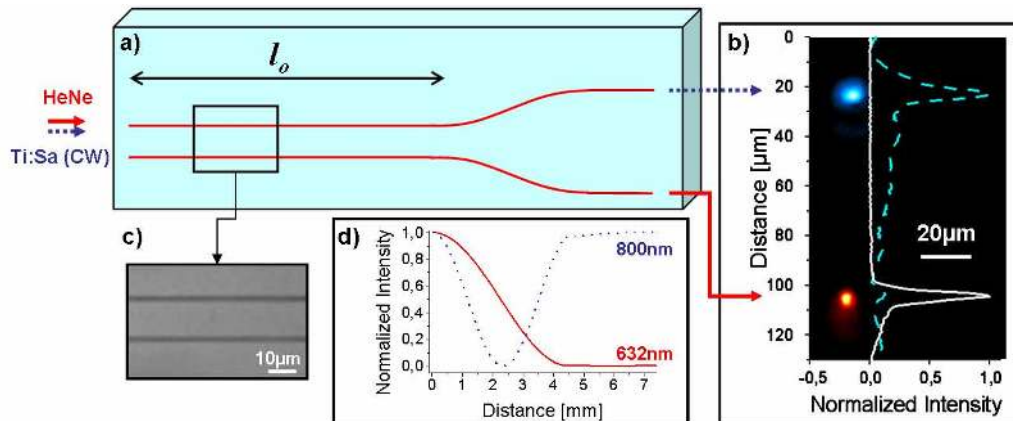


Fig. 4. (color online): Bulk photowritten WDD device achieved through double spot operation at 24 mW total power and 5 $\mu\text{m/s}$ scan velocity. (a) Schematic view of the structure (condition followed by l_o is given in the text). (b) Nearfield profile under 633 nm (solid) and 800 nm (dashed) simultaneous injection in the top arm. (c) PCM side-image of the overlapping region. (d) Theoretical prediction of the 633 nm (solid) and 800 nm (dashed) intensity variations in the excited waveguide according to [31,32] taking into account the wavelength dependence of the coupling coefficient. The total length of the structure is 7.4 mm.

ing wavelength modifies the coupling coefficient and length according to Eq. (3) and (4). More precisely, for a given structure, increasing the wavelength will shorten the coupling length. In the case of two available wavelengths λ_1 and λ_2 with $\lambda_1 > \lambda_2$, it is possible to create a device for which the coupling length $l_{c\lambda_2}$ for λ_2 is twice as big as the coupling length $l_{c\lambda_1}$ for λ_1 . Then, if the total overlapping length l_o of the waveguides verifies $l_o = l_{c\lambda_2} = 2 \times l_{c\lambda_1}$, exciting one arm with both λ_1 and λ_2 generates total evanescent coupling of the λ_2 light in the other arm whereas the λ_1 excitation is back coupled to the initial arm demultiplexing the input frequencies.

Figure 4 shows a device performing the wavelength-division demultiplexing (WDD) operation. The entire device was photowritten with DMSO in a single motor scan in similar exposure conditions as already described. At the beginning of the irradiation, the laser beam was spatially modulated with a BPM having $v = 20$ periods resulting in two 84 μm separated spots. The number of periods v was dynamically decreased while the sample was moving thus lowering the separation to $s = 16 \mu\text{m}$ in synchronization with the photoinscription procedure. At 633 nm, the coupling length for this separation is $l_{c633} = 4.5$ mm. For injection with 800 nm CW laser radiation, the length becomes $l_{c800} = 2.4$ mm. To take into account the weak coupling in the non-parallel part of the structure, we used the formalism proposed by McIntyre and Snyder [32] for non-parallel structures. Consequently, the overlapping length $l_o = 4.4$ mm is slightly smaller than l_{c633} . Calculation results for the structure are depicted in Fig. 4(d) showing clean WDD between 633 nm and 800 nm. The experimental nearfield modes of the excited device at 633 nm and 800 nm are presented in Fig. 4(b), in agreement with the expected behavior.

4.3. 3D photonic components

The beam shaping properties allow easy access to the 3D space. In order to underline further three-dimensional capabilities as well as the high flexibility of the DMSO technique, two optical components are presented hereafter. First, a simple twisted X-coupler is depicted on Fig. 5 where a structure rotation from the vertical to the horizontal plane occurs. This device was pho-

photowritten in a single scan of the sample during which the wavefront was continuously controlled in order to draw simultaneously the two arms of the structure. At the beginning of the move, the spatial phase mask was driven the same way as for the above-mentioned WDD device i.e by changing the BPM cycling frequency. Then, it was gradually rotated by 90° during the writing of the central part (Fig. 5(b)). Finally, the number ν of periods was increased to augment the separation of the two arms. The structure dimensions (separation, overlapping length l_o) were designed with the help of the above-mentioned formalism in order to transmit the totality of the 633 nm light injected in the bottom arm to the top one. Fig. 5(c) depicts the experimentally obtained nearfield mode at the output of the device.

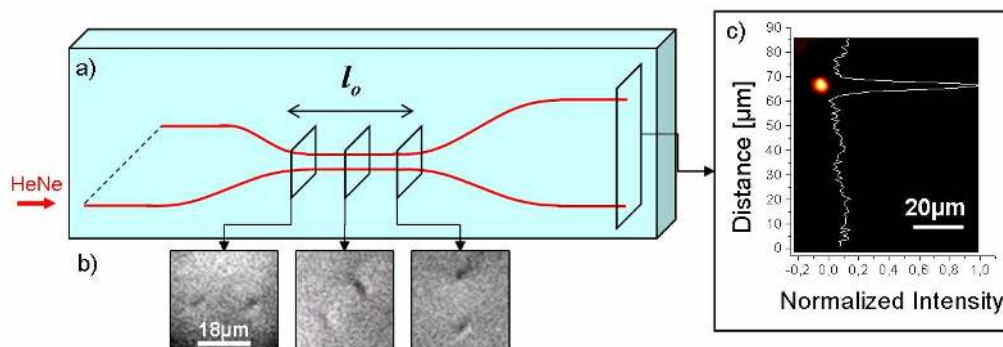


Fig. 5. (color online): (a) Schematic view of a bulk photowritten twisted X coupler achieved through DMSO in a single scan. (b) Optical transmission microscopy pictures of the central region, showing 90° rotation. (c) Nearfield profile at the output of the top arm under 633 nm injection in the bottom waveguide.

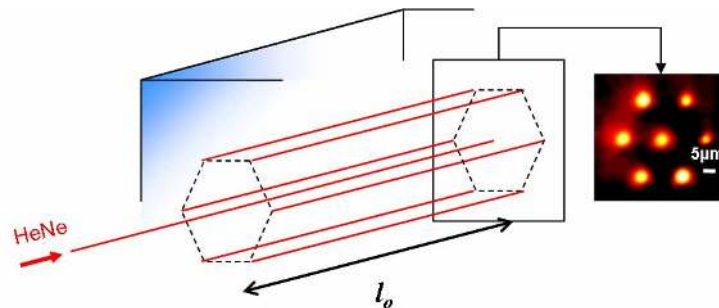


Fig. 6. (color online): Schematic view of a bulk photowritten 3D hexagonal light divider achieved through DMSO. The condition followed by l_o is given in the text. Insert: Nearfield profile under 633 nm injection in the central waveguide.

The second structure of interest achieved by DMSO consists of a hexagonal light divider for 633 nm (Fig. 6). Hexagonal waveguide arrays written by femtosecond SSO were recently achieved and light propagation in such structures was investigated [33]. The light divider presented here was photoinscribed taking advantage of the flexibility and the 3D access of DMSO. Four sample scans were necessary to achieve the device in similar exposure conditions as already described. We recall here that DMSO was restricted to two processing spots in order to preserve sufficient enough energy to trigger the proper photowriting regime in fused silica.

First, the sample was irradiated with the wavefront modulated laser beam offering two processing spots separated by $30\ \mu\text{m}$. The two subsequent scans were performed with the same mask rotated by an angle of 60° and 120° , successively. Finally, the central guide was photowritten without any wavefront modulation at lower power. The distance s_{AA} between two adjacent guides equals the separation s_{CA} between the central guide and the six others having $s = 15\ \mu\text{m}$, the whole structure forming a regular hexagon.

In order to obtain optimal coupling, the overlapping length l_o (Fig. 6) verifies $l_o = l_{c6} = 1.5\ \text{mm}$ obtained from Eq. (7). Having $s_{AA} = s_{CA}$, it is straightforward to show that $\kappa_{ss} = \kappa_{cs}$. Thus, using Eq.(8), it is expected to obtain $F = 0.85$, meaning that 85% of the injected light is theoretically retrieved at the output of the six external guides ($\sim 14\%$ per guide), the rest remaining in the seed waveguide. In other words, each of the seven outputs is expected to have the same nearfield mode peak intensity. The insert of (Fig. 6) depicts the experimental nearfield intensity distribution, being in good agreement with the foreseen distribution.

5. Conclusion

An innovative technique is proposed to photoinscribe optical 3D devices in the bulk of transparent materials using spatial ultrafast beam shaping. The parallel photowriting technique uses time-evolutive modulation of femtosecond laser wavefront, producing two laser processing spots for parallel photoinscription of light guiding structures. The method relies on the employment of a periodical binary phase mask where a variation of the period (cycling frequency) results in a modification of the spots separation, a feature permitting dynamic positioning of the processing spots during laser exposure. Provided that sufficient energy is available, the technique can be scaled up to a higher number of machining foci. Several devices are demonstrated in the longitudinal writing configuration, thus underlining the high processing flexibility of this technique easily applicable for more demanding photowritten optical components. Examples are given emphasizing waveguide arrays where parallel processing appears as a natural choice. Two and three dimensional photonic structures relying on evanescent coupling were achieved with this method performing functions of light coupling, division and wavelength demultiplexing.

Acknowledgments

Support of ANR and PICS programs is gratefully acknowledged. We also thank J.-P. Meunier for useful discussions.

7.5 Ultrafast laser micro-cutting of stainless steel and PZT using a modulated line of multiple foci formed by spatial beam shaping

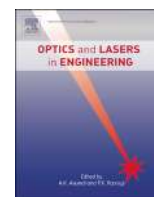
Cyril Mauclair, David Pietroy, Yoan Di Maio, Emmanuel Baubeau, Jean-Philippe Colombier, Razvan Stoian, and Florent Pigeon (2015b). “Ultrafast laser micro-cutting of stainless steel and {PZT} using a modulated line of multiple foci formed by spatial beam shaping”. In: *Optics and Lasers in Engineering* 67.0, pp. 212 –217. ISSN: 0143-8166. DOI: <http://dx.doi.org/10.1016/j.optlaseng.2014.11.018>. URL: <http://www.sciencedirect.com/science/article/pii/S0143816614002905>

This article was written during the PhD thesis of Y. Di Maio. Interestingly, the PhD funding was shared with a private company whose scope was rapid and high precision cutting of PZT wafer, without disturbing the PZT piezo electric properties. Spatial beam shaping could be use to accelerate the process. Thus, this is an example of industrial transfer of the spatial beam shaping technique.



Contents lists available at ScienceDirect

Optics and Lasers in Engineering

journal homepage: www.elsevier.com/locate/optlaseng

Ultrafast laser micro-cutting of stainless steel and PZT using a modulated line of multiple foci formed by spatial beam shaping



Cyril Mauclair^{a,b,*}, David Pietroy^a, Yoan Di Maïo^{a,c}, Emmanuel Baubeau^b,
Jean-Philippe Colombier^a, Razvan Stoian^a, Florent Pigeon^{a,b}

^a Laboratoire Hubert Curien, UMR 5516 CNRS, Université de Lyon, Université Jean Monnet, 42000 Saint Etienne, France

^b GIE Manutech-USD, 42000 Saint Etienne, France

^c SAFRAN Group, 75724 Paris, France

ARTICLE INFO

Article history:

Received 24 July 2014

Received in revised form

22 October 2014

Accepted 30 November 2014

Available online 23 December 2014

Keywords:

Femtosecond laser machining

Spatial beam shaping

Ultrashort laser cutting

ABSTRACT

Femtosecond laser surface processing of materials allows for precise micrometer cutting with restricted detrimental side effects. An efficient way to increase the ablation or cutting speed and energy efficiency of the process is the generation of N parallel laser spots in the focal plane of a lens on the sample surface, each spot simultaneously following a defined cutting trajectory. However, the cutting scheme is then limited in area to avoid overlap of the spot trajectories. We present in this paper a technique to overcome this limitation. The ultrafast laser beam wavefront is spatially modulated, generating a line of multiple processing spots in the lens focal plane. Micro-cutting is then conducted by translation of the sample along the spot line. That way, no restriction on the cutting trajectory length is imposed while preserving the increase in the cutting speed and energy efficiency of the process compared to single spot machining. Successful cutting of PZT ceramic and stainless steel is achieved with the spot array and compared to single spot machining in terms of processing time. In the case of PZT, the cutting efficiency and speed is compared to single spot laser machining with various focal lenses. We also investigate the effect of intensity gradient on the spots line for micro-cutting on stainless steel. The method efficiency is discussed relying on surface characterization using scanning electron microscopy.

© 2014 Elsevier Ltd. All rights reserved.

1. Introduction

Femtosecond laser processing of materials is becoming an increasingly spread technique for rapid structuring on the micro or sub micrometer scale with high potential for applications [1–7]. Due to the nonlinear character of the interaction, femtosecond laser processing can be used for a wide variety of materials. For surface treatment, the technique has been employed with success in various fields of application including surgery [8], biology [9], tribology [10], wettability [11], color marking [12] or material ablation and cutting [5,6,13,14]. Interestingly, physical properties of the laser-irradiated surfaces can be controlled to a certain extent by tuning the irradiation conditions. A major field of applications concerns micro-cutting of thin samples of various materials. The laser tool ensures an obvious advantage for flexible non-contact machining and/or cutting, thanks to the possibility to control the laser spot trajectory. However, the requirements of

high processing speed, with minimum deterioration of the surface physical properties (notably on the residual cutting walls) remain a challenge. As a solution to the need of increased machining speed, beam shaping methods have been developed [15–21] based on amplitude and/or phase modulation using a spatial modulator. The technique allows for multiplication of the machining laser focus into several spots enabling parallel machining. This parallelization of the process has the advantage of reducing the processing time by a factor equal or close to the number of processing foci. As an example, for a given micro-cutting trajectory on a surface, reduction of the processing time can be obtained by defining N trajectories with the N laser spots side by side on the sample surface. However, to avoid overlap of the irradiated areas, the spot separation distance has an upper limitation. This distance corresponds to the lateral dimension of the optical field in the processing plane D (which depends on the focusing lens) divided by the number of parallel laser spots N . Keeping a spot separation below D/N is necessary to avoid overlap of the cutting trajectories of the N laser spots. Thus, only beam trajectories corresponding to a small enough area are eligible to this technique to avoid overlap of the irradiation paths. Moreover, the greater N is (which is a natural aim in reducing the processing time), the smaller the beam

* Corresponding author at: Laboratoire Hubert Curien, UMR 5516 CNRS, Université de Lyon, Université Jean Monnet, 42000 Saint Etienne, France.

E-mail address: cyril.mauclair@univ-st-etienne.fr (C. Mauclair).

separation ought to be. This reduces the potential of parallel processing with spatial beam shaping to restricted micromachining schemes.

We propose here a beam shaping strategy that can overcome this limitation and successfully apply it for micro-cutting of stainless steel and PZT. A line of N close and identical laser spots is formed at the focal plane of a lens using wavefront modulation. During irradiation, the sample surface is translated along the spot line for micro ablation and/or cutting. That way, a single sample translation corresponds to N passes of the laser. This reduces the processing time while keeping the maximal attainable machining area independently of the number of spots N . In this work, we employ and compare this technique with single spot laser machining in terms of processing time and ablation efficiency. We also investigate the possibility to generate intensity gradients along the line of laser spots when irradiating stainless steel. Finally, the efficiency of the method is discussed in light of the surface characterization using scanning electron microscopy on PZT.

2. Experimental details

A femtosecond amplified laser system (Thales Bright) operating at a repetition rate of 5 kHz delivers 120 fs (full width half maximum) light pulses at 800 nm with an average power of 2 W and linear polarization. As illustrated in Fig. 1, the laser beam is reflected on a Spatial Light Modulator (SLM) (Holoeye Pluto NIR). The laser wavefront undergoes a phase computer-controlled modulation which spatially shapes its intensity distribution in the far field (i.e. here the focal plane of the focusing lens). The beam is then reduced in size by passing through a telescope (T) before reaching the focusing objective or lens (FL). In this report, focal lengths of 20, 25, 50, 88 and 250 mm were used to focus the ultrashort pulses on the surface of the sample. Here, common stainless steel (316 L) and PZT are employed with a mirror-like polished surface. A home-made microscope sharing the focusing lens with an additional tube lens ($f=250$ mm) and a two-dimensional CMOS sensor is set up for in-situ observation of the interaction zone and rapid monitoring of the laser intensity distribution on the surface. The sample is mounted on translation stages with sub-micrometric precision. The laser energy is adjusted using half wave plate with polarizing cube before the SLM to ensure a constant fluence on the device as well as proper and fine polarization orientation for pure phase modulation.

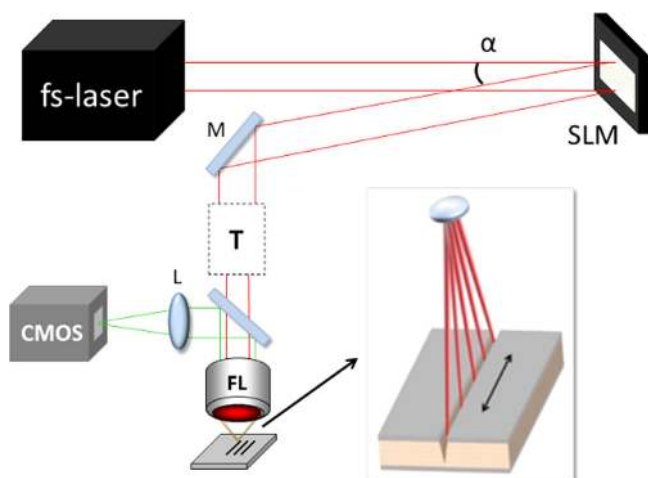


Fig. 1. Experimental setup M: mirror, T: telescope, L: lens, FL: focusing objective or lens, α : reflection angle (4°). The inset shows the sample translation direction with respect to the line of laser spots.

Density filters are positioned in front of the FL to adjust the laser fluence on the sample (not shown).

Using an Iterative Fourier Transform Algorithm (IFTA) based on the Gerchberg–Saxton algorithm [15], we have calculated phase masks to generate the lines of 3, 4, 5 and 7 laser spots with constant peak intensity or with an arbitrary gradient. The central spot of the intensity distribution was set to a lower relative intensity in the target processed by the IFTA. This permits to compensate for excess of intensity in the 0th order of diffraction and thus control the experimental regularity of the spots. To generate a single laser spot, the SLM was displaying a uniform phase mask. An additional laser beam analyzer (not shown) with a higher magnification has been used for fine spatial characterization of the laser intensity profile before any sample machining to ensure the success of the phase modulation to generate the line of laser spots. The laser fluence cartographies presented in the following were calculated from the measured pulse energy, and correspond to peak fluences.

Micro-grooves and micro-cutting were achieved by translating in a single scan the sample during femtosecond irradiation with continuous air blowing. The beam polarization is perpendicular to the translation direction. The lens focal plane is precisely adjusted on the surface of the sample. To evaluate the cross sectional profile of the micro-grooves, the samples were immersed in an ultrasonic bath for cleaning and mechanically cut perpendicularly to the micro-grooves with a diamond saw. Then samples were immersed in a self-polymerizing liquid and polished to reveal the micro-groove cross sections which were observed under episcopic microscopy. Scanning Electron Microscopy was also used to observe the aspect on the nano-scale of the walls after cutting of PZT.

3. Results and discussion

3.1. Comparison of micro-cutting with single and multiple laser spots

Micro-cutting of PZT samples was achieved using the femtosecond beam focused into a single spot or into a line of several spots. Fig. 2 presents the phase modulation applied to the SLM and the corresponding experimental laser intensity distributions for various FL. The efficiency of the beam shaping apparatus ensures a good control of the beam shape. The spot profiles in the line shaping in all cases are regular (less than 10% variation in peak intensity) and are identical to the single spot. The laser power was adjusted with the density filter to obtain the same peak fluence per spot in the single spot and in the multi-spot operation. There were no necessity of screening the usually problematic 0th order of diffraction [19] as it was used as one of the processing spots, thus yielding a better transmission of the whole beam shaping and focusing system (60%).

Micro-cutting of 180 μm thick PZT sample was conducted using the above-mentioned beam profiles in order to put in light the gain of speed using the spatially-shaped intensity distribution. Fig. 1 presents the experimental results of the number N_{scan} of laser scans necessary to cut the 180 μm thick PZT sample for single and multi-spot operation for the two lenses. The scanning speed was 2 mm/s in all cases and the scanning length was 2 mm. As an indication, the Rayleigh length associated to the 50 mm and 25 mm lens are 350 μm and 1400 μm respectively, well above the desired cutting depth.

The gain of speed with the multi-spot operation is evident from the data in Fig. 3. For the 50 mm lens, the number of scans to achieve sample cutting is divided by around three compared to the single spot machining. This coefficient corresponds to the number of simultaneous machining spots. This relationship is also noticeable from the total number of pulses necessary to cut through the sample.

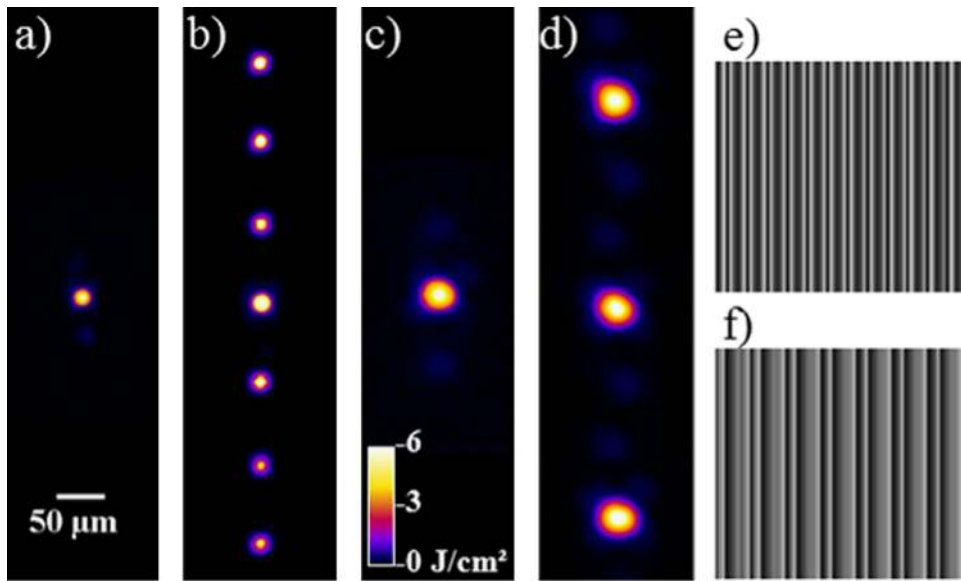


Fig. 2. Experimental beam profiles using a 25 mm (a and b) and a 50 mm (c and d) converging lens with phase modulation to generate the spot line (b and d) and without, yielding a single laser spot (a and c). (e and f) represent the phase modulation applied on the SLM to generate the spot line (b and d) respectively. The spots obtained with the phase modulation are identical (fluence, profile) to the single spot for a given lens.

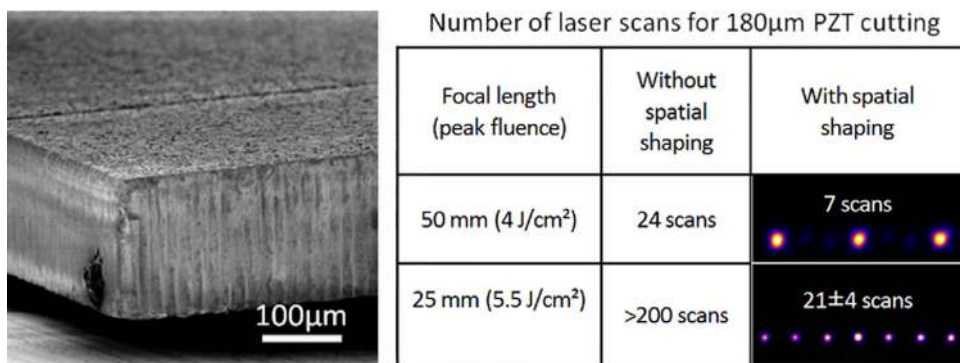


Fig. 3. Comparison of cutting speeds for single and multi-spot machining on an 180 μm thick PZT sample. Left: Scanning Electron Microscopy picture of after cutting. Right: table comparing the number of needed laser scans at 2 mm/s to achieve a complete cut of the 180 μm thick PZT sample with and without multi-spot spatial shaping for two focusing lenses. A line of 3 spots was generated with the 50 mm lens, yielding a gain of time of approximately 3 (7 scans instead of 24). A line of 7 spots was generated with the 25 mm lens, yielding a gain of time of more than 10.

For the 25 mm lens, not only the gain of efficiency is evident, but also a noticeable difference in the machining process appears. Using a single spot, we were not able to cut through the 180 μm of PZT even after more than 200 laser scans, whereas using the multi-spot operation, the cutting was achieved after 21 ± 4 laser scans. The experiment was repeated several times, confirming the saturation of the cutting process in the single spot case (see Fig. 3). We presumably associate this behavior with the lower dynamic of cumulative effects in the case of the single spot, compared to the line of the seven simultaneous processing spots. A more detailed discussion is given in the last section of this paper.

A similar experiment was conducted on stainless steel (316 L) using a focusing objective of 0.3 numerical aperture (20 mm focal length). There, a line of 4 spots was formed with the spatial shaping apparatus (see Fig. 4(b)). The machining of grooves with single and multi-spot operation was compared in terms of groove depth for various scan speeds and different peak fluences. Fig. 4(e) presents an example of a micro-machined groove pictured with optical microscopy after cutting, polymerization and polishing. The peak intensity of each machining spot was precisely adjusted to be the same for the single and multi-spot operation (see Fig. 4(a and b)). In order to have the same energetic dose deposited in the two cases,

one laser scan was applied when using the line of 4 spots whereas 4 successive laser scans were conducted when using the single spot.

The cutting depth, related to the depth of the groove versus the peak laser fluence is presented in Fig. 4(d). As the same depth is obtained for the two processes, a gain of speed by a factor of 4 is demonstrated using the spatially-shaped intensity distribution for all the scanning speeds and fluence levels presented here. This confirms the interest of this beam shaping technique as in the case of PZT cutting.

3.2. Experimental intensity gradient

As an illustration of the flexibility offered by the spatial beam shaping apparatus, an intensity gradient along the spot array was achieved yielding 4 spots of increasing peak intensity. The experimental conditions were the same as described in the previous paragraph. The experimental profile of the gradient is shown in Fig. 5(b). The total power for irradiation was the same as for the previous case with the line of 4 uniform spots. Therefore the peak laser fluences of the different spots in the gradient were above and below the level of the 4 uniform spots configuration. The machining

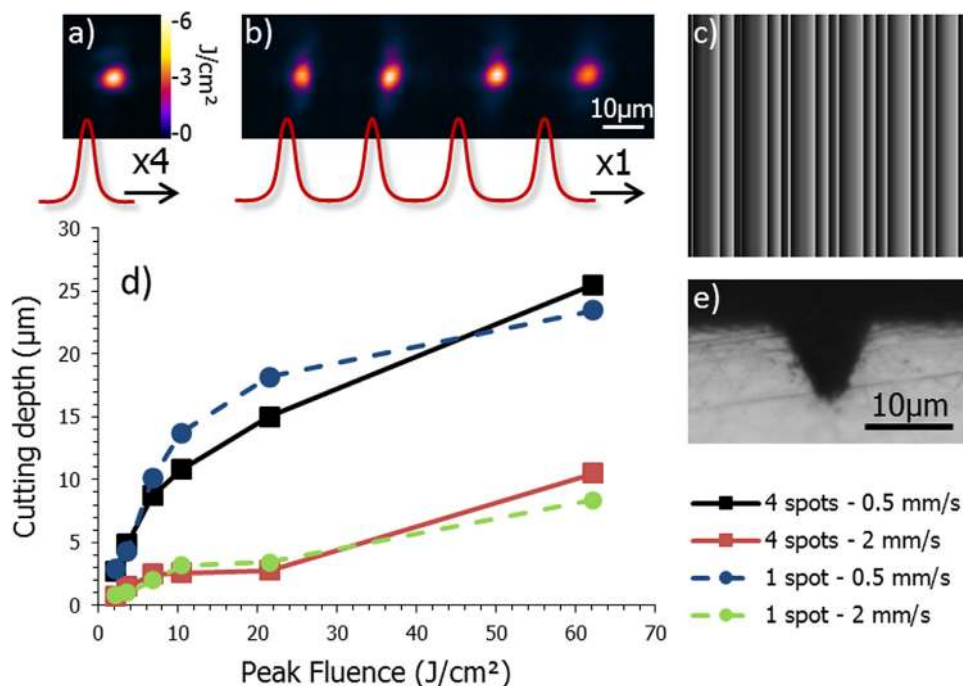


Fig. 4. Comparison of cutting speeds for single and multi-spot machining on stainless steel. Intensity distribution on the sample for single (a) and multi (b) spot operation. (c) Phase mask applied to generate the line of 4 spots. (d) Cutting depth versus peak laser fluence for different translation speeds. Squares: after one laser scan with the 4-spots line. Disks: after 4 laser scans with the single spot (a). The achieved cutting depth is the same in the two cases also for the two scanning speeds showing the expected 4-times gain in processing time with the 4 spots line. (e) Example of micro-machined groove under optical microscopy.

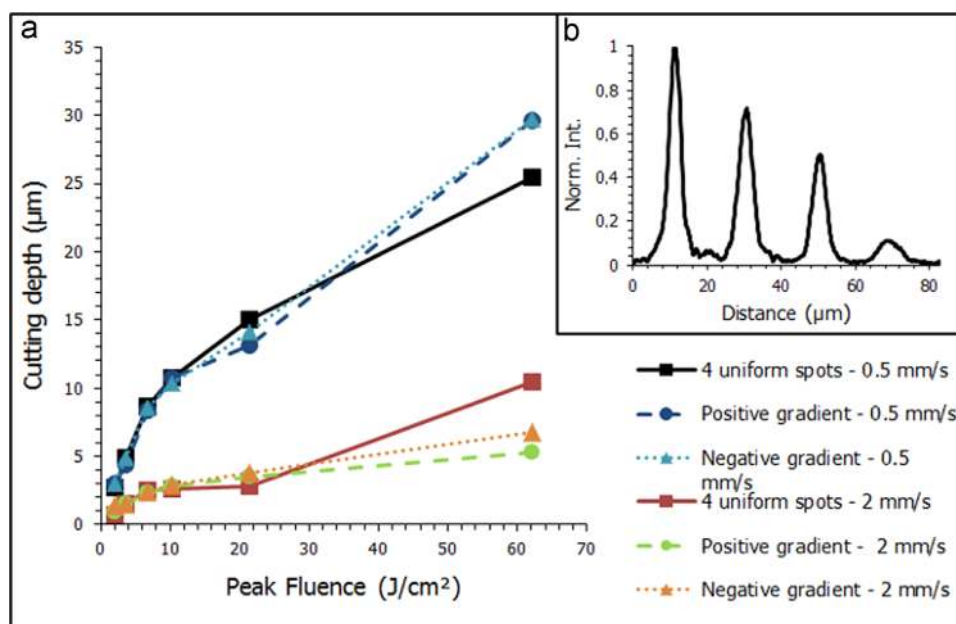


Fig. 5. Comparison of cutting speeds for multi-spot machining on stainless steel with uniform and gradient intensity (a) cutting depth versus peak laser fluence for different translation speeds. Squares: after one laser scan with the uniform 4-spots line. Disks: after one laser scan with the positive gradient distribution (experimental profile of is given in (b), the weaker spot opened the way on the sample). Triangles: after one laser scan with the negative gradient distribution (the stronger laser spot was first on the sample). The achieved cutting depth is similar in the three cases also for the two scanning speeds.

of microgrooves on stainless steel was performed using this intensity distribution with the sample scan along the spot line in the direction of the gradient (denoted as positive gradient – the disks – in Fig. 5(a)) and in the opposite direction for various scan speeds (triangles in Fig. 5(a)). Fig. 5 presents the cutting depths versus the peak laser fluence for the positive, negative gradient and the uniform line of spots. The cutting speed appears constant regardless

of the intensity gradient. Looking closer at the fluence levels in play here, one realizes that we remain well above the ablation threshold even for the weaker spots. Therefore, it is expected that the intensity gradient do not affect the cutting depth. However, the idea here was to illustrate the potential of the technique and may have applications for other types of materials exhibiting deviations from linear behaviors from upon, accumulation.

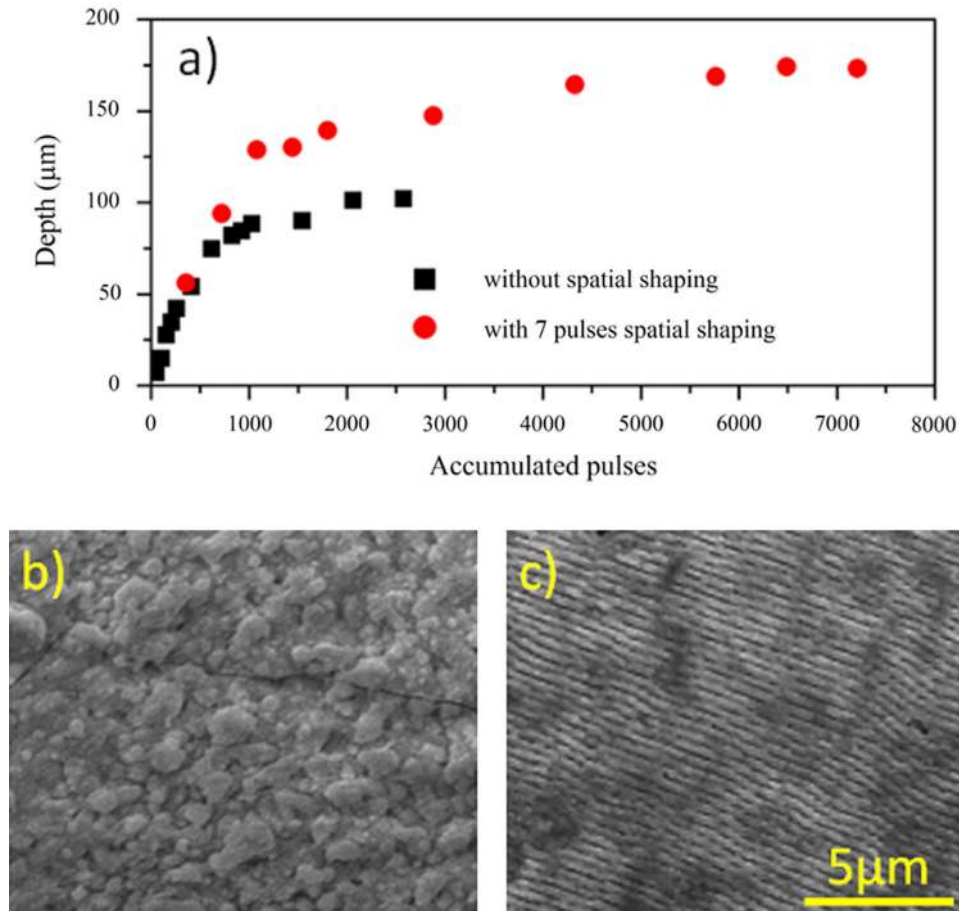


Fig. 6. (a) Cutting depth with respect to the number of accumulated femtosecond pulses in the single spot operation (black squares) and 7-spot operation (red disks) with the 25 mm lens. A saturation of the cutting process appears earlier without spatial shaping presumably due to a lower dynamic of cumulative effects with the single spot. (b) SEM pictures of the walls after cutting the 50 mm focal lens, 3 points shaping at 2 mm/s and (c) the 50 mm focal lens, 3 points shaping at 8 mm/s.

3.3. Surface quality after cutting, cumulative effects

Having in mind the laser repetition rate (5 kHz) and the ultrashort pulse duration, it is not expected to observe significant accumulation effects [22,23] even at low cutting speeds. However, the results on PZT presented in Fig. 3 for the 25 mm lens denote a clear increase in the cutting pace when using a line of 7 spots. Noteworthy, not only the cutting speed is augmented, but it is only with the 7 spots line that the cutting through the 180 μm thick sample is achieved. On the contrary, using a single spot, a cutting saturation is observed. As the only difference between the two processes is the number of pulses during one scan, (7 times higher in the case of the 7 spots line beam shape), a dynamic accumulation effect is therefore expected to explain the higher cutting speed observed with the 7 spots line. A more detailed investigation of the phenomena is reported in Fig. 6(a). There, the cutting depth is plotted versus the number of accumulated pulses (calculated with the top hat approximation [24]) for single spot cutting and 7 spot line cutting. While the single spot machining saturates after 1000 accumulated pulses at a depth of approximately 100 μm, the multi-spot method reaches 180 μm before saturation. In order to clarify the situation, the surface of the PZT wall after cutting through the 180 μm thick sample is observed under SEM (see Fig. 6(b and c)). With same cutting parameters (50 mm lens and a line of 3 spots) and a different scanning speed, Fig. 6(b and c), do not present the same surface finishing. The slower scanning speed at 2 mm/s generates a fleecy texturation probably due to matter re-deposition, while the faster 8 mm/s case

exhibits well defined ripples usually associated with a softer ablation and a lower onset of accumulation effects. Let us determine the possible role of thermal accumulation.

Briefly, cumulative thermal processes are supposed to occur when the cooling time τ_c is longer than the duration between two laser pulses τ_r . For PZT, the energy deposited by one pulse can be estimated by the optical penetration depth l_{abs} at low fluences ($< 10 \text{ J/cm}^2$ for PZT [24]).

From a previous study on the PZT ablation gives $l_{abs} \approx 158 \text{ nm}$ [24]. Considering $\tau_c = l_{abs}^2/D$ [25] where D is the thermal diffusivity ($\sim 3.6 \cdot 10^{-7} \text{ m}^2/\text{s}$ for PZT), we obtain a cooling time $\tau_c = 70 \text{ ns}$ which is more than four orders of magnitude below the duration between two irradiations ($\tau_r = 0.2 \text{ ms}$) at the repetition rate employed here (5 kHz), meaning that the material has time to cool down between to pulses, regardless of the beam shape (single spot or multispot). Therefore, thermal effects only cannot explain the cutting speed difference nor the surface finishing discrepancy. Dynamic cumulative effects possibly linked to material fatigue and incubation may be responsible. A detailed discussion on cumulative effects is beyond the scope of this paper (see [26] for a detailed investigation and optimization of PZT cutting). However, these results put in light possible limitations of ultrafast micro-machining with a line of spots due to higher recovering rates than single spot machining.

However, this also depends on the material properties. For instance, this behavior was not observed on stainless steel where no cutting speed difference was observed between the 4 spot line and 4 scans with a single spot – see Fig. 4(d).

4. Conclusion

We propose and successfully employ an efficient technique to increase the cutting speed and energy efficiency of ultrafast laser micro-cutting by generating a line of N laser spots in the focal plane of a lens. Micro-cutting is then conducted by translation of the sample along the spot line. This method avoids restriction on the cutting trajectory length and increases the cutting speed and energy efficiency of the process compared to single spot machining. Successful cutting of PZT ceramic and stainless steel is demonstrated with the spot line. The processing time is compared to single spot machining showing the advantage of the technique with various focal lenses. We also investigate the effect of intensity gradient on the spots line for micro-cutting on stainless steel. The efficiency and limitations of the method is discussed in light of the surface characterization using scanning electron microscopy on PZT.

Acknowledgment

We gratefully acknowledge the support of Equipex Manutech-USD (ANR-10-EQPX-36-01) and OSEO Artemis (0904148W) funding.

References

- [1] Nolte S, Momma C, Jacobs H, Tunnermann A, Chichkov BN, Wellegehausen B, et al. *J Opt Soc Am B* 1997;14:2716–22.
- [2] Rizvi NH. *Riken Rev* 2003;50:107–12.
- [3] Liu X, Du D, Mourou G. *IEEE J. Quant Electron* 1997;33:1706–16.
- [4] Wang HC, Zheng HY, Chu PL, Tan JL, Teh KM, Liu T, et al. *Appl Phys A* 2010;101:271–8.
- [5] Kamlage G, Bauer T, Ostendorf A, Chichkov BN. *Appl Phys A* 2003;77:307–10.
- [6] Wang XC, Zheng HY, Chu PL, Tan JL, Teh KM, Liu T, et al. *Opt Lasers Eng* 2010;48:657–63.
- [7] Korte F, Serbin J, Koch J, Egbert A, Fallnich C, Ostendorf A, et al. *Appl Phys A* 2003;77:229–35.
- [8] Chung S, Mazur E. *J Biophoton* 2009;2:557–72.
- [9] Dumas V, Rattner A, Vico L, Audouard E, Dumas JC, Naisson P, et al. *Mater Res A* 2012;100(11):3108.
- [10] Mourier L, Mazuyer D, Lubrecht AA, Donnet C, Audouard E. *Wear* 2008;264(5–6):450–6.
- [11] Bizi-Bandoki P, Benayoun S, Valette S, Beaugiraud B, Audouard E. *Appl Surf Sci* 2011;257:5213–8.
- [12] Dusser B, Sagan Z, Soder H, Faure N, Colombier JP, Jourlin M, et al. *Opt Express* 2010;18:2913–23.
- [13] Bruneel D, Matras G, le Harzic R, Huot N, Koenig K, Audouard E. *Opt Laser Eng* 2010;48(3):268–71.
- [14] Pietroy D, Di Maio Y, Moine B, Baubeau E, Audouard E. *Opt Express* 2012;31:29900–8.
- [15] Sanner N, Huot N, Audouard E, Larat C, Huignard J-P, Loiseaux B. *Opt Lett* 2005;30:1479–81.
- [16] Maclair C, Cheng G, Huot N, Audouard E, Rosenfeld A, Hertel IV, et al. *Opt Express* 2009;17:3531–42.
- [17] Campbell S, Triphan SMF, El-Agmy R, Greenaway AH, Reid DT. *J Opt A* 2007;9:1100–4.
- [18] Glückstad J. *Opt Commun* 1996;130:225–30.
- [19] Kuang Z, Liu D, Perrie W, Edwardson S, Sharp M, Fearon E, et al. *Appl Surf Sci* 2009;255(13–14):6582–8.
- [20] Hayasaki Y, Sugimoto T, Takita A, Nishida N. *Appl Phys Lett* 2005;87:031101.
- [21] Hasegawa S, Hayasaki Y, Nishida N. *Opt Lett* 2006;31:1705.
- [22] Mannion PT, Magee J, Coyne E, O'Connor GM, Glynn TJ. *Appl Surf Sci* 2004;233:275–87.
- [23] Di Niso F, Gaudiuso C, Sibillano T, Mezzapapa FP, Ancona A, Lugarà PM. *Opt Express* 2014;22:12200–10.
- [24] Di Maio Y, Colombier JP, Cazottes P, Audouard E. *Opt Laser Eng* 2012;50(11):1582–91.
- [25] Gamaly E. *Phys Rep* 2011;508:91–243.
- [26] Di Maio Y. Etude de l'interaction laser matière en régime d'impulsions ultra courtes: applications au micro usinage de matériaux destination de senseurs. (Ph.D. thesis). Université Jean Monnet St Etienne; 2013.

7.6 Ultrafast laser spatial beam shaping based on Zernike polynomials for surface processing

Julien Houzet, Nicolas Faure, Mathieu Larochette, A-C Brulez, Stephane Benayoun, and Cyril Mauclair (2016). “Ultrafast laser spatial beam shaping based on Zernike polynomials for surface processing”. In: *Optics express* 24.6, pp. 6542–6552

This paper corresponds to the postdoctoral stay of J. Houzet in the frame of the ANR Topoinjection project with the LTDS laboratory as the lead partner. Arbitrary controlled groove section were demanded by the consortium. To achieve this in a efficient manner, we developed a wavefront shaping strategy based on the adjustments of the Zernike polynomials. Using a self learning routine, the algorithm eventually found a proper phase mask that could modulate the beam intensity distribution, thus forming the desired ablation profile upon scanning. This pioneering work, involving a self-learning loop, is also original considering that the phase mask calculation takes into account the experimental limitations of the phase modulator.

Ultrafast laser spatial beam shaping based on Zernike polynomials for surface processing

J. Houzet,¹ N. Faure,^{1,2} M. Larochette,³ A.-C. Brulez,^{3,4} S. Benayoun,³ and C. Maclair^{1,2,*}

¹Laboratoire Hubert Curien, UMR 5516 CNRS, Université de Lyon, Université Jean Monnet, 42000 Saint Etienne, France

²GIE Manutech-USD, 42000 Saint Etienne, France

³Laboratoire de Tribologie et Dynamique des Systèmes, UMR CNRS 5513, Ecole Centrale de Lyon, 36 avenue Guy de Collongues, 69134 Ecully cedex, France

⁴Laboratoire de Génie de la Fonctionnalisation des Matériaux Polymères, Institut Textile et Chimique de Lyon, 87 chemin des Mouilles, 69134 Ecully cedex, France

*cyril.maclair@univ-st-etienne.fr

Abstract: In femtosecond laser machining, spatial beam shaping can be achieved with wavefront modulators. The wavefront modulator displays a pre-calculated phase mask that modulates the laser wavefront to generate a target intensity distribution in the processing plane. Due to the non-perfect optical response of wavefront modulators, the experimental distribution may significantly differ from the target, especially for continuous shapes. We propose an alternative phase mask calculation method that can be adapted to the phase modulator optical performance. From an adjustable number of Zernike polynomials according to this performance, a least square fitting algorithm numerically determines their coefficients to obtain the desired wavefront modulation. We illustrate the technique with an optically addressed liquid-crystal light valve to produce continuous intensity distributions matching a desired ablation profile, without the need of a wavefront sensor. The projection of the experimental laser distribution shows a 5% RMS error compared to the calculated one. Ablation of steel is achieved following user-defined micro-dimples and micro-grooves targets on mold surfaces. The profiles of the microgrooves and the injected polycarbonate closely match the target (RMS below 4%).

© 2016 Optical Society of America

OCIS codes: (140.3300) Laser beam shaping; (070.7145) Ultrafast processing; (350.3390) Laser materials processing.

References and links

1. B. Chichkov, C. Momma, S. Nolte, F. von Alvensleben, and A. Tuennermann, "Femtosecond, picosecond and nanosecond laser ablation of solids," *Appl. Phys. A* **63**, 109–115 (1996).
2. Y. D. Maio, J. Colombier, P. Cazottes, and E. Audouard, "Ultrafast laser ablation characteristics of pzt ceramic: Analysis methods and comparison with metals," *Opt. Lasers Eng.* **50**, 1582–1591 (2012).
3. X. Zhu, A. Y. Naumov, D. M. Villeneuve, and P. B. Corkum, "Influence of laser parameters and material properties on micro drilling with femtosecond laser pulses," *Appl. Phys. A* **69**, S367–S371 (1999).
4. S. Hasegawa, Y. Hayasaki, and N. Nishida, "Holographic femtosecond laser processing with multiplexed phase fresnel lenses," *Opt. Lett.* **31**, 1705–1707 (2006).
5. A. Jesacher and M. J. Booth, "Parallel direct laser writing in three dimensions with spatially dependent aberration correction," *Opt. Express* **18**, 21090–21099 (2010).

6. C. Mauchair, D. Pietroy, Y. D. Mao, E. Baubeau, J.-P. Colombier, R. Stoian, and F. Pigeon, "Ultrafast laser micro-cutting of stainless steel and pzt using a modulated line of multiple foci formed by spatial beam shaping," *Opt. Lasers Eng.* **67**, 212–217 (2015).
7. C. Mauchair, G. Cheng, N. Huot, E. Audouard, A. Rosenfeld, I. V. Hertel, and R. Stoian, "Dynamic ultrafast laser spatial tailoring for parallel micromachining of photonic devices in transparent materials," *Opt. Express* **17**, 3531–3542 (2009).
8. J. P. Parry, R. J. Beck, J. D. Shephard, and D. P. Hand, "Application of a liquid crystal spatial light modulator to laser marking," *Appl. Opt.* **50**, 1779–1785 (2011).
9. S. Hasegawa and Y. Hayasaki, "Adaptive optimization of a hologram in holographic femtosecond laser processing system," *Opt. Lett.* **34**, 22–24 (2009).
10. M. Silvennoinen, J. Kaakkunen, K. Paivasaari, and P. Vahimaa, "Parallel femtosecond laser ablation with individually controlled intensity," *Opt. Express* **22**, 2603–2608 (2014).
11. C. Mauchair, S. Landon, D. Pietroy, E. Baubeau, R. Stoian, and E. Audouard, "Ultrafast laser machining of micro grooves on stainless steel with spatially optimized intensity distribution," *J. Laser Micro Nanoen.* **8**, 11–14 (2013).
12. V. Arrizón, U. Ruiz, R. Carrada, and L. A. González, "Pixelated phase computer holograms for the accurate encoding of scalar complex fields," *J. Opt. Soc. Am. A* **24**, 3500–3507 (2007).
13. R. J. Noll, "Zernike polynomials and atmospheric turbulence," *J. Opt. Soc. Am.* **66**, 207–211 (1976).
14. A. Jewel, V. Akondi, and B. Vohnsen, "A direct comparison between a mems deformable mirror and a liquid crystal spatial light modulator in signal-based wavefront sensing," *J. Eur. Opt. Soc, Rapid Publ. A* **8** (2013).
15. L. Zhu, P.-C. Sun, D.-U. Bartsch, W. R. Freeman, and Y. Fainman, "Wave-front generation of zernike polynomial modes with a micromachined membrane deformable mirror," *Appl. Opt.* **38**, 6019–6026 (1999).
16. E. J. Fernández and P. Artal, "Membrane deformable mirror for adaptive optics: performance limits in visual optics," *Opt. Express* **11**, 1056–1069 (2003).
17. K. Nemoto, Y. Kazu Kanai, T. Fujii, N. Goto, and T. Nayuki, "Transformation of a laser beam intensity profile by a deformable mirror," *Opt. Lett.* **21**, 168–170 (1996).
18. C. Schulze, A. Dudley, D. Flamm, M. Duparré, and A. Forbes, "Reconstruction of laser beam wavefronts based on mode analysis," *Appl. Opt.* **52**, 5312–5317 (2013).
19. N. Sanner, N. Huot, E. Audouard, C. Larat, J.-P. Huignard, and B. Loiseaux, "Programmable focal spot shaping of amplified femtosecond laser pulses," *Opt. Lett.* **30**, 1479–1481 (2005).
20. P. Mannion, J. Magee, E. Coyne, G. O. Connor, and T. Glynn, "The effect of damage accumulation behaviour on ablation thresholds and damage morphology in ultrafast laser micro-machining of common metals in air," *Appl. Surf. Sci.* **233**, 275–287 (2004).
21. N. Sanner, N. Huot, E. Audouard, C. Larat, P. Laporte, and J. Huignard, "100-khz diffraction-limited femtosecond laser micromachining," *Appl. Phys. B* **80**, 27–30 (2004).
22. J. Hahn, H. Kim, K. Choi, and B. Lee, "Real-time digital holographic beam-shaping system with a genetic feedback tuning loop," *Appl. Opt.* **45**, 915–924 (2006).
23. D. Pietroy, E. Baubeau, N. Faure, and C. Mauchair, "Intensity profile distortion at the processing image plane of a focused femtosecond laser below the critical power: analysis and counteraction," *Opt. Lasers Eng.* **66**, 138–143 (2015).
24. A. Ancona, F. Röser, K. Rademaker, J. Limpert, S. Nolte, and A. Tünnermann, "High speed laser drilling of metals using a high repetition rate, high average power ultrafast fiber cpa system," *Opt. Express* **16**, 8958–8968 (2008).
25. C. J. Zapata-Rodríguez and M. T. Caballero, "Ultrafast beam shaping with high-numerical-aperture microscope objectives," *Opt. Express* **15**, 15308–15313 (2007).

1. Introduction

Femtosecond laser utilisation for surface micromachining has been widely studied in past years [1–3]. The main advantage of ultrashort light pulses lies in their particular interaction with materials where very restricted thermal and collateral effects are observed compared to longer irradiations (nanosecond and beyond). Very accurate ablation profiles with a precise control of the removed layer thickness (down to a few tens of nm) can thus be achieved. Spatial beam shaping aims at controlling the intensity distribution in the processing plane by means of wavefront modulation [4]. Dynamic wavefront modulators can be divided in two main families, the Spatial Light Modulators (SLM) based on an addressable liquid crystal layer and Deformable Mirrors (DM) based on a reflective surface.

Due to their high resolution, SLMs permit to deal with high spatial frequency phase masks involving sharp phase jumps. SLMs are highly suitable for multispot operation processes [5, 6].

This has a major interest in reducing the processing time and cost of femtosecond machining [7]. However, due to their imperfect optical response, these devices induce deformations of the experimental intensity distribution when compared to the desired one [8].

To compensate for these shaping discrepancies, research groups have proposed optical feedback loops based on a measurement of the experimental intensity distribution enabling homogenization of multispot distributions [9, 10]. In the case of continuous intensity targets, solutions based on averaging the shaping discrepancies by beam scanning on the sample [11], phase mask change during irradiations [8] or spatial filtering in a Fourier plane [12] have been reported, though adding a constraint to the laser process. Nevertheless, the calculated phase mask (using Iterative Fourier Transform Algorithm, lens and grating [5], Multi Fresnel lenses [4]) cannot be perfectly reproduced by the SLMs. There is a need of a phase mask calculation strategy that takes into account the limitations of the SLMs optical response. These limitations, regardless of their physical origin, can be described with the help of Zernike polynomials [13] as they constitute an orthogonal basis of surface functions on the unit circle. Thus the limitations of any modulator's optical response can be defined evaluating the ability of the modulator to correctly reproduce a set of Zernike polynomials [14, 15]. This characterization can also be conducted on any other orthogonal basis, e.g the spatial modes of a DM [16].

The DM can also be used to perform laser spatial beam shaping [17]. Currently, the maximum resolution is attained by MEMS DM having a few thousands of actuators of $300\mu\text{m}$ pitch. If DM are able to generate continuous phase modulations, their restricted resolution limits their optical response and their capacity to reproduce a calculated phase mask. Since both DMs and SLMs cannot perfectly reproduce phase masks for beam shaping, there is a need to consider the wavefront modulator limitations in the phase mask computation.

We propose a calculation strategy of the modulation phase mask for a desired target intensity that takes into account the limited optical response of the phase modulator in terms of Zernike polynomials. We apply it to generate arbitrary continuous intensity shapes. It is an alternative to other phase mask calculation algorithms (such as Iterative Fourier Transform Algorithm, lens and grating, Multi Fresnel lenses...) that disregard the phase modulator ability to reproduce the phase mask. The advantage of our method is that the number of Zernike polynomials coefficients involved in the calculation can be adjusted to the performance of the wavefront modulator that is employed. Indeed, the optical performance of a wavefront modulator is often characterized by the number of well-reproduced Zernike polynomials [15, 16]. Taking this optical response into account is not easily achievable with the usual phase mask calculation algorithms. The proposed calculation determines the coefficients of a chosen number of Zernike polynomials, each of them having an effect on the laser intensity distribution after propagation [18]. To illustrate the technique, an optically addressed liquid-crystal light valve is used as a programmable wavefront tailoring device [19]. The phase mask is calculated using a least-square fitting algorithm on an adjustable number of Zernike polynomials coefficients [13], optimized to generate a user-defined intensity distribution in the far field. The latter is related to a desired groove profile on steel by the experimental ablation rate [11]. We demonstrate the efficiency of the technique with numerical calculations of phase masks for target intensities and experimental intensity shaping along with characterizations of the laser-processed surfaces. We point out that no wavefront measurements was necessary as the phase modulation is numerically calculated and then displayed on the SLM for experimental evaluation of intensity distribution shaping. The comparison between experimental and numerically calculated laser distributions reveals a low RMS error ($< 5\%$) on cross section. The technique is demonstrated in the case of surface processing, where laser-machined grooves and dimples on steel molds are evaluated using classic and interferometric microscopy. The groove depth closely matches the expected profile (RMS $< 4\%$). As a further illustration, the surface of the corresponding injected polycarbonate

is presented, showing the desired profile as well.

2. Experimental details

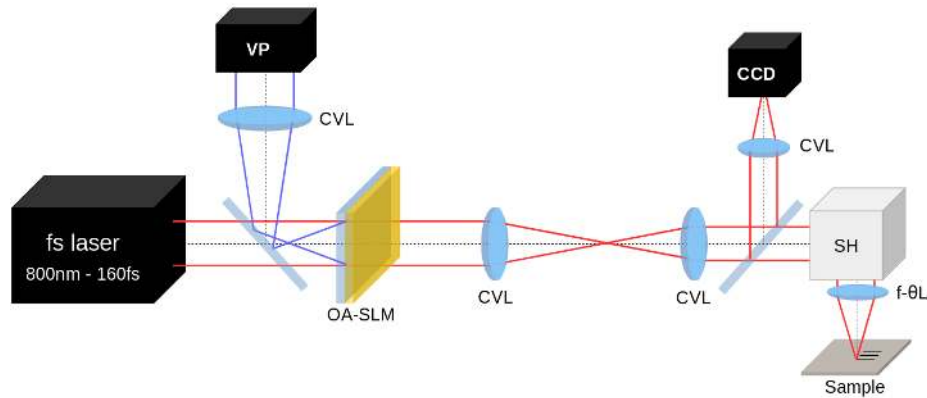


Fig. 1. Scheme of the experimental set-up. The femtosecond laser wavefront is spatially modulated by the optically addressed spatial light modulator (OA-SLM). The phase mask displayed by the video projector (VP) is imaged on the OA-SLM by a converging lens (CVL). The plane OA-SLM plane is optically conjugated with the object focal plane of the scanner head (SH) f-theta lens ($f\text{-}\theta\text{L}$) through a telescope (100 cm and 75 cm focal lengths). The shaped intensity distribution is employed to process the sample surface and is observed at the focal plane of a lens on a CCD sensor. Also a home made beam analysis set up (not shown) with the same CCD sensor has been used to measure the intensity in the focal plane of the f-theta lens.

As depicted on Fig. 1, a femtosecond amplified laser system (Thales Bright) operating at a repetition rate of 5 kHz delivers 160 fs light pulses at 800 nm with a maximum average power of 2 W, a linear polarization and a spectral bandwidth of 8 nm. The laser beam goes through an optically addressed SLM (OA-SLM). The phase modulation is achieved with a blue light beam impinging a photo-conductive layer stuck to the liquid crystal layer (parallel nematic). The nonpixelated OA-SLM has a spatial resolution close to $100\ \mu\text{m}$ on a 1 cm diameter pupil. Its measured dynamic phase range, linked to the thickness of the liquid-crystal layer, is 6π or 3λ at 800 nm. The device can handle 1 W of the femtosecond laser power. We have experimentally verified that the OA-SLM does not affect the laser pulse duration with autocorrelation measurements. Further details can be found in [19]. By displaying a grey level mask with a video projector imaged on the OA-SLM, the optical retardation due to the liquid crystal molecules orientation is modulated in two dimensions. The femtosecond beam wavefront thus is modulated and therefore spatially shapes the beam intensity distribution in the far field. The beam is enlarged before the OA-SLM and truncated by an iris of 1 cm diameter just before passing through the OA-SLM in order to approach an uniform illumination. Considering the $100\ \mu\text{m}$ spatial resolution over the 1 cm active area and the phase stroke, we can securely say that this modulator permits to address a very large number of Zernike polynomials, up to at least 30. After the OA-SLM, the beam is reduced in size passing through a telescope constituted of two converging lenses of 75 cm and 100 cm focal lengths. The telescope is positioned to optically conjugate the SLM plane with the object focal plane of the F-theta lens of a scanner (ScanLab). This lens focuses (focal length = 88 mm) the laser beam on a steel surface and allows for rapid beam scanning on the surface for groove micro processing. The beam profile is

measured with a CCD sensor (Thorlabs DCU224M) at the focal plane of a long focal length lens and as well in the focal plane of the F-theta lens using a home made beam analyser. The steel (X105CrMo17) is a specific metal for injection molds.

First, the steel ablation rate (i.e the depth of ablated material per pulse with respect to the laser fluence [20]) was experimentally determined for fluences below 1 J/cm^2 . For fluences below 1 J/cm^2 , in the so-called gentle ablation region on steel (see [20]), the empirical relationship between the ablated depth per pulse and the laser fluence can be approximated with a logarithmic function [11]. For the X105CrMo17 steel, the ablation rate relating the laser peak fluence F in J/cm^2 to the depth D of the ablated layer per pulse in nm could be experimentally approximated by $D = 40 \times \log F + 45$. This permits to calculate the target fluence distribution from a desired ablation profile, see Fig. 2 (I) and 2 (II). Then, a numerical optimization algorithm (detailed hereafter) determines the Zernike polynomials coefficients permitting to obtain the intensity target, see Fig. 2 (III). The corresponding phase mask, see Fig. 2 (IV), is displayed on the OA-SLM. By going through the OA-SLM, the femtosecond beam is spatially modulated and reaches the surface to be processed with the desired intensity profile.

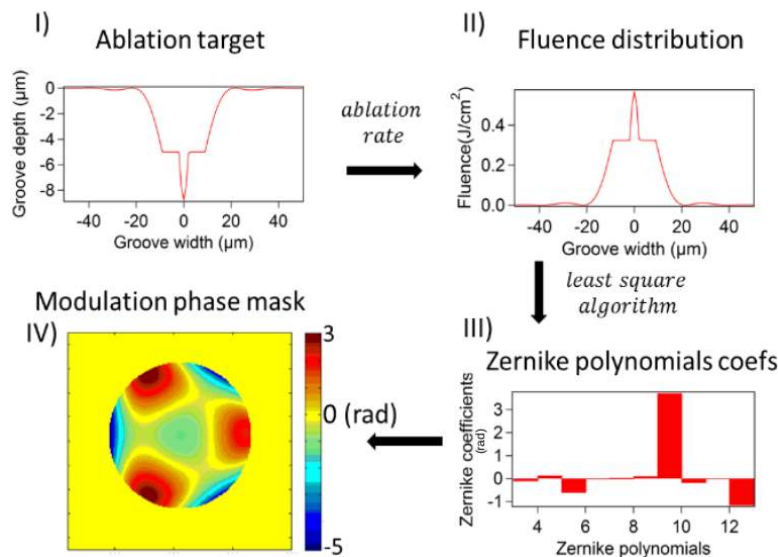


Fig. 2. Calculation strategy for the modulation phase mask I) desired groove profile II) numerical calculation of corresponding fluence distribution based on the empirical ablation rate [11] III) Zernike polynomials coefficients obtained by least square fitting from II) IV) corresponding phase mask obtained numerically that can be applied to the phase modulator. The number of optimized Zernike polynomials can be adjusted according to the performances of the phase modulator.

The optimization algorithm consists of a least square fitting method coupled to a Fresnel propagation code. The least square fitting algorithm iteratively optimizes a vector of Zernike polynomials coefficients C_j (radians) of the wavefront function in radians $W(r, \theta) = \sum_j C_j Z_j(r, \theta)$ where r and θ are polar coordinates on the unity disk and $Z_j(r, \theta)$ a Zernike polynomial following the Noll's sequential indices convention in [13]. At each iteration, the intensity is numerically calculated for the current C_j and the 2D root mean square (RMS) error ϵ_{RMS} between the calculated intensity $I(i, j)$ and the target intensity $I_t(i, j)$ is evaluated following:

$$\epsilon_{RMS} = \frac{\sum_{i,j} (I(i,j) - I_t(i,j))^2}{\sum_{i,j} I_t(i,j)^2} \quad (1)$$

The least square fitting algorithm iteratively minimizes ϵ_{RMS} by optimizing the vector of C_j . The starting vector is constituted of zeros for each Zernike coefficient. Each run of the least square fitting algorithm produces a new vector that is the starting vector for the subsequent run. We have performed 30 to 50 iterations for the results presented hereafter, lasting altogether a few minutes on a standard PC. We mention here that we have also used a simulated annealing approach with very similar phase mask results requiring however a few hundreds of iterations (thus lasting a few tens of minutes on the same PC). The stopping point of the algorithm was defined by the user, when the ϵ_{RMS} started to show little improvement (less than a few %).

The least square fitting method (see Fig. 2) determines the C_j by iteratively reducing ϵ_{RMS} to numerically determine the C_j yielding the desired beam shaping. The optimization is implemented from the third to the twentieth polynomials as the first (piston) and second (tilt) do not modify the shape of the diffracted beam. The piston only creates a constant phase shift equal for every part of the incident beam, and the tilt spatially shifts the diffracted beam.

We underline here that the least square fitting algorithm is not employed with a wavefront sensor for an experimental verification of the applied phase mask on the laser wavefront as for adaptive beam shaping. Instead, the least square fitting method is used for an optimization of the C_j , i.e the calculation of the phase mask. The corresponding calculated phase mask is applied to the optical valve that modulates the femtosecond laser wavefront. The experimental verification of the beam shaping success is conducted by recording the laser intensity distribution in the focal plane of a lens on a CCD sensor. Micro grooves were machined by scanning the shaped beam on the steel sample at a speed of 25 mm/s with 500 passages.

3. Results and discussion

3.1. Phase mask calculations

The numerical results of optimization of C_j to generate a phase mask producing a top hat intensity distribution in the far field are shown in Fig. 3. The target includes the point spread function associated with the focusing lens by a convolution. The influence of number of optimized C_j on the beam shaping accuracy is numerically studied. As the top hat distribution has a circular symmetry, we have used only polynomials with a spherical symmetry, i.e defocus and spherical aberrations (C_4 , C_{11} and so on). When calculating the phase mask generating a top hat distribution with a minimum number of Zernike coefficients (see Fig. 3 first and second rows), we were not able to lower the 2D ϵ_{RMS} between the top hat target and the calculated intensity below 6%. When using just one Zernike coefficient (defocus - Noll's index C_4), it is clear that a top hat distribution is out of reach as adding an aberration of defocus simply enlarges the spot size in the geometrical focal plane of a lens, see Figs. 3(b) and 3(c). In that case, the algorithm finds a coefficient that enlarges the spot size to its best fit with the top hat distribution yielding a ϵ_{RMS} of 11%. When the optimization is conducted on the 3 first spherical Zernike polynomials coefficients, the ϵ_{RMS} drops to 6.4%, see Fig. 3(e) and 3(f). When 5 coefficients are involved, the performance increases with a reduced root mean square errors to 3.1%, see Fig. 3(h) and 3(i). The corresponding optimized phase masks are shown in Fig. 3(a), 3(d), and 3(g). Clearly, this numerical study shows that by using an increased number of optimized C_j , the beam shaping quality is superior in the case of the top hat target.

Additional results are depicted on Fig. 4 for the top hat 4(a) and the three-steps 4(b) intensity profiles. The number of optimized C_j was 5 and 10 respectively. The number of optimized C_j was determined after several trials of the optimization with various number of C_j just as for

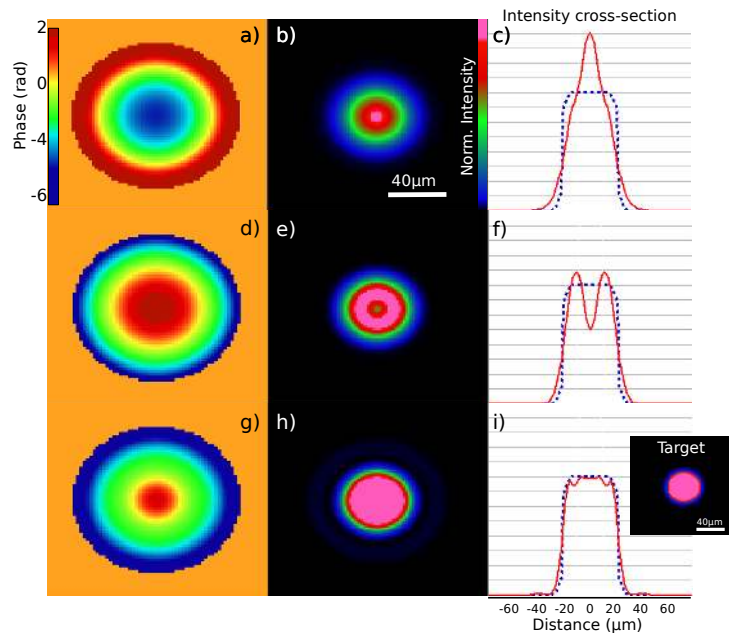


Fig. 3. Numerical results of phase mask calculation through optimization of C_j to achieve a top hat disk intensity distribution for an increasing number of optimized C_j (due to the circular symmetry of the target, only the spherical C_j terms were included here). a) d) and g) Optimized calculated phase modulation shown on the unit circle, b) e) and h) optimized calculated intensity distribution, c), f) and i) cross section of the intensity distribution compared with the target shown in the inset bottom right. First row, optimization of the first spherical term C_4 alone (defocus) yielding a ϵ_{RMS} of 11%. Second row, optimization with the 3 first spherical terms yielding 6.4% ϵ_{RMS} . Third row, with the 5 first spherical terms yielding 3.1% ϵ_{RMS} .

Fig. 3. Here also, the targets include the point spread function influence. The ϵ_{RMS} between the target and the intensity distribution obtained after phase mask optimization is below 5% in both cases. We point out here that the ϵ_{RMS} is calculated slightly differently for the three steps shape. This target comes from a desired ablation profile obtained by beam scanning on a surface. Thus, the calculated intensity levels are accumulated along the direction of beam scanning yielding a vector of accumulated intensity levels. The ϵ_{RMS} is calculated following Eq.(1) in only one dimension. The benefit of the method is that the number of optimized C_j can be tuned according to the SLM or DM's ability to achieve high orders of Zernike polynomials. Naturally, for a SLM or a DM with a limited number of correctly reproduced Zernike polynomials, some intensity targets may remain out of reach. The Fig. 4(c) addresses this point for the three-steps target intensity and the top hat target. Fig. 4 (c) is a numerical calculation of the dependence of best attainable ϵ_{RMS} with the number of C_j . ϵ_{RMS} decreases with the number of optimized C_j for both targets. This result strengthens the intuitive expectation that the more C_j are optimized, the more precise the beam shaping is. Noteworthy, a higher number of optimized C_j is required to obtain a satisfactory three-steps profile (ϵ_{RMS} below 5% for 10 C_j and more), than for the top-hat profile (ϵ_{RMS} below 5% for 4 C_j and more). As a rule of thumb, one may infer that a more complex target (e.g with multiple fluence levels, as for the three-steps profile) requires a

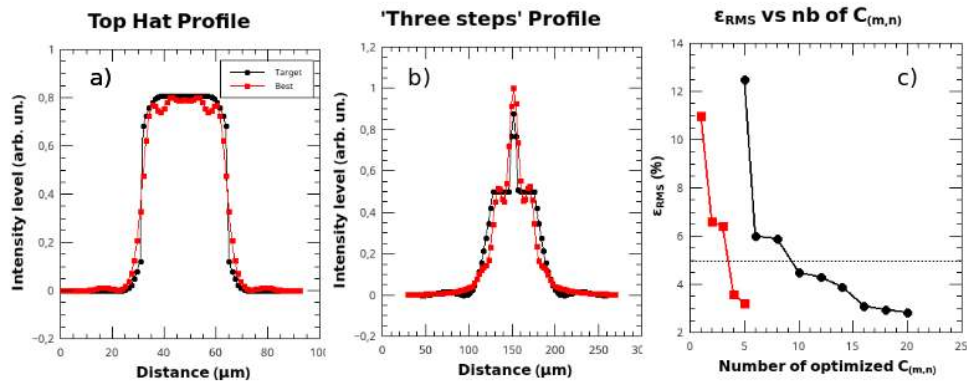


Fig. 4. Numerical results of phase mask calculation through optimization of C_j . Comparison of the calculated intensity cross section (red squares) and the target (black disks) for a top-hat distribution a) and 'three steps' intensity distribution b) at the focal plane of a lens. c) Evaluation of the best attainable RMS error ϵ_{RMS} with the number of C_j involved in the optimization for the top-hat (red squares) and three-steps (black disks) target. A higher number of optimized C_j is required to obtain a satisfactory three-steps profile (ϵ_{RMS} below 5% for 10 C_j and more), than for the top-hat profile (ϵ_{RMS} below 5% for 4 C_j and more).

higher number of optimized C_j than a 'simple' target. Though, a detailed study of this possible trend is outside the scope of this paper. In practice, the number of optimized C_j is a trade-off between a sufficiently low ϵ_{RMS} numerically and the number of C_j correctly reproduced by the SLM.

Among the limitations of the proposed technique, one should mention the reduction of the calculation performance when reducing the number of Zernike coefficients. Also, the computation cost may greatly increase for a large number of C_j and high resolution modulator requiring high sampling rates for the beam propagation calculations. Also, we mention here that this method requires that the phase modulator to be well described by its ability to reproduce Zernike polynomials [3, 14] or other functions forming a basis (e.g spatial modes of a DM [16]) on which the same optimization can be conducted.

3.2. Experimental intensity profiles and surface processing

Experimental intensity distributions are compared to calculated distributions in Fig. 5. The C_j represented on Fig. 2 (III) and the phase mask represented on Fig. 2 (IV) are those that permitted to obtain the experimental shaped beam on Fig. 5(b). The intensity distributions are close to the theoretical ones, although residual aberrations of the optical system worsen the comparison. The spatially shaped beam in a) was obtained by applying 3.7 of vertical trefoil (C_9), -1.17 of 1st order spherical aberration (C_{11}) and -0.61 of vertical astigmatism (C_6). The spatially shaped beam in c) was obtained by applying 2.3 of astigmatism in the x direction (C_5), -3.7 of astigmatism in the y direction (C_6), 0.3 of coma in the y direction (C_7), -0.8 of coma in the x direction (C_8) and 2.8 of 2nd order astigmatism in the x direction (C_{13}). The RMS error between experimental (a) and calculated (b) right spatial is calculated as follows. We recall that the scope of this beam shaping is to generate a groove with a controlled section (three-steps shape). For that, the beam is translated during laser machining along the horizontal direction of Fig. 5. Therefore, for both calculated and experimental beam profiles, a sum of the intensity levels along the scanning direction is achieved, yielding an accumulated intensity profile, similarly to our previous work [11]. The RMS error is then calculated between the

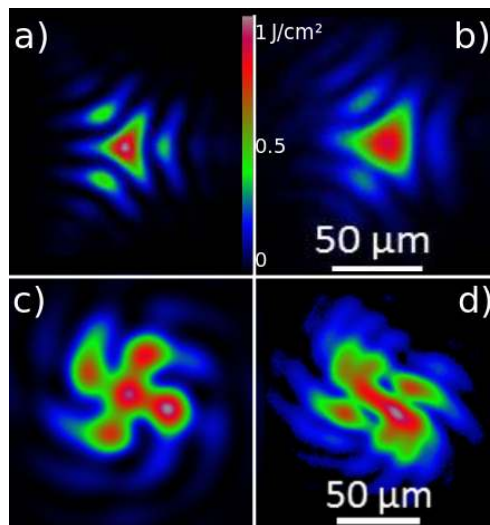


Fig. 5. a), c) theoretical and b), d) experimental intensity distributions of spatially shaped beams in the processing focal plane obtained with phase modulation by the SLM. The beam shape in a) is the intensity distribution that permits to generate a three step shaped micro-groove by scanning the beam on the steel surface along the horizontal direction of this Fig. The Zernike polynomials coefficients C_j permitting to obtain a) are represented in Fig. 2 (III) and the corresponding phase in Fig. 2 (IV).

two profiles and is below 3%. This is a sufficient precision for the surface machining reported hereafter. We underline here that the experimental verification does not require any wavefront sensor, nor adaptive optics loop, which eases the applicability of this method. Naturally, as for any wavefront modulation system, the experimental beam shaping quality can be improved by using an adaptive loop for corrections of the aberrations of the optical system (e.g as we have previously employed [19, 21]). This correction can also be done with the help of Zernike polynomials [14, 22]. However, this is not the scope of this paper that presents a phase mask calculation based on Zernike polynomials as an alternative to more common techniques (Iterative Fourier Transform Algorithm, Lens an gratings...) and demonstrate its applicability to surface machining. Also, this would add complexity to the experimental set up by adding a wavefront sensor and running the adaptive loop. Lastly, the obtained beam shaping quality is more than sufficient for the surface machining application that is discussed hereafter.

To illustrate the potential of this technique in surface machining, some surface processing results (grooves and dimples) achieved using this beam shaping technique are presented in Fig. 6. With rather low peak fluences (below 1 J/cm^2), the interaction takes place in the gentle ablation regime where the ablation shows very low collateral effects [20]. It is well-known that a variety of detrimental effects take place during the light matter interaction e.g nonlinear propagation in the air before reaching the target [23], heat accumulation or particle shielding effect in the case of multiple pulses irradiation [24] with consequences on the energy coupling efficiency and on the post-irradiation surface topology. However, using the empirical fluence/ablation depth relationship presented above is sufficient to assess for the efficiency of the laser beam shaping technique presented here. Moreover, the fairly low repetition rate (5 kHz), peak fluence (1 J/cm^2) and pulse energy puts the interaction on steel in a regime where any nonlinear propagation, heat accumulation or particle shielding effects can be neglected [23, 24].

Figure 6 shows an example of micro-groove (a) and dimples (b) machined on steel observed

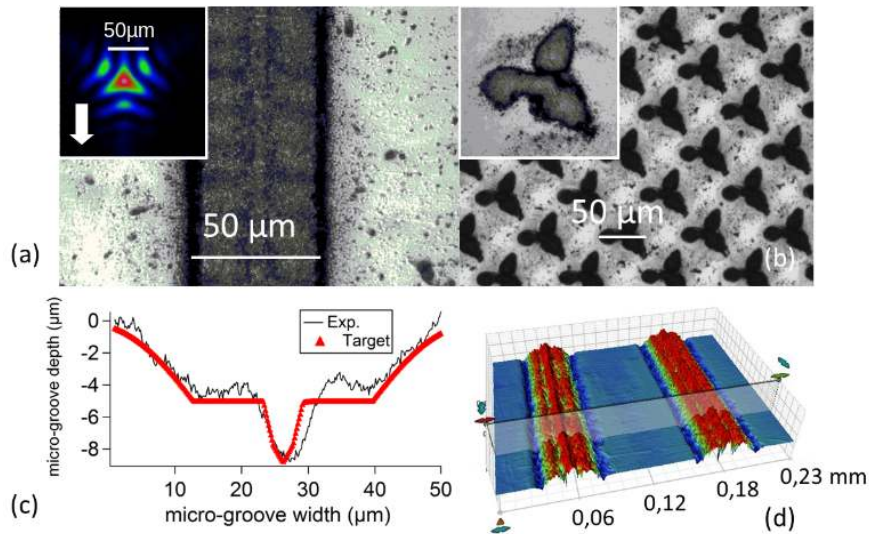


Fig. 6. a): "three-steps" shape micro-groove (optical microscopy) processed by translating the spatially shaped beam illustrated in the insert corresponding to the beam in Fig. 5 (b), b): micro-dimples achieved with the same beam (zoom in the insert). c) horizontal profile of the micro-groove (black line) a) compared to the targeted ablation profile (red triangles), RMS error is below 4%. d) corresponding injected polycarbonate topology (interferometric microscopy).

by optical microscopy. The inset shows the experimental beam profile. The horizontal profile of the micro-groove (a) compares well to the ablation target in Fig. 6(c). The goal here is to obtain a three-steps shaped groove. The micro-groove is obtained by translating the beam in the insert in Fig. 6(a) along the white arrow at a speed of 25 mm/s . The desired three-steps section appears clearly. The RMS error between these the target profile (red triangles) and the actual micro-groove profile (black line) is below 4%. We point out here that the beam was translated with respect to the sample surface with the scanner head while keeping small scanning angles to avoid beam distortions at high scanning angle. In practice the laser-induced micro grooves appeared uniform all along their length (2 cm). The spatially shaped beam was also implemented to generate dimples shown in Fig. 6(b). The resulting three-steps cross sectional profile can not be easily obtained without spatial shaping considering the different intensity levels inside the distribution. These ablation profiles have a strong interest in machining injection molds to confer specific wettability properties on polymer parts. A detailed study of these surface effects will be the subject of a future report. We point out here that this technique is not limited to ultrafast lasers as it relies on a modulation of the spatial wavefront. Indeed, lasers having a thinner spectral bandwidth are more adapted to spatial beam shaping [25]. However, the possibility offered by ultrafast lasers to finely control the ablated layer with the number of pulses and the laser fluence level makes easier the illustration of the possibility to control the ablation profile according to a user-defined fluence distribution, which is a key element of this report.

4. Conclusion

We report on an efficient method to implement Zernike polynomials for ultrafast laser machining of surfaces, and experimentally demonstrate its efficiency with an optically addressed

spatial light modulator. An wavefront modulation function resulting from the sum of different balanced Zernike polynomials is used to modulate the spatial phase of an incident femtosecond beam. The weight of each polynomial is determined by a least square algorithm to fit a user defined target intensity, matching an arbitrary ablation profile. This method allows for unique machining profiles very difficult to reproduce without spatial tailoring because of the different intensity levels inside the distribution. Thanks to the possibility to adjust the number of optimized Zernike coefficients, it can be implemented taking into account the optical performance of the phase modulator. Microtexturations with arbitrary profiles are achieved using this technique on steel injection molds for the fabrication of polymer objects.

Acknowledgments

We gratefully thank Kassem Saab and Razvan Stoian for fruitful discussions. The financial support of ANR Topoinjection (ANR-13-RMNP-0010) and Equipex Manutech-USD (ANR-10-EQPX-36-01) are gratefully acknowledged.

7.7 Delivery of molecules into human corneal endothelial cells by carbon nanoparticles activated by femtosecond laser

Clotilde Jumelle, Cyril Mauclair, Julien Houzet, Aurélien Bernard, Zhiguo He, Fabien Forest, Michel Peoc'h, Sophie Acquart, Philippe Gain, and Gilles Thuret (2015c). "Delivery of molecules into human corneal endothelial cells by carbon nanoparticles activated by femtosecond laser". In: *PloS one* 10.7, e0132023

This work corresponds to the PhD work of C. Jumelle during the ANR SupCo project in collaboration with the BIIGC. Despite the fact that this paper does not report strong advances on the subject of spatial beam shaping and in-situ monitoring, it is still interesting to note that a very fine tuning of the laser beam size and energy was indispensable to find the proper irradiation conditions for cell transfection in a reproducible manner. A home-made brightfield microscope was built to observe the cellular layer and analyze at the same time the femtosecond laser spot in that very plane. Indeed, this was indispensable for reproducible transfection results, showing the importance of in-situ monitoring.

RESEARCH ARTICLE

Delivery of Molecules into Human Corneal Endothelial Cells by Carbon Nanoparticles Activated by Femtosecond Laser

Clotilde Jumelle¹, Cyril Mauclair^{2,3}, Julien Houzet², Aurélien Bernard¹, Zhiguo He¹, Fabien Forest^{1,4}, Michel Peoc'h^{1,4}, Sophie Acquart⁶, Philippe Gain^{1,5}, Gilles Thuret^{1,5,7*}

1 Corneal Graft Biology, Engineering and Imaging Laboratory, EA2521, SFR143, Faculty of Medicine, Saint-Etienne, France, **2** Hubert Curien Laboratory, UMR-CNRS 5516, Pôle Optique Rhône-Alpes, Saint-Etienne, France, **3** GIE Manutech-Ultrafast Surfacing Design, Saint-Etienne, France, **4** Department of Pathology, University Hospital, Saint-Etienne, France, **5** Department of Ophthalmology, University Hospital, Saint-Etienne, France, **6** Eye Bank, Etablissement Français du Sang Loire/Auvergne, Saint-Etienne, France, **7** Institut Universitaire de France, Paris, France

* gilles.thuret@univ-st-etienne.fr



OPEN ACCESS

Citation: Jumelle C, Mauclair C, Houzet J, Bernard A, He Z, Forest F, et al. (2015) Delivery of Molecules into Human Corneal Endothelial Cells by Carbon Nanoparticles Activated by Femtosecond Laser. PLoS ONE 10(7): e0132023. doi:10.1371/journal.pone.0132023

Editor: Alfred S Lewin, University of Florida, UNITED STATES

Received: September 22, 2014

Accepted: June 9, 2015

Published: July 2, 2015

Copyright: © 2015 Jumelle et al. This is an open access article distributed under the terms of the [Creative Commons Attribution License](https://creativecommons.org/licenses/by/4.0/), which permits unrestricted use, distribution, and reproduction in any medium, provided the original author and source are credited.

Data Availability Statement: All relevant data are within the paper.

Funding: This work was supported by grants from the Fédération des Aveugles de France 2012, Jean Monnet University (appel à projet 2012), the Fondation de l'Avenir ET7-468, and by the Equipex MANUTECH-USD (ANR-10-EQPX-36-01) of the Communauté d'universités et établissements (Comue) de Lyon Saint-Etienne, operated by the French National Research Agency (ANR). The funders had no role in study design, data collection

Abstract

Corneal endothelial cells (CECs) form a monolayer at the innermost face of the cornea and are the engine of corneal transparency. Nevertheless, they are a vulnerable population incapable of regeneration in humans, and their diseases are responsible for one third of corneal grafts performed worldwide. Donor corneas are stored in eye banks for security and quality controls, then delivered to surgeons. This period could allow specific interventions to modify the characteristics of CECs in order to increase their proliferative capacity, increase their resistance to apoptosis, or release immunosuppressive molecules. Delivery of molecules specifically into CECs during storage would therefore open up new therapeutic perspectives. For clinical applications, physical methods have a more favorable individual and general benefit/risk ratio than most biological vectors, but are often less efficient. The delivery of molecules into cells by carbon nanoparticles activated by femtosecond laser pulses is a promising recent technique developed on non-adherent cells. The nanoparticles are partly consummated by the reaction releasing CO and H₂ gas bubbles responsible for the shockwave at the origin of cell transient permeation. Our aim was to develop an experimental setting to deliver a small molecule (calcein) into the monolayer of adherent CECs. We confirmed that increased laser fluence and time exposure increased uptake efficiency while keeping cell mortality below 5%. We optimized the area covered by the laser beam by using a motorized stage allowing homogeneous scanning of the cell culture surface using a spiral path. Calcein uptake reached median efficiency of 54.5% (range 50.3–57.3) of CECs with low mortality (0.5%, range (0.55–1.0)). After sorting by flow cytometry, CECs having taken calcein remained viable and presented normal morphological characteristics. Delivery of molecules into CECs by carbon nanoparticles activated by femtosecond laser could prove useful for future cell or tissue therapy.

and analysis, decision to publish, or preparation of the manuscript.

Competing Interests: The authors have declared that no competing interests exist.

Introduction

Corneal endothelial cells (CECs) are the sole engine for corneal transparency but cannot divide *in vivo* in humans and are therefore vulnerable. They form a monolayer of tightly packed cells in the posterior part of the cornea, separating it from the aqueous humor. Equipped with numerous ionic pumps of different and complementary functions and with a rich mitochondrial network, they permanently maintain the gradient of concentration of ionic species between the corneal stroma and aqueous humor, which extract water from the hydrophilic stroma. This active deswelling maintains the organization of collagen fibers implicated in crystal-clear corneal transparency. This population of approximately 350,000 CECs in each cornea is therefore paramount in visual function, but several diseases specifically target CECs, resulting in permanent corneal edema. Up to now, the only option for treating corneal edema is corneal grafting using a donor cornea. Corneal endothelial diseases are responsible for one third of corneal grafts performed worldwide. There is a great global scarcity of corneal tissue. We recently identified 185,000 grafts performed annually in the world (personal communication) whereas several million would be necessary to eradicate the 5 million cases of bilateral corneal blindness [1] and 10–12 million unilateral cases [2]. Alternative solutions are therefore crucial. Among possibilities, is improving the endothelial quality of stored corneas to reduce the number of tissues discarded at the end of storage period. By increasing endothelial cell density (ECD) during storage period, an estimated 20–30% of usually discarded grafts could be spared. In addition, corneas with super-high ECD would survive longer in recipients, thus avoiding or postponing re-grafting which, in very active centers, may be one of the three main indications for corneal grafting. Increasing ECD seems possible by interfering with cell cycle regulation [3]. Complementarily, production by CECs of anti-apoptotic molecules like p35 of Bcl-x(L) would reduce ECD attrition during storage [4] and probably also during and post operation. Another solution to prolong graft survival in recipients is to reduce the number of immune rejection episodes. Repeated rejections, particularly the most severe ones with delayed treatment, decrease ECD and result in chronic endothelial dysfunction that requires re-grafting in a difficult situation of higher failure risk due to allosensitization. Gene therapy of CECs, allowing a release of immunosuppressive molecules like IL10, would reduce rejection episode frequency and severity [5]. All these potential interventions require pre-graft altering of CECs with minimal toxicity. Fortunately, the cornea can be stored in eye banks for several weeks using organ culture, the preferred method in Europe [6]. This long period in conditions that favor metabolic activity (unlike short-term cold storage) provides an exceptional opportunity to alter CECs while controlling the efficiency and safety of the intervention, with a high level of safety before grafting the modified cornea in the recipient.

Numerous methods have previously been experimentally assessed to deliver molecules into CECs. Overall, viral vectors are the most efficient methods for delivering nucleic acids into cells, and CECs are no exception [7–10]. Nevertheless, for clinical applications in this field, an important issue is method acceptance by the health authorities. For instance, gene therapy using viruses, which can induce endogenous recombination, oncogenic effects and immunological stimulation, would unlikely be accepted for non-lethal diseases, nor for visual disability less severe than blindness caused by diffuse retinal or optic nerve diseases. Additionally, unlike transfection of cells for experimental purposes where high mortality may be tolerable, delivery of molecules into CECs for therapeutic purpose requires minimal collateral damage. It also seems unrealistic to remove the 350,000 CECs from the cornea, treat them in suspension, then reseed them in their initial location, therefore only *in situ* delivery methods on the intact endothelial monolayer would be a useful approach.

Among non-viral methods, various categories of chemical vectors have been developed (phospholipids, polymers, chitosan) and some have been applied to CECs [11–13]. They have similar modes of action, based on natural pathways of molecule internalization by cells, like endocytosis. Mostly used for gene delivery, they usually have low toxicity but also low efficiency compared to viruses, because of the high risk of nucleic acid degradation during internalization.

Physical methods are the last category used to deliver molecules directly and specifically into target cells. They work by transiently destabilizing the phospholipid bilayer cell membrane to allow therapeutic molecules crossing of the impermeable barrier. Several physical principles have been used in numerous cell types. Ballistic: the gene gun propels gold nanoparticles conjugated with genes at high velocity directly into cells. This may be efficient but is difficult to control and showed high damage to cells, especially CECs [14]. Electricity: electroporation by very short high voltage pulses triggers the formation of holes in cell membranes and electrophoresis of charged molecules. We previously reported $7 \pm 11\%$ of CECs transfected by GFP genes *in situ* in stored human corneas [15]. Iontophoresis uses low voltage current to push charged molecules across cell membranes, but is limited by the size of molecules delivered, precluding gene delivery in particular [16]. Both electrical methods have been combined to deliver siRNA into mice corneal epithelial cells [17]. Ultrasound: sonoporation uses ultrasound waves to disrupt cell membranes thanks to contrast agents such as microbubbles that collapse and create membrane pores. This has already allowed *in vitro* and *in vivo* transfection of rabbit corneal keratocytes [18]. Light: photoporation uses lasers to permeabilize cell membranes, with two principles described for gene therapy. Optoinjection by focusing a laser beam onto the cell surface to create a pore is an efficient single-cell treatment but remains of limited use for application to whole tissues. Transfection by laser-induced stress waves uses short laser pulses to generate stress waves that induce a transient increase of cell permeability without affecting cell viability [19]. However, none of these photoporation techniques has been tested on ocular tissues. Recently, nanoparticles (i.e. between 1 and 100 nanometers in size) activated by femtosecond laser (FsL) pulses have been used to deliver molecules of a wide range of sizes into cells with very high efficiency and without significant toxicity. Plasmonic effect induced by gold nanoparticles activated by FsL pulses has been used to transfect plasmids into non-confluent adherent melanoma cells [20], and photoacoustic effect of carbon nanoparticles (CNPs) activated by FsL (Fig 1) has been used to deliver calcein, albumin and plasmid into prostate cancer cells in suspension [21].

In the present article, we describe for the first time the delivery of a small molecule (calcein) into a fully confluent adherent monolayer of CECs, mimicking the human corneal endothelium, using carbon nanoparticles activated by FsL pulses.

Materials and Methods

Materials

Immortalized CEC line B4G12 (ACC 647) was purchased from DSMZ (Braunschweig, Germany). Human Endothelial Serum-Free Medium (SFM), 24 well tissue culture plates, ZO-1 antibodies and AlexaFluor 488 Goat anti-mouse IgG (H+L) antibodies were purchased from Fisher Bioblock Scientific (Vaulx-Milieu, France). Fibroblast Growth Factor (FGF-2), calcein, sodium dodecyl sulfate (SDS), propidium iodide (PI), trypsin/EDTA 1X and Hoechst 33342 were purchased from Sigma-Aldrich (Saint-Quentin Fallavier, France). Balanced Salt Solution (BSS) was purchased from Alcon (Rueil-Malmaison, France). Black carbon nanoparticles of 15-nanometer diameter (Black Pearls 470) were purchased from Cabot Corp and Business (Billerica, MA). Ti:Sa laser system was purchased from Thalès (Neuilly-sur-Seine, France).

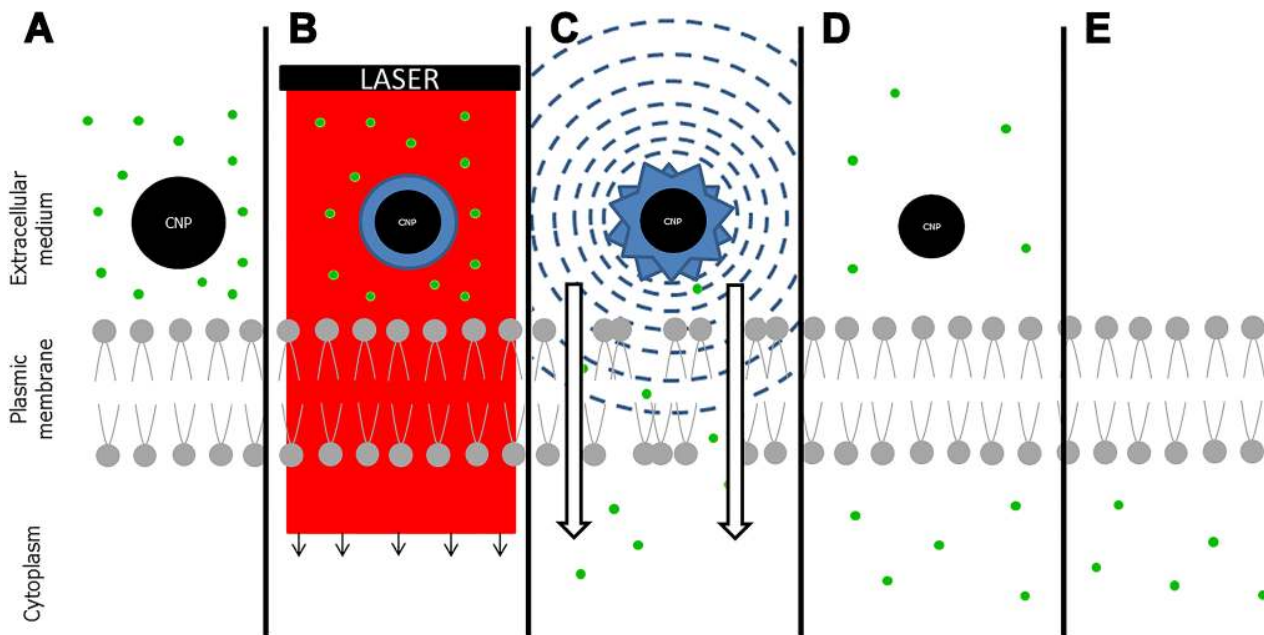


Fig 1. Principle of delivery of molecules by carbon nanoparticles activated by femtosecond laser pulses (adapted from Chakravarty et al. [21]). (A) Cells are immersed in a solution of carbon nanoparticles (CNPs) and molecules of interest; (B) a laser pulse triggers CNP heating, $C(s)+H_2O(l) = CO(g)+H_2(g)$ (s: solid; l: liquid; g: gas) and gas bubble formation. (C) once laser stops, bubbles collapse, resulting in shockwave propagation to cells. Cell membranes are permeabilized and the molecules penetrate into the cells; (D) cell membranes quickly return to their normal organization, limiting mortality; (E) rinsing removes the CNPs not consumed during reaction and molecules of interest that did not penetrate into cells.

doi:10.1371/journal.pone.0132023.g001

ANT-130 XYZ motorized stage and A3200 Software-Based Machine Controller were purchased from Aerotech (Pittsburgh, PA). The inverted fluorescence microscope was purchased from Olympus (Tokyo, Japan). FACSCalibur flow cytometer was purchased from Becton Dickinson (Franklin Lakes, NJ). Gentamycin was purchased from PAA Laboratories, (Pasching, Austria). Phalloidin was purchased from Cytoskeleton (Denver, CO).

Human Corneal Endothelial Cells

The immortalized CEC line B4G12 was cultivated in Human-Endothelial-SFM supplemented by 10 ng/mL FGF-2 at 37°C in a humidified atmosphere with 5% CO₂. In order to obtain a cell monolayer with an area close to the actual human corneal endothelium area, CECs were seeded in 24-well plates. The well diameter of 15.6 mm, larger than corneal diameter, prevented artifacts caused by the vertical well walls during laser exposure. To ensure reproducible ECD, 1x10⁴ cells were seeded in each well and cultivated for 10 days, corresponding to a tightly packed cell monolayer similar to the native corneal endothelium.

Nanoparticles and irradiation medium

Stock CNP suspension solution was prepared by sonication of 0.03g of carbon nanoparticles in 50mL of BSS with 0.077g SDS. This solution was autoclaved as per the three phases recommended for liquids: air evacuation, sterilization at 121°C for 20 min (norm NFS 90–320), and natural cooling. This stock solution was stored at room temperature until use. Stock solution of 90µg/mL of calcein was prepared by dissolution in BSS and sonication for 2 minutes. Just before the experiments, an intermediate CNP solution was prepared with 5 mL of stock CNP solution and 28.5 mL of BSS, and a solution containing CNPs, calcein and CEC culture

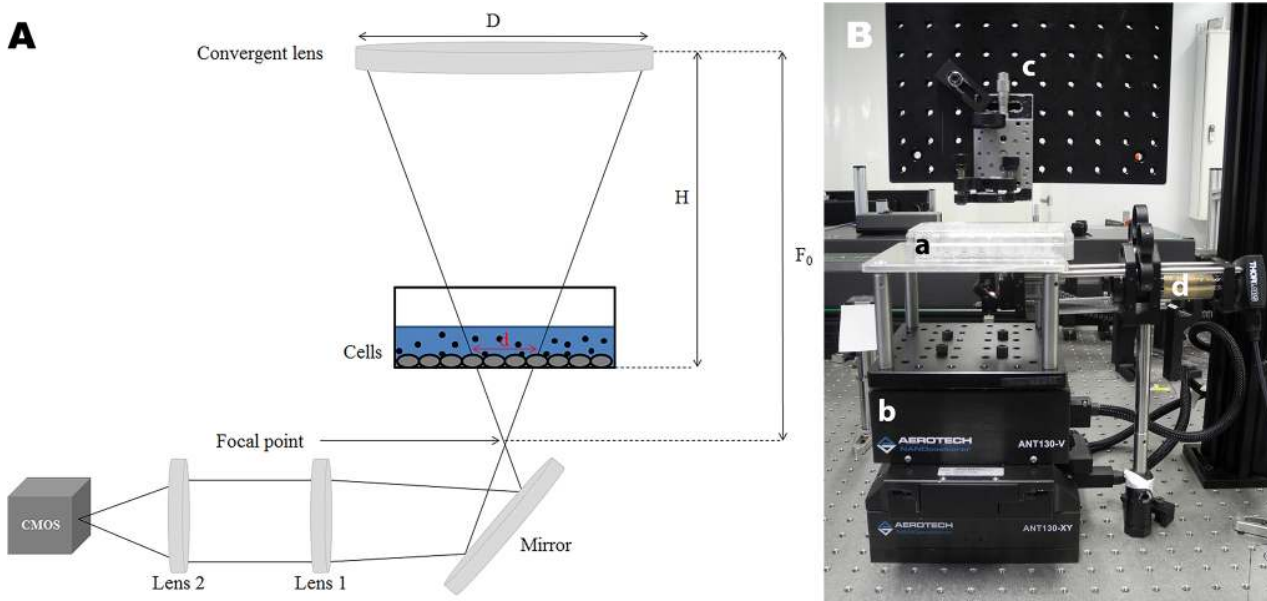


Fig 2. Adjustment of femtosecond laser fluence. (A) Schematic layout. D: Laser beam diameter before focus, H: Distance between lens/cells, d: Effective local spot area, F_0 : Focal distance of the convergent lens; The beam shape was observed in real time in order to verify the actual irradiated area and allow precise calculation of fluence. (B) Experimental settings. a: cell culture plate, b: XYZ motorized stage, c: femtosecond laser path, d: in situ system of beam observation.

doi:10.1371/journal.pone.0132023.g002

medium 1:1:1 v/v/v was prepared. Final concentration of calcein was 10 $\mu\text{g}/\text{mL}$ in the irradiation medium. Three concentrations of CNPs were first assessed (10, 30 and 90 $\mu\text{g}/\text{mL}$), and 30 $\mu\text{g}/\text{mL}$ finally used for all the subsequent experiments.

Femtosecond laser irradiation

Prior to laser irradiation, culture medium was removed and 600 μL of the irradiation medium was added. The culture plate was irradiated by a focal spot of a Ti:Sapphire FsL at a wavelength of 800 nm, with a pulse duration of 150 fs and a frequency of 5 kHz. Mean fluence received by CNPs closest to the cells was calculated by dividing the pulse energy delivered by the laser system (in joules) by the focal spot area (in cm^2). The FsL irradiation system is shown in Fig 2. The FsL spot diameter was set by the micrometric adjustment of the height of a convergent lens. It was measured precisely using an in situ system of beam observation, composed of two lenses and a camera (CMOS). We successively used two types of FsL irradiation: static and scanning.

Firstly, static irradiation was performed in order to establish the relationships between FsL/CNP/cells interactions and calcein uptake. A 1 mm diameter FsL spot was used to irradiate only a specific zone of the CEC monolayer. Using exposure time of 5 minutes and fluence of 8 mJ/cm^2 , we had previously determined that efficiency of calcein uptake decreased with the 3 CNPs concentrations of 10, 30 and 90 $\mu\text{g}/\text{mL}$ (data not shown). The intermediate value of 30 $\mu\text{g}/\text{mL}$ was then chosen because it allowed testing a wider range of laser parameters. Three exposure times (3, 5 and 10 min) and three mean fluences (6, 8 and 10 mJ/cm^2) were used, as per the initial work of Chakravarty et al. who worked on non-adherent cells [21], and our own preliminary studies.

Secondly, a scanning irradiation was performed in order to irradiate the whole area of the cell monolayer cultivated in a well. An XYZ motorized stage was used to displace the culture

plate under the FsL spot by following a spiral trajectory with a velocity of 3.5 mm/s (the same as Baumgart et al. [20]). Preliminary experiments using velocities of 2.0, 3.5 and 5.0 mm/s, all other parameters being fixed, had established a relationship between velocity and efficiency of calcein uptake, with higher uptake with a 2.0 mm/s displacement than with the 2 others (data not shown). The intermediate value was chosen because it allowed testing a wide range of laser energy; Movements of this stage were controlled with a precision of 250 nm for XY axis. Contrary to static irradiation, the exposure time was considerably reduced due to culture plate displacement, and mean fluences were increased to allow CNP activation. To obtain sufficient fluences (from 38 to 96 mJ/cm²), we used a 500 μm diameter FsL spot.

Immediately after FsL irradiation, the irradiation medium was gently removed, cells were then rinsed with BSS to remove excess calcein and CNPs, and culture medium was renewed. The culture plates were returned to the incubator for 2 hours to reduce cell stress. Three types of controls were performed in the same conditions: (1) CECs alone (no CNPs, calcein or FSL) to determine cell autofluorescence, (2) CECs incubated with CNPs and calcein without FSL to determine spontaneous calcein uptake, and (3) CECs exposed to FSL in presence of calcein but without CNPs to confirm the necessity of laser-CNP interaction. In the latter condition, the absence of CNPs in the medium led to increased laser exposure of CECs because no CNPs absorbed the light, resulting in high cell mortality (data not shown). After having measured, using spectrophotometry, that CNPs alone absorbed half of the energy (data not shown), we divided by two the fluence for this control. Experiments were repeated on three independent cell cultures and for each point at least two wells were considered (2–4).

Assessment of calcein uptake and mortality

A qualitative method and a quantitative method were used. Two hours after irradiation, cells were first observed with an inverted fluorescence microscope to determine the localization of cells with uptake of calcein (calcein + CECs) and of dead cells, as well as alterations in monolayer organization. After FsL irradiation, a working solution with Propidium Iodide (PI) stock solution (1 mg/mL) at 1:200 in culture medium was prepared and incubated with cells for 15 min at 37°C. Cells were then rinsed and culture medium was renewed. Cultures were observed using a FITC filter set (ex: 460–500/em: 512–542). Secondly, cells were studied using flow cytometry to quantify delivery efficiency and toxicity. Briefly, cells were harvested from the culture plates using 200 μL trypsin/EDTA 1X for 3 min at 37°C, resuspended in culture medium to neutralize trypsin, centrifuged at 1400 rpm for 10 minutes at 20°C, and diluted at 1x 10⁶ cells/mL in BSS. Cell suspension was assessed using a FACSCalibur flow cytometer in order to quantify the percentage of calcein+ cells (FITC+) and the percentage of PI+ cells (Cy3+). Cell autofluorescence was first determined on cells exposed to neither CNPs nor calcein.

Subcultivation of cells with calcein uptake

In order to verify whether calcein+ CECs remained viable and kept a normal phenotype, calcein+ CECs were sorted by flow cytometry and subcultured by seeding 3x10⁵ per well in 12-well plates (22.1 mm diameter, 3.8 cm²) until confluence in the medium previously described supplemented by 50 μg/mL gentamycin to prevent any contamination. At confluence, medium was removed and cell monolayer was gently rinsed with BSS, fixed with 4% PFA for staining or methanol 100% for immunostaining for 10 minutes at room temperature and permeabilized with Triton 100X at 0.5% in BSS for 5 minutes at room temperature. The CEC cytoskeletons were then stained with phalloidin at 1:500 for 15 min at room temperature to reveal F-actin, cell nuclei with Hoechst 33342 at 1:200 for 15 min at room temperature to allow determination of endothelial cell density (ECD), and apical tight-junctions were immunolabeled

with anti-ZO-1 antibodies at 1:400 for 1 night at 4°C and revealed by AlexaFluor 488 Goat anti-mouse IgG (H+L) antibody secondary antibodies using a protocol that we previously described [22].

Statistics

Percentages of cells with calcein uptake and of dead cells, quantified by flow cytometry, were described as median (range) and compared with the non-parametric Mann-Whitney test. Analyses were done using IBM SPSS Statistics V.20.

Results

Static irradiation

No spontaneous calcein uptake was observed in the absence of either FsL irradiation or CNPs. With constant fluence of 10 mJ/cm², calcein+ CECs were visible even for 3 min exposure, but their number seemed to increase with exposure time. The area of the cell culture where uptake of calcein was present was strictly restricted to the area irradiated by the FsL (1 mm in diameter), showing that the reaction was very localized. With a constant exposure of 10 min, calcein + CECs were visible only from 8 mJ/cm² and increased with fluence (Fig 3). The static irradiation proved the concept of delivery of a small molecule by CNPs activated by a FsL in a monolayer of adherent cells, and of the possibility to modulate efficiency with the laser parameters (fluence and exposure time).

Scanning irradiation and optimization of laser path

The whole culture plate area was irradiated using a scanning displacement under the FsL spot with a 15.6 mm diameter Archimedean spiral trajectory. With a spiral space interval (pitch) of 500 μm, corresponding to the FsL spot width, and a velocity of 3.5 mm/sec, the scanning

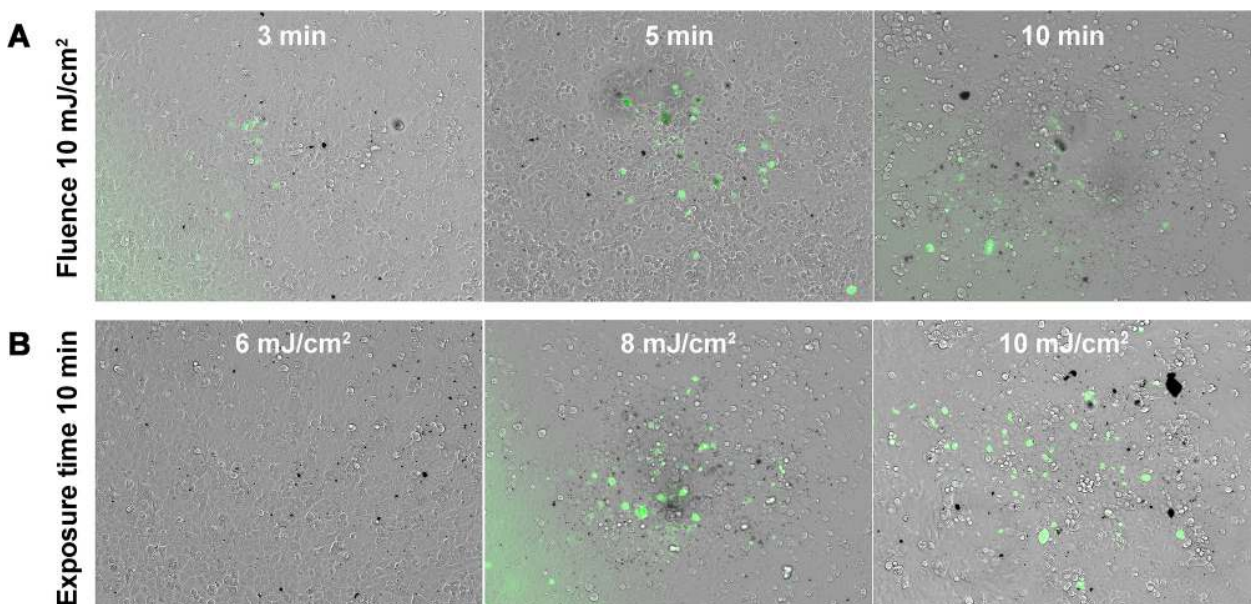


Fig 3. Static laser beam: Effect of fluence and exposure time on calcein delivery into adherent corneal endothelial cells. (A) constant fluence at 10 mJ/cm² and increasing exposure times; (B) constant exposure time at 10 min and increasing fluences. All images were obtained with a x10 objective and merged phase contrast/FITC. Green fluorescence (FITC+) indicated uptake of calcein. Scale bar 200 μm.

doi:10.1371/journal.pone.0132023.g003

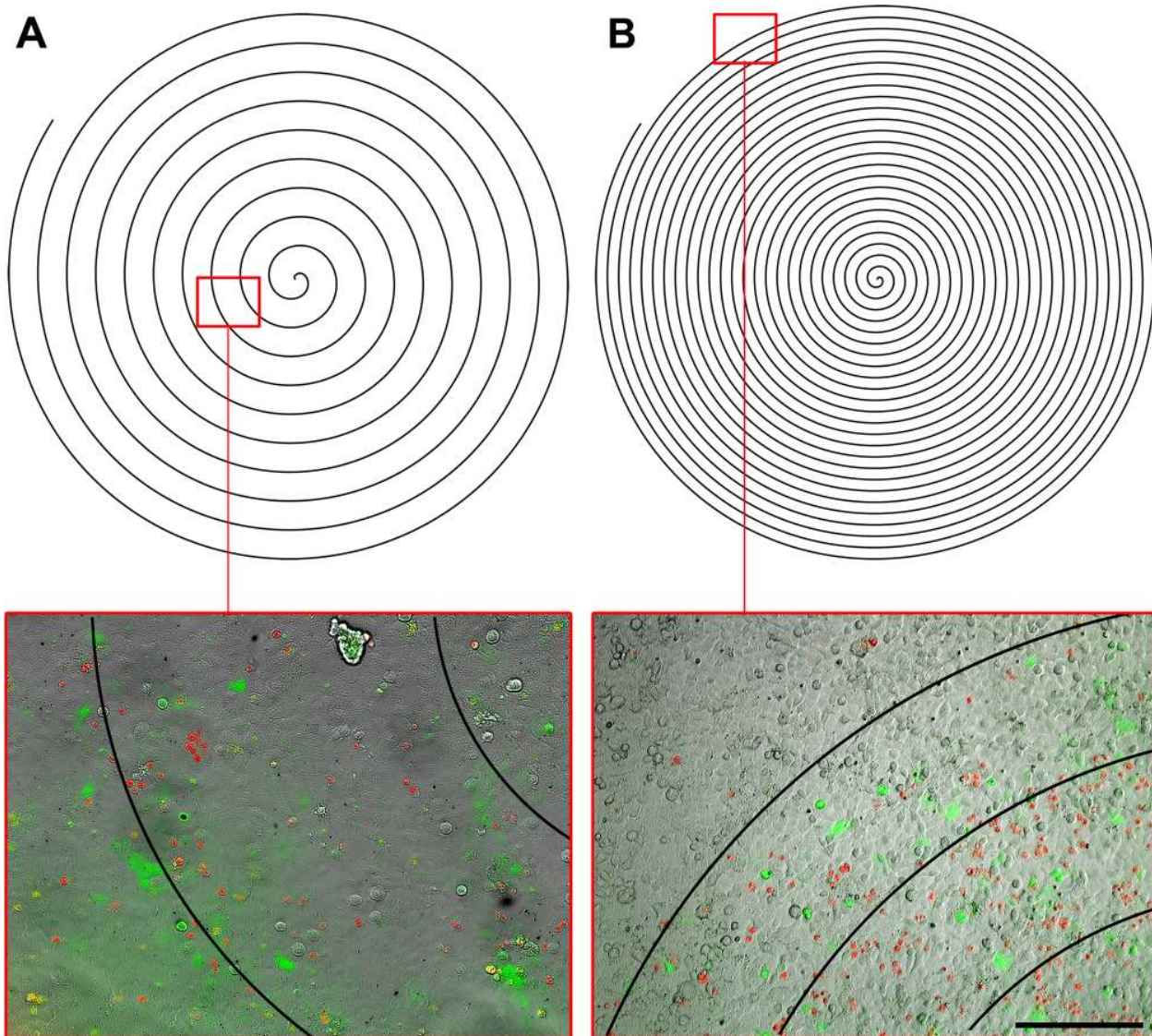


Fig 4. Scanning laser beam: Effect of beam pitch on calcein delivery into adherent corneal endothelial cells. (A) 500 μm pitch; (B) 200 μm pitch; All wells were irradiated at $142 \text{ mJ}/\text{cm}^2$ with a velocity of $3.5 \text{ mm}/\text{s}$. Merged phase contrast/Cy3/FITC/overlay representing the laser path. Note that mortality (red PI+ cells) was high in this experiment because fluence was purposely high in order to be sure to obtain uptake of calcein. It was reduced in the subsequent experiments. Green fluorescence (FITC+) indicated uptake of calcein. Scale bar 200 μm .

doi:10.1371/journal.pone.0132023.g004

irradiation lasted 2 min but microscopy observations showed that calcein uptake was not homogeneous within the monolayer. The calcein+ CECs seemed more evenly distributed in two 100 μm bands on either side of the FsL spot trajectory. With a space interval readjusted to 200 μm but the same velocity, irradiation lasted 5 min and calcein uptake was more homogeneous (Fig 4).

Scanning irradiation—Quantification of efficiency and toxicity

Calcein uptake increased significantly and almost linearly with fluence, from $38 \text{ mJ}/\text{cm}^2$ to $96 \text{ mJ}/\text{cm}^2$, while it remained almost nil for the three controls (Fig 5). The best efficiency,

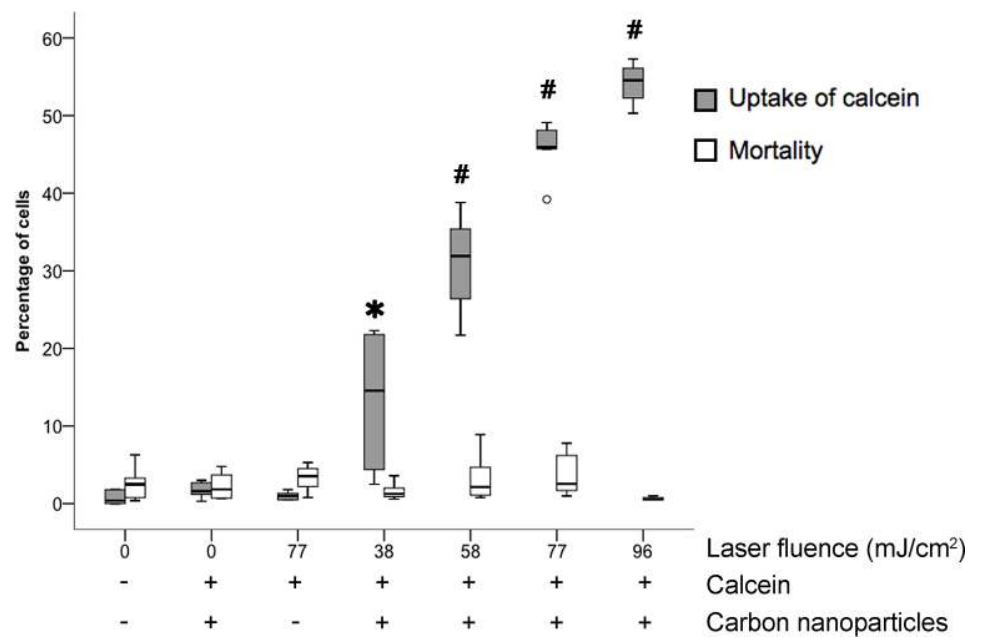


Fig 5. Effect of laser fluence on intracellular uptake of calcein and mortality of corneal endothelial cells. Box plots of the percentage of cells. The thick horizontal lines show the distribution median; boxes, the interquartile range (IQR); and individual circles, outliers. Whiskers show the highest and lowest non-outlying values. A circle is between 1.5 and 3 times the IQR. * $P < 0.05$ for calcein uptake compared to non-irradiated cells. # $P < 0.05$ for calcein uptake compared to the previous point.

doi:10.1371/journal.pone.0132023.g005

median 54.5% (range 50.3–57.3) of calcein+ CECs, was obtained with 96 mJ/cm². Toxicity on adherent cells was not significantly increased by any of the fluences of the scanning laser beam tested. However, we did not measure the rate of cell shedding following FsL irradiation.

Subcultivation of cells with calcein uptake

With 3×10^5 calcein+ CECs seeded in 3.8 cm²-well, confluence was reached after 1 week (triplicate), as for untreated CECs (7±1 day for 60 cultures). Twenty-four hours after seeding, cells lost their green fluorescence. At confluence, ECD, phalloidin and ZO-1 staining patterns were fully comparable with unirradiated control CECs (Fig 6).

Discussion

Permanent or transient alteration of CECs by delivery of specific molecules during corneal storage would help improve the availability, quality and/or outcomes of corneal grafts. The use of an efficient and non-toxic method, easily acceptable by health authorities is essential to envisage clinical applications. In the present study, we reported for the first time the use of CNPs activated by FsL to deliver a small molecule into fully confluent in vitro cultures of CECs, mimicking the native corneal endothelium, which ECD typically varies between 2000 and 3000 cells/mm² in eye banks [23]. For target applications like stimulating CEC proliferation, increasing their resistance to apoptosis and releasing immunomodulators, an efficiency of up to 54% of cells with uptake of a specific molecule and toxicity below 5% can be sufficient.

Delivery of molecules into cells using FsL activated nanoparticles is a recent, highly effective method, described to date on a non-confluent adherent melanoma cell line [20] and on cells of a human prostate cancer line and rat gliosarcoma cells in suspension [21]. The efficiency of

this new method, which can compete with viral vectors, led us to first apply the method to a confluent monolayer of tightly packed CECs, before adapting the principle to human corneas. We chose to work with B4G12 cells, one of the three well characterized immortalized lines of CECs, instead of primary CEC cultures, which present huge donor to donor variability in terms of population doubling time, of ECD at confluence, and of morphology, and risk presenting endothelial-mesenchymal transition resulting in major changes in phenotype. We also chose CNPs and not gold nanoparticles because their incubation time was shorter and less expensive, both important characteristics for future routine applications. We found a logical relationship between exposure time, laser fluence, area of cells irradiated with the scanning displacement under the FsL spot, and efficiency of delivery. Like Baumgart et al. [20], we used a scanning irradiation to increase the area of adherent cells exposed. We used irradiation of CECs along a spiral path in order to keep the displacement speed constant and consequently avoid local variation in fluence potentially associated with changes in direction in case of irradiation along parallel lines. Nevertheless, we obtained a lower rate of cells with calcein uptake than previously reported. Indeed, although we probably did not reach maximum efficiency because our FsL settings did not allow us to increase laser power, our maximum rate of 54.5%

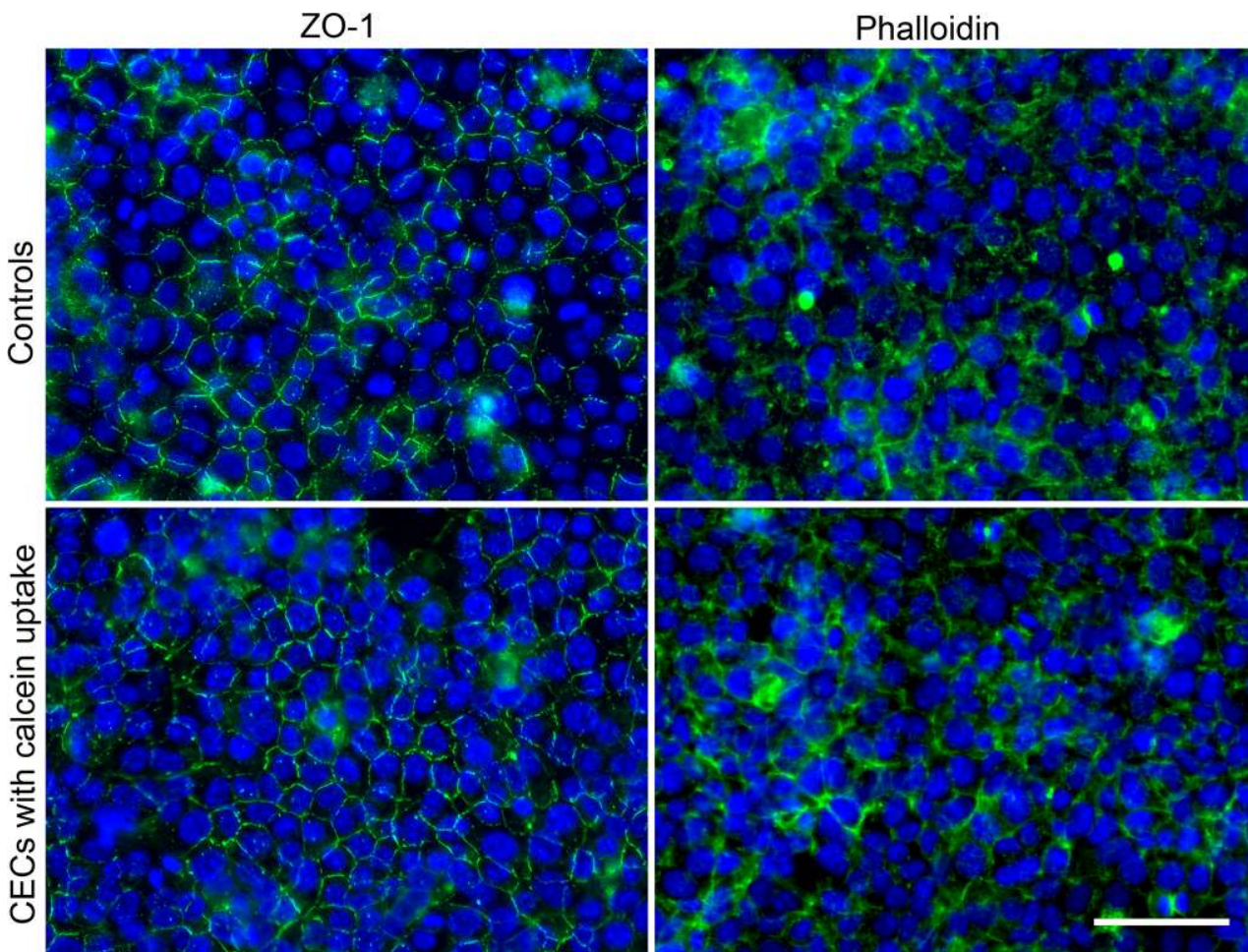


Fig 6. Morphology of calcein positive corneal endothelial cells after subsequent cultivation. ZO-1 and Phalloidin staining on calcein+ cells sorted by flow cytometry and further subcultured for 1 week were compared to control seeded at the same initial density. Nuclei were counterstained with Hoechst 33342. Merged DAPI/FITC. Scale bar 100 μ m.

doi:10.1371/journal.pone.0132023.g006

of cells with calcein uptake is far below the near 100% efficiency reached by both previously described techniques. Baumgart et al. [20] presented efficiency up to 70% and mortality around 80% with fluence of 100–120 mJ/cm². For Chakravarty et al. [21], the best efficiency/toxicity ratio was obtained at a fluence of 10 mJ/cm² for 3 min with 80% efficiency and toxicity under 10%. The main difference with our experiments is the ratio between nanoparticles and the plasma membrane area of each single cell freely exposed to the medium. The entire surface of cells in suspension and approximately half of the surface of non-confluent adherent cells are accessible. In the case of confluent CECs with high ECD, this surface is significantly smaller. Further optimizations remain possible to increase fluence, such as reducing spot diameter and scanning velocity.

Solutions also exist to decrease the mortality triggered by molecule delivery. As plasma membrane damage may be the first cause of toxicity, the use of surfactants that help heal wounds in the phospholipid bilayer after induction of holes by the photoacoustic shockwave could reduce CEC mortality. We previously showed that poloxamers and poloxamines, two macromolecules with surfactant properties, are well tolerated by CECs [24, 25]. Our next step is therefore to assess the extent to which poloxamers and poloxamines could reduce CEC death during molecule delivery by FsL-activated CNPs, while retaining high efficiency.

We must acknowledge several limitations in our study. First, we did not take account of cell detachment inside a well during irradiation and only focused on adherent cells, because it remains difficult to distinguish between whole cells and debris in culture supernatant. However, it is likely that overall mortality is slightly higher than mortality measured only on the adherent fraction. This is also a reason why, as mentioned above, we plan to assess poloxamers and poloxamines in further experiments, especially on whole corneas. Secondly, we assessed the delivery only of a small molecule of 622 Da, and results cannot be extrapolated to bigger ones like proteins or nucleic acids, which require specific experiments in our laboratory. However, delivery of high quantities of small molecules specifically into CECs can in itself be a useful goal because, for instance, rapamycin (approx. 900 Da) or ROCK-inhibitors (approx. 320 Da) have shown potential high interest respectively in corneal endothelial protection against oxidative stress [26] and in wound healing [27]. Finally, *in vitro* experiments cannot be directly extrapolated to the intact endothelium of stored cornea, although we used the human cell line most similar to the native tissue. To take a step forward, we are determining the parameters to deliver molecules directly into CECs of whole corneas during organ culture. This is particularly challenging because the shape of the cornea and the endothelial folds may induce variation of exposure to the shockwave triggered by the reaction between laser and CNPs.

Notably, cornea is by far the human tissue most exposed to FsL, a fact that could also facilitate the health authorities' acceptance of this new technique. Delivery of molecules into corneal cells using an FsL could be a new application for ophthalmology FsL, which at present is devoted solely to corneal cutting for refractive surgery and corneal graft. As the FsL is a common device easily available in Western countries and already present in several eye banks for corneal graft preparation, it could be a way to disseminate the new technique while avoiding the need for access to a research FsL.

In conclusion, this study demonstrates that the delivery of small molecules by CNPs activated by a femtosecond laser is efficient and has low toxicity in confluent adherent CECs mimicking the corneal endothelium, and anticipates what could be done on whole human corneas to improve outcomes of corneal transplantations.

Acknowledgments

We thank Julien Granier and Grégory Egaud from Manutech-USD for their help with femtosecond laser settings.

Author Contributions

Conceived and designed the experiments: CJ CM JH MP SA PG GT. Performed the experiments: CJ JH AB ZH FF. Analyzed the data: CJ CM AB GT. Contributed reagents/materials/analysis tools: ZH FF MP SA. Wrote the paper: CJ PG GT.

References

1. Oliva MS, Schottman T, Gulati M. Turning the tide of corneal blindness. *Indian journal of ophthalmology*. 2012; 60(5):423–7. doi: [10.4103/0301-4738.100540](https://doi.org/10.4103/0301-4738.100540) PMID: [22944753](https://pubmed.ncbi.nlm.nih.gov/22944753/)
2. Pascolini D, Mariotti SP. Global estimates of visual impairment: 2010. *Br J Ophthalmol*. 2012; 96(5):616–8.
3. McAlister JC, Joyce NC, Harris DL, Ali RR, Larkin DF. Induction of replication in human corneal endothelial cells by E2F2 transcription factor cDNA transfer. *Invest Ophthalmol Vis Sci*. 2005; 46(10):3597–603. PMID: [16186339](https://pubmed.ncbi.nlm.nih.gov/16186339/).
4. Fuchsluger TA, Jurkunas U, Kazlauskas A, Dana R. Anti-apoptotic gene therapy prolongs survival of corneal endothelial cells during storage. *Gene Ther*. 2011. Epub 2011/03/18. doi: [gt201120](https://doi.org/10.1038/gt.2011.20) [pii] doi: [10.1038/gt.2011.20](https://doi.org/10.1038/gt.2011.20) PMID: [21412281](https://pubmed.ncbi.nlm.nih.gov/21412281/).
5. Klebe S, Sykes PJ, Coster DJ, Krishnan R, Williams KA. Prolongation of sheep corneal allograft survival by ex vivo transfer of the gene encoding interleukin-10. *Transplantation*. 2001; 71(9):1214–20. PMID: [11397952](https://pubmed.ncbi.nlm.nih.gov/11397952/)
6. Pels L. Organ culture: the method of choice for preservation of human donor corneas. *Br J Ophthalmol*. 1997; 81(7):523–5. PMID: [9290360](https://pubmed.ncbi.nlm.nih.gov/9290360/)
7. Oral HB, Larkin DF, Fehervari Z, Byrnes AP, Rankin AM, Haskard DO, et al. Ex vivo adenovirus-mediated gene transfer and immunomodulatory protein production in human cornea. *Gene Ther*. 1997; 4(7):639–47. PMID: [9282165](https://pubmed.ncbi.nlm.nih.gov/9282165/)
8. Hudde T, Rayner SA, De Alwis M, Thrasher AJ, Smith J, Coffin RS, et al. Adeno-associated and herpes simplex viruses as vectors for gene transfer to the corneal endothelium. *Cornea*. 2000; 19(3):369–73. PMID: [10832701](https://pubmed.ncbi.nlm.nih.gov/10832701/).
9. Wilson SE, Weng J, Blair S, He YG, Lloyd S. Expression of E6/E7 or SV40 large T antigen-coding oncogenes in human corneal endothelial cells indicates regulated high-proliferative capacity. *Invest Ophthalmol Vis Sci*. 1995; 36(1):32–40. PMID: [7822156](https://pubmed.ncbi.nlm.nih.gov/7822156/)
10. Wang X, Appukuttan B, Ott S, Patel R, Irvine J, Song J, et al. Efficient and sustained transgene expression in human corneal cells mediated by a lentiviral vector. *Gene Ther*. 2000; 7(3):196–200. PMID: [10694795](https://pubmed.ncbi.nlm.nih.gov/10694795/).
11. Hudde T, Rayner SA, Comer RM, Weber M, Isaacs JD, Waldmann H, et al. Activated polyamidoamine dendrimers, a non-viral vector for gene transfer to the corneal endothelium [In Process Citation]. *Gene Ther*. 1999; 6(5):939–43. PMID: [10505120](https://pubmed.ncbi.nlm.nih.gov/10505120/)
12. Tan PH, King WJ, Chen D, Awad HM, Mackett M, Lechler RI, et al. Transferrin receptor-mediated gene transfer to the corneal endothelium. *Transplantation*. 2001; 71(4):552–60. PMID: [11258435](https://pubmed.ncbi.nlm.nih.gov/11258435/)
13. Dannowski H, Bednarz J, Reszka R, Engelmann K, Pleyer U. Lipid-mediated gene transfer of acidic fibroblast growth factor into human corneal endothelial cells. *Exp Eye Res*. 2005; 80(1):93–101. PMID: [15652530](https://pubmed.ncbi.nlm.nih.gov/15652530/).
14. Klebe S, Stirling JW, Williams KA. Corneal endothelial cell nuclei are damaged after DNA transfer using a gene gun. *Clin Experiment Ophthalmol*. 2000; 28(1):58–9. PMID: [11345348](https://pubmed.ncbi.nlm.nih.gov/11345348/)
15. He Z, Pipparelli A, Manissolle C, Acquart S, Garraud O, Gain P, et al. Ex vivo gene electrotransfer to the endothelium of organ cultured human corneas. *Ophthalmic Res*. 2010; 43(1):43–55. Epub 2009/10/16. doi: [000246577](https://doi.org/10.1159/000246577) [pii] doi: [10.1159/000246577](https://doi.org/10.1159/000246577) PMID: [19829011](https://pubmed.ncbi.nlm.nih.gov/19829011/).
16. Hao J, Li SK, Kao WW, Liu CY. Gene delivery to cornea. *Brain Res Bull*. 2010; 81(2–3):256–61. Epub 2009/06/30. doi: [S0361-9230\(09\)00193-2](https://doi.org/10.1016/j.brainresbull.2009.06.011) [pii] doi: [10.1016/j.brainresbull.2009.06.011](https://doi.org/10.1016/j.brainresbull.2009.06.011) PMID: [19560524](https://pubmed.ncbi.nlm.nih.gov/19560524/).
17. Hao J, Li SK, Liu CY, Kao WW. Electrically assisted delivery of macromolecules into the corneal epithelium. *Exp Eye Res*. 2009; 89(6):934–41. Epub 2009/08/18. doi: [S0014-4835\(09\)00230-9](https://doi.org/10.1016/j.exer.2009.08.001) [pii] doi: [10.1016/j.exer.2009.08.001](https://doi.org/10.1016/j.exer.2009.08.001) PMID: [19682448](https://pubmed.ncbi.nlm.nih.gov/19682448/).
18. Sonoda S, Tachibana K, Uchino E, Okubo A, Yamamoto M, Sakoda K, et al. Gene transfer to corneal epithelium and keratocytes mediated by ultrasound with microbubbles. *Invest Ophthalmol Vis Sci*. 2006; 47(2):558–64. Epub 2006/01/25. doi: [47/2/558](https://doi.org/10.1167/iovs.05-0889) [pii] doi: [10.1167/iovs.05-0889](https://doi.org/10.1167/iovs.05-0889) PMID: [16431951](https://pubmed.ncbi.nlm.nih.gov/16431951/).

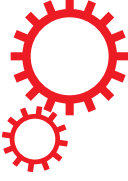
19. Doukas AG, McAuliffe DJ, Flotte TJ. Biological effects of laser-induced shock waves: structural and functional cell damage in vitro. *Ultrasound Med Biol.* 1993; 19(2):137–46. Epub 1993/01/01. PMID: [8516960](#).
20. Baumgart J, Humbert L, Boulais E, Lachaine R, Lebrun JJ, Meunier M. Off-resonance plasmonic enhanced femtosecond laser optoporation and transfection of cancer cells. *Biomaterials.* 2011; 33(7):2345–50. Epub 2011/12/20. doi: S0142-9612(11)01416-5 [pii] doi: [10.1016/j.biomaterials.2011.11.062](#) PMID: [22177619](#).
21. Chakravarty P, Qian W, El-Sayed MA, Prausnitz MR. Delivery of molecules into cells using carbon nanoparticles activated by femtosecond laser pulses. *Nat Nanotechnol.* 2010; 5(8):607–11. Epub 2010/07/20. doi: nnano.2010.126 [pii] doi: [10.1038/nnano.2010.126](#) PMID: [20639882](#).
22. He Z, Campolmi N, Ha Thi BM, Dumollard JM, Peoc'h M, Garraud O, et al. Optimization of immunolocalization of cell cycle proteins in human corneal endothelial cells. *Mol Vis.* 2011; 17:3494–511. Epub 2012/01/06. doi: 376 [pii]. PMID: [22219645](#).
23. Campolmi N, He Z, Acquart S, Trone MC, Bernard A, Gauthier AS, et al. Comparison of endothelial cell density of organ cultured corneas with the cornea donor study. *Cornea.* 2014; 33(6):597–603. Epub 2014/05/09. doi: [10.1097/ICO.000000000000124](#) 00003226-201406000-00010 [pii]. PMID: [24809309](#).
24. Zhao M, Thuret G, Piselli S, Pipparelli A, Acquart S, Peoc'h M, et al. Use of poloxamers for deswelling of organ-cultured corneas. *Invest Ophthalmol Vis Sci.* 2008; 49(2):550–9. Epub 2008/02/01. doi: 49/2/550 [pii] doi: [10.1167/iovs.07-1037](#) PMID: [18234998](#).
25. Zhao M, Campolmi N, Thuret G, Piselli S, Acquart S, Peoc'h M, et al. Poloxamines for Deswelling of Organ-Cultured Corneas. *Ophthalmic Res.* 2012; 48(3):124–33. Epub 2012/05/11. doi: 000334981 [pii] doi: [10.1159/000334981](#) PMID: [22572891](#).
26. Shin YJ, Cho DY, Chung TY, Han SB, Hyon JY, Wee WR. Rapamycin reduces reactive oxygen species in cultured human corneal endothelial cells. *Curr Eye Res.* 2011; 36(12):1116–22. Epub 2011/10/18. doi: [10.3109/02713683.2011.614372](#) PMID: [21999191](#).
27. Okumura N, Koizumi N, Ueno M, Sakamoto Y, Takahashi H, Tsuchiya H, et al. ROCK inhibitor converts corneal endothelial cells into a phenotype capable of regenerating in vivo endothelial tissue. *Am J Pathol.* 2012; 181(1):268–77. Epub 2012/06/19. doi: S0002-9440(12)00322-7 [pii] doi: [10.1016/j.ajpath.2012.03.033](#) PMID: [22704232](#).

7.8 In-situ high-resolution visualization of laser-induced periodic nanostructures driven by optical feedback

Alberto Aguilar, Cyril Mauclair, Nicolas Faure, Jean-Philippe Colombier, and Razvan Stoian (2017a). “In-situ high-resolution visualization of laser-induced periodic nanostructures driven by optical feedback”. In: *Scientific reports* 7.1, p. 16509

This paper corresponds to the postdoctoral stay of A. Aguilar in the frame of the LABEX project SERMONIS. There, high resolution in-situ monitoring of the femtosecond laser irradiated surface unveils fundamental physical phenomena in play during the formation of HSFL LIPSS. Noteworthy, the experimental effort of building a structured light microscope on a ultrafast laser irradiation beam path is not the strongest message here. It is rather the observation of the physics that triggers one’s attention. Again, these physical phenomena (stable LIPSS pattern and absolute LIPSS phase) would not have been observed without the in-situ scheme.

SCIENTIFIC REPORTS



OPEN

In-situ high-resolution visualization of laser-induced periodic nanostructures driven by optical feedback

Alberto Aguilar, Cyril Maclair, Nicolas Faure, Jean-Philippe Colombier & Razvan Stoian

Optical feedback is often evoked in laser-induced periodic nanostructures. Visualizing the coupling between surfaces and light requires highly-resolved imaging methods. We propose *in-situ* structured-illumination-microscopy to observe ultrafast-laser-induced nanostructures during fabrication on metallic glass surfaces. This resolves the pulse-to-pulse development of periodic structures on a single irradiation site and indicates the optical feedback on surface topographies. Firstly, the quasi-constancy of the ripples pattern and the reinforcement of the surface relief with the same spatial positioning indicates a phase-locking mechanism that stabilizes and amplifies the ordered corrugation. Secondly, on sites with uncorrelated initial corrugation, we observe ripple patterns spatially in-phase. These feedback aspects rely on the electromagnetic interplay between the laser pulse and the surface relief, stabilizing the pattern in period and position. They are critically dependent on the space-time coherence of the exciting pulse. This suggests a modulation of energy according to the topography of the surface with a pattern phase imposed by the driving pulse. A scattering and interference model for ripple formation on surfaces supports the experimental observations. This relies on self-phase-stabilized far-field interaction between surface scattered wavelets and the incoming pulse front.

The interaction of ultrafast pulsed laser radiation with materials in ablative regimes is at the origin of spectacular material structures with characteristic sizes beyond the diffraction limit at the incident wavelength¹. These fabricated features are then able to add a range of novel properties to the engineered material. From a process control perspective, the fundamental challenge stays with defining those light and material characteristics able to facilitate structuring of matter on mesoscopic scales. The controlled and reproducible fabrication of laser-induced structures significantly smaller than the processing optical wavelengths has thus the potential to open up the way towards efficient laser-based nanostructuring strategies. In this perspective, the ability to go on sub-micron dimensions in a controlled manner is critical for the development of laser nanotechnologies and for the design of multiscale structured materials. New surface functions can be obtained from combining structures sizes into hierarchical ensembles mixing micron and nanoscale features. These functions span a large application field, from optical and surface color design^{2,3} to controlled hydrophobicity⁴⁻⁶, hydrophilicity⁷ and bio-mimetic properties^{8,9}. Besides the fabrication aspect and in a perspective of enforcing control, the challenge consists of visualising structures with the highest achievable accuracy¹⁰. The need to monitor the fabrication process in a rapid manner makes optical technologies of interest. A tremendous effort was made recently in interrogating structures and objects with optical means giving access to the nanoscale. To overcome the diffraction limit in optical microscopy, a variety of techniques have been developed preserving at the same time the advantages of non contact investigations¹¹. For instance, Stimulated Emission Depletion (STED) microscopy, a super-resolution technique based on functional groups of molecules that show fluorescence can achieve a lateral resolution of 20 nm¹². Also, stochastic super resolution techniques such as Stochastic Optical Reconstruction Microscopy (STORM) and Photoactivated Localization Microscopy (PALM) can be used to overcome optical diffraction limit with similar performance¹³⁻¹⁵. These developments together with the present laser processing techniques enable an increased ability to produce

Laboratoire Hubert Curien, UMR 5516 CNRS, Université de Lyon, Université Jean Monnet, 42000, St. Etienne, France. Correspondence and requests for materials should be addressed to C.M. (email: cyril.maclair@univ-st-etienne.fr) or R.S. (email: razvan.stoian@univ-st-etienne.fr)

and observe at the same time laser-induced structures at and below the diffraction limit, during fabrication, improving the understanding and facilitating the control of the structuring process.

The nonlinear interaction involving ultrafast laser radiation can confine the energy on spatial scales below 100 nm via direct focusing^{1,16}. This represents a localized absorption event that can structure matter beyond the diffraction limit. The ultimate size of the modification is then defined mainly by the material response to energy absorption and transport, with scales significantly smaller than those related to light confinement. This response can be of thermomechanical, hydrodynamic, or ablative nature^{1,17,18}. One of the most spectacular laser nanostructuring processes is the formation of sub-wavelength ripples on materials ranging from metals to dielectrics. Specifically, laser radiation can trigger periodic arrangements of matter with periods going down to $\lambda/5n$, with λ being the processing wavelength and n the material optical index, (see refs^{19,20} and references therein) in spite of spatially smooth, slowly-varying incident optical fields. The so-called laser-induced periodic structures (LIPSS)²¹ combine nonlinear interaction with matter destabilization and light effects on surface topographies and are dynamically driven by optical feedback. This represents an intricate relation between the field, surface topography and its growth dynamics, where the coupling will spatially shape laser fields and local domains of energy absorption into the material. The definition of local and nonlocal collective interactions are key to the development of nanoprocessing control strategies on larger areas²². Thus, the understanding of the behavior of dynamical surfaces and the evolving coupling between topography and light is of paramount importance in upgrading the ripples arrangement quality, but equally in providing the physical insights behind material periodic rearrangement. Visualizing the process *in-situ* with resolutions capable of resolving the arrangement periods is therefore key to grasping the material dynamics and its feedback-driven topography. In the context of periodic arrangements, the sub-wavelength λ/n spaced low-spatial-frequency LIPSS (LSFL) carry a particular interest for developing patterning methods that can render particular optical, mechanical and tactile functions. Their periodicities in the range of 500–700 nm (for the typical 800 nm processing wavelength) can create optical effects in the visible domain and morphology effects on liquid contact angles on surfaces. Therefore, there is a particular interest in observing *in-situ* how the optical response of a real surface in the context of ripple formation can be drastically influenced by the surface morphology and its evolution towards ordered corrugation.

We discuss here using *in-situ* spatially-resolved observations the development of LSFL on metallic glass surfaces on a single site, from the pristine surface to the full development of the ripple pattern. The material choice is motivated the quality of ripples formation. The LIPSS alignment, which suffers often from periodicity errors and bifurcations believed to originate from self-organizational dynamics²³, has a particular quality in laser irradiated metallic glasses²⁴. In the ripple development we indicate the action range of two types of optical feedback; one related to surface topography (scattering and localization at inhomogeneities) and the second determined by the self-driven coherent interactions between driving and scattered light at constant relative phase. We apply a super-resolution optical method based on structured illumination microscopy (SIM) to observe and reconstruct LIPSS behavior during multipulse formation with ≈ 100 nm accuracy. This allows to clearly define the topography role in establishing and growing rippled patterns. The optical resolution allows for a very high quality in the optical imaging with resolving features not observable in standard optical microscopy. The *in-situ* implementation of the technique permits to observe the gradual development of regular structures from rough surfaces under multipulse exposure on the same site and allows to put forward a mechanism that stabilizes the pattern spatially. By analyzing the evolving relief on the single site, an accurate analysis of the role of light coupling on complex topographies and pattern locking mechanisms is conducted. We demonstrate intrinsic phase-locking stabilizing patterns and periodicities during ripples growth that is related to surface corrugation and light scattering. The technique allows equally to define a second feedback that can phase-lock and stabilize the pattern from independent random sites. The mechanism is intrinsically related to the self-interference between the driving and scattered light at constant relative phase. We believe that this approach carries a significant potential to observe features that are essential for nanostructures formation, that were only elusively indicated before. The understanding of periodic arrangement is essential for strategies of large area patterning using laser-based technologies.

Results and Discussion

High-resolution microscopy observation. A $Zr_{41.2}Ti_{13.8}Cu_{12.5}Ni_{10}Be_{25.5}$ (atom%) metallic superalloy undercooled to a glassy structure (bulk metallic glass, BMG)^{25,26} is used for laser nanostructuring, in the conditions where its thermoplasticity above the glass transition temperature can render high quality LIPSS^{24,27}. Single-side polished Zr-BMG samples ($Ra < 20$ nm) with a diameter of 8 mm and a thickness of 3 mm were used in the experiment. Polishing was done using diamond paste and alumina powder with grit size down to 0.1 μ m. The sample, positioned on high precision XYZ stages, was then subject to ultrafast laser irradiation derived from an amplified Ti:Sapphire laser system delivering 120 fs laser pulses at a nominal repetition rate of 1 kHz and 800 nm incident wavelength. Single pulse where selected using electro-optical and mechanical shutters and are impinging on the surface along the normal direction. The irradiation geometry follows a common path with the observation tool, as described in the Methods section, with a rather tight focusing. For each pulse, the *in-situ* SIM-picture acquisition was performed in order to follow the pulse-to-pulse LIPSS growth.

The results of laser irradiation on the Zr-based metallic glass sample are depicted in Fig. 1(a–c) using different microscopy techniques including standard optical reflection microscopy (Fig. 1(a), OM), structured illumination microscopy with contrast enhancement (Fig. 1(b), SIM) and scanning electron microscopy (Fig. 1(c), SEM). The figure shows clearly the potential of structured illumination microscopy to resolve topography details with high resolution, matching in this type of observations the information provided by SEM. We will then apply the SIM technique for *in-situ* observation of ripple development on specific sites with the number of pulses incident on the same spot. Various fluence regimes are used, unveiling explicit behaviors of LIPSS formations.

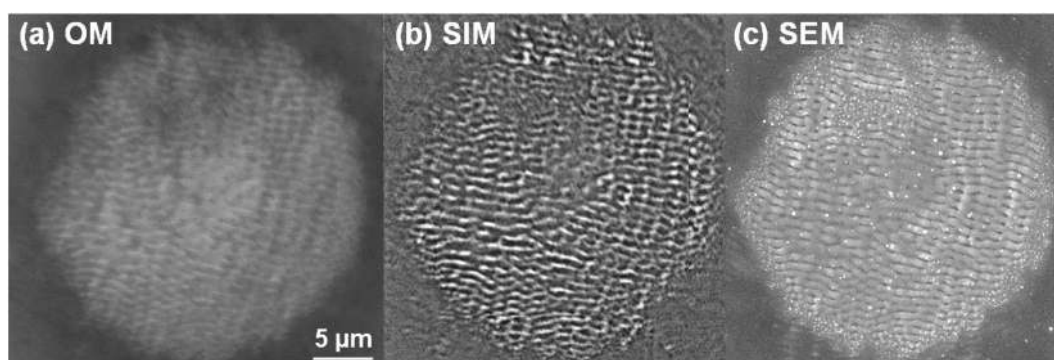


Figure 1. Visualisation of sub-wavelength ripples. LIPSS on a Zr-based BMG surface created after $N = 5$ ultrafast laser pulses using a peak fluence of 0.3 J/cm^2 . The same pattern is visualized by a range of imaging techniques. (a) Impact zone observed using a conventional bright field optical microscope (OM) in reflection mode. (b) Impact zone observed *in-situ* using SIM based technique during structuring (see text for details). (c) Impact observed *ex-situ* using a SEM technique.

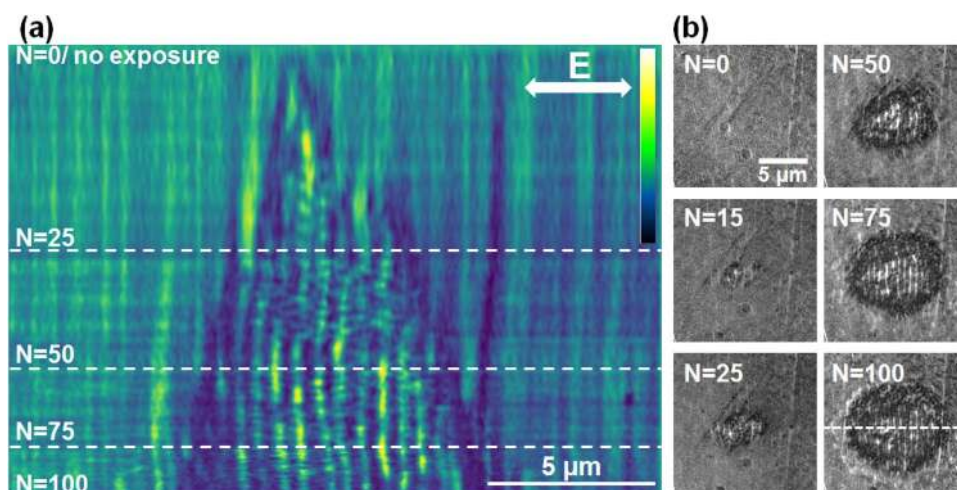


Figure 2. Evolution on LSFL formation on Zr-BMG in the low fluence regime (peak fluence of 0.09 J/cm^2). (a) Evolution of a section profile with the number of pulses N (false colors). Sectional cuts made on LIPSS images are concatenated together for each N . The LIPSS pattern is visible after a relatively high number of pulses. Light colors represent zones of higher elevation. (b) Samples of the original SIM images. The direction of the electric field and the position of the sectioning line are given on the figures.

Fluence-dependent ripple evolution. We observe now the gradual development of ripples on a single irradiated site for different incident laser fluences, starting from the threshold vicinity to ablative regimes. The results are shown in Figs 2, 3 and 4. The irradiation sequence commences on the pristine polished surface and stops at the full development of the ripples pattern.

First a low fluence dose (peak fluence of 0.09 J/cm^2) is used that generates topography ripples on the BMG surface with a period in the range of 600 nm , slightly evolving with the number of incident pulses and fluence. The pattern begins to be observable at a relatively high number of pulses ($N > 10$). This indicates that the modifications after each pulse are minimal, the structures growth is slow, almost erosion-like, and rely heavily on incubation effects. The results of irradiation with increasing number of pulses (N) on the same site are given in Fig. 2. The patterns are analyzed in the following way. For successive number of pulses incident on the same site, SIM images were taken and processed. A section is then made across the impact zone and, for each image corresponding to a given N , the resulting profiles (ripples relief) are concatenated and displayed in Fig. 2(a) for the whole N sequence. Thus the evolution at a specific location can be reconstructed. These profiles are horizontal cuts across a vertical arrangement of ripples and display the regular modulation. This representation gives an indication of the topography development with N , where the lateral dimension corresponds to structure periodic topography and the vertical dimension shows the irradiation development with the number of pulses (N). Figure 2(b) shows examples of different N sequences at the same spot, from where the section was sampled (the position of the sectioning line is given in the figure for the case $N = 100$). If topography features appear after several pulses, they are ill-defined up to $N = 30$. The pattern acquires good visibility after $N = 50$ and shows a remarkable spatial stability

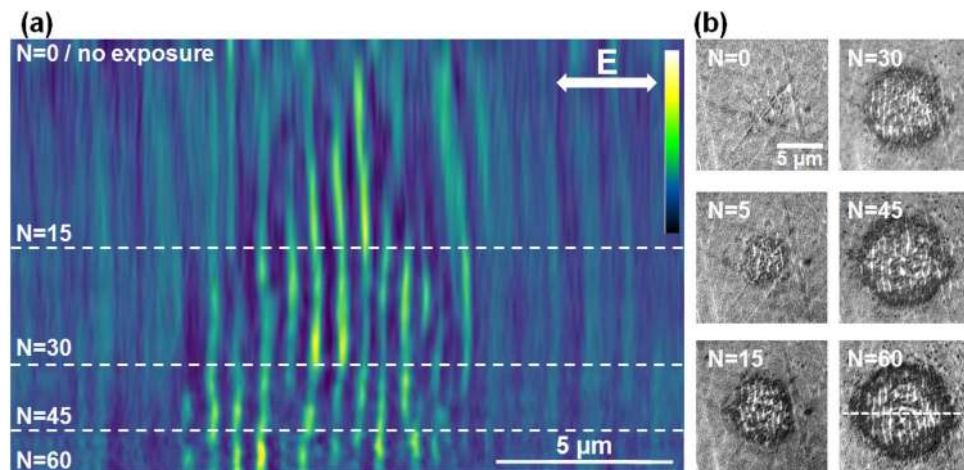


Figure 3. Evolution on LIPSS formation on Zr-BMG in the moderate fluence regime (peak fluence of 0.15 J/cm^2). **(a)** Evolution of a section profile with the number of pulses N (false colors). Sectional cuts made on LIPSS images are concatenated together for each N . The LIPSS pattern is detectable earlier in the pulse sequence. Topography features appear already from the first pulses and novel features develop laterally. Light colors represent zones of higher elevation. **(b)** Samples of the original SIM images. The direction of the electric field and the position of the sectioning line are given on the figures.

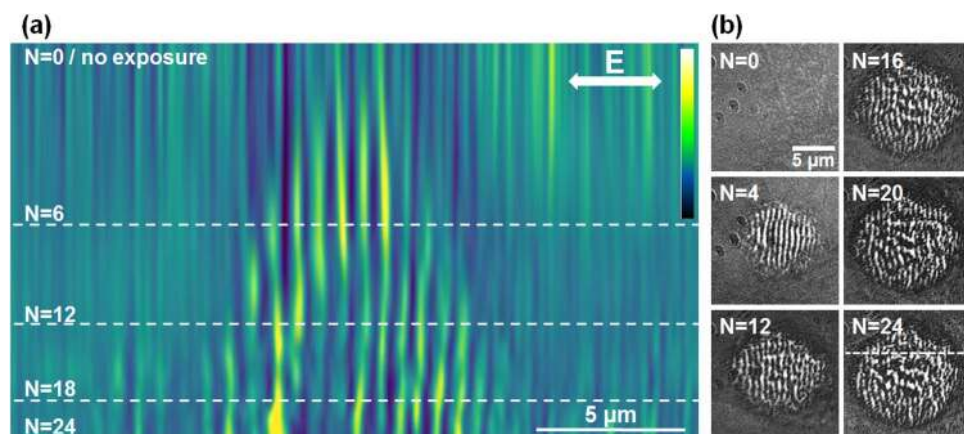


Figure 4. Evolution on LIPSS formation on Zr-BMG in a high fluence regime (peak fluence of 0.31 J/cm^2). **(a)** Evolution of a section profile with the number of pulses N (false colors). Sectional cuts made on LIPSS images are concatenated together for each N . At this regime, the rippled pattern appears early in the pulse sequence and is then followed by the formation of an ablation crater. Light colors represent zones of higher elevation. **(b)** Samples of the original SIM images. The direction of the electric field and the position of the sectioning line are given on the figures.

with well-defined topographical features preserving their positions for the present experimental conditions. It is though expectable that the period will further decrease for a high number of pulses, a situation not analysed here.

We underline here that the observation of this pattern stability is greatly facilitated by the *in-situ* SIM imaging. A similar analysis is applied for a moderate fluence regime (peak value 0.15 J/cm^2) where rippled patterns appear early in the pulse sequence and resist for a large number of pulses. The results are displayed in Fig. 3(a,b). The pattern develops gradually and grows laterally from pulse to pulse, but preserves constant topography in the affected region from pulse to pulse, with ripple peaks holding constant positions.

The last fluence regime corresponding analysis relates to a relatively high fluence (peak fluence of 0.31 J/cm^2) where rippled patterns disappear after a certain number of pulses leaving place for an ablation crater. The results are displayed in Fig. 4(a,b). We see that the topography features appear already from the first pulse and the structures are well defined for a low number of pulses. A slightly higher period of 750 nm is found here. With the number of pulses, hydrodynamic movement from the melt is observed culminating with large disordered melting and ablation feature appearing in the crater.

In all cases we observe a continuity of the pattern from pulse to pulse. The features of the profiles are spatially invariant. This is a remarkable outcome, observable only with an *in-situ* observation technique with a sufficiently-high resolution, such as the SIM microscopy employed here. The ripple pattern stays stable during

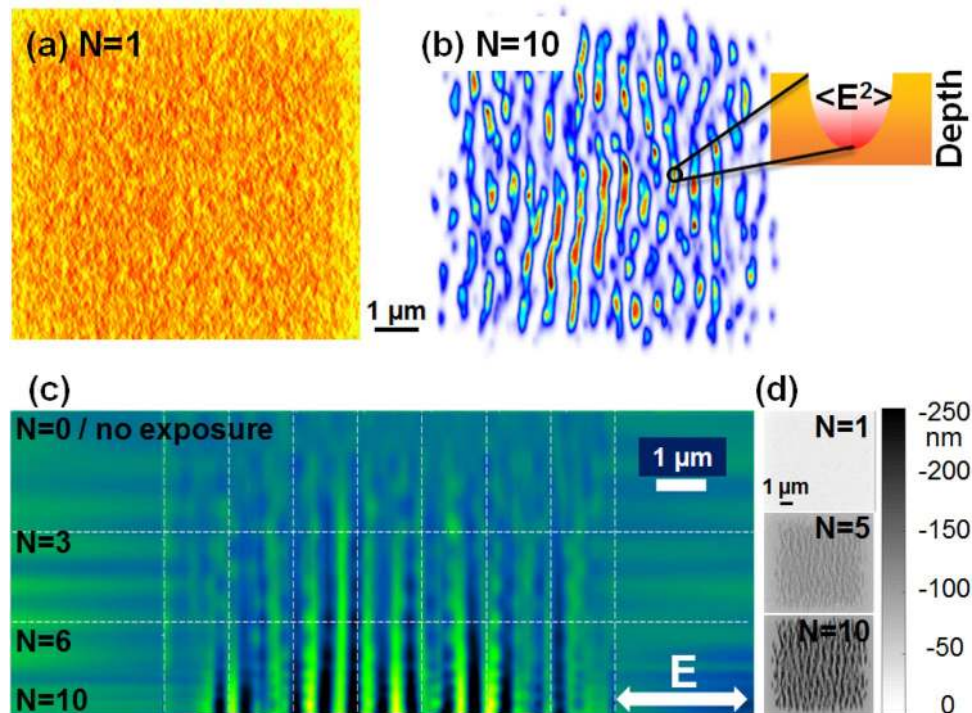


Figure 5. Electromagnetic field computations. **(a)** Simulated energy deposition pattern on Zr-BMG after exposure to a single fs laser pulse on a rough surface. A surface model is used where roughness is estimated via a distribution of 15 nm size nanoparticles and 50% filling factor. **(b)** Simulated energy deposition pattern on Zr-BMG after exposure to $N = 10$ laser pulses. We observe the onset of a clear regular pattern with a periodicity below the wavelength. The insert indicates preferential light trapping and localization at surface depressions. **(c)** Evolution on a sectional topography profile (line section of the surface relief) with the number of pulses. **(d)** Typical computed 2D surface topography profiles for an increasing sequence of incoming pulses.

the ripples growth with the increasing number of pulses for all fluence ranges. The surface relief stabilizes and becomes reinforced with each pulse, indicating that the topography can lock the pattern distribution. The relief acts as an effective phase and mode-locking mechanism in position and period. This type of stabilizing mechanism is important in developing strategies for patterning large areas, stitching together nanostructured domains and achieving high-quality corrugation upon laser scanning. A feedback mechanism based on both local (plasma evolution and near-field scattering/enhancement) and non-local (far-field scattering and interference) contributions that filters periods and drives the modulation on large domains, growing seamlessly nanostructures was considered essential^{22,28} to develop aligned structures on different periodicity scales, a mechanism which was suggested already in the early studies²⁹. The potential origin and the action range of such mechanism are discussed below from an electromagnetic perspective.

Scattering, interference, and light trapping. The experimental behavior is analyzed first from an electromagnetic perspective. The electromagnetic approach described in the *Methods* section includes an electromagnetic scattering model associated with a straightforward ablation model reflecting the local fluence dependencies and the deposited energy via evanescent components. With this simplified approach we simulate the growth of a specific laser-induced relief. We recall that for metal surface nanostructuring, two different scales of LIPSS formation are usually reported. They correspond to scattering events implying local field enhancement and near-field interactions at roughness features, referred to as high spatial frequency LIPSS (HSFL), and superposition of far-field scattered fields on these roughness centers with incident/refracted fields, referred to as low spatial frequency LIPSS (LSFL)³⁰. Let us now concentrate on the most regular ripples pattern, the LSFL.

Scattering and interference on rough surfaces. If an optical influence was early recognized²¹ for ripple formation, a comprehensive electromagnetic theory associated with roughness features appeared almost two decades later³¹. Sipe *et al.*³¹ indicated that a rough surface induces inhomogeneous absorption, where particular spatial frequencies are being preferentially absorbed and imprinted in the material. Thus, the numerical description of the field distribution on surfaces with given topographies is becoming important to evaluate the experimental observations. Following the Sipe analytical approach developed for predicting for which Fourier components the rough surface will concentrate the incident laser energy, we have first simulated a statistical rough surface defining the “selvedge region” where modulation and field enhancement will occur. A typical example of a spatial pattern of deposited energy on a randomly rough surface is given in Fig. 5(a) showing that the energy distribution becomes structured and spatially inhomogeneous. The initial roughness is assimilated to a distribution of 15 nm size nanoparticles and a filling factor of 50%. This distribution was chosen to optimize the field

modulation contrast for the sake of visibility, on the expense on a slight reduction of period. The period can be adjusted via the particles size and spacing³². The physical origin of the initial roughness can be intrinsic (polishing effects) or extrinsic (laser-induced). The latter is most probably the consequence of a laser-induced nucleation or spallation process at fluences around the melting threshold, process that exhibits a statistical dependence of an Arrhenius-like activation energy. A first laser pulse interacting with an initially flat surface close to ablation threshold nucleates solid-liquid transitions^{17,33} at specific “weak” sites, triggering subsurface voids formation, swelling or hydrodynamic instabilities³⁴. This randomly modifies the topography of the surface seen by a second pulse, for which the light coupling will be more complex. The coupling complexity involves polarization and scattering effects on the roughness centers, as well as interaction with the incoming field, defining a surface wave pattern³⁵. From the near- and far-field interaction of scattered and incident wavelets different distributions of evanescent fields emerge, imprinting their pattern on surfaces, where regular features may appear. In other words, the first step is the appearance of an interference pattern containing the beginning of regular features. For LSFL, with periodicities close to the incident wavelength, the driving field represents the interference between scattered light and the incident wavefront³⁰.

The corrugation mechanism and light trapping. To describe evolving surface topographies, the electromagnetic simulation is coupled to an ablation model, whenever the threshold is surpassed by the local fluence. In the present model the inter-pulse feedback mechanism was simplified using an holographic ablation model³⁶, where the material numerical domains (cells) absorbing more energy were considered to be removed, being replaced by air medium in our simulation. This way, both concentration and amplitude of roughness can evolve during a multipulse simulation. Using the absorption energy map with local concentration of energy driven by interference and near-field enhancement²⁷, the application of an ablation model creates an evolving surface topography with elongated surface depressions at the place of energy absorption peaks. Considering the ablation after each pulse, the topography after N irradiation events can be reconstituted. Figure 5(b) represents a typical energy deposition pattern upon normal incidence on an initially rough surface, showing the relative value of the electromagnetic energy absorption on the irradiated surface after $N = 10$ absorption-removal cycles. With increasing number of pulses, the order imposes itself with clear ordered patterns. It is noteworthy to mention that a second process occurs in addition to the interference pattern. Local surface depressions of certain depth trap preferentially the light energy, as indicated in the inset in Fig. 5(b). The region between crests is becoming more hollow, developing the ripple contrast pattern at fixed locations. With the evolution of the profile the field distribution becomes potentially more complex, with the appearance of additional Fourier components in its spatial spectrum.

The evolution of the topography. We follow now the evolution of the topography contrast upon the arrival of a successive number of pulses. The gradual exposure with increasing number of pulses acquires a structural profile. Using a section cut in the simulated 2D surface profile and concatenating the sequences as before, similar to the experimental situation, Fig. 5(c) retraces the evolution of the surface profile with the number of pulses. Each profile is derived from sectioning computed surface topography charts exposed to a varying number of pulses given in Fig. 5(d). The single site condition is ensured by adopting the same initial surface for each simulated N -case. From the profile evolution in Fig. 5(c) we observed a similar representation to that derived from the experimental results in Figs 2, 3 and 4. The simulation clearly shows that, within the removal feedback assumption here, the location of maximal energy absorption does not evolve from pulse to pulse. This strongly corroborates the phase-locked profile amplification scenario reported above based on a scattering and interference effect creating the periodicity and strong light trapping into surface depressions, reinforcing the contrast. This indicates that the main physical features are well grasped by the model, supporting the physical mechanisms proposed above. If the corrugation effect related to pulse-to-pulse evolution can involve a more complex physical picture relying on local ablation, growth, or lateral diffusion of the resulting pattern via liquid displacement, depending on the thermomechanical conditions, the main features of the stabilising feedback are essentially related to interference and potential light trapping.

Stabilizing patterns on random roughness distribution. We have defined above a first type of optical feedback related to a corrugated topography based on the interference of scattered wavelets with the incident field and light trapping into the corrugated profile. This was facilitated by super-resolved observations enabling to follow *in-situ* the gradual development of ripples on a unique irradiated site. A unique site means explicitly a single initial distribution of scattering centers and a singular ablation path, which deterministically constraints the corrugation. Following a scattering model with local and de-localized actions, we indicate that the corrugation defines the scattered pattern and field accumulation regions.

The question that appears now is: will a statistical ensemble of different initial sites with *a priori* random roughness distributions affect the pattern arrangement within the laser spot? The *in-situ* method allows to compare the irradiation results on different zones on the surface. We have performed the experiment for $N = 4$ laser pulses per site and 40 different initial zones on the sample surface. After acquiring all images, where the relative alignment is ensured by the observation method, we add the images and observe the average result. The procedure is schematically described in Fig. 6(a) and the averaging result is given in Fig. 6(b). The result preserves clearly a periodic character indicating a common absolute pattern of the LIPSS despite the random character of features on the irradiation sites, i.e. the initial surface inhomogeneities. The average of random corrugation patterns before irradiation would have given an uniform gray level distribution. The results is confirmed by performing random image correlations, with the average shift of correlation peak (a measure of the spatial phase) being smaller than $\Lambda/4$, Λ being the average pattern period. We have equally performed using the electromagnetic model described above simulations starting from several random initial distributions and summed up the results. A total of 16 simulated profile charts for $N = 10$ starting from initial random roughness functions were calculated and summed up in Fig. 6(c). We equally observe (as indicated in Fig. 6(c)) a permanent corrugation despite the initial random character of the distribution of scattering centers. The reason for this behavior lies in a subtle effect of the

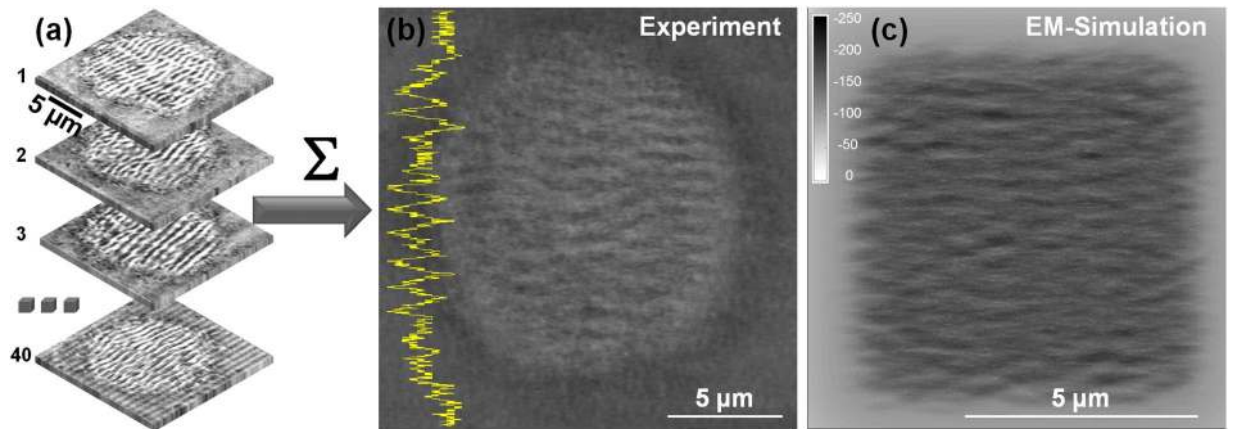


Figure 6. Statistics on random sites. (a) Individual images (40) of rippled sites irradiated on various different surface zones of the sample are summed up and averaged. (b) The mean result of the images in (a) showing a visible corrugation pattern in the sum of the various irradiated zones, suggesting a quasi-stable pattern in spite of different initial roughness conditions. A line section is equally given, emphasising spatial modulation. (c) Electromagnetic calculations showing the average pattern obtained by summing up 16 computed images initiated from a corresponding set of random initial distributions. The average of random corrugation patterns would give an uniform gray level distribution.

electromagnetic interaction between scattered waves and the incident field. Assuming that the scattered field E_{scatt} on a surface point (x_s, y_s) will contain a random phase $\phi(x_s, y_s)$ compared to the incident field E_{inc} , the modulated energy on the surface is related to the interference pattern $I_{int} \sim E_{inc} E_{scatt} \sim e^{i\phi(x_s, y_s)}$. As the correlation function ϕ is the single random variable and that the diffuser center (x_s, y_s) is δ -correlated, it can be shown that the correlation function is independent of the surface properties. This means that the phase of the final pattern will be defined by the phase of the laser electric field but not by the roughness properties. This is what we observe both numerically and experimentally where the initial surface roughness is randomly distributed.

The ensemble of experimental and numerical results indicate that an electromagnetic scattering and interference approach is able to reproduce and explain the observed facts, specifically the pattern stability within the laser spot, delivering at the same time the mechanism of spatial phase locking. A generalized electromagnetic approach as originally proposed by ref.³¹ is therefore a good approximation. A relevant question in this perspective is if the observed facts can equally be explained by a surface plasmon interference^{20,37}. Similar as scattered wave interference with the incident field, the plasmon interference (surface plasmon polariton model) would lead in our opinion to a similar conclusion with respect to the spatial arrangement. A detailed inspection of the nature of the created evanescent fields exceeds however the frame of this work and requires detailed analysis of the scattered waves³⁵. The present scattering approach has however no explicit requirement to rely on plasmonic excitation (in view to their propagation limitations on rough surfaces³⁸) as evanescent fields can be coherently generated by scattering mechanisms, and it thus represents a more general case.

Methods

Experimental procedure: structured illumination microscopy. The irradiation system presented in Fig. 7 uses a common path excitation and observation module. The SIM is integrated in the irradiation setup following the same path as the processing ultrafast laser beam. This allows the *in-situ* observation of the nanostructures during the laser structuring events.

Structured illumination microscopy (SIM) is a full-field super resolution optical technique enabling super resolution using a sinusoidal modulation on the light projected over the sample. It allows to improve by a factor of two the standard optical resolution defined by the imaging optics. Conceptually, the structured illumination is equivalent to an artificial augmentation of the observation numerical aperture, collecting and adding high-spatial frequency information to the image that is missing in standard optical microscopy. This type of microscopy was first demonstrated on fluorescent polystyrene micro-spheres³⁹ and is adapted here to investigate the LIPSS growth *in-situ* on surfaces. The SIM concept is briefly recalled here. A regular optical microscope has a resolution limit mainly related to the objective's numerical aperture (NA), leading to a cut-off in the spatial frequency domain. Thus, the microscope acts as a low-pass filter whose cut-off frequency limits the optical transfer function (OTF) of the microscope. For simplicity, this can be represented as a limiting circle in the Fourier Domain (FD) (see Fig. 7(a)). Any high frequency information of the object outside this circle is lost when imaging through the microscope. With SIM, a sinusoidal modulation of the illuminating light is performed using e.g. an amplitude grating. This modulation acts as a frequency shift of the object in the Fourier domain. If the modulation period equals the optical microscope diffraction limit, the object high spatial frequencies can be moved within the microscope's OTF (see Fig. 7(b)). By recording several images with different angles and translations of the grating, a super resolution image can be reconstructed (see Fig. 7(c)) with a resolution overcoming the diffraction limit by a factor of two. The technical description of the microscopy setup is provided below. A LED source is used for the setup with a central wavelength of $\lambda = 405$ nm and a bandwidth of 13 nm; the light is filtered by a diffuser

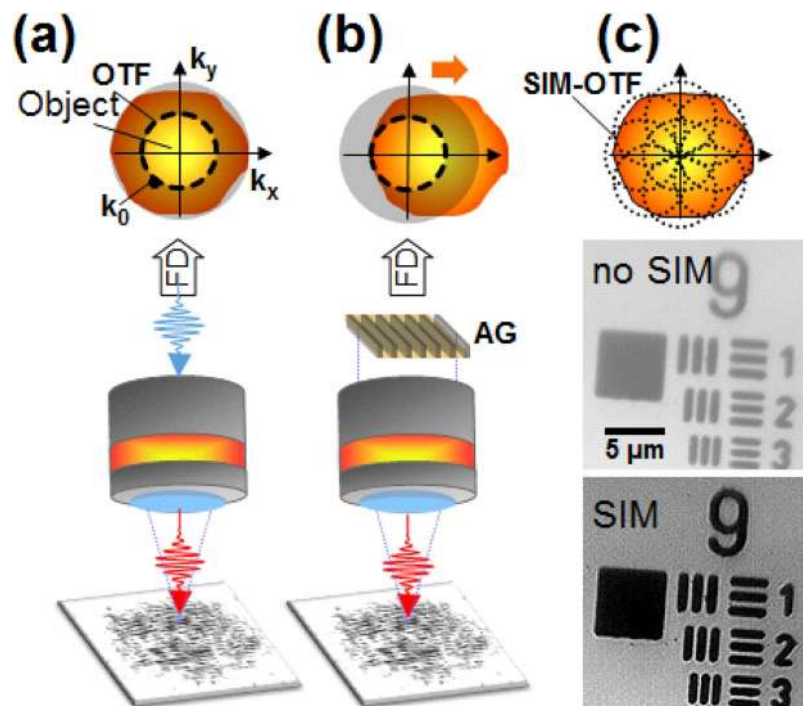


Figure 7. Experimental set-up for *in-situ* investigations of LIPSS growth using SIM. The fs laser beam in red is injected into the light path of the microscope. **(a)** Bright-field epi-illumination microscopy whose OTF is limited by the Rayleigh criterion k_0 . **(b)** SIM microscopy where a sinusoidal amplitude grating (AG) is imaged onto the sample surface. This sinusoidal modulation yields a frequency shift in the FD allowing to observe a fraction of the higher object spatial frequencies. **(c)** By recording images for an ensemble of AG positions, the SIM permits to achieve an extension of the OTF as illustrated by the pictures with and without SIM of the USAF target. The achieved lateral resolution is 150 nm.

and collimated, achieving an uniform incoherent epi-illumination. The objective NA is 0.9, yielding a Rayleigh criterion of $k_0 = 275$ nm in bright-field mode. The structured illumination light projection is performed using an amplitude grating. The grating used in our experiment is a Ronchi ruling with a period of 60 lines/mm. The grating is mounted on rotation and translation stages, such as its position and rotation can be adjusted for data gathering for the spectral domain OTF extension process. The grating can be projected onto the back focal plane of the microscope objective by means of a beam splitter. The grating magnification is given by imaging system, achieving a period of the fringes on the samples of 300 nm, which is purposely very close to k_0 . Using this experimental apparatus, the attained SIM resolution is 150 nm.

To enhance the figure contrast a image treatment procedure was applied. Periodic nanostructures contrast was enhanced using a band pass filter in the spatial frequency domain. The filter was designed to cut off the information with spatial frequency not corresponding to the nanostructures; once the filtered image was processed, an average of the filtered nanostructured image and the background image was done.

Modeling approach: electromagnetic model. An electromagnetic model in 3D geometry^{30,40} is used to calculate field irradiation patterns. The light pattern is assumed to result from a superposition of scattered wavelets from individual scattering centers with the incoming field. The inhomogeneous energy deposition below the material rough surface is computed based on 3D Maxwell's equations solved within the Finite-Difference Time-Domain (FDTD) method depicted in ref.³⁰. To construct a rough surface, the dielectric function of the top layer of the simulated material is described by a two-value function $\varepsilon_r(x, y)$. That is, $\varepsilon_r(x, y) = \varepsilon_{BMG}$, for the filled region and $\varepsilon_r(x, y) = 1$ for the unfilled region, where ε_{BMG} is the dielectric function of the simulated material. The filling factor F defined as the mean value of the binary function $f(f(x, y) = 1$ for the filled region and $f(x, y) = 0$, otherwise) was set to 0.5. Above the roughness layer, the source consisting of the electric field component E_x is injected into the computation grid as a soft source. The pulse duration was fixed to $\tau = 30$ fs to ensure a steady state solution. The pulse travels downward towards the material, impinging the surface at normal incidence. To maximize the interaction area between the incident pulse and the rough surface, the fluence distribution was a super-Gaussian type of order 7. To simulate the increasing dose a simplified ablation model is used implying material removal (15 nm rate, equivalent to 1 cell) where local fields exceed the ablation threshold. The energy absorbed in the selvedge zone is calculated in the medium assuming non-evolving optical properties, BMG $\varepsilon = -6 + 15.16i$ and air $\varepsilon = 1$. The dielectric function of the BMG does not vary significantly during the excitation period as measured by time-resolved ellipsometry³², particularly due to its multicomponent nature resulting in a large electronic density of states.

Conclusion

In conclusion, we have developed a super-resolved optical method for *in-situ* observation of laser nanostructuring processes relying on structured light illumination microscopy in a common path with the irradiation beam steering. Based on the achieved resolution and optical contrast, we have monitored the ripple formation on metallic glasses with the accumulated dose in various fluence regimes involving slow, gradual erosion-like changes at low fluence as well as the apparition of molten phases at higher fluences. We have established the action of a spatial phase-locking mechanism in the generation of laser-induced periodic structures, originating from the coherent interaction of incoming and scattered waves. This involves an implicit effect where the initial field repartition on a rough surface with corrugation in a periodic pattern will fix the light distribution for the incoming pulse. This corrugation effect acts as an effective mode-locking mechanism, filtering the resulting periodicity. The effect relies on field scattering, interference and light enforcement in surface topographical depressions. Additionally, a more subtle effect can spatially fix the pattern even on surfaces with random roughness and topographies. This is based on the fact that the superposition of scattered wavelets are self-referenced on the driving field, fixing their far-field interaction with the incoming incident light front. The phase of the pattern fixing its relative position is thus imposed by the incoming field. The highly-resolved *in-situ* observation allows thus novel essential features into the development of laser periodic nanostructures, with feedback that corrects and stabilizes period and shift. The understanding of laser-driven self-arrangement of surfaces and the driving feedback will contribute to a high level of process control in emerging laser large-scale nanostructuring techniques.

References

- Joglekar, A. P., Liu, H.-H., Meyhöfer, E., Mourou, G. & Hunt, A. J. Optics at critical intensity: Applications to nanomorphing. *Proc. Natl. Acad. Sci. USA* **101**, 5856–5861 (2004).
- Vorobyev, A. Y. & Guo, C. Colorizing metals with femtosecond laser pulses. *Appl. Phys. Lett.* **92**, 041914 (2008).
- Dusser, B. *et al.* Controlled nanostructures formation by ultra fast laser pulses for color marking. *Opt. Express* **18**, 2913–2924 (2010).
- Zorba, V. *et al.* Biomimetic artificial surfaces quantitatively reproduce the water repellency of a lotus leaf. *Adv. Matter* **20**, 4049–4054 (2008).
- Baldacchini, T., Carey, J. E., Zhou, M. & Mazur, E. Superhydrophobic surfaces prepared by microstructuring of silicon using a femtosecond laser. *Langmuir* **22**, 4917–4919 (2006).
- Bizi-Bandoki, P., Benayoun, S., Valette, S., Beaugiraud, B. & Audouard, E. Modifications of roughness and wettability properties of metals induced by femtosecond laser treatment. *Appl. Surf. Sci.* **257**, 5213–5218 (2011).
- Vorobyev, A. Y. & Guo, C. Metal pumps liquid uphill. *Appl. Phys. Lett.* **94**, 224102 (2009).
- Skoulas, E., Manousaki, A., Fotakis, C. & Stratakis, E. Biomimetic surface structuring using cylindrical vector femtosecond laser beams. *Sci. Rep.* **7**, 45114 (2017).
- Dumas, V. *et al.* Femtosecond laser nano/micro patterning of titanium influences mesenchymal stem cell adhesion and commitment. *Biomed. Mater.* **10**, 055002 (2015).
- Csete, M. & Bor Zs. Laser-induced periodic surface structure formation on polyethylene-terephthalate. *Appl. Surf. Sci.* **33**, 5–16 (1998).
- Tkaczyk, T. S. *Field guide to microscopy* (SPIE Press, Beillingham, 2010).
- Hell, S. W. & Wichmann, J. Breaking the diffraction resolution limit by stimulated emission: stimulated-emission-depletion fluorescence microscopy. *Opt. Lett.* **19**, 780–782 (1994).
- Rust, M., Bates, M. & Zhuang, X. Sub-diffraction-limit imaging by stochastic optical reconstruction microscopy (storm). *Nat. Methods* **3**, 793–796, <https://doi.org/10.1038/nmeth929> (2006).
- Betzig, E. *et al.* Imaging intracellular fluorescent proteins at nanometer resolution. *Science* **313**, 1642–1645 (2006).
- Hess, S. T., Girirajan, T. P. K. & Mason, M. D. Ultra-high resolution imaging by fluorescence photoactivation localization microscopy. *Biophys. Journal* **91**, 4258–4272 (2006).
- Korte, F. *et al.* Sub-diffraction limited structuring of solid targets with femtosecond laser pulses. *Opt. Express*, *OE* **7**, 41–49 (2000).
- Ashitkov, S. I. *et al.* Ablation and nanostructuring of metals by femtosecond laser pulses. *Quant. Electron.* **44**, 535–539 (2014).
- Bhuyan, M. K. *et al.* Ultrafast laser nanostructuring in bulk silica, a “slow” microexplosion. *Optica* **4**, 951–958 (2017).
- Buividas, R., Mikutis, M. & Juodkazis, S. Surface and bulk structuring of materials by ripples with long and short laser pulses: Recent advances. *Prog. Quant. Electron.* **38**, 119–156 (2014).
- Bonse, J., Höhm, S., Kirner, S. V., Rosenfeld, A. & Krüger, J. Laser-induced periodic surface structures—a scientific evergreen. *IEEE J. Sel. Top. Quant. Electron.* **23**, 9000615 (2017).
- Birnbaum, M. Semiconductor surface damage produced by ruby lasers. *J. Appl. Phys.* **36**, 3688–3689 (1965).
- Öktem, B. *et al.* Nonlinear laser lithography for indefinitely large-area nanostructuring with femtosecond pulses. *Nat. Photon.* **7**, 897–901, <https://doi.org/10.1038/nphoton.2013.272> (2013).
- Varlamov, S., Bestehorn, M., Varlamova, O. & Reif, J. The laser polarization as control parameter in the pattern formation. Preprint at <https://arxiv.org/abs/0902.4374> (2009).
- Zhang, W., Cheng, G., Hui, X. D. & Feng, Q. Abnormal ripple patterns with enhanced regularity and continuity in a bulk metallic glass induced by femtosecond laser irradiation. *Appl. Phys. A: Mat. Sci. Process.* **115**, 1451–1455 (2014).
- Schroers, J., Nguyen, T., O’Keeffe, S. & Desai, A. Thermoplastic forming of bulk metallic glass—Applications for MEMS and microstructure fabrication. *Mater. Sci. Eng. A-Struct* **449–451**, 898–902 (2007).
- Wang, W. H., Dong, C. & Shek, C. H. Bulk metallic glasses. *Mater. Sci. Eng. R* **44**, 45–89 (2004).
- Li, C. *et al.* Scattering effects and high-spatial-frequency nanostructures on ultrafast laser irradiated surfaces of zirconium metallic alloys with nanoscaled topographies. *Opt. Express*, *OE* **24**, 11558–11568 (2016).
- Liang, F., Vallée, R. & Chin, S. L. Mechanism of nanograting formation on the surface of fused silica. *Opt. Express* **20**, 4389–4396 (2012).
- Guosheng, Z., Fauchet, P. M. & Siegman, A. E. Growth of spontaneous periodic surface structures on solids during laser illumination. *Phys. Rev. B* **26**, 5366–5382 (1982).
- Zhang, H. *et al.* Coherence in ultrafast laser-induced periodic surface structures. *Phys. Rev. B* **92**, 174109 (2015).
- Sipe, J. E., Young, J. F., Preston, J. S. & van Driel, H. M. Laser-induced periodic surface structure. I. Theory. *Phys. Rev. B* **27**, 1141–1154 (1983).
- Li, C. *et al.* Initial cumulative effects in femtosecond pulsed laser-induced periodic surface structures on bulk metallic glasses. *J. Las. Micro/Nanoeng.* **11**, 357–365 (2016).
- Sedao, X. *et al.* Growth twinning and generation of high-frequency surface nanostructures in ultrafast laser-induced transient melting and resolidification. *ACS Nano* **10**, 6995–7007 (2016).

34. Shih, C.-Y., Shugaev, M. V., Wu, C. & Zhigilei, L. V. Generation of subsurface voids, incubation effect, and formation of nanoparticles in short pulse laser interactions with bulk metal targets in liquid: Molecular dynamics study. *J. of Phys. Chem. C* (2017).
35. Lezec, H. J. & Thio, T. Diffracted evanescent wave model for enhanced and suppressed optical transmission through subwavelength hole arrays. *Opt. Express* **12**, 3629–3651 (2004).
36. Skolski, J. Z. P., Römer, G. R. B. E., Obona, J. V. & Huis in't Veld, A. J. Modeling laser-induced periodic surface structures: Finite-difference time-domain feedback simulations. *J. Appl. Phys.* **115**, 103102 (2014).
37. Huang, M., Zhao, F., Cheng, Y., Xu, N. & Xu, Z. Origin of laser-induced near-subwavelength ripples: interference between surface plasmons and incident laser. *ACS Nano* **3**, 4062–4070 (2009).
38. Raether, H. *Surface plasmons on smooth and rough surfaces and on gratings* (Springer-Verlag, Berlin, 1988).
39. Gustafsson, M. G. Surpassing the lateral resolution limit by a factor of two using structured illumination microscopy. *J. Microsc.* **198**, 82–87 (2000).
40. Skolski, J. Z. P. *et al.* Laser-induced periodic surface structures: Fingerprints of light localization. *Phys. Rev. B* **85**, 075320 (2012).

Acknowledgements

We thank Chen Li for providing the bulk metallic glass samples and Guanghua Cheng for insightful discussions on laser structuring of metallic glasses. We equally thank Hao Zhang for the development of the FDTD code. We acknowledge the support of LABEX MANUTECH-SISE (ANR-10-LABX-0075) of the Université de Lyon, within the program “Investissements d’Avenir” (ANR-11-IDEX-0007).

Author Contributions

A.A., C.M., J.P.C., N.F., and R.S. conceived the experiments. A.A. developed the experimental setup. A.A., N.F. and C.M. conducted the experiments. A.A., C.M., J.P.C., and R.S. analyzed the data and interpreted results. J.P.C. performed the simulations. R.S. and C.M. wrote the manuscript. The authors jointly reviewed the manuscript.

Additional Information

Competing Interests: The authors declare that they have no competing interests.

Publisher's note: Springer Nature remains neutral with regard to jurisdictional claims in published maps and institutional affiliations.



Open Access This article is licensed under a Creative Commons Attribution 4.0 International License, which permits use, sharing, adaptation, distribution and reproduction in any medium or format, as long as you give appropriate credit to the original author(s) and the source, provide a link to the Creative Commons license, and indicate if changes were made. The images or other third party material in this article are included in the article's Creative Commons license, unless indicated otherwise in a credit line to the material. If material is not included in the article's Creative Commons license and your intended use is not permitted by statutory regulation or exceeds the permitted use, you will need to obtain permission directly from the copyright holder. To view a copy of this license, visit <http://creativecommons.org/licenses/by/4.0/>.

© The Author(s) 2017